# Design of a Numerical Model for Simulation of Blood Microcirculation and Study of Sickle Cell Disease



by
François Thomas Le Floch-Yin

Master of Science in Aeronautics and Astronautics, Massachusetts Institute of Technology, 2006
Ingénieur, École Centrale Paris, 2004
Master Recherche (D.E.A.) en Énergétique, Physique des Transferts et Combustion, École Centrale Paris, 2004

Submitted to the Department of Aeronautics and Astronautics in Partial Fulfillment of the Requirements for the Degree of
Doctor of Philosophy in Biomechanics and Fluid Dynamics
at the



MASSACHUSETTS INSTITUTE OF TECHNOLOGY
June 2010



Signature of Author : .....
Department of Aeronautics and Astronautics
May 20, 2010

Certified by : .....
Wesley L. Harris
Professor of Aeronautics and Astronautics, Associate Provost for Faculty Equity
Thesis Supervisor

Certified by : .....
Dava J. Newman
Professor of Aeronautics and Astronautics and Engineering Systems
MacVicar Faculty Fellow

Certified by : .....
Jonathan P. How
Richard Cockburn Maclaurin Professor of Aeronautics and Astronautics

Certified by : .....
Roger D. Kamm
Germeshausen Professor of Mechanical and Biological Engineering

Certified by : .....
Jaime Peraire
Professor of Aeronautics and Astronautics

Accepted by : .....
Eytan H. Modiano
Associate Professor of Aeronautics and Astronautics
Chair, Department Committee on Graduate Students

# Design of a Numerical Model for Simulation of Blood Microcirculation and Study of Sickle Cell Disease

by
François T. Le Floch-Yin

Submitted to the Department of Aeronautics and Astronautics on May 20, 2010
in Partial Fulfillment of the Requirements for the Degree of
Doctor of Philosophy in Biomechanics and Fluid Dynamics at the
MASSACHUSETTS INSTITUTE OF TECHNOLOGY

## ABSTRACT

Sickle cell disease is nowadays one of the most challenging blood diseases, where patients suffer from both chronic and acute episodes of painful medical conditions. In particular, unpredictable crises due to blood vessel occlusion remain one of the least understood stages of the disease, which focuses the attention of medical research. A novel methodology has been developed to address sickle cell disease, based on highly descriptive mathematical models for blood flow in the capillaries. The main focus of our original sickle cell model is the coupling between oxygen delivery and red blood cell dynamics, which is crucial to understanding sickle cell crises and is unique to this blood disease. Based on an original physical description of polymerizing sickle hemoglobin (HbS), an extensive study of blood dynamics was initiated through simulations of red cells deforming within the capillary vessels. Our investigations relied on the use of a large mathematical system of equations describing oxygen transfer, blood plasma dynamics and red cell membrane mechanics. Abnormal dynamics were characterized in terms of resistance to blood flow (apparent viscosity), and oxygen delivery performance. The results presented in this thesis describe successfully qualitative and quantitative aspects of blood dynamics preceding sickle cell crises, through a detailed comparison of normal blood with sickle cell blood. Potential therapeutical directions were successfully identified, and assessed through simulations and systematic analysis of our results. This research is expected to spur the development of innovative strategies to study sickle cell disease, and also raise interest in other related fields of blood research, promoting analysis-driven development of new therapeutical directions.

Thesis supervisor : Wesley L. Harris
Title : Professor of Aeronautics and Astronautics, Associate Provost for Faculty Equity.

# AKNOWLEDGMENTS

*A ma famille,*

*A la mémoire de mon grand-père*
*et de mes arrière-grands-mères.*
謹以此論文獻給親愛的祖父 應長生

First, I wish to express my gratitude to Professor Wesley L. Harris, for giving me this great opportunity to work together on this exciting project. More than an advisor, Professor Harris was a great permanent source of support, advice and mentorship throughout the past few years. I will always remember our discussions and times of scientific debate as a deep, profitable and enjoyable experience.

I also want to thank all my thesis committee members for their considerable input. It has been my great privilege to benefit from an incredibly large range of expertise, point of views and experiences provided by Professors Dava J. Newman, Jonathan P. How, Roger D. Kamm, and Jaime Peraire. I am also very grateful for the invaluable contributions of Medical Doctor John M. Higgins and Professor Subra Suresh who served as thesis readers.

My doctoral thesis is first and foremost dedicated to my family, whose endless love and care allowed me to always look and move forward. My work not only benefited from their everlasting support, but also bears useful contributions from my parents, M. D. Ai-Mei Le Floch née Yin and M. D. Jean-Pierre Le Floch. I only regret not having been able to spend more time with them and with my dear grandmothers, Mrs. Yin Yuen Yin née Ting and Mrs. Charlette Le Floch née Michaud.

I also thank warmly Ardemis Boghossian for all the moments shared with me, which undeniably added to my own motivation.

My years at MIT would also not have been as enjoyable without the incredible group of friends, talented individuals and free spirits that I found here. Never had I imagined that I would be surrounded by such a diversity of characters, coming from so many places all around the world.

These include my labmates at the Gas Turbine Lab (Andreas Peters, Björn Benneke, Jon Everitt, Leo Ng, Sho Sato, Shinji Tanaka, Sean Nolan, Ryan Tam, Isabelle Delefortrie, David Tarr, Alfonso Daniel Villanueva Villarreal and Barbara Brenda Botros), and my past and present roommates (Fabio Fachin a.k.a. "bibbidouche", Namiko Yamamoto and Sunny Wicks). Big up ("big casse-dédi") to Khaldoun Makhoul, Ilan Lobel, Théophane Weber and Katy Miller. Also special thanks to MIT Masters Swimming, the Baccardi Topspins, MIT Aero-Astro Water-polo team and the Unified Engineering Class of 2010.

I would like to add also an -incomplete- list of other MIT-and-around friends : Elza Brunelle-Yeung, Britt Rasmussen, Been Kim, Sameera Ponda, Caley Burke, Lucy Cohan, Eveline Steine, Allison Anderson, Blair Brettmann, Rebecca Hemenway, Natacha Yemelyanova, Corina Onderstijn, Hedde Van Horn, Rogier Kievit, Jeffrey Chambers, Jaime Mateus, Ulric Ferner, Joshua Bialkowski, Torin Clark, François-Xavier Dub, and also Anneli Jaeger, Elizabeth Butler, Heidi Rayala, Kayla Keefe, Angela Fortuna, Holly Jeffrey, Marisa Jenkins, Irene Chen, Eva Casoni, Melissa Read, Nanako Takahashi, Ghassan Fayad, David Forney, Roberto Guzman de Villoria, Roedolph Opperman, Masayuki Yano, Joachim Blanco, Daniel Greisokh, Daniel Massimini and Anton Aboukhalil. I apologize for the many other friends I forgot to mention here – you all have made my days and nights in Beantown truly unforgettable.

Finally, I wanted to thank all the faculty and staff of the Gas Turbine Laboratory, the Department of Aeronautics and Astronautics (Course 16), and to a larger extent the Massachusetts Institute of Technology who provided incommensurable advice, assistance and support to each and every step of my academic career. The MIT staff I wish to thank in particular includes Marie Stuppard and Barbara Lechner, Margaret Edwards, Susan Whitehead, Peggy Udden, Sally Chapman, Jean Sofronas, Annmarie Donovan, Kathryn Fischer and Lisa Magnano Bleheen.

# Table of Contents

# List of Figures

# List of Tables

# Conventions and Nomenclature

**Conventions :**

References to the cylindrical coordinate system use $z$ as the axial coordinate, $r$ as the radial coordinate, and $\theta$ as the polar angle coordinate. Additionally, we define for each point of the axisymmetric red blood cell membrane, $\phi$ as the azimuthal angle between the surface normal vector and the axis of symmetry, and $s$ as the curvilinear coordinate (see Figure 2.1.3). The time variable is represented by $t$.

**General Nomenclature** (notations used only in Appendices are not reported for clarity) **:**

Latin letters :

| | |
|---|---|
| $A$ | numerical state vector |
| $a, b, c, d$ | Apori-Harris model parameters |
| $B$ | bending modulus (N.m = kg.m$^2$/s$^2$ = J) |
| | numerical second term |
| $c$ | oxygen concentration ($c$ : mol/m$^3$ or kg/m$^3$) |
| $D$ | diffusion constant, a.k.a. diffusivity (m$^2$/s) |
| $d$ | rate of production of free oxygen ($c$/s) |
| | distance to membrane function of sickle cell hemoglobin polymer (m) |
| $dA$ | local area differential element (m$^2$) |
| $F$ | membrane force component (N = kg.m/s$^2$ = J/m) |
| $f$ | membrane force per unit area component (Pa) |
| $h$ | gap size between red blood cell and capillary wall (m) |
| $[Hb]$ | total hemoglobin concentration ($c$) |
| $Hct$ | hematocrit (dimensionless) |
| $K$ | Hill factor (mmHg $^{-n}$) |
| | elastic modulus (Pa.m = kg/s$^2$ = J/m$^2$) |
| | misc. model constant |
| $k$ | kinetic dissociation rate constant of oxyhemoglobin (1/s) |
| | membrane curvature (1/m) |
| | spring constant of sickle hemoglobin model (N/m = kg/s$^2$ = J/m$^2$) |
| $L$ | half-axial elongation of bolus flow (m) |
| | spatial period (m) |
| $l$ | length function of sickle cell hemoglobin polymer (m) |
| $M$ | rate of oxygen consumption ($c$/s) |
| | numerical rigidity matrix |
| $[Mb]$ | total myoglobin concentration ($c$) |
| $m$ | bending moment (N = kg.m/s$^2$ = J/m) |

| | |
|---|---|
| $N$ | oxygen-binding capacity of hemoglobin ($c$) |
| $n$ | Hill coefficient/exponent (dimensionless) |
| $p$ | static pressure (Pa) |
| $p_{O_2}$ | oxygen partial pressure (mmHg) |
| $Q$ | volume flow ($m^3/s$) |
| $q$ | shear force per unit length ($N/m = kg/s^2 = J/m^2$) |
| $R$ | fixed radius (m)<br>red blood cell membrane radius function (m) |
| $S$ | fractional saturation of oxygen-binding molecule (dimensionless) |
| $s$ | fractional saturation of oxyhemoglobin (dimensionless)<br>red blood cell stiffness |
| $t$ | surface tension component ($Pa.m = kg/s^2 = J/m^2$) |
| $U$ | velocity constant (m) |
| $u$ | Apori-Harris model velocity (m/s) |
| $V_{RBC}$ | red blood cell volume ($m^3$) |
| $v$ | velocity field component (m/s) |
| $Z$ | red blood cell membrane axial coordinate function (m) |

Greek letters and mathematical symbols :

| | |
|---|---|
| $\nabla$ | nabla operator (gradient, divergence) |
| $\partial$ | partial derivative symbol |
| $D$, $d$ | material derivative/differential quantity symbols |
| ln, sin, cos | mathematical functions (logarithm, sine, cosine) |
| $\alpha$ | oxygen solubility constant ($c$/mmHg)<br>misc. model constant (dimensionless) |
| $\Delta$ | difference between 2 values |
| $\delta$ | Dirac distribution |
| $\lambda$ | membrane extension ratio (dimensionless) |
| $\mu$ | dynamic viscosity (Pa.s for fluid, Pa.m.s for 2-D membrane) |
| $\pi$ | pi constant |
| $\rho$ | fluid density ($kg/m^3$) |
| $\Sigma$ | summation symbol |
| $\sigma_0$ | isotropic tension constant ($Pa.m = kg/s^2 = J/m^2$) |
| $\tau$ | viscous stress value/tensor |
| $\propto$ | proportional to |
| $\cdot$ | dot product |
| $\infty$ | infinity |
| $\approx$, $\sim$ | approximately equal to |

Subscripts and superscripts :

| | |
|---|---|
| 0, *ref* | reference value |
| 1, 2 | reference directions |

| | |
|---|---|
| $1, 2 (,3)$ | misc. model constants (enumerated) |
| 50% | equilibrium value at 50% saturation |
| *app* | apparent (or effective) value for whole blood |
| *b* | value in whole blood<br>boundary component |
| *bu* | bulk |
| *d* | deviatoric component |
| *Hb* | hemoglobin |
| *HbS* | sickle cell hemoglobin |
| *i* | value in the interstitium<br>at the capillary wall-interstitium interface ( $R_i$ ) |
| $i, j, k$ | numerical indices |
| *in* | boundary value at capillary vessel inlet |
| *K* | at the Krogh cylinder radius ( $R_K$ ) |
| *Mb* | myoglobin |
| max | maximal model ratio constant |
| $n, t$ | normal and tangential components on the membrane |
| *p* | value in blood plasma |
| *RBC* | value in the red blood cell cytoplasm<br>steady-state value for the whole red blood cell ( $v_{RBC}$ )<br>red blood cell membrane model value ( $\mu^{RBC}$ ) |
| $s, \theta$ | curvilinear components on the membrane |
| *sh* | shear |
| *t* | value in the surrounding tissue<br>at the interstitium-surrounding tissue interface ( $R_t$ ) |
| *w* | value in the capillary wall<br>at the capillary vessel-capillary wall interface ( $R_w$ ) |
| $z, r$ | spatial vector components |

Overbar symbols :

| | |
|---|---|
| $\rightarrow$ (e.g. $\vec{v}$ ) | vector |
| ' (e.g. $z'$ ) | moving reference frame with the red blood cell at steady-state |
| $-$ (e.g. $\bar{t}$ ) | average quantity/main component |

# 1. Motivation and relevant background research

## 1.1. Presentation of sickle cell disease

Sickle cell disease is a blood disorder that affects millions of people. Patients with sickle cell disease are characterized by a state of anemia, or deficiency of hemoglobin, the molecule carrying oxygen and found in erythrocytes (also commonly called red blood cells). In sickle cell disease, red blood cells take an abnormal crescent shape upon deoxygenating (see Figure 1.1.1), which causes major complications in blood circulation, including ischemia (restriction in blood supply), vaso-occlusion (formation of blood clots), and as a result, hypoxia (lack of oxygen in the organs), multiple organ damage and periodic painful attacks, also known as sickle cell crises.

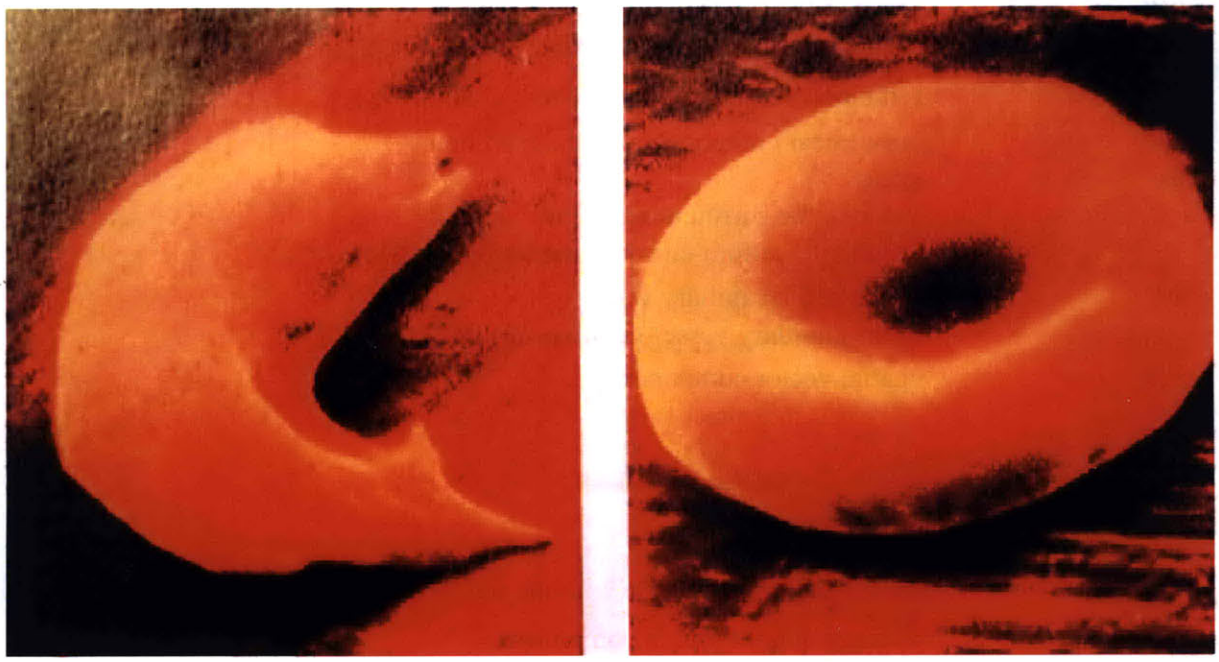

*Figure 1.1.1 : Normal (right) and Sickle (left) Red Blood Cells (source:http://carnegieinstitution.org).*

Although the medical symptoms related to sickle cell disease have been known for centuries, the clinical observations and documentation of sickle cells appeared only very lately in 1874 by surgeon A. Horton from Sierra Leone, and in 1904, by the Chicago cardiologist James B. Herrick. The disease was named sickle cell anemia in 1922 by Vernon Mason. Linus Pauling and colleagues were the first,

in 1949, to demonstrate that sickle-cell disease occurs as a result of an abnormality in the hemoglobin molecule. This was the first time a genetic disease was linked to a mutation of a specific protein, which is seen a major milestone in the emergence of molecular biology (source : http://en.wikipedia.org/wiki/Sickle-cell_disease).

### 1.1.1. Genetics of sickle cell disease

Sickle cell disease is an "autosomal recessive disease caused by a point mutation in the hemoglobin beta gene found on chromosome 11p15.5" (source : http://www.ncbi.nlm.nih.gov). Although sickle cell disease causes multiple pathologies and can be lethal, it has proven to be an evolutionary advantage against malaria : the presence of the parasite responsible for malaria in sickle red blood cells causes the rupture of the cell, making it effectively unable to reproduce. Additionally, the polymerization of hemoglobin caused by sickle cell disease prevents the parasite to digest it. In sickle cell disease, while a patient receiving the sickle cell trait from both parents (homozygous) will develop the disease, a patient with both normal and abnormal genes (heterozygous) will remain healthy, but nonetheless a carrier. Heterozygous patients produce both sickle and normal red blood cells, and have an evolutionary advantage in malaria-stricken areas [88]. Consequently, this genetic disease is mainly persistent in Africa, the Mediterranean, India and the Middle East (see Figure 1.1.2). It is also the most common inherited blood disorder in the United States, affecting an estimated number of 75,000 African Americans in 2009 (source : http://www.ncbi.nlm.nih.gov – see Figure 1.1.3).

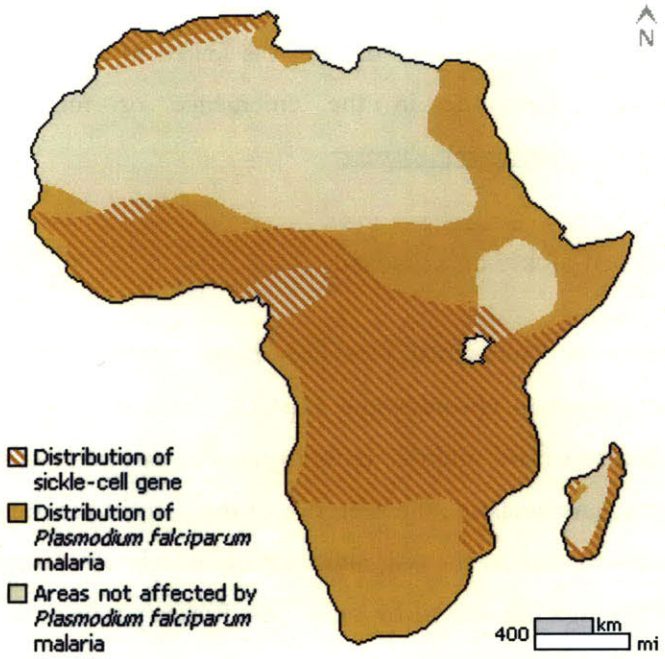


*Figure 1.1.2 : Compared geographical distributions of malaria and sickle cell trait in Africa (source:http://images.encarta.msn.com).*

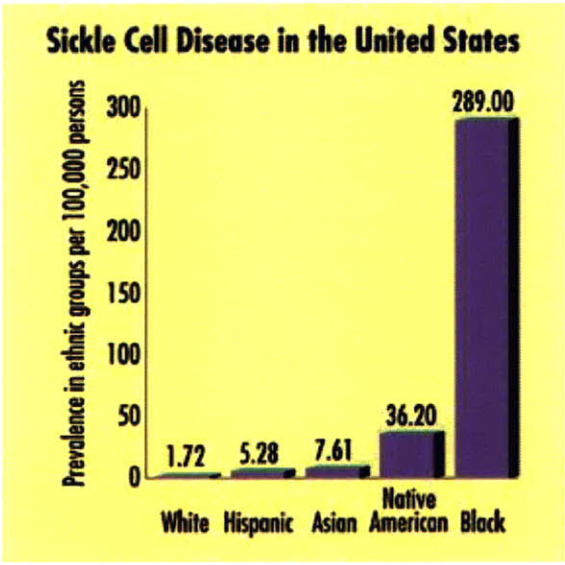


*Figure 1.1.3 : Sickle cell disease among ethnic groups in the United States (May 1996 FDA Consumer - source:http://www.pueblo.gsa.gov).*

### 1.1.2. Pathophysiology

Carriers of the sickle cell gene produce structurally abnormal hemoglobin (HbS) due to the mutation of a single nucleotide, which is normally benign but causes the hemoglobin to polymerize under low oxygen conditions (see Figure 1.1.4).

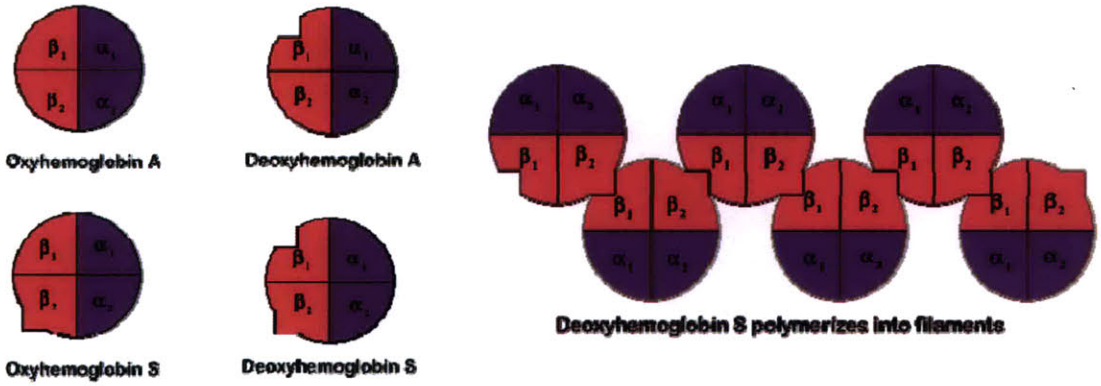


*Figure 1.1.4 : Schematic representation of normal (HbA) and sickle (HbS) haemoglobin. The haemoglobin tetramer is composed of 2 α-proteins and 2 β-proteins. The β6 mutation is indicated as a protrusion from the tetramer in the β2 subunit and the hydrophobic pocket is a nick in the β1 subunit (source:http://www.sicklecellinfo.net).*

Polymerization of hemoglobin is a major alteration of the internal structure of the red blood cell, by facilitating the emergence of long, stiff fibers in the cytoplasm (see Figure 1.1.5). These are responsible for the distortion of the shape of the cell (sickling), and a decreased global elasticity of the erythrocyte.

Elasticity is of crucial importance for red cells, which need to be able to deform to pass through capillary vessels (capillary vessels are present in every organ of the body and are the narrowest vessels, with a diameter ranging from 2 μm to 10 μm, typically smaller than a normal red blood cell at rest). Sickle cells forced into capillaries consequently suffer from membrane damage, progressively lose their ability to return to a normal shape upon reoxygenation, and can eventually block blood flow, leading to inflammatory reactions, vessel occlusion, and ischemia.

Sickle cell damages also dramatically reduce their lifespan to 10 to 20 days, while healthy red blood cells typically live 90 to 120 days (source : http://emedicine.medscape.com/article/778971-overview). This effectively reduces the hematocrit (relative volume of red cells in blood), from values between 0.36 and 0.54 in a healthy adult, to values between 0.2 and 0.3 [85].

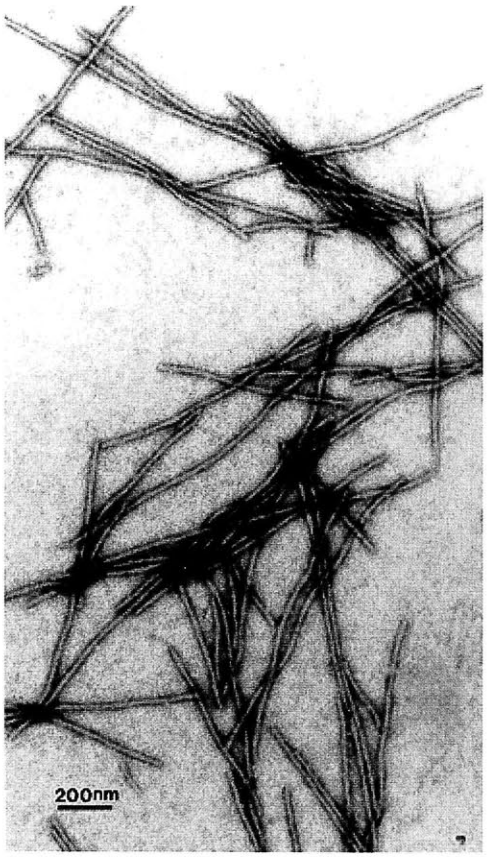


*Figure 1.1.5 : Electron micrograph of deoxy-HbS fibers (source:http://www.sicklecellinfo.net).*

However, the high variability in formation rates of the HbS fibers explains why red blood cells do not sickle systematically before getting reoxygenated in the lungs. Blood samples thus present two types of red blood cells : reversibly sickled cells (RSC) and irreversibly sickled cells (ISC). As of 2009, it is not exactly known whether ISC formation results from "gradual alteration of RSC properties during repeated cycles of sickling", or whether "they form as a consequence of a single event of sequestration and prolonged hypoxia" [67].

### 1.1.3. Treatment of sickle cell disease

Sickle cell disease has currently no fully efficient treatment, and remains a chronic and lifelong disease. Modern medicine administered to patients mainly aims at avoiding crises, relieving symptoms and preventing complications.

Acute vaso-occlusive crises are mostly treated symptomatically through analgesics, together with opioids for pain management. Further complications leading to bone, joints and organ damage or

stroke usually require hospitalization, where HbA hemoglobin is administered. Further treatment essentially consists in limiting long-term sequelae.

The only approved treatment as of today, for prevention of chronic attacks and other complications of the disease, consists in administering hydroxyurea, a drug that has been approved very recently in the United States (1998). The main benefic effect of hydroxyurea is to reactivate fetal hemoglobin (HbF) as a replacement to the deficient hemoglobin (HbS). There is however little knowledge of long-term effects of the drug, and its use does certainly not eliminate the risks of acute states.

In addition to drug research and crises management, recent medical research has also included bone marrow transplantation (proven to be effective in children), and gene therapy.

One of the main challenges of sickle cell disease remains in fully understanding the onset of vaso-occlusive crises, which has been investigated for only a few decades. The emergence of improved models for blood circulation in the capillaries, reinforced by the most recent techniques used to investigate mechanical and chemical properties of blood cells, creates the opportunity for new tools to study sickle cell disease, and potentially identify new therapeutic orientations. This is the main motivation of this doctoral work.

## 1.2. Blood models and background work towards a chemical and mechanical description of red blood cells (RBC)

A mathematical model for sickle cell disease needs to take into account three aspects of blood circulation. As oxygen is a major factor affecting blood dynamics in sickle cell disease, we first include a model to analyze oxygen transport, from Red Blood Cells (RBC) where the oxygen is bound to hemoglobin, to the surrounding tissue. A proper fluid dynamics model incorporates oxygen convection, and allows us to characterize blood flow with respect to pressure drop, viscosity of the blood plasma and cytoplasm, and other geometrical and physical parameters. Since RBCs essentially flow individually at the capillary level, blood dynamics are mainly dependent upon their individual mechanical properties, which are also to be incorporated with a membrane model.

This section presents successful theoretical works which constitute major inputs to our current simulation model, reviewing main hypotheses and modeling choices that have evolved with research.

### 1.2.1. Blood as an oxygen carrier : chemical modeling of the capillaries and surrounding tissue

The first successful model describing oxygen transport from the capillaries to surrounding tissues was achieved by Krogh [1] as early as 1919, and updated only recently by Hoofd [2], McGuire and Secomb [3], then Vadapalli, Goldman and Popel [108]. The original Krogh model was extensively used until the 1990's by many theoretical researchers such as Berger [123], because of its simplicity and flexibility. This conceptual model was based on Krogh's observation of the distribution of capillary vessels in muscular tissues (see Figure 1.2.1), and consequently distinguished 3 areas of interest : (1) the cytoplasm contained in the RBC, (2) the plasma surrounding it, and (3) the tissue surrounding the capillary vessel, where oxygen is consumed. These 3 areas correspond to regions where oxygen production/diffusion, convection/diffusion and consumption/diffusion respectively, are the main characteristics of oxygen transport. This 3-layer model is represented in Figure 1.2.2, as used by Berger.

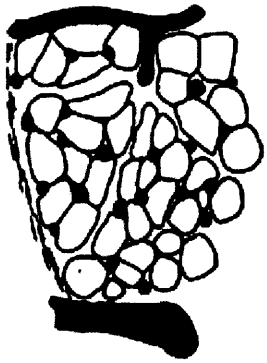

Fig. 5. Transverse section of injected muscle of the tongue of the cat. × 260.

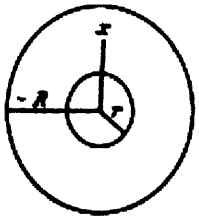

Fig. 6. See text.

*Figure 1.2.1 : Schematic representation of the distribution of capillaries in muscular tissue (black dots), and Krogh's subsequent modeling [1].*

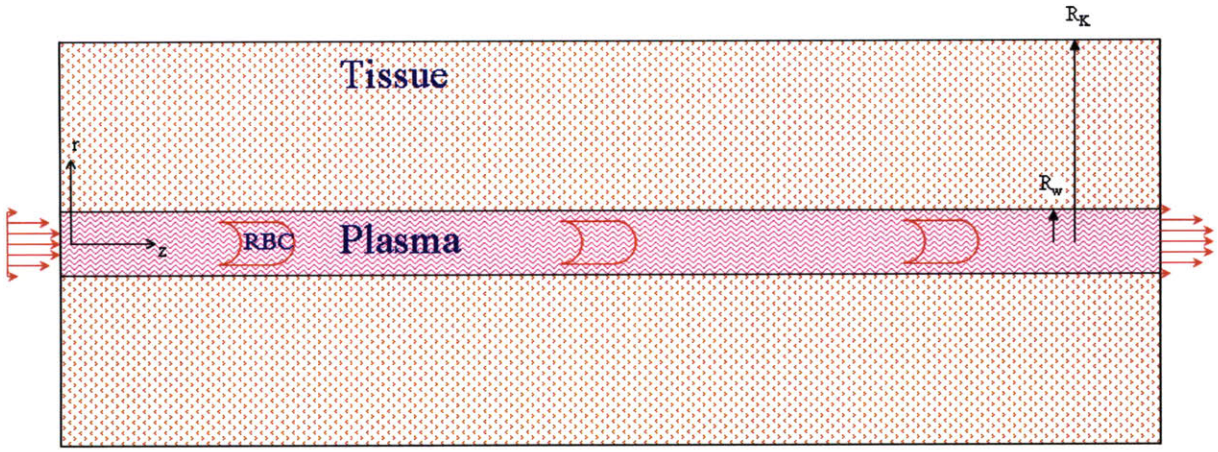


*Figure 1.2.2 : Krogh's model for oxygen delivery in the capillaries, as used by Berger [123].*

Following Krogh's model and until recently, the 3-layer model was described by the following equations, under the assumptions of steady state and axisymmetric, unidirectional flow :

- In the capillary :

$$v_z \frac{\partial c}{\partial z} - D_b \left( \frac{\partial^2 c}{\partial r^2} + \frac{1}{r} \frac{\partial c}{\partial r} \right) = d(c), \tag{1}$$

where $z$, $r$ are spatial variables (cylindrical coordinates), $c$ represents the oxygen concentration (typically expressed in molar volume or in volume fraction), $v_z$ is the axial blood velocity (taken as a constant, i.e. as the radial area average), $D_b$ is the (radial) oxygen diffusivity in blood, and $d(c)$ represents the rate of production of free oxygen through dissociation of oxyhemoglobin (oxygen-bound hemoglobin found in RBCs). In Berger and King [123], $d(c)$ is expressed as linearly related to the rate of fractional saturation of hemoglobin :

$$d(c) = - N \frac{Ds}{Dt}, \tag{2}$$

where $N$ is the oxygen-binding capacity of hemoglobin and $s$ is the fractional saturation. Using the Hill equation for the oxygen partial pressure $p_{O_2}$ [123] :

$$s = \frac{K \, {p_{O_2}}^n}{1 + K \, {p_{O_2}}^n}, \tag{3}$$

where $K$ and n are coefficients depending on ionic strength and pH, and Henry's law [123] :

$$c = \alpha \, p_{O_2}, \tag{4}$$

where $\alpha$ is the solubility constant taking the value $\alpha_b$ in blood, Equation (1) can be reduced to :

$$v_z \left( 1 + N \frac{n K \alpha_b^{-n} c^{n-1}}{(1 + K \alpha_b^{-n} c^n)^2} \right) \frac{\partial c}{\partial z} = D_b \left( \frac{\partial^2 c}{\partial r^2} + \frac{1}{r} \frac{\partial c}{\partial r} \right). \quad (5)$$

More details about hemoglobin dissociation are given in Appendix A. Alternatively, Equation (5) can be normalized with the value of oxygen partial pressure at 50% saturation of hemoglobin, to be used in replacement of $K$, $p_{O_2,50\%}{}^n = K^{-1}$ :

$$v_z \left( 1 + N \frac{n p_{O_2,50\%}{}^n \alpha_b^{-n} c^{n-1}}{(p_{O_2,50\%}{}^n + \alpha_b^{-n} c^n)^2} \right) \frac{\partial c}{\partial z} = D_b \left( \frac{\partial^2 c}{\partial r^2} + \frac{1}{r} \frac{\partial c}{\partial r} \right) \quad (5')$$

- In the surrounding tissue :

$$D_t \left( \frac{\partial^2 c}{\partial r^2} + \frac{1}{r} \frac{\partial c}{\partial r} \right) = M, \quad (6)$$

where $D_t$ is the (radial) oxygen diffusivity in the tissue (axial diffusion being simply neglected), and $M$ is the rate of consumption of oxygen (given as a constant).

- At the capillary-tissue interface :

$$D_b \left. \frac{\partial c}{\partial r} \right|_{r=R_w^-} = D_t \left. \frac{\partial c}{\partial r} \right|_{r=R_w^+}, \quad (7)$$

which represents continuity of the oxygen flux and where $R_w$ is the radius at the capillary wall, and :

$$\left. \frac{c}{\alpha_b} \right|_{r=R_w^-} = \left. \frac{c}{\alpha_t} \right|_{r=R_w^+}, \quad (8)$$

which represents continuity of oxygen partial pressure, assuming an infinitely thin membrane, with $\alpha_t$ the oxygen solubility constant in the tissue.

- At the axis of symmetry :

$$\left. \frac{\partial c}{\partial r} \right|_{r=0} = 0, \quad (9)$$

which is a necessary condition for $c$ to be continuously derivable everywhere (the oxygen radial flux must cancel at $r = 0$).

- At the Krogh cylinder radius :

$$\left.\frac{\partial c}{\partial r}\right|_{r=R_K} = 0, \tag{10}$$

where $R_K$ is the average half-distance between two capillaries in this ideal model (it can also be interpreted as a characteristic radius of "effective oxygen supply" of the capillary).

Berger and King used these simple equations to solve mathematically the oxygen distribution for given flows along capillary vessels, depending on rheological parameters and other parameters derived from modeling the flow of blood for normal and sickle red blood cells. These models and their results will be discussed further in Section 1.2.5.

The main contribution of Hoofd [2] was to introduce the myoglobin as an oxygen-binding protein to describe unsteady oxygen consumption in the surrounding tissue. This essentially led to replace Equation (6) with the following equation :

$$\frac{\partial c}{\partial t} = D_t \left( \frac{\partial^2 c}{\partial r^2} + \frac{1}{r} \frac{\partial c}{\partial r} \right) - M + d_{Mb}(c), \tag{11}$$

where $d_{Mb}(c)$ represents the rate of oxygen released by myoglobin, which can be expressed in a similar way than for hemoglobin, leading to the equation :

$$\left( 1 + N^{Mb} \frac{\alpha_t^{-1}}{(p_{O_2,50\%}^{Mb} + \alpha_t^{-1} c)^2} \right) \frac{\partial c}{\partial t} = D_t \left( \frac{\partial^2 c}{\partial r^2} + \frac{1}{r} \frac{\partial c}{\partial r} \right) - M, \tag{12}$$

where we used a Hill constant n equal to 1 for myoglobin, which is characteristic of non-cooperative binding (see Appendix A).

McGuire and Secomb [3] later added considerations about intravascular resistance to oxygen diffusion, as an apparent jump in oxygen partial pressure. Vadapalli, Goldman and Popel [108] eventually used a more advanced model, adding the 2 layers of the vascular wall and interstitial space between the capillary vessel and the surrounding tissue, defining the RBC as a separate region with specific equations, and taking into account hemoglobin-bound oxygen kinetics inside the RBC. Assuming unidirectional steady flow, their full equations for unsteady oxygen transport are expressed in terms of the oxygen partial pressure $p_{O_2}$ :

- In the RBC :

$$\alpha_{RBC} \left( \frac{\partial p_{O_2}}{\partial t} + v_{RBC} \frac{\partial p_{O_2}}{\partial z} \right) = \alpha_{RBC} D_{RBC} \left( \frac{1}{r} \frac{\partial}{\partial r} \left( r \frac{\partial p_{O_2}}{\partial r} \right) + \frac{\partial^2 p_{O_2}}{\partial z^2} \right)$$

$$+ k^{Hb}\,[Hb]\left(S^{Hb} - \left(1 - S^{Hb}\right)\left(\frac{p_{O_2}}{p^{Hb}_{O_2,50\%}}\right)^n\right), \qquad (13)$$

where $\alpha_{RBC}$ is the oxygen solubility constant in the cytoplasm, $v_{RBC}$ is the RBC (axial) velocity (constant for steady flow), $D_{RBC}$ is the isotropic oxygen diffusivity, $k^{Hb}$ is the kinetic dissociation rate constant of oxyhemoglobin, $[Hb]$ is the total concentration of hemoglobin (bound and not bound to oxygen) present in the RBC, $S^{Hb}$ is the fractional saturation of oxyhemoglobin, $n$ is the Hill coefficient of the oxyhemoglobin dissociation curve, and $p^{Hb}_{O_2,50\%}$ is the oxygen partial pressure at an equilibrium corresponding to $S^{Hb} = 0.5$ . To this equation must be added the transport equation of oxyhemoglobin :

$$\frac{\partial S^{Hb}}{\partial t} + v_{RBC}\frac{\partial S^{Hb}}{\partial z} = D^{Hb}_{RBC}\left(\frac{1}{r}\frac{\partial}{\partial r}\left(r\frac{\partial S^{Hb}}{\partial r}\right) + \frac{\partial^2 S^{Hb}}{\partial z^2}\right)$$

$$- k^{Hb}\left(S^{Hb} - \left(1 - S^{Hb}\right)\left(\frac{p_{O_2}}{p^{Hb}_{O_2,50\%}}\right)^n\right), \qquad (14)$$

where $D^{Hb}_{RBC}$ is the isotropic diffusivity of oxyhemoglobin. Equations (13) and (14) naturally reduce to Equation (5') under steady state and at chemical equilibrium, neglecting diffusion of oxyhemoglobin compared to diffusion of oxygen, and with $N = [Hb]$.

- In the blood plasma surrounding RBCs :

$$\alpha_p\left(\frac{\partial p_{O_2}}{\partial t} + v_r\frac{\partial p_{O_2}}{\partial r} + v_z\frac{\partial p_{O_2}}{\partial z}\right) = \alpha_p D_p\left(\frac{1}{r}\frac{\partial}{\partial r}\left(r\frac{\partial p_{O_2}}{\partial r}\right) + \frac{\partial^2 p_{O_2}}{\partial z^2}\right), \qquad (15)$$

where $\alpha_p$ is the oxygen solubility constant in the plasma, $v_r$ and $v_z$ are the velocity components of the flow (in this model reduced to Stokes flow for low Reynolds number), and $D_p$ is the corresponding isotropic oxygen diffusivity.

- In the capillary wall :

$$\alpha_w\frac{\partial p_{O_2}}{\partial t} = \alpha_w D_w\left(\frac{1}{r}\frac{\partial}{\partial r}\left(r\frac{\partial p_{O_2}}{\partial r}\right) + \frac{\partial^2 p_{O_2}}{\partial z^2}\right) - M_w, \qquad (16)$$

where $\alpha_w$ is the oxygen solubility constant, $D_w$ is the isotropic oxygen diffusivity, and $M_w$ is the rate of oxygen consumption.

- In the interstitium :

$$\alpha_i \frac{\partial p_{O_2}}{\partial t} = \alpha_i D_i \left( \frac{1}{r} \frac{\partial}{\partial r} \left( r \frac{\partial p_{O_2}}{\partial r} \right) + \frac{\partial^2 p_{O_2}}{\partial z^2} \right), \quad (17)$$

where $\alpha_i$ is the oxygen solubility constant and $D_i$ the isotropic oxygen diffusivity specific to this region.

- In the muscular tissue :

$$\left( \alpha_t + [Mb] \frac{p^{Mb}_{O_2,50\%}}{(p^{Mb}_{O_2,50\%} + p_{O_2})^2} \right) \frac{\partial p_{O_2}}{\partial t} =$$

$$\left( \alpha_t D_t + D_t^{Mb} [Mb] \frac{p^{Mb}_{O_2,50\%}}{(p^{Mb}_{O_2,50\%} + p_{O_2})^2} \right) \left( \frac{1}{r} \frac{\partial}{\partial r} \left( r \frac{\partial p_{O_2}}{\partial r} \right) + \frac{\partial^2 p_{O_2}}{\partial z^2} \right) - M_t , \quad (18)$$

where $\alpha_t$ is the oxygen solubility constant, $[Mb]$ is the total concentration of myoglobin (bound and not bound to oxygen) present in the tissue, $D_t^{Mb}$ is the isotropic diffusivity of myoglobin, $D_t$ the isotropic oxygen diffusivity, and $M_t$ the rate of oxygen consumption.

This model of Vadapalli, Goldman and Popel being the most advanced to this date, we will use it as our main reference for oxygen transport equations, with an adapted set of flow hypotheses.

### 1.2.2. Blood as a viscous flow : fluid dynamics of microcirculation

Burton [4] and Fung [5] [6] [12] were pioneers in developing hemodynamics, which is the study of fluid dynamics applied to blood flow. Their work, together with the work of Batchelor [7], Charm [8] and Cokelet [9], has largely contributed to provide detailed and accurate models to describe blood flow, both specifically in large vessels, as described in Pedley [10], and in the microcirculation, as described by Wiedeman [11]. In particular, Charm's work includes an extensive study of blood viscosity, its non-Newtonian properties and potential models, and the influence of red blood cells in shear-thinning and shear-thickening situations [8]. Also, Wiedeman's book includes a description of capillary networks and flow distribution. A couple of other useful sources include Milnor [13], Sumpio [14], and Pedrizzetti [15].

Fung defines blood as "a non-Newtonian incompressible viscoplastic fluid", behaving when it is not flowing "like an elastic solid", with a small yield stress (when the yield condition is reached, the blood flows) [12]. One of the main reasons for blood to be non-Newtonian is the presence of red

blood cells, which tend to flow away from the vessel walls and aggregate. In capillary vessels, the flow was first described similarly to larger vessels with steady flow, using Poiseuille's equation for a homogeneous, viscous flow down a cylinder. Poiseuille's assumptions lead to the classical pressure-flow relation :

$$\frac{dp}{dz} = -\frac{8\,\mu\,Q}{\pi\,R_w^{\,4}}, \tag{19}$$

where $z$ is the axial coordinate along the vessel, $p$ is the static pressure, $\mu$ is the dynamic viscosity of whole blood, $R_w$ is the radius of the cylinder, and $Q$ is the total volume flow. This result assumes a parabolic distribution of the axial velocity $v_z$ across the cylinder. To accommodate non-Newtonian flow, experiments were carried out to determine the equivalent $\mu_{app}$, or apparent whole blood viscosity, matching Equation (19) for different values of $Q$, $R_w$ or the shear stress at the vessel wall.

However the previous model proved to be insufficient, as none of these parameters could individually determine $\mu_{app}$, and a better insight was desired. Fung's study of the bolus flow (flow between 2 red cells in the capillaries) originated an idealized geometry separating individual cells periodically (see Figure 1.2.3). In this model the RBCs flow one-by-one, effectively dragging a thin cylinder of flow at velocity U. The flow between 2 cells can be determined solving Stokes flow, and Fung determined that for a low Reynolds number the velocity profile differs from a Poiseuille flow by less than 1% at an axial distance of 1.3 $R_w$ from the RBC cylinders [12].

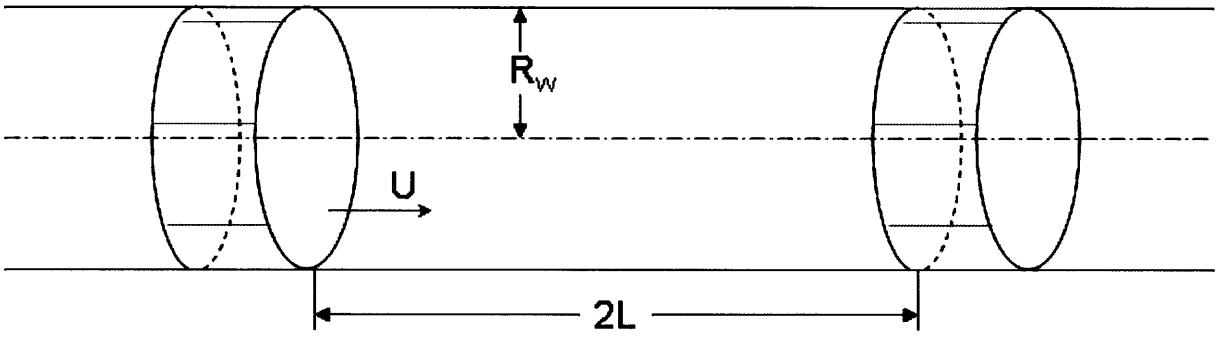


*Figure 1.2.3 : Idealized geometry for bolus flow (from Fung [12]).*

In this last model, the actual flow around a red blood cell remains to be calculated, and depends on the modeling of the RBC itself as a deformable cell (see Section 1.2.3). More advanced models emerged eventually with advanced numerical capabilities to solve more complicated fluid dynamics,

so that currently the flow is generally computed everywhere using the full Navier-Stokes equations or Stokes flow for low Reynolds number under steady conditions.

### 1.2.3. Blood as a cell suspension : mechanical modeling of the red blood cell membrane

One of the main features of the microcirculation is its non-homogeneous flow. With typical vessel diameter ranging from 2 μm to 10 μm, simple microscope observation shows that red blood cells flow individually in the smallest vessels (see Figure 1.2.4), and therefore need to be taken into account to describe blood dynamics appropriately. Basic descriptions of red blood cells refer to them as "pellets", or "sacks" filled with cytoplasm and oxygen-fixing hemoglobin. Therefore they are usually described by a deformable, infinitely thin membrane, filled with homogeneous fluid of identical or close properties to blood plasma (with a few exceptions such as dynamic viscosity). Fung and Skalak were among the main researchers who developed this model, producing until the late 1970's major results for rigid spheres, disks, mathematically-modeled RBC shapes (see Figure 1.2.5), and other rigid axisymmetric particles under steady axisymmetric flow. Skalak later defined for the isotropic 2-dimensional model of the RBC membrane the strain energy [17] and elastic moduli, studied the variability of the defined elastic moduli, and determined numerical solutions for deformable shapes under different conditions of flow and capillary sizes [19] [20] [22] [24]. In Evans and Skalak's *Mechanics and Thermodynamics of Biomembranes*[19], the constitutive equations describing isotropic RBC membranes are derived for small isothermal deformations :

$$\bar{t} = \sigma_0 + K_{bu} \frac{dA}{dA_0} , \tag{20}$$

$$t_d = \frac{1}{2} \frac{1}{\left(1+\frac{dA}{dA_0}\right)^2} K_{sh} (\lambda_1^2 - \lambda_2^2) , \tag{21}$$

$$m = \left(1 + \frac{dA}{dA_0}\right) B (k - k_0) , \tag{22}$$

where $\bar{t}$ and $t_d$ are the principal components of tension ($\bar{t}$ is the isotropic or mean term, and $t_d$ the shear or deviatoric term, derived directly from the stress tensor), $\sigma_0$ is the isotropic tension for the reference state (commonly called surface tension for liquids), $K_{bu}$ is the isothermal area

compressibility modulus (or 2-D bulk modulus), $K_{sh}$ is the 2-D shear modulus, $\frac{dA}{dA_0}$ represents the area change with respect to the reference state, and $\lambda_1$ and $\lambda_2$ are the extension ratio in the reference directions (hence $\frac{dA}{dA_0} = \lambda_1 \lambda_2 - 1$). In Equation (22), $m$ is the bending moment in any principal direction, $B$ is the bending modulus, $k$ is the total curvature (sum of curvatures in reference directions), and $k_0$ the reference value of $k$ at rest ("natural" curvature).

A more complex model incorporates viscoelastic behavior, although it was designed for low-stress situations where viscous stresses are not negligible (i.e. in-vitro, micropipette testing experiments) [22]. In that particular case, Equations (20) and (21) take the form :

$$\bar{t} = \sigma_0 + K_{bu} \frac{dA}{dA_0} + \frac{\mu_{bu}^{RBC}}{1 + \frac{dA}{dA_0}} \frac{\partial\left(\frac{dA}{dA_0}\right)}{\partial t}, \tag{20'}$$

$$t_d = \frac{1}{2} \frac{1}{\left(1+\frac{dA}{dA_0}\right)^2} K_{sh} \left(\lambda_1^{\,2} - \lambda_2^{\,2}\right) + \mu^{RBC} \left(\frac{1}{\lambda_1} \frac{\partial \lambda_1}{\partial t} - \frac{1}{\lambda_2} \frac{\partial \lambda_2}{\partial t}\right), \tag{21'}$$

where $\mu^{RBC}$ and $\mu_{bu}^{RBC}$ are the coefficients of dynamic (shear) viscosity and bulk viscosity of the modeled 2-D RBC membrane.

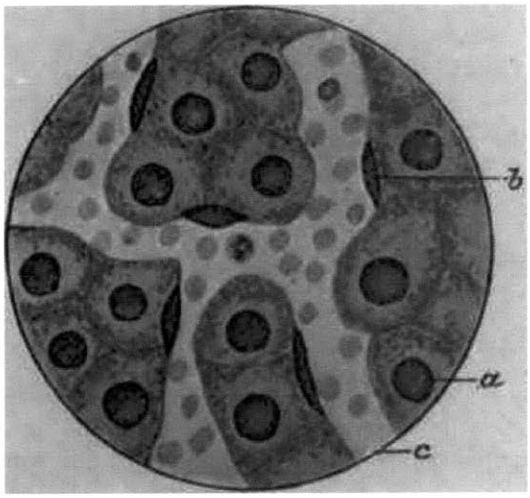


*Figure 1.2.4 : Microscopical section of human liver : c-capillary vessels with RBCs (anucleated) and white cells (nucleated), a-nucleus of liver cell, 3-nucleus of cell from capillary wall (source: Alcohol, Its Production, Properties, Chemistry, And Industrial Applications, by Charles Simmonds).*

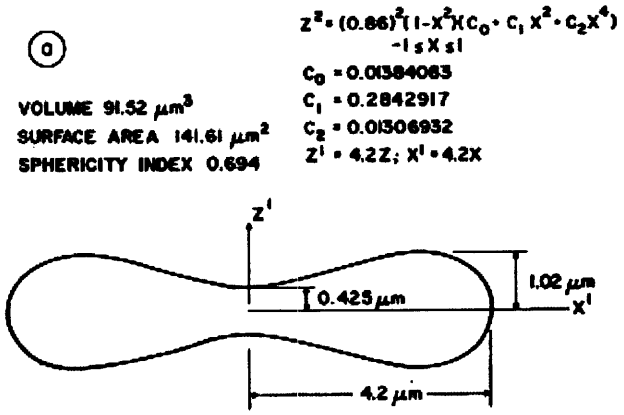


*Figure 1.2.5 : Skalak's modeled RBC shape [17].*

Secomb has also largely contributed to the modeling of RBC membranes, and in a 1988 paper rederived the first order linear stresses for a model of superposed leaflets, leading to a modification of the membrane model to incorporate the interaction between bending and tension forces [23]. To simplify the model, Secomb also added the hypothesis of axisymmetry, removed non-leading-order terms related to area changes, and used curvilinear coordinates following the RBC geometry (see Figure 1.2.6). The new equations are [101] :

$$\bar{t} = \frac{t_s + t_\theta}{2} = \sigma_0 + K_{bu} \frac{dA}{dA_0}, \tag{23}$$

$$t_d = \frac{t_s - t_\theta}{2} = \frac{1}{2} K_{sh} \left(\lambda_s^{\,2} - \lambda_s^{\,-2}\right) - \frac{1}{2} B \left(k_s - k_\theta\right)\left(k_s + k_\theta - k_0\right), \tag{24}$$

$$m = B \left(k_s + k_\theta - k_0\right), \tag{25}$$

where $t_d$ is given for a set of principal axes on the RBC along $s$ and $\theta$. The viscoelastic variant can be easily obtained by adding the last term of equation (21') to (24) :

$$t_d = \frac{1}{2} K_{sh} \left(\lambda_s^{\,2} - \lambda_s^{\,-2}\right) - \frac{1}{2} B \left(k_s - k_\theta\right)\left(k_s + k_\theta - k_0\right) + 2\,\mu^{RBC} \left(\frac{1}{\lambda_s} \frac{\partial \lambda_s}{\partial t}\right). \tag{24'}$$

These constitutive equations were completed by equilibrium equations to successfully achieve the computation of RBC shapes at rest. In Secomb's model, the equilibrium equations reduced to [101] :

$$\Delta p = - t_s k_s - t_\theta k_\theta - \frac{1}{R} \frac{d(R\, q_s)}{ds}, \tag{26}$$

$$-\tau = \frac{1}{R}\frac{d(R\,t_s)}{ds} - t_\theta \frac{1}{R}\frac{dR}{ds} - q_s\,k_s\,, \tag{27}$$

$$0 = \frac{dm}{ds} + q_s\,, \tag{28}$$

where $\Delta p$ is the local pressure difference between external and internal fluids, $\tau$ is the local tangential (shear) stress in the $s$ direction, caused by both external and internal fluids, $q_s$ is the shear force per unit length in the membrane, and $R$ is the membrane radius (function of $s$). Derivation of Equations (26)-(28) is detailed in Appendix E. Figure 1.2.6 shows these membrane stresses with the chosen conventional orientations.

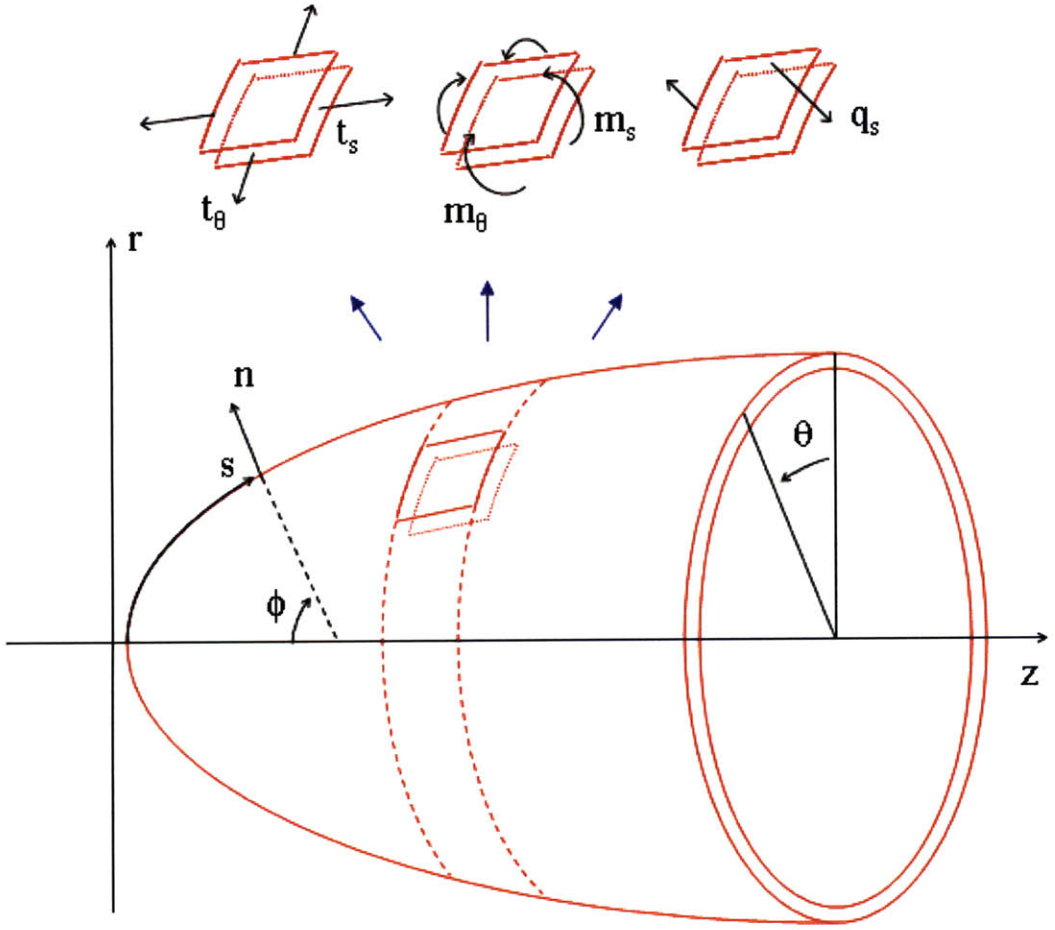


*Figure 1.2.6 : Curvilinear coordinates for axisymmetric RBC membrane and membrane stresses convention (model of superposed leaflets).*

In 2005, Arslan and Boyce have defined a model for the lipid bilayer and underlying spectrin network, representing the RBC membrane at the molecular level [27]. Hianik's 2006 presentation of RBC membrane models also contributes to encourage more research in this direction [28]. Both these works show the opportunities to use molecular-scale models for the RBC membrane, with possible benefits over 2-D homogeneous surface models.

To complement these models and determine the corresponding (visco)elastic properties of RBC membranes, early models used viscometric measurements, sieving and micropipette experiments. Some more recent techniques use optical tweezers [25] [26], and ferrimagnetic microbead [30]. Also, recent researchers have investigated the influence of cytoskeleton remodeling on RBC deformation response[29], paving the way for an increasing complexity in modeling RBC mechanics.

### 1.2.4. Combined models of red blood cell dynamics and oxygen delivery

Together with Fung, Lighthill is one of the first scientists to research hemodynamics, and study the motion of RBCs through narrow vessels. In a 1968 paper [96], Lighthill tries to resolve mathematically the flow for this specific problem using some very simple, yet justified assumptions. Using Burton's [4], and Fung's [5] analysis of blood flow in capillary vessels, and the observation of low Reynolds numbers for capillary flow, Lighthill develops a lubrication layer model to effectively determine the flow around the RBC. Following his work, Fitz-Gerald extended the lubrication model and obtained a series of equations between the leakback flow per circumferential length $Q'$ around the RBC, the gap size between the RBC and the capillary wall $h(z')$, and the pressure gradient along the capillary $\frac{dp}{dz'}$. Assuming axisymmetric, steady, quasi-unidirectional, viscous-dominated flow, with the RBC moving at a constant speed, the Lighthill-Fitz-Gerald equations for the lubrication layer lead to:

$$\frac{1}{16\,\mu}\,\frac{dp}{dz'}\,(2\,R_w\,h - h^2)\left[2\,R_w^{\,2} - 2\,R_w\,h + h^2 - \frac{2\,R_w\,h - h^2}{\ln\left(\frac{R_w}{R_w - h}\right)}\right] =$$

$$- U \left[ \frac{1}{2} R_w^2 - \frac{2 R_w h - h^2}{4 \ln\left( \frac{R_w}{R_w - h} \right)} \right] + R_w Q' . \quad (29)$$

Assuming a small gap thickness compared to the capillary radius $h(z') << R_w$, Equation (29) reduces to :

$$\frac{dp}{dz'} = - \frac{6 \mu U}{h^2} + \frac{12 \mu Q'}{h^3} , \quad (30)$$

where $U$ is the (constant) velocity of the RBC, $z' = z - U t$ is the reference frame moving with the RBC and centered at its upstream front or "head", and $\mu$ is the dynamic viscosity of blood plasma. Details of the derivation of (29) and (30) are given in Appendix D. In addition to Equations (29) and (30) a very simple elastic model for the RBC is added :

$$h = R_w \left( 1 - \sqrt{1 - \frac{K_1 z'^2}{R_w}} \right) + K_2 (p - p_0) , \quad (31)$$

where the basic RBC shape is assumed to be elliptic at a reference pressure $p_0$ taken to be the pressure at the "head" of the RBC. $K_1$ and $K_2$ are model constants. These two equations allow to determine the pressure everywhere for a given leakback flow, and through an integral equation one can also estimate the pressure drop across the RBC (a simple control volume analysis around the RBC, writing equilibrium of forces gives the pressure drop as a function of the leakback flow $Q'$).

In this early model one of the most limiting assumptions was undoubtedly the elliptic RBC shape. Although inferred from observations and following the purpose of a simple descriptive example, it mostly illustrated the absence of detailed insight about RBC membrane stresses. With the emergence of Skalak's model of the RBC membrane [17], the first calculations of equilibrium RBC shapes were developed. Jenkins derived and solved a system of 4 differential equations, and obtained families of mathematical solutions for varying pressure differences between the interior and exterior of the RBC, with encouraging biconcave shapes [98]. Fischer et al. calculated buckling solutions for RBC membranes as a function of RBC volume, using Evans and Skalak's equations incorporating the shear modulus $K_{sh}$ and the bending stiffness $B$, and assuming constant surface area [99].

Secomb's important breakthrough was to combine the equations of lubrication theory with Skalak's complete equations of membrane mechanics. Secomb thus gathered Equations (20), (21),

(22), (26), (27), (28) with (29) to obtain a closed system of equations, fully describing RBC dynamics in capillary vessels [100]. Secomb then obtained numerically the first parametric results for different sizes of capillaries and RBC velocity (see Figure 1.2.7). Subsequent work by Secomb included updates and extensions to this model, using Equations (23), (24), (25) instead of (20), (21), (22) [101]. Secomb successfully calculated theoretical RBC shapes for very narrow capillaries (see Figure 1.2.8), larger capillaries (see Figure 1.2.9), between 2 parallel plates (instead of a cylindrical vessel) [103], through micropores [104], and for a viscoelastic RBC membrane flowing in capillaries of slightly varying diameters [115]. Extensions on microvascular networks were also researched [114], as well as asymmetric tank-treading behavior (migration of RBC towards the centerline) [117], and tumbling behavior [118].

Pozrikidis's work focused on deformations through time of RBCs modeled as oblate or prolate spheroids [102], and as elastic biconcave disks [109] under shear flow. His calculations included advanced 3-D models of the full RBC membrane. Similar developments of 3-D calculations were reviewed in 2005 in a paper by Christini and Kassab [112]. Other work on the dynamics of capillary blood flow includes Chakraborty's simulations of flowing RBCs using a modeled apparent viscosity [111].

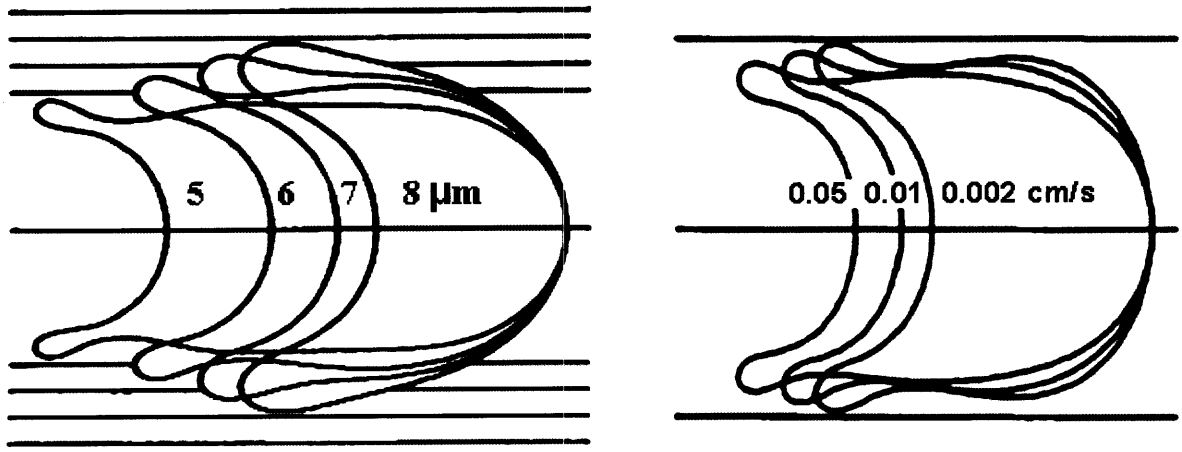


*Figure 1.2.7 : Cell shapes calculated for different vessel diameters - U=0.01cm/s (left), and different RBC velocities – $R_w$=3µm (right) (from Secomb [100]).*

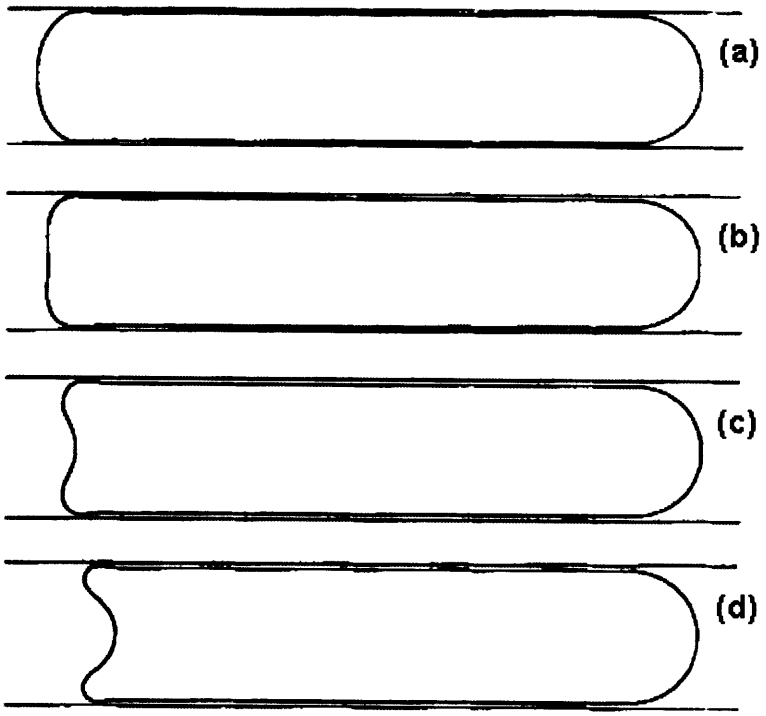


*Figure 1.2.8 : Cell shapes calculated for different vessel diameters – (a) $R_w$=1.5μm (b) $R_w$=1.52μm (c) $R_w$=1.55μm (d) $R_w$=1.6μm. Critical radius is 1.42 μm (from Halpern and Secomb [101]).*

A 2009 paper by Kaoui and coworkers has shown recent studies of the asymmetric RBC shapes observed in some experimental results [121]. Interestingly, slipper-like asymmetric shapes may be preferred configurations under low flow velocity due to bending stiffness and membrane rigidity only. The calculations made by Kaoui do not correspond to confined, small capillaries at this point, but developments in this direction may lead to seriously reconsider the assumption of axisymmetry.

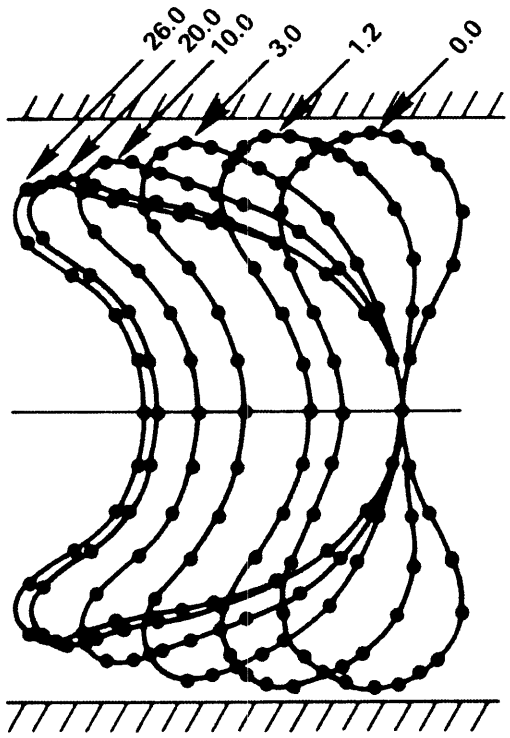


*Figure 1.2.9 : Cell shapes calculated for different RBC velocities, $R_w$=4.5μm (units unknown) (from Secomb [116]).*

Adding to RBC dynamics the problem of oxygen delivery, one of the major contributions in the recent years has been achieved by Popel. Popel with his collaborators developed a two-phase model for the capillary flow [105], before starting to study oxygen delivery in brain [106] and pursued studies of RBC dynamics in various blood vessels such as in venules [107]. In 2002 together with Vadapalli and Goldman, gathering a large amount of data from various researchers, they formulated one of the most advanced models of oxygen diffusion, incorporating oxygen binding to hemoglobin and myoglobin, as well as oxygen transport through a 5-layer model, with specific equations within the RBC, blood plasma, capillary wall, interstitium, and surrounding tissue where oxygen is consumed [108] (see Equations (13) to (18) given in Section 1.2.1). Popel's ongoing research focuses on RBC aggregation dynamics [110] [120] [122], and oxygen delivery through capillary networks [119]. A 2005 paper reviews the major advances made in hemorheology [113]. Interestingly, RBC dynamics and oxygen delivery are **uncoupled problems** for normal RBCs, which explains why Popel like other researchers always addressed both separately. Sickle cell modeling, on the other hand, needs to address the coupling of oxygen delivery and blood dynamics, and has been pursued by a different group of researchers.

### 1.2.5. Modeling sickle cell disease : challenges and outcomes

A few researchers have investigated theoretical models for sickle cell disease, trying to understand how affected RBC dynamics could explain episodic vaso-occlusion and crises. Early observations of sickling RBCs upon deoxygenation thus made it crucial to study the apparent coupling between oxygen transfer and RBC dynamics.

Berger was one of the first researchers to develop a model for sickle cell blood. In 1980 Berger and King assumed a direct relation between RBC global compliance (a measure of its membrane elasticity) and average oxygen concentration in the capillary at a given section [123]. Berger and King also included the rightward shift of sickle oxyhemoglobin dissociation curve, observed experimentally (and showed in Appendix A). Their results show increased blood speed and higher oxygen levels on average in capillaries of sickle cell patients, potentially explaining how sickling could be compensated by a dynamic "feedback" and how crises would remain rare despite the rheological changes caused by the disease. Berger and King's model includes the Krogh model corresponding to Equations (1) to (10), with the rightward shift of sickle oxyhemoglobin corresponding mathematically to :

$$\frac{N^{sickle}\left(\frac{ds}{dc}\right)^{sickle}}{N^{normal}\left(\frac{ds}{dc}\right)^{normal}} \approx \frac{N^{sickle}\,K^{normal}}{N^{normal}\,K^{sickle}} \approx 1.4\ . \tag{32}$$

RBC dynamics are described using the Lighthill-Fitz-Gerald lubrication layer model given in Equations(29) and (30), combined with the assumption of a simple crescent ("parachute") shape for the RBC, with membrane mechanics described by a global compliance coefficient between local pressure and RBC radius at a given section ("fairly crude approximation to the truth", as reported by Fitz-Gerald [97]). Finally, the RBC stiffness (inverse of the compliance) is coupled to average oxygen concentration using an "ad-hoc and speculative" power law [123] based on microsieving data collected by Usami, Chien and Bertles [63], and can be written essentially as :

$$s = s_{ref}\left(\frac{1}{\alpha + (1-\alpha)\left(\frac{c}{c_{ref}}\right)^2}\right) \quad \text{for} \quad c \geq c_{ref}\ , \tag{33}$$

$$s = s_{ref} \qquad \text{for} \quad c \leq c_{ref}\,, \tag{34}$$

where $s$ is the RBC stiffness, $\alpha$ is a model constant, and $s_{ref}$ and $c_{ref}$ are reference values for RBC stiffness and oxygen concentration. In 2004 Berger and Carlson extended this model to a network of capillaries, showing aggravated consequences at macroscopic levels, with the possibility of large scale stasis [134].

Following Berger and King's model, Discher and Cima investigated possible causes of acute crises [124] [128]. The observed increase in plasma viscosity during sickle cell crises states [65] was hypothesized as a critical factor initiating sickle cell crises. Their collaborative work successfully identified a theoretical multivalued solution for the RBC velocity for different values of plasma viscosity and other fixed parameters (see Figure 1.2.10). The lower-velocity solution at high plasma viscosities would then explain a sudden drop in blood flow, followed by inflammatory reactions and further complications. The increased plasma viscosity is believed to be related to an elevated level of proteins (caused by infection or thrombosis of ischemic injury), in particular fibrinogen (a clotting protein), and globulin (with an observed increased ratio with respect to albumin). Arguably, it is important to note that in this model the increased plasma viscosity is assumed to be a **cause** of the crises, and not a **consequence** of a pre-crises state of blood (Cima also discusses the probable correlation of both factors, acting as a vicious cycle).

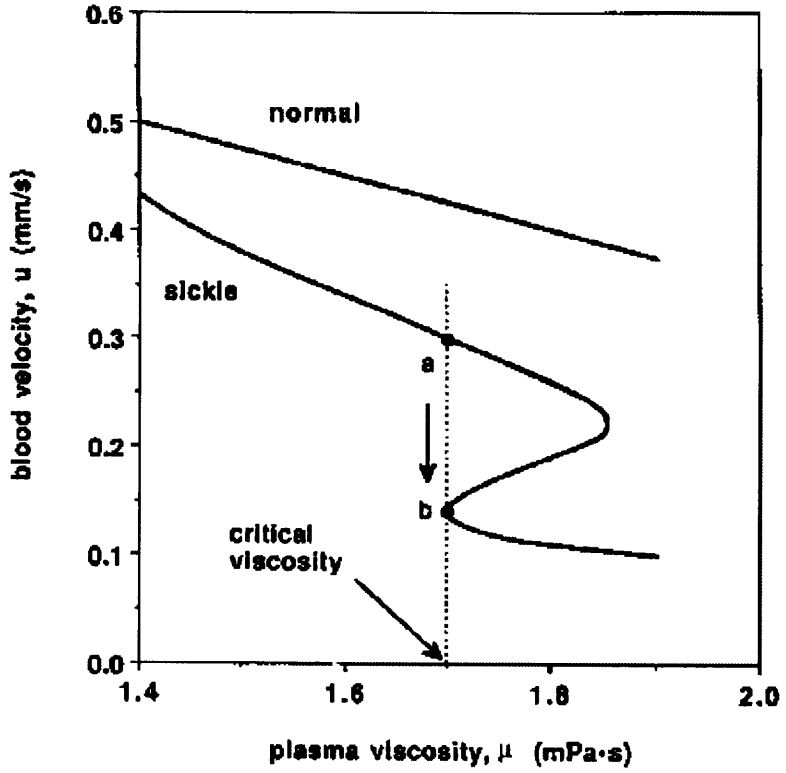


*Figure 1.2.10 : blood velocity vs. plasma viscosity -normal level is 1.42mPa.s (from Cima et al [128]).*

One of the main challenges of modeling sickle cell disease resides in the polymerization process of sickle hemoglobin (HbS) and its consequences. Early research includes various intracellular and extracellular models with limited success, in general due to apparent incompleteness of the models [125]. Dou and Ferrone were among the first researchers to develop a convincing kinetic model for HbS polymerization, obtaining striking qualitative results showing the development of a sickle shape (see Figure 1.2.11) [127]. However, this molecular approach remains far from being applicable to a blood flow model, and Ferrone's ongoing investigations (which include estimations of elastic properties of HbS polymers [50]) are promising and should be carefully followed.

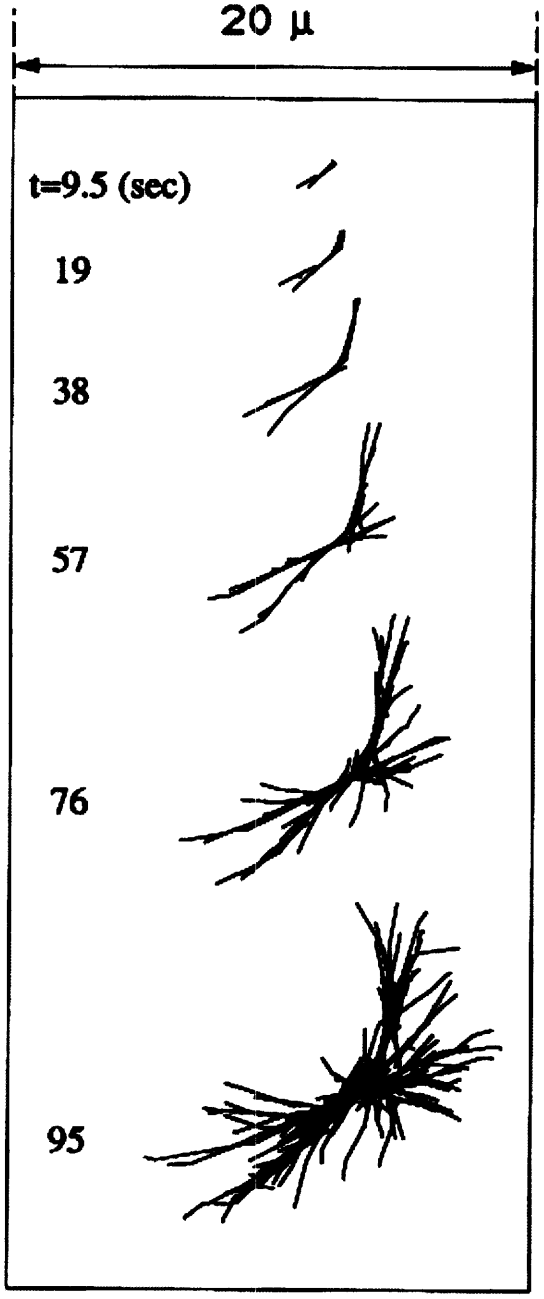


Typical results of two-dimensional simulation. $b$ = 0.08 deflections per polymer per sec; $g = 6 \times 10^{-6}$ nucleation events per incorporated monomer per second, and $j$ = 0.11 μm/s. As can be seen, the domain grows longer and wider. Because of the random curvature of the polymers, the patterns are generally skewed to one side or the other. The number of monomers polymerized in a typical simulation is about $10^6$.

*Figure 1.2.11 : Simulated formation of polymerized sickle hemoglobin HbS (from Dou and Ferrone [127]).*

Another model for sickle HbS polymerization was achieved by Makhijani et al., focusing on the complex chemical mechanisms of oxygen unloading, transport, and HbS polymerization reactions solved altogether [126]. The results show a parametric study of oxygen unloading times for sickle cells.

Some attempts to interpret sickle blood dynamics at a larger scale have also been developed, such as Rocsoreanu, Georgescu and Giurgiteanu's hemodynamic model [130]. However, the extensive study of its mathematical implications, with such results as bifurcation models, relies on many simplifications and mathematical assumptions that seem difficult to interpret physically.

In 1998 Apori and Harris attempted to reformulate Cima's model with a simple set of 4 autonomous equations with time as the only variable (see Equations (35) to (38)), to be studied as a chaotic dynamical system simulating sickle cell crises [129] [131] [132] [133]. Although Apori's thesis was used as a preliminary study to this doctoral work [135], the difficulties of interpreting the Apori-Harris system of equations physically led us to a new direction corresponding to the present thesis. This model remains nonetheless a potential simplification to keep in sight and be researched.

$$\frac{dc}{dt} = a_1 c + a_2 u \mu + a_3 u , \tag{35}$$

$$\frac{du}{dt} = b_1 u + b_2 \mu s + b_3 s , \tag{36}$$

$$\frac{ds}{dt} = c_1 s + c_2 c , \tag{37}$$

$$\frac{d\mu}{dt} = d_1 \mu + d_2 c , \tag{38}$$

where $c$, $u$, $s$ and $\mu$ are the 4 state variables describing capillary flow (oxygen concentration, blood velocity, cell stiffness and plasma viscosity), and $a_1$, $a_2$, $a_3$, $b_1$, $b_2$, $b_3$, $c_1$, $c_2$, $d_1$ and $d_2$ are coupling parameters of the system, corresponding to the main physical relationships between the 4 state variables, and that Apori determined based on dimensional considerations, leaving a more precise physical interpretation to further research. In his work, Apori showed that a change of the parameter $c_2$ relating RBC stiffness to oxygen, transformed the Apori-Harris system of equations from a stable, asymptotically periodic solution, to a chaotic system. Based on Berger's work and Cima's calculations, Apori related qualitatively $c_2$ to the stiffness-concentration relation (Equations (33)-(34)), and concluded that this coefficient might indeed be crucial to represent the onset of sickle cell crises.

Finally, Higgins's successful experiment proved that vessel occlusion was due to the characteristics of sickle blood only (and not to any interaction with the capillary wall), and led him to

suggest a new mathematical model describing blood flow and apparent viscosity as a function of oxygen concentration, with the proportion of sickled RBCs as a dependent variable [136]. Higgins's model lacks precise figures to be applied to this day (see Figure 1.2.12), but represents one of the most promising paths between mathematical models and experimental results.

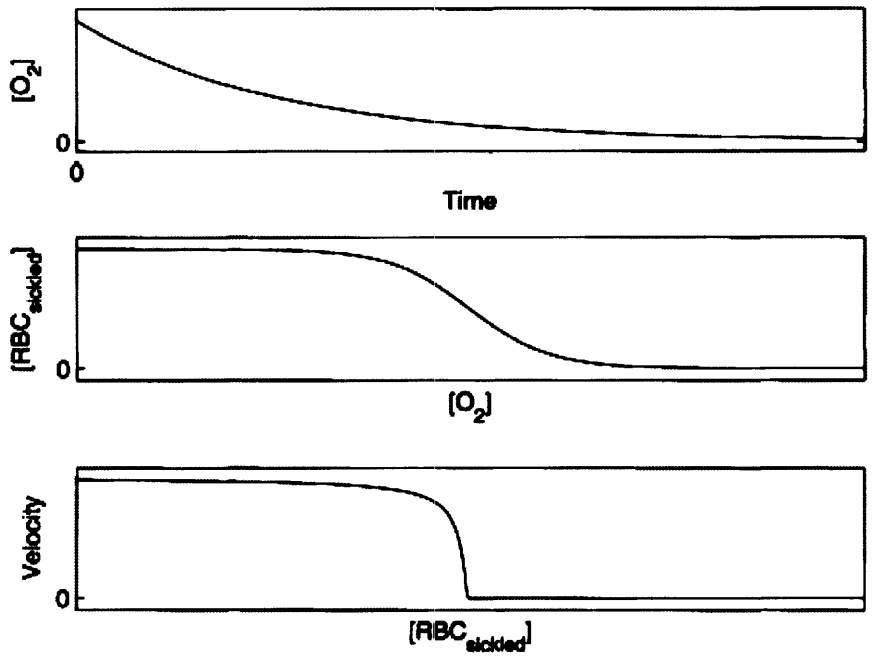


**Simplified qualitative model of vaso-occlusion. As the concentration of oxygen decreases with time, the sickle cell concentration increases leading to a diverging viscosity of the blood which stops flowing.**

*Figure 1.2.12 : Qualitative model of sickle cell vaso-occlusion (from Higgins [136]).*

In light of the different existing models for sickle cell disease, a couple of noteworthy points can be made at this point :

- Models of sickle cell disease exist at 2 different length scales : the molecular scale (Ferrone, Makhijani), and the blood flow scale (Berger, Discher, Cima, Apori, Rocsoreanu, Higgins). Despite increasing knowledge of the different abnormal factors affecting sickle cell patients, there is still very little understanding of how sickling affects directly the shape of RBCs, and the resulting abnormal blood flow.

- The lack of an apparent connection between these models mainly results from differences in the investigators' objectives and research goals. Whether one factor is put forward (plasma viscosity in

Berger), or another (sickling RBCs in Higgins), whether a model is designed for a transitional situation (pre-crises state in Berger) or an asymptotic one (crises state in Apori), various conclusions tend to come from different models, and confusion arises as to what really causes the impaired sickle blood dynamics, and sickle cell crises.

- Some recent models seem to ignore recent advances in capillary flow modeling or do not attempt to improve older models and question certain assumptions, although increasing complexity is now possible and may be beneficial to our understanding of the disease.

Consequently, this research will seek to define a mathematical model for sickle cell disease, which would both try to fill the gap between molecular and vascular descriptions of the disease, and extend the previous models to incorporate improved knowledge of capillary flow, oxygen transfer and RBC mechanical behavior. An important factor limiting the complexity of our model will also be the experimental data available to characterize both normal and sickle blood flow.

## 1.3. Relevant experimental research

All blood models have physical constants that need to be determined by experimental data. A careful review of the related research will also address the ranges of acceptable values for the cases studied, and assess to some extent the validity of the chosen models. In this section we present some of these experimental works, to be used eventually to either justify the hypotheses of our model, or validate its results.

### 1.3.1. Normal blood properties and their variability

Mortillaro's *Physiology and Pharmacology of the Microcirculation* is one of the many books that describe specific properties of capillary vessels [32], together with Fung's *Biodynamics : Circulation* [12] and Charm and Kurland's *Blood Flow and Microcirculation* [8]. In particular Mortillaro gives very detailed specific characteristics of the microcirculation for 14 different organs. Among general facts (vessel sizes, typical pressure ranges, oxygen levels, blood composition and density), it is noticeable that capillary vessels, unlike larger arteries, do not have a strongly pulsatile flow, i.e. oscillations are highly damped between the heart and the arterioles to reach a quasi-steady pressure input (this is due mainly to the viscoelastic response of the artery walls, and the action of smooth muscle surrounding them). Capillary flow, unlike arterial or vein flow, is characterized by large viscous stresses in comparison to inertia, with small Reynolds number (see dimensional analysis in Appendix C). Because of their

important role as an exchange surface, the capillary walls also have very particular characteristics compared to other vessels, such as the absence of smooth muscles used in vasoconstriction and vasodilatation (see Figure 1.3.1 and Table 1.3.1).

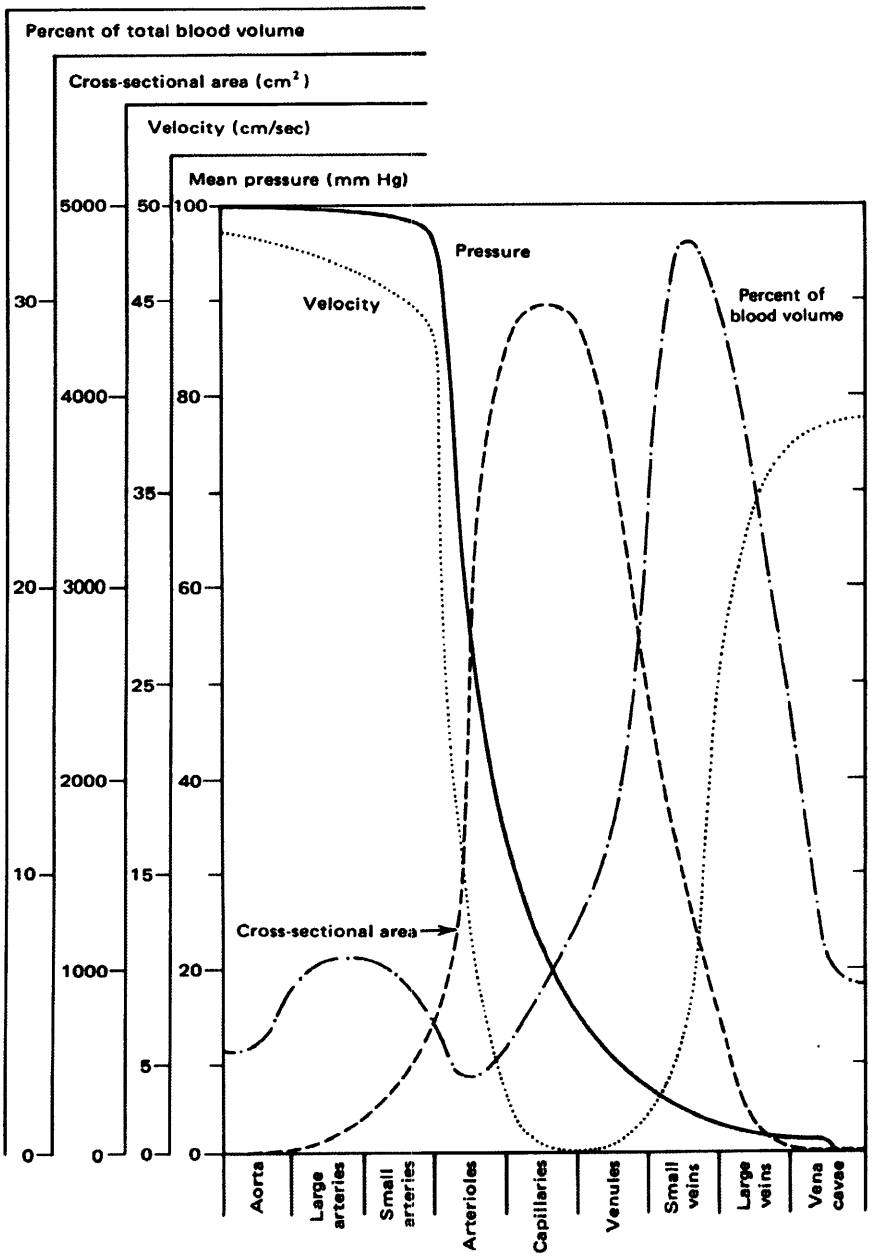


Quantitative aspects of the circulatory system (from Berne and Levy, 1972, Cardiovascular Physiology, C. V. Mosby Co.).

*Figure 1.3.1 : Comparison of blood vessels (from Charm and Kurland [8]).*

| Vessel | Length (mm) | Diameter (μm) | Wall Thickness (μm) | Composition (%) | | | |
|---|---|---|---|---|---|---|---|
| | | | | Endothelium | Elastic Tissue | Smooth Muscle | Fibrous Muscle |
| Aorta | 500 | 25000 | 2000 | 5 | 40 | 25 | 30 |
| Artery | 500 | 4000 | 1000 | 5 | 35 | 40 | 20 |
| Arteriole | 10 | 50 | 2000 | 5 | 25 | 45 | 25 |
| Precapillary sphincter | 0.2 | 35 | 30 | 15 | 15 | 50 | 20 |
| Capillary | 1 | 8 | 1 | 100 | 0 | 0 | 0 |
| Venule | 2 | 20 | 2 | 25 | 0 | 0 | 0 |
| Vein | 250 | 5000 | 500 | 5 | 40 | 30 | 25 |
| Vena cava | 500 | 30000 | 1500 | 5 | 25 | 35 | 35 |

*Table 1.3.1 : Typical geometry and structure of various blood vessels (from Charm and Kurland [8]).*

As mentioned in the previous sections, 3 physical models need to be considered : a model for fluid flow, a model for oxygen transport, and a model for the elastic RBC membrane. All these models come with physical assumptions supported by observations or thorough dimensional analysis (see Appendix C).

The "fluid" part consists in blood plasma and RBC cytoplasm. Both are to be modelled with continuous fluid mechanics. Blood plasma and RBC cytoplasm are also modelled as a homogeneous fluid of constant density (incompressible) and constant viscosity, with the viscosity of cytoplasm about 8 times the viscosity of blood plasma. The very low compressibility of blood (about $4.10^{-10}$

$m^2/N$, which corresponds to a bulk modulus of $2.5.10^9$ Pa) justifies the assumption of constant density [43]. As for neutrophils, both plasma and cytoplasm have a decreasing viscosity with temperature, and little variation with pH [31]. However, the regulation of blood in vivo is such as to not induce significant changes in normal situations. Also, physical activity leads to systemic control of blood flow through regulated vasoconstrictions and vasodilatations of arterioles and venules [34]. This leaves further fine regulation to capillary walls and generally ensures stable conditions of temperature, pressure and blood composition. Hence circulatory adjustments to dynamic exercise allow us to consider constant blood properties. Additionally, ionic and osmotic equilibria regulate RBC volume and cytoplasm properties, which can also generally be considered as constants [33]. Nevertheless, deoxygenation of blood leads to an increase of about 2% of the RBC volume, and of about 5% for the hematocrit [41]. Although not entirely negligible, this doesn't seem to have ever been accounted for in any model. Also interestingly, RBC internal viscosity increases with haemoglobin concentration [38]. Although in normal cases both remain quasi-constant, in sickle cell cases the observed small dehydration of RBCs leads to a small increase in cytoplasmic viscosity [84]. Finally, the role of the cytoskeleton in cytoplasm dynamics is usually ignored because not entirely known, despite ongoing research [29].

Oxygen transport is best described by the Vadapalli-Goldman-Popel extension of the Krogh cylinder model, using various research sources to determine oxygen, hemoglobin, and myoglobin constants, with a large set of diffusion constants from Bouwer et al [40], but also oxygen solubility coefficients, characteristic concentrations, kinetic dissociation rate and Hill dissociation curve parameters [108].

RBC membrane properties are evidently associated with the models used by researchers to interpret their experimental measurements. Steck was one of the first to study the composition of the RBC membrane and infer some of its properties [18]. Hochmut et al. calculated in 1983 a membrane thickness of 7.8 nm with a light-microscope technique [21], which justified largely the use of 2-D models as presented in Section 1.2.3. Recent experiments by Dao et al. [25], Mills et al. [26], and Puig-de-Morales-Marinkovic et al. [30] show the ongoing research to determine precisely nonlinear and viscoelastic properties of the RBC membrane.

Global blood dynamics have also been subject to recent experiments, to determine whole blood properties such as apparent viscosity and RBC shapes in the microcirculation. To this end, Kubota et al. have carried experiments on RBCs flowing in vitro [39]. Long et al. measured blood viscosity by hemodilution without assumptions regarding the Fåhræus and Fåhræus-Lindqvist effects (see Appendix F), which can arguably differ between in vivo and in vitro situations [44]. Pries and Secomb,

in a recent paper modelling the influence of the endothelial surface layer, produced micrographs of both in vivo and in vitro capillary blood flow, showing expected RBC shapes in the microcirculation [46] (see Figure 1.3.2). Finally, one of the rare experiments on transient dynamics has been made by Alonso et al. in vitro with tubes of variable diameter [37]. Transient dynamics remain rarely studied in the microcirculation because of the expected small and slow variation of blood flow. This is not the case with sickle cell disease though, where transient dynamics need to be studied to understand irregular blood flow leading to vessel occlusion.

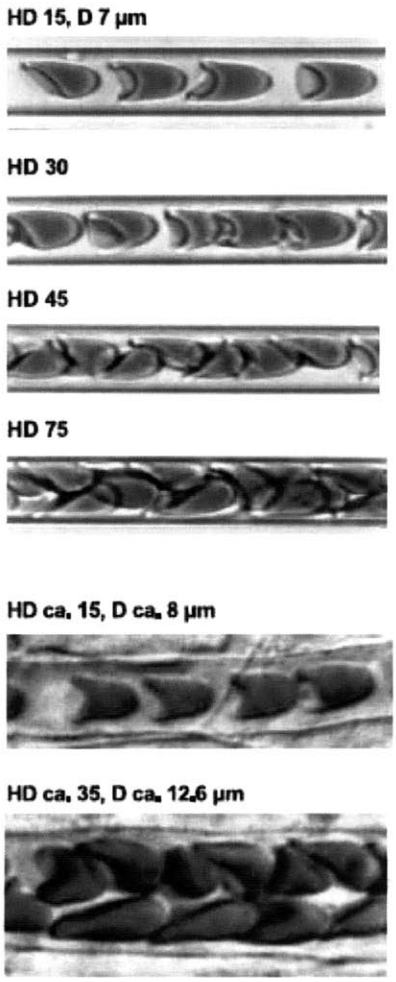


Micrographs of red blood cells flowing through small-bore glass tubes (*top 4 micrographs*) and mesenteric microvessels (*bottom 2 micrographs*). In the intermediate range of vessel diameters from ~6–13 µm, cells may flow in single file at low hematocrits. With increasing hematocrit, more cells are present in a vessel cross section, leading to a transition to multifile flow and increased interaction of cells with the wall.

*Figure 1.3.2 : Micrographs of capillary blood flow (from Pries and Secomb [46] [115]).*

## 1.3.2. Experimental observations and studies of sickle cell disease

As presented in the introduction, the observation and systematic study of sickle cell disease is less only about a century old. Chien, Usami and Bertles were among the first to study the abnormal rheology of sickle cell blood. Their experiments successfully showed the decreased hematocrit and increased whole blood viscosity among sickle cell patients [62] [63] (see Figure 1.3.3). Plasma protein concentration and its influence on blood viscosity were also documented, and the rheological difference between Reversibly Sickled Cells (RSC) and Irreversibly Sickled Cells (ISC) was investigated. Figure 1.3.4 shows how the actual RBC sickling is directly responsible for most of the rheological changes. Based on these results, a large number of models for sickle cell disease have made the hypothesis that RBC changes of shape is primarily responsible for affected blood dynamics, which lead eventually to blood clots and sickle cell crises.

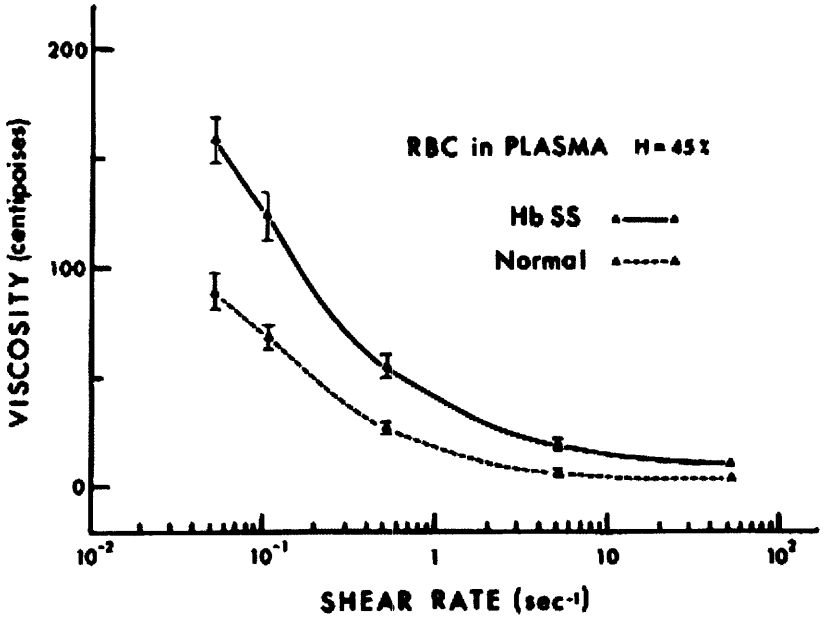


Relationship between viscosity (linear scale) and shear rate (log scale) for oxygenated Hb SS blood (n = 5) and normal blood (n = 6) at 45% hematocrit. Values shown are means ±SEM.

*Figure 1.3.3 : Compared whole blood viscosities between normal and sickle blood (from Chien, Usami and Bertles [62]).*

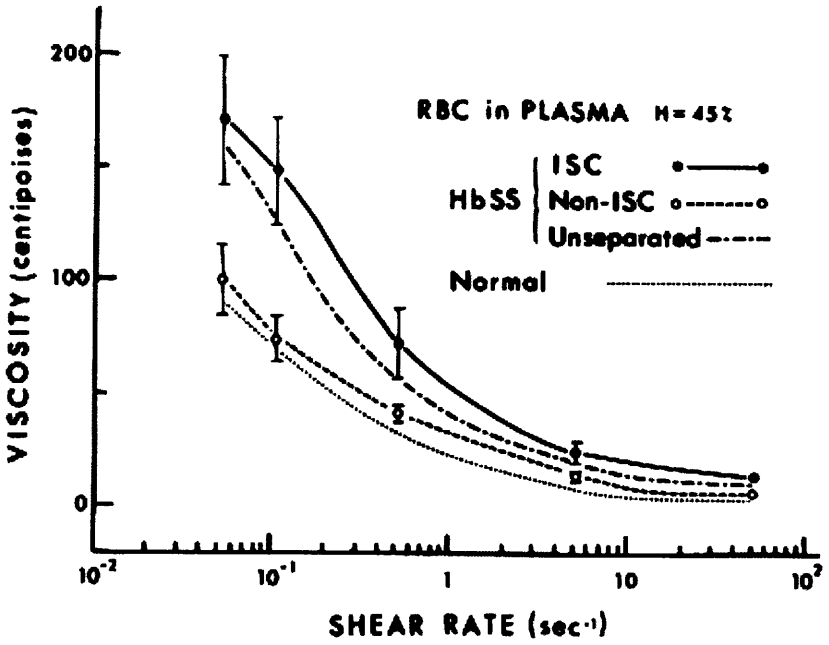


**Relationship between viscosity and shear rate for suspensions of oxygenated ISC and non-ISC in plasma. Values shown are means ±SEM. Also shown for comparison are data on unseparated Hb SS blood and normal blood. Hematocrit equals 45% in all suspensions.**

*Figure 1.3.4 : Compared whole blood viscosities between sickle cell types (from Chien, Usami and Bertles [62]).*

As sickle cell crises is a consequence of vessel occlusion, the interactions of the endothelium with sickle cells were also investigated (endothelial cells are the cells lining the interior surface of the capillary wall). Until the very recent interest in endothelial cells, and growing understanding of their large role in blood regulation, the description of blood clotting was mainly though platelet adhesion and the extensive documentation of coagulation factors, as given by Fogelson [55]. Later, abnormal levels of endothelium-regulated proteins associated with blood vessel inflammation were found in sickle cell patients [56], paving the way for potential novel therapeutic studies. These included reducing endothelial cell activation [57], counter-acting it with vaso-dilating agents [58], using circulating endothelial cells as markers of pre-occlusive states [59], using inhibitors to endothelial cell activation [60], and prevent sickle cell adhesion to endothelial cells by changing its adhesive potential [61].

In 1975 Zarkowsky investigated sickling times of RBCs. It was found that RSCs had a sickling time of about 2 seconds, while ISCs were sickling faster than the experiment could measure [64]. Higgins's recent experiments using a microfluidic device showed the occlusion of capillary vessels under sudden deoxygenation [80] [81] (see Figure 1.3.5). Zarkowsky's and Higgins's results suggest that vessel occlusion can be achieved independently from any interaction with the endothelium, and that

this interaction would rather be an aggravating factor, coming with if not accelerating complications associated with vessel inflammation. Further similar experiments, with several controlled oxygen levels, pressure constraints, and different channel widths, may be key to understanding the behavior of sickle RBCs undergoing deoxygenation. These are also very interesting to simulation models, as they may give more quantitative information on the different steps preceding vessel occlusion, independently of a lot of chemical factors (onset of sickling, RBC shape and apparent viscosity vs. oxygen level and volumetric flow, differences between RSCs and ISCs, and critical pressure/volumetric flow couples leading to vessel occlusion).

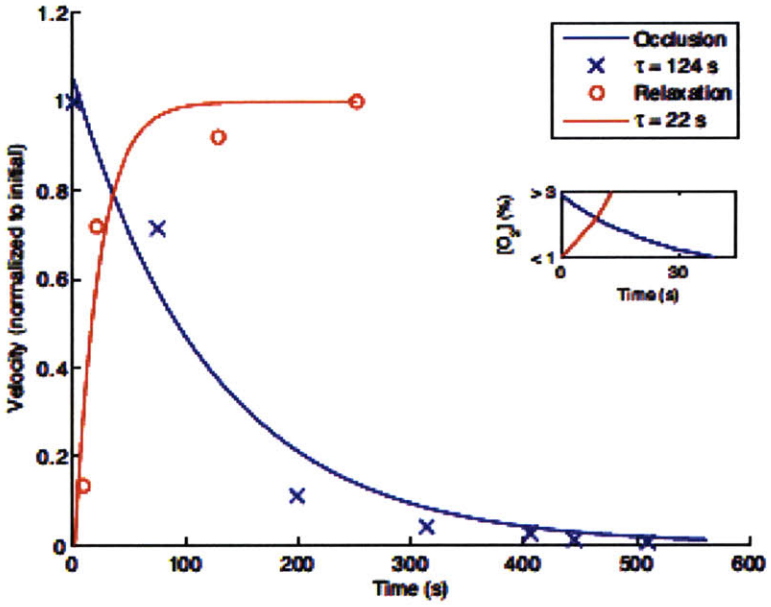


*Figure 1.3.5 : Vessel occlusion in oxygen-deprived microfluidic device (from Higgins [81]).*

Various studies have been pursued to determine the apparent viscosity of blood for different types of RBCs, following the work of Chien, Usami and Bertles. Kaul and coworkers studied the 3 main sickle erythrocyte types in detail, isolating ISCs and 3 types of RSCs (see Figure 1.3.6). ISCs are the most flow-obstructing cells, with under a shear rate of 230 $s^{-1}$, a measured viscosity in oxygenated blood of about $3.10^{-3}$ Pa.s ($5.5.10^{-3}$ Pa.s in deoxygenated blood), 10% more than the most viscous subpopulation [66]. Tripette and coworkers have compared sickle cell disease with the rare form of sickle-hemoglobin C disease, where a patient combines sickle-cell hemoglobin trait (HbS) with another abnormal hemoglobin allele (HbC), with enhanced sickling compensated by the presence of HbC, but other consequences leading to a less severe condition [85] (some details of the sickle cell

disease variants are given in *Interpretation of diagnostic tests* by Jacques Wallach, pp.408-409 [83], and in *Disorders of Hemoglobin* by Steinberg et al.). Damay has also investigated white blood cells in sickle cell disease, which were shown not to have a significant role on vaso-occlusion at the dynamical level (through measured viscosity), as opposed to their known involvement in the resulting vessel inflammation [76].

Another set of studies have explored the clinical aspects of sickle cell disease, such as abnormal venous function leading to leg ulceration [77], and variation of rheological and physiological factors preceding, during and following the crises [73]. Steady-state viscosity was also shown to be correlated with frequency of painful events and end organ failures [72], as well as measured viscosity of flow in oscillating harmonic sinusoidal mode [82].

With the increasing efficiency of blood separation techniques, more details of the blood rheology were also found. As mentioned in previous sections, Laogun et al. showed an average increase of plasma viscosity from $1.4.10^{-3}$ Pa.s to $1.7.10^{-3}$ Pa.s for sickle cell patients in crises state, suggesting a strong connection between the crises and the plasma protein content, either as a cause, consequence or correlated factor [65]. However, the pre-crises state doesn't present any particular increase in plasma viscosity. Finally, as stated in Greer et al.'s *Wintrobe's clinical hematology* (p.1042) [84], the little dehydration of sickle cells causes a decrease in RBC volume, and a little increase in cytoplasmic viscosity.

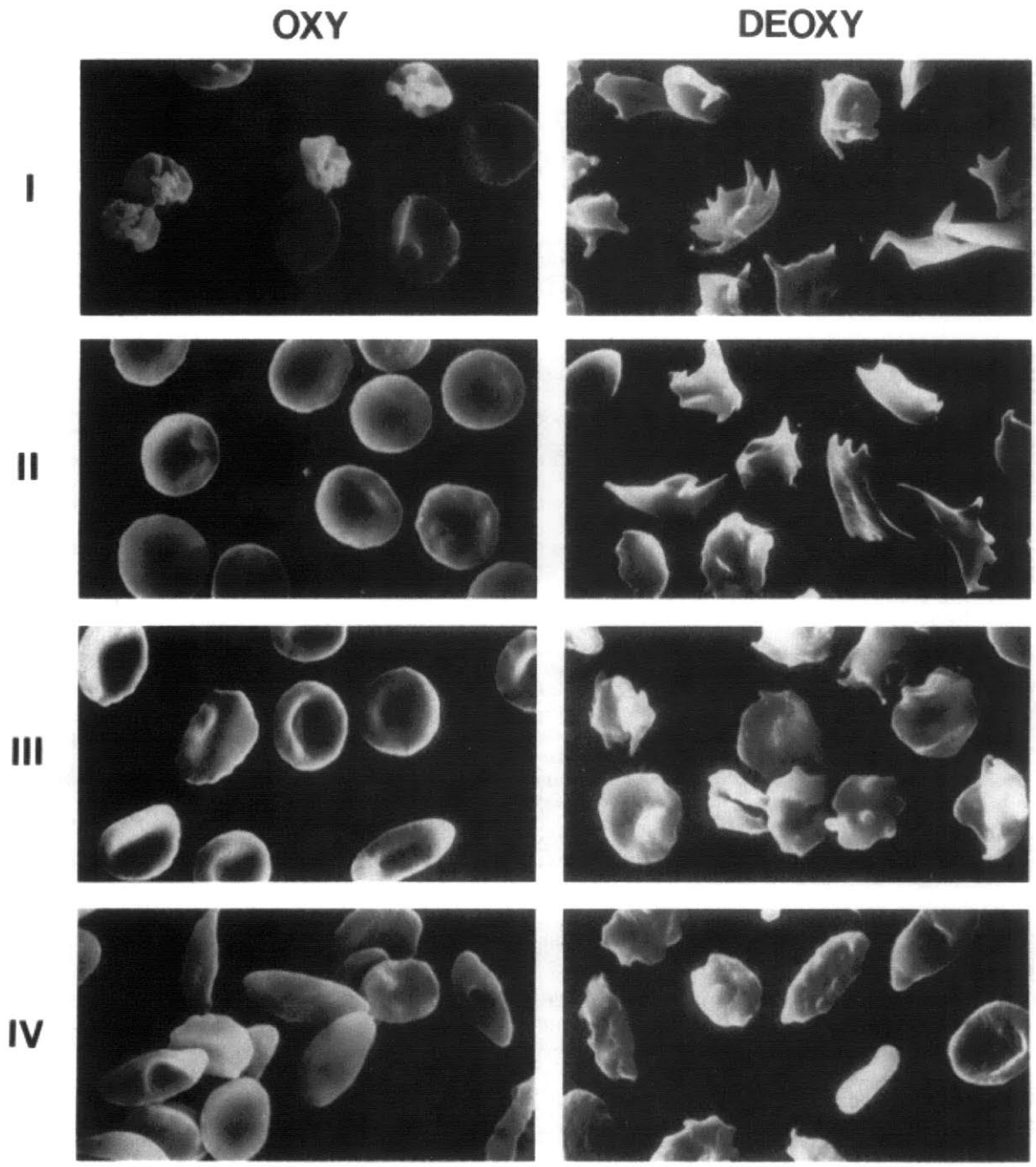


**SEM of the four major HbSS erythrocyte subpopulations (fractions I-IV) of a single patient (S.M.) separated on Percoll-Renografin density gradients. Oxy fractions: Fraction I is characterized by the presence of a large number of reticulocytes; young reticulocytes appear multilobulated (7). Fraction II is composed mainly of discocytes. Fraction III contains dense discocytes and some ISC. Fraction IV is comprised mainly of ISC. Deoxy fractions: Following deoxygenation typical sickle forms are seen in fraction I and II. The multilobulated reticulocytes appear to assume multispiculated appearance. Little or no transformation is seen in fractions III and IV.**

*Figure 1.3.6 : The 4 major RBC subpopulations in sickle cell disease (from Kaul et al. [66]).*

Another major breakthrough was achieved in 1984 by Nash, Johnson and Meiselman, who were among the first to focus their attention on mechanical properties of the RBCs, and successfully showed an important decrease of flexibility of the RBC membrane [67] (see Figure 1.3.7). This led to new studies considering the variation of RBC viscoelasticity with oxygen partial pressure [68], temperature and hemoglobin concentration [70]. As shown in Figure 1.3.8, the RBC viscosity increases with temperature and depravation of oxygen. Another study showed the decreased elasticity of RBCs among heterozygous sickle gene (HbS-HbA) carriers [79].

| Sample | Shear Elastic Modulus ($10^{-3}$ dyne/cm) | Time Constant (sec) | Calculated Surface Viscosity ($10^{-4}$ dyne · sec/cm) | Dimensions (μm) |
|---|---|---|---|---|
| ISC† | 12.9 ± 2.5 | 0.161 ± 0.037 | 20.8 ± 6.2 | *L* = 12.6 ± 0.8 |
| (*n* = 7) | (36%) | (37%) | (50%) | *W* = 6.3 ± 0.5 |
| RSC‡ | 6.7 ± 0.8 | 0.131 ± 0.025 | 8.9 ± 2.2 | *D* = 8.8 ± 0.3 |
| (*n* = 10) | (20%) | (16%) | (23%) | |
| Controls I§ | 5.6 ± 0.4 | 0.144 ± 0.017 | 8.1 ± 1.1 | *D* = 8.5 ± 0.2 |
| (*n* = 10) | (11%) | (16%) | (24%) | |
| Controls II (*n* = 4) | | | | |
| Fresh | 5.6 ± 0.4 | 0.132 ± 0.023 | 7.4 ± 1.4 | |
| Stored 24 hr | 5.8 ± 0.5 | 0.135 ± 0.014 | 7.9 ± 1.4 | |

*Data represent mean ± standard deviation of means from *n* donors; figures in parentheses are the average *CV* for the samples. For controls and RSC, 8 cells were measured in each donor sample; and for ISC, 6 cells were measured per donor. The RSC data are mainly from measurements on the MID fraction (8 donors) although for 2 donors, RSC from unfractionated blood were studied. *L*, ISC length; *W*, ISC width; *D*, disc diameter.

†The differences between ISC and Control I shear elastic modulus and surface viscosity are significant ($p < 0.001$).

‡The difference between RSC and Control I shear elastic modulus is significant ($p < 0.005$).

§Controls I are for 10 donors whose RBC were measured on day of blood withdrawal. Controls II are for 4 donors whose red cells were measured both on the day of blood withdrawal and after 24-hr storage at 4°C in heparinized plasma.

*Figure 1.3.7 : Mechanical properties of ISCs, RSCs, and normal RBCs (from Nash et al. [67]).*

At the same time, other experiments were successfully isolating sickle hemoglobin HbS and showing its polymerization upon deoxygenation. Kinetics of HbS fiber aggregation was studied by Wilson and Makinen [48], and Christoph, Hofrichter and Eaton [52]. Wang et al. determined the mechanical properties of isolated HbS fiber, modeled as long cylindrical rods [50]. While a promising path, polymerization and crowding of sickle hemoglobin still has to be fully understood to determine larger-size mechanical properties. These mechanisms are currently investigated by Ferrone and Rotter [51]. Recent research is also investigating depolymerization of sickle hemoglobin [53], and affected membrane permeability in sickle cell disease, which could be responsible for changes in osmotic equilibrium and RBC dehydration [54].

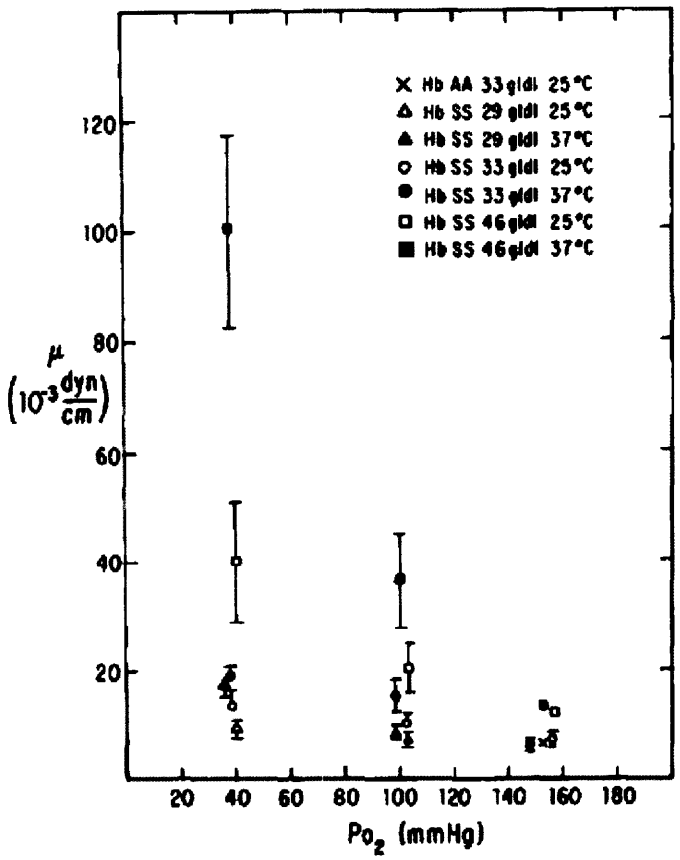


**The shear modulus of membrane elasticity, $\mu$, of SS erythrocytes (29 g/dL, 33 g/dL, 46 g/dL, 25°C and 37°C) and AA erythrocytes (33 g/dL, 25°C) is shown versus $pO_2$. In the SS cells at 46 g/dL, 40 mm Hg (25°C and 37°C), $\mu$ represents an "effective cell rigidity." Each data point represents between three to 14 cells except for the two data points without error brackets, which represent only two cells. Brackets correspond to standard deviations.**

*Figure 1.3.8 : Mechanical properties of sickle RBCs at different temperatures and oxygen partial pressures (from Mackie and Hochmut [70]).*

The studies of hemoglobin polymerization introduced a new research problem, since measured viscoelasticities of RBCs, first attributed to the membrane, were indeed "effective cell" elasticities, as remarked by Mackie and Hochmut [70]. Messman et al.'s calculations of membrane properties also showed variability among cell types, with an increased rigidity associated with ISCs [71]. Reciprocally, Liu, Derick and Palek showed how induced deformation of RBCs by the polymerized hemoglobin would produce a permanently reorganized RBC membrane structure, hence changing membrane properties irreversibly [49]. In 1992 Dong, Chadwick and Schechter were the first to address directly the problem of determining whether impaired blood dynamics were due primarily to the presence of

hemoglobin polymers, or to affected membrane properties [74]. In their model the RBC interior is modeled as a Voigt viscoelastic homogeneous solid to account for the polymerized HbS structures, while the membrane has a simple shear elastic modulus. Using experimental data, they successfully showed a "transition from membrane to internal polymer dominance of deformability" as oxygen level is lowered. Nevertheless, as reported by Hiruma et al. this transition is at a very high oxygen level, and even a small polymer fraction can be primarily responsible for impaired dynamics (the transition is estimated by Hiruma et al. at a level of oxyhemoglobin saturation above 95%) [75]. These contributions are a major argument in favor of not modeling the RBC membrane as a primary cause of affected dynamics, but modeling instead the RBC interior. Modeling both contributions should be nevertheless an eventual objective.

As a side note, therapeutic research has produced another considerable set of data supporting the abnormal blood flow as a cause of complications leading to sickle cell crises. This was shown in particular through the effects on blood flow of blood transfusion [87], and of hydroxyurea, which reactivates the production of the benign fetal hemoglobin HbF [89] [90] [94]. Another noteworthy research result is the 2006 Stroke Prevention Trials, which successfully used transcranial Doppler ultrasonography on children having sickle cell disease, to detect increased velocity in the internal carotid artery and correlate it with proven increased risks of stroke [91] [92] [93].

The importance of all the experiments described in this section is undeniable. Not only these results provide rheological parameters applicable to our model, but they also justify the hypotheses that will be made in Section 2.1, since the complexity of blood chemistry and mechanics cannot be entirely, fully modeled to this day. Alternatively, some data will also be used as validation to our results.

## 1.4. Conclusions : objectives and hypotheses of current research

In light of the current existing models for blood microcirculation, and the experimental data available, the present doctoral work proposes to design a novel advanced model, combining the most recent sub-models available for oxygen transfer, fluid dynamics, and RBC membrane mechanics. This model will first extend the existing models for normal blood and reconsider some hypotheses, in order to be applicable to sickle cell disease. Secondly, we will develop a new model for sickle cell disease, based on an intermediate description between the molecular level (HbS polymerization), and the vascular level (effect on blood dynamics). Physical parameters will be adjusted with experimental data, and we will compare our results with various sources for validation of the model. Thirdly, a

numerical model will be implemented to produce simulation results, which will be carefully examined to identify the main parameters affecting blood microcirculation, and crucial to study sickle cell disease. Finally, based on a systematic analysis, we will consider potential therapeutic directions that have been or may be further researched.

With these research goals defined, our specific objectives are :

(1) to derive and validate a "standard" mathematical model describing blood flow in capillary vessels. This model and its range of application will be rigorously defined to address the complexity of microcirculation using the most recent theoretical descriptions available, and as a consequence will be usable as a base for any further study of blood dynamics. Also, the model will be designed specifically to allow the inclusion of the sickle cell problematic (oxygen-dependent dynamics).

(2) to design a comprehensive model to address sickle cell disease. This model is to be based on our understanding of the pathophysiology leading to abnormal blood dynamics. Therefore, we will propose to build a new original model, as a tradeoff between the molecular complexity of sickle hemoglobin polymerization and vascular flow observations.

(3) to identify the driving factors of blood dynamics and sickle cell disease. The model derived will be used extensively for numerical simulations, and will be used to determine a few useful synthetic quantities. Some results will be presented to show implications of single parameter changes, reflecting natural or induced variations in the body, and giving us an interpretation of various situations affecting blood flow and sickle cell dynamics.

(4) to identify, assess and propose new therapeutic opportunities based on simulation results. Varying parameters will first be selected based on potential interest for medical research, then a systematic analysis will allow us to quantify the resulting effects, and conclude on the opportunities of existing or new therapeutic targets.

(5) to open larger investigations on blood dynamics. Our model is expected to constitute a strong basis to elaborate advanced tools useful to medical research and study of the blood microcirculation. Extensions of our work may be pursued to investigate other blood diseases, incorporate more realistic variable-inflow models, study vessel networks, or simulate the effect of various drugs. The results obtained may also help the elaboration of new diagnostic tools. All these bear a large range of potential benefits for the pharmaceutical industry.

This work will be based on the following main hypotheses :

(1) The system of equations assembled gives an accurate description of the dynamics of red blood cells, and the numerical model associated allows us to perform realistic simulations for a large range

of situations. Furthermore, the proposed model used to describe sickle cell disease is a correct approximation to the underlying mechanisms, and leads to significant progress in the understanding of the disease. A careful validation through previous theoretical and experimental results will address this hypothesis.

(2) Our choice of a few representative quantities correctly synthesizes the state of blood microcirculation for all the simulations performed. We will show that blood microcirculation and the problematic of sickle cell disease can be successfully reduced to some key features, described efficiently by those macroscopic quantities. This will eventually constitute our basis to analyze the efficiency of potential therapeutic actions.

(3) Our systematic parametric analysis correctly assesses some opportunities of available therapeutical action. We assume that our choice of therapeutical targets reflect current possibilities of medical intervention leading to reasonable changes in blood properties. Our simulation results will give decisive conclusions on these hypotheses, and allow us to devise which specific targets may be relevant for further therapeutical research.

# 2. Simulation model for RBC dynamics and sickle cell disease

In this chapter we first present the physical model used to determine the characteristics of capillary blood flow, with its assumptions and extension to sickle cell disease. Secondly we define a numerical model to allow simulations to be performed, and determine appropriate numerical parameters. Finally, we validate our simulation results with some basic case studies corresponding to results found in the literature.

## 2.1. Physical model : constitutive equations and flow hypotheses

The mathematical problem is defined in this section through 3 steps. The scope of our calculations is defined in the first part, by stating precisely the modeling hypotheses and geometrical constraints. Then, we present the system of equations to be solved for the normal RBCs, and discuss the values of all the associated physical parameters. Finally, we present the design of our proposed model for sickle cells.

### 2.1.1. Physical model hypotheses, geometry and conventions

To study sickle blood and compare its characteristics to normal blood, we intend to isolate specific factors that influence blood dynamics. Hence, we will generally distinguish 2 categories of differing features between normal and sickle blood. Physical properties that differ by small relative amounts will be generally ignored, while other varying physical properties will be addressed separately to isolate their respective influences (quantitative discussion of the varying parameters will be explicitly addressed in Section 2.1.3). All properties will be given in the S.I. (metric) system of units, except for pressure, usually expressed in millimeters of mercury (mmHg) in medical science.

In order to study the abnormal rheology of sickle blood, we assume that a main feature of sickle cell disease, eventually responsible for vessel occlusion, is the abnormal dynamics caused by sickle blood. This hypothesis is generally admitted among researchers, and is supported by numerous experiments such as Higgins's experiments on vessel occlusion [81]. Since vessel occlusion can be obtained without participation of endothelial cells, we will therefore ignore all possible chemical interactions of the RBCs with the blood vessel environment. RBCs will be also considered in local

chemical equilibrium with the blood plasma. In other terms, no osmotic imbalance or chemical interaction will be taken into account besides oxygen transfer, consumption, and binding to hemoglobin and myoglobin.

Consequently, RBC **volume** is to be considered **constant**. Typical volume of RBCs is between 80 and 95 fL (1 fL = 1 femtoliter = $10^{-18}$ $m^3$) [85]. In our study we will use **$9.10^{-17}$ $m^3$**. The decrease in RBC volume observed in sickle cells is relatively small [85], and will be ignored, although it could be easily included in further models.

To represent a capillary vessel, we will use an **axisymmetric** cylinder of **constant radius**. This restriction emphasizes geometrical simplicity to avoid fluctuations due to varying vessel sizes and focus our interest on other factors. Despite this constraint, but in order to observe various situations, our study will use radius sizes **between 2.5 μm and 5.0 μm**, a representative range where significant changes of the RBC geometry are expected (see Figure 1.2.7). At this scale, RBCs flow individually along the capillary vessel. Thus, although RBC-RBC interactions and formation of rouleaux (trains of agglutinated cells) is an important factor of blood flow for larger vessels, in our case we will assume that RBCs flow at a regular pace, and our calculations will focus on the dynamics of a **single RBC**. To set appropriate boundaries to our domain, we will assume **periodic flow** of RBCs. For normal cells, the uncoupling of oxygen transfer equations and RBC dynamics allows this assumption to be valid far from the capillary entrance, and corresponds to what is commonly called "fully developed flow" (see detailed mathematical formulation in Appendix D). In the case of sickle cells, we will simply assume that the changes due to oxygen consumption are relatively small on the scale of a spatial period, which is supported by the observation of typical capillary lengths [8], and verified in our results. This implies that given a set of oxygen levels, we can reconstruct sickle RBC behavior based on **local pseudo-periodicity**. Figure 2.1.1 illustrates our geometrical model with the given boundary conditions.

The model for oxygen transport will have the same geometry as in Vadapalli, Goldman and Popel's model of **extended Krogh cylinder**, completed with periodic conditions on the oxygen pattern (oxygen level is assumed to have the same profile at inlet and exit). Again, this assumed **local pseudo-periodicity** is expected to allow us to interpolate the trend at larger length scales, and was retrospectively checked in our results. The **radial thicknesses** of the **capillary wall** and **interstitium** are taken as respectively **0.3 μm** and **0.35 μm**, and the **Kroch cylinder radius** is taken as **20 μm** [108]. Figure 2.1.2 illustrates these geometrical constraints.

The **spatial period** $L$ is easily calculated using the hematocrit (proportion of RBC in volume) :

$$L = \frac{V_{RBC}}{Hct\ \pi\ R_w^{\ 2}}, \tag{39}$$

where $V_{RBC}$ is the RBC volume, $Hct$ is the hematocrit, and $R_w$ is the radius of the blood vessel up to the capillary wall. The most important factors of variability for the hematocrit are age and gender (source : http://www.medicinenet.com/hematocrit/article.htm), and normal values for adults are between 0.36 and 0.54 [85]. Although the hematocrit of any individual is sensitive to a large variety of environmental factors (altitude, smoking, dehydration, nutrition, sickness…), its changes are generally incremental (unless the integrity of the vasculature is compromised). Hence we will use a reference value of **0.45** for **normal blood hematocrit**. Sickle cell patients, on the other hand, present a reduced hematocrit between 0.2 and 0.3 [85]. In order to isolate the effects of the reduced hematocrit from other factors, we will study **sickle cell blood** using both values of **0.45** and **0.25**.

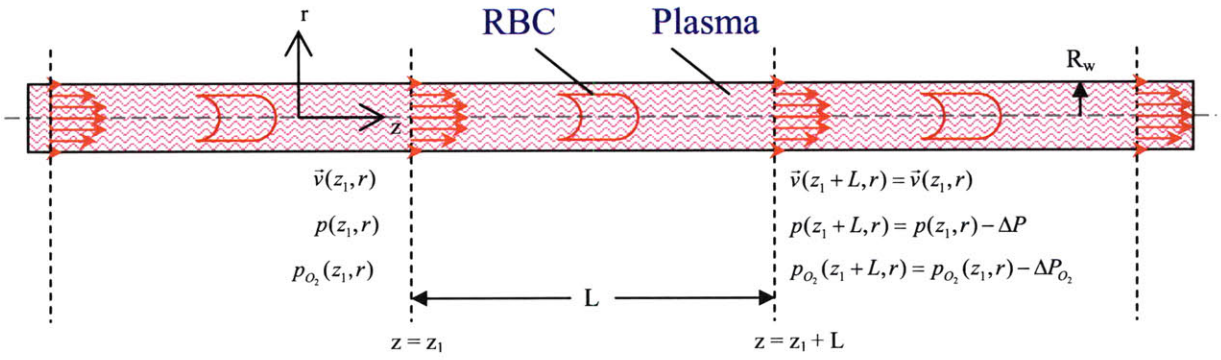


*Figure 2.1.1 : Individual RBCs periodic flow model.*

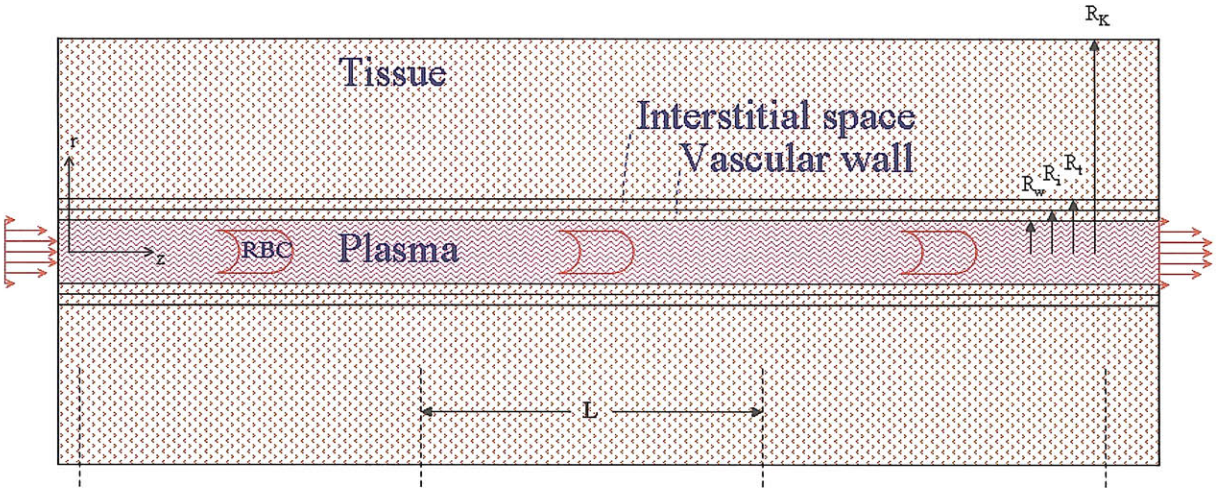


*Figure 2.1.2 : Extended Krogh cylinder model (periodic).*

The use of an axisymmetric geometry justifies assumptions of axisymmetry for all the field variables under fully developed flow. We will naturally use **cylindrical coordinates** $(z,r,\theta)$ and assume independence of all variables with respect to $\theta$.

With a thickness of less than 10 nm [21], the **RBC membrane** is to be modeled as a **2-D surface** containing a **homogeneous solution of hemoglobin**. Modeling the cytoplasm as a continuous fluid is justified by the size of a hemoglobin molecule (hemoglobin is nearly spherical with a diameter of 5.5 nm - source : http://biology.kenyon.edu/BMB/Chime/Lisa/FRAMES/hemetext.htm), and its non-binding normal characteristics (the sickle case will be discussed later).

Following Secomb's work, the RBC membrane will be modeled as an **elastic surface** made of **superposed leaflets** generating **tension, moments and shear stresses** [23]. Figure 2.1.3 recalls this model already presented in Section 1.2.3, with the **curvilinear coordinates** defined along the membrane and the conventional orientations used. As discussed in Section 1.2.3, viscous properties of the membrane can be neglected for normal flow situations. The **RBC surface area** at minimal surface tension is taken as **135 μm²** [101], and is also to be used as initial parameter.

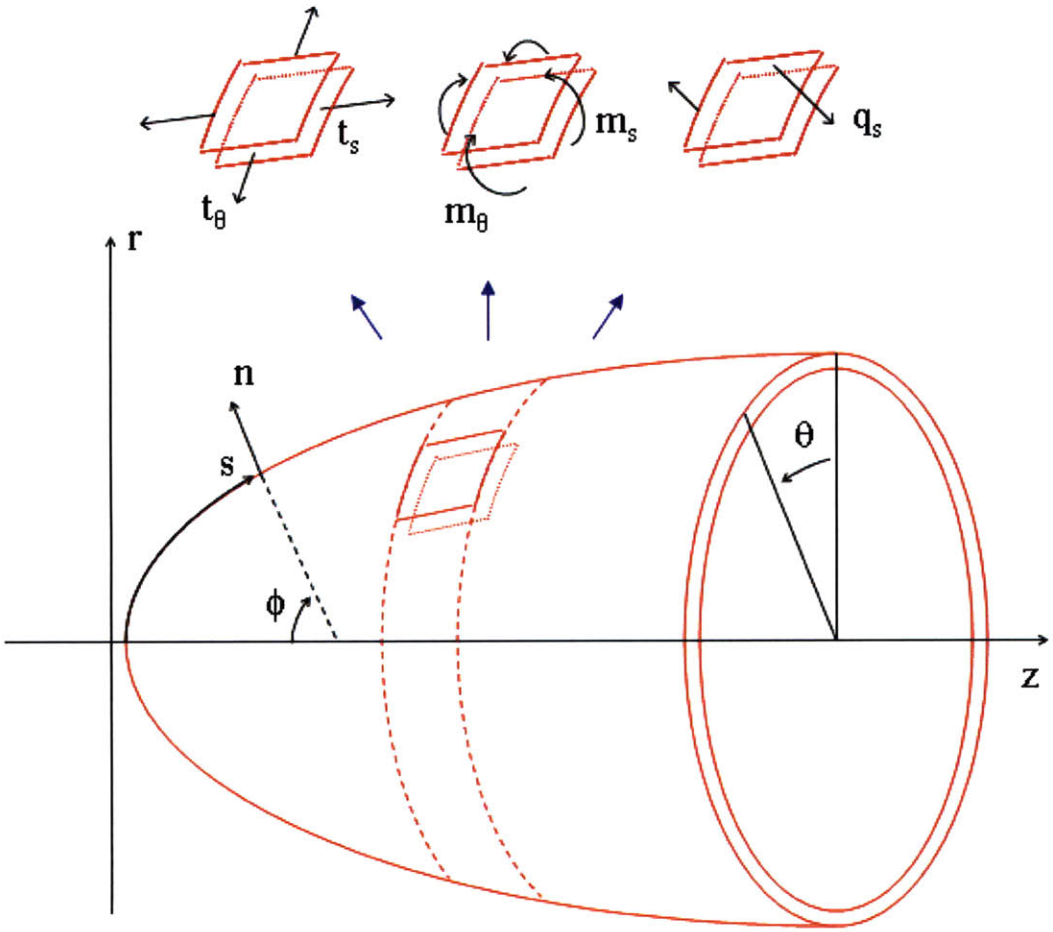


*Figure 2.1.3 : Curvilinear coordinates for axisymmetric RBC membrane and membrane stresses convention (model of superposed leaflets).*

## 2.1.2. System of equations and physical parameters for normal RBCs

With the geometry defined in Section 2.1.1, the constitutive equations used to calculate fluid flow everywhere are simply the axisymmetric Navier-Stokes equations written in cylindrical coordinates. As mentioned in Section 1.3.1, both plasma and cytoplasm are assumed to be incompressible, Newtonian viscous fluids :

$$\vec{\nabla}\cdot\vec{v} \;=\; \frac{1}{r}\,\frac{\partial}{\partial r}(r\,v_r) \;+\; \frac{\partial}{\partial z}v_z \;=\; 0\,, \tag{40}$$

$$\rho\left(\frac{\partial v_r}{\partial t} \;+\; v_r\frac{\partial v_r}{\partial r} \;+\; v_z\frac{\partial v_r}{\partial z}\right) \;=\; -\;\frac{\partial p}{\partial r} \;+\; \mu\left(\frac{1}{r}\,\frac{\partial}{\partial r}\left(r\frac{\partial v_r}{\partial r}\right) \;+\; \frac{\partial^2 v_r}{\partial z^2} \;-\; \frac{v_r}{r^2}\right), \tag{41}$$

$$\rho\left(\frac{\partial v_z}{\partial t} + v_r\frac{\partial v_z}{\partial r} + v_z\frac{\partial v_z}{\partial z}\right) = -\frac{\partial p}{\partial z} + \mu\left(\frac{1}{r}\frac{\partial}{\partial r}\left(r\frac{\partial v_z}{\partial r}\right) + \frac{\partial^2 v_z}{\partial z^2}\right), \tag{42}$$

where $v_r(z,r,t)$ and $v_z(z,r,t)$ are the components of the velocity field, $p(z,r,t)$ is the static (mechanical or thermodynamic) pressure, $\mu$ is the **dynamic viscosity**, taken as equal to **$1.4.10^{-3}$ Pa.s** in the **plasma** [65] and **$5.89.10^{-3}$ Pa.s** in the RBC **cytoplasm** [108], and $\rho$ is the plasma/cytoplasm **density**, taken as equal to **1025 kg/m$^3$**. Although density is reported as slightly higher in the cytoplasm (1125 kg/m$^3$), we ignore this small difference for simplicity (source : http://hypertextbook.com/facts/2004/MichaelShmukler.shtml), especially since the cytoplasm is constrained spatially by the RBC membrane and does not deform as much as the surrounding fluid. Additionally, all fluid motion is ignored outside the capillary, i.e. $\vec{v} = \vec{0}$ for $r \geq R_w$.

The constitutive equations for oxygen transport are based on Vadapalli, Goldman and Popel's model [108]. The generalized equations are :

$$\left(\alpha + [Mb]\frac{p^{Mb}_{O_2,50\%}}{(p^{Mb}_{O_2,50\%} + p_{O_2})^2}\right)\left(\frac{\partial p_{O_2}}{\partial t} + v_r\frac{\partial p_{O_2}}{\partial r} + v_z\frac{\partial p_{O_2}}{\partial z}\right) =$$

$$\left(\alpha D + D^{Mb}[Mb]\frac{p^{Mb}_{O_2,50\%}}{(p^{Mb}_{O_2,50\%} + p_{O_2})^2}\right)\left(\frac{1}{r}\frac{\partial}{\partial r}\left(r\frac{\partial p_{O_2}}{\partial r}\right) + \frac{\partial^2 p_{O_2}}{\partial z^2}\right)$$

$$+ k^{Hb}[Hb]\left(S^{Hb} - (1 - S^{Hb})\left(\frac{p_{O_2}}{p^{Hb}_{O_2,50\%}}\right)^n\right) - M \tag{43}$$

$$\frac{\partial S^{Hb}}{\partial t} + v_r\frac{\partial S^{Hb}}{\partial r} + v_z\frac{\partial S^{Hb}}{\partial z} = D^{Hb}\left(\frac{1}{r}\frac{\partial}{\partial r}\left(r\frac{\partial S^{Hb}}{\partial r}\right) + \frac{\partial^2 S^{Hb}}{\partial z^2}\right)$$

$$- k^{Hb}\left(S^{Hb} - (1 - S^{Hb})\left(\frac{p_{O_2}}{p^{Hb}_{O_2,50\%}}\right)^n\right), \tag{44}$$

where $p_{O_2}(z,r,t)$ is the partial pressure of dissolved oxygen, $S^{Hb}(z,r,t)$ is the fractional saturation of oxyhemoglobin, $p^{Mb}_{O_2,50\%}$ is the oxygen partial pressure at an equilibrium corresponding to 50% saturation of myoglobin (taken as **5.3 mmHg = 706.6 Pa**), $p^{Hb}_{O_2,50\%}$ is the oxygen partial pressure at an equilibrium corresponding to $S^{Hb} = 0.5$ (taken as **29.3 mmHg = 3906.3 Pa**), $\alpha$ is the oxygen solubility constant, $D$ is the (isotropic) oxygen diffusivity, $D^{Mb}$ is the (isotropic) **diffusivity of**

**myoglobin** (taken as $\mathbf{6.10^{-11}\ m^2/s}$), $D^{Hb}$ is the (isotropic) **diffusivity of oxyhemoglobin** (taken as $\mathbf{1.3783.10^{-11}\ m^2/s}$), $[Mb]$ is the total concentration of myoglobin (bound and not bound to oxygen), $[Hb]$ is the total concentration of hemoglobin (bound and not bound to oxygen), $k^{Hb}$ is the **kinetic dissociation rate constant** of oxyhemoglobin (taken as $\mathbf{44\ s^{-1}}$), n is the **Hill coefficient** of the oxyhemoglobin dissociation curve (taken as **2.2**), and $M$ is the rate of oxygen consumption. All the parameters given above are determined using Vadapalli, Goldman and Popel's sources [108], with the other parameters having different values in the 5 regions reported in Table 2.1.1. Conversions were made using standard data for the molar mass of hemoglobin, 16.11 kg/mol (the definition of "mole" is applied to each of the 4 tetramers or protein subunits assembled in hemoglobin), and 25.766 L/mol as the molar volume of oxygen, which has been calculated from standard conditions using the Van der Waals equation for oxygen, at body temperature 37°C (source : http://www.combro.co.uk/nigelh/diver/vdw.html).

| | $\vec{v}$ | $\mu$ (Pa.s) | $\alpha$ (mol/m$^3$ /mmHg) | $D$ (m$^2$/s) | $[Hb]$ (mol/m$^3$) | $[Mb]$ (mol/m$^3$) | $M$ (mol/m$^3$/s) |
|---|---|---|---|---|---|---|---|
| Tissue | $\vec{0}$ | / | $1.5059.10^{-3}$ | $2.41.10^{-9}$ | 0 | 0.4 | $6.1321.10^{-3}$ |
| Interstitium | $\vec{0}$ | / | $1.0906.10^{-3}$ | $2.18.10^{-9}$ | 0 | 0 | 0 |
| Capillary wall | $\vec{0}$ | / | $1.5097.10^{-3}$ | $8.73.10^{-10}$ | 0 | 0 | $3.8811.10^{-3}$ |
| Plasma | $(v_z, v_r)$ | $1.4.10^{-3}$ [65] | $1.0906.10^{-3}$ | $2.4.10^{-9}$ | 0 | 0 | 0 |
| RBC cytoplasm | $(v_z, v_r)$ | $5.89.10^{-3}$ | $1.3118.10^{-3}$ | $9.47.10^{-10}$ | 21.099 | 0 | 0 |

*Table 2.1.1 : Velocity and varying parameters in the 5 layers (from Vadapalli, Goldman and Popel [108]).*

Finally, the constitutive equations for the RBC 2-D elastic membrane are taken from Secomb's model presented in Section 1.2.3 [101] :

$$\bar{t} = \frac{t_s + t_\theta}{2} = \sigma_0 + K_{bu}\left(\frac{ds}{ds_0}\frac{R}{R_0} - 1\right), \tag{45}$$

$$t_d = \frac{t_s - t_\theta}{2} = \frac{K_{sh}}{2}\left(\left(\frac{ds}{ds_0}\right)^2 - \left(\frac{R}{R_0}\right)^2\right) - \frac{B}{2}\left(\frac{d\phi}{ds} - \frac{\sin\phi}{R}\right)\left(\frac{d\phi}{ds} + \frac{\sin\phi}{R} - k_0\right), \tag{46}$$

$$q_s = -B\left(\frac{d^2\phi}{ds^2} + \frac{d}{ds}\left(\frac{\sin\phi}{R}\right)\right), \tag{47}$$

where $s(s_0,t)$ is the curvilinear coordinate of a point on the RBC membrane, function of time and its position at initial time ($s(s_0,0)=s_0$), $ds(s_0,t)$ is a local distance between 2 infinitesimally close points of the membrane along the s direction (with $ds(s_0,0)=ds_0$), $R(s)$ is the membrane radius (with $R(s_0)=R_0$) and $\phi(s)$ is the local angle of the normal vector to the axis of symmetry $r=0$ (see Figure 2.1.3), $t_s(s)$ and $t_\theta(s)$ are the surface tensions in the $s$ and $\theta$ directions, $\bar{t}(s)$ and $t_d(s)$ are the isotropic (mean) tension and shear (deviatoric) tension, $q_s(s)$ is the shear force per unit length in the s direction, $\sigma_0$ is the **isotropic tension** at the reference state (estimated at **$7.10^{-2}$ kg/s$^2$** [19]), $K_{bu}$ is the **isothermal area compressibility** modulus (or 2-D bulk elasticity modulus, taken as **0.5 kg/s$^2$** [101]), $K_{sh}$ is the 2-D **shear modulus** (taken as **$4.2.10^{-6}$ kg/s$^2$** [101]), $B$ is the **bending modulus** (taken as **$1.8.10^{-19}$ kg.m$^2$/s$^2$** [101]), and $k_0$ is the total curvature at the reference moment-free state (chosen to be a spherical configuration, i.e. homogeneous curvature, for the same RBC volume) :

$$k_0 = \left.\frac{d\phi}{ds}\right|_{m=0} + \left.\frac{\sin\phi}{R}\right|_{m=0} . \tag{48}$$

Using the reference **RBC volume** of **90 µm$^3$** [101], we get for $k_0$ **$7.1941.10^5$ m$^{-1}$**.

The membrane radius and local angle at any position $s$ are also simply related by :

$$\frac{dR}{ds} = \cos\phi . \tag{49}$$

Finally, these stresses are combined into the local normal and tangential forces per unit area of the membrane :

$$\frac{dF_n}{dA} = -t_s\frac{d\phi}{ds} - t_\theta\frac{\sin\phi}{R} - \frac{1}{R}\frac{d(R\,q_s)}{ds}, \tag{50}$$

$$\frac{dF_t}{dA} = \frac{1}{R}\frac{d(R\,t_s)}{ds} - t_\theta\frac{\cos\phi}{R} - q_s\frac{d\phi}{ds}, \tag{51}$$

and Equations (50) and (51) can be projected onto cylindrical coordinates, to give the total force components per unit area exerted from any point on the membrane :

$$f_r(s) = \frac{dF_n}{dA}\sin\phi + \frac{dF_t}{dA}\cos\phi , \tag{52}$$

$$f_z(s) = -\frac{dF_n}{dA}\cos\phi + \frac{dF_t}{dA}\sin\phi \ . \tag{53}$$

All the derivation details of Equations (40) to (51) can be found in Appendices B-1, B-2 and B-3.

In order to "connect" the membrane surface equations to the Navier Stokes equations, one can either use boundary conditions or discretize Equations (52)-(53). The first method consists in integrating Equations (41)-(42) in an infinitesimal volume over the membrane surface, and balancing the result with the membrane contribution. The second method consists in discretizing a Dirac distribution localizing the membrane in space, to add an equivalent force per unit volume to the Navier-Stokes equations (The added term is presented in a generalized form of the Navier-Stokes equations in Appendix B-2). This choice is closely related to the numerical method used to solve the boundary problem. Hence its mathematical formulation will be later discussed in Section 2.2.

To close the mathematical problem, we use the following boundary conditions : no-slip at the capillary wall, continuity of oxygen partial pressure and oxygen transport across the model layers, and no-radial-transport at the Krogh radius. The **absolute static pressure** level at the inlet can be set arbitrarily to **30 mmHg + 1 atm ≃ 101325 Pa** (average pulse at capillary entrance – see Figure 1.3.1). We also set the conditions on the inlet side for the **average blood velocity** and **oxygen partial pressure**. The values used will be case-dependent, with reference values of **0.25 mm/s**, and **95 mmHg and 40 mmHg** respectively. At the RBC membrane, the no-slip condition is equivalent to an implicit convection equation :

$$\frac{d}{dt}\begin{pmatrix} Z \\ R \end{pmatrix} = \frac{ds}{dt}\begin{pmatrix} \sin(\phi) \\ \cos(\phi) \end{pmatrix} = \vec{v}\left(Z(s), R(s)\right) , \tag{54}$$

where $Z(s)$ and $R(s)$ are the two functions mapping the RBC membrane position in the cylindrical reference frame. Equation (54) forms the "implicit feedback" of the fluid dynamics to the membrane (i.e. defines implicitly $s$ as a function of time).

In the following section, we present the model used for sickle cells and the physical parameters associated.

### 2.1.3. System of equations and physical parameters for sickle RBCs

In accordance with our work hypotheses, abnormal sickle RBC dynamics are primarily the consequence of both a shift in the values of some parameters, and the emergence of a polymerized structure inside the RBC. While the first can easily be implemented in a blood flow model, the

second needs a specific physical model for sickling RBCs. More precisely, we want to investigate Reversibly Sickled Cells (RSCs) as they turn into Irreversibly Sickled Cells (ISCs), i.e. we want to capture the sickling mechanism happening upon deoxygenation, within the capillary vessels (RSCs travel too quickly to undergo significant sickling, while ISCs are permanently sickled).

Our motivation to design a novel model for sickling RBCs, is to use and combine the knowledge from Dou and Ferrone's work at the molecular level, showing the growth of sickling hemoglobin polymers [127], and Berger's model at the cellular level, using modified RBC membrane stiffness for sickle cell patients [123]. While implementing Ferrone's model would require unprecedented levels of complexity due to large multi-scale computations, Berger's model can be modified to reflect more accurately the sickling phenomenon with its molecular origin, keeping in mind Usami's experimental results showing modified RBC dynamics [62]. Based on Dou and Ferrone's results, we hence propose to model the sickling hemoglobin polymer chain as a long, C-shaped structure growing inside the RBC. As a first approach, the position of the polymer chain will follow an approximate RBC midline (the midline formulation is described in Section 2.2). This structure will generate elastic stresses on the RBC membrane, both axially and laterally (see Figure 2.1.4). To preserve the axisymmetry of the problem, we assume that the sickling polymer structure is also axisymmetric, effectively making it a deforming "curved plate" generating additional forces on the membrane, directed outwards.

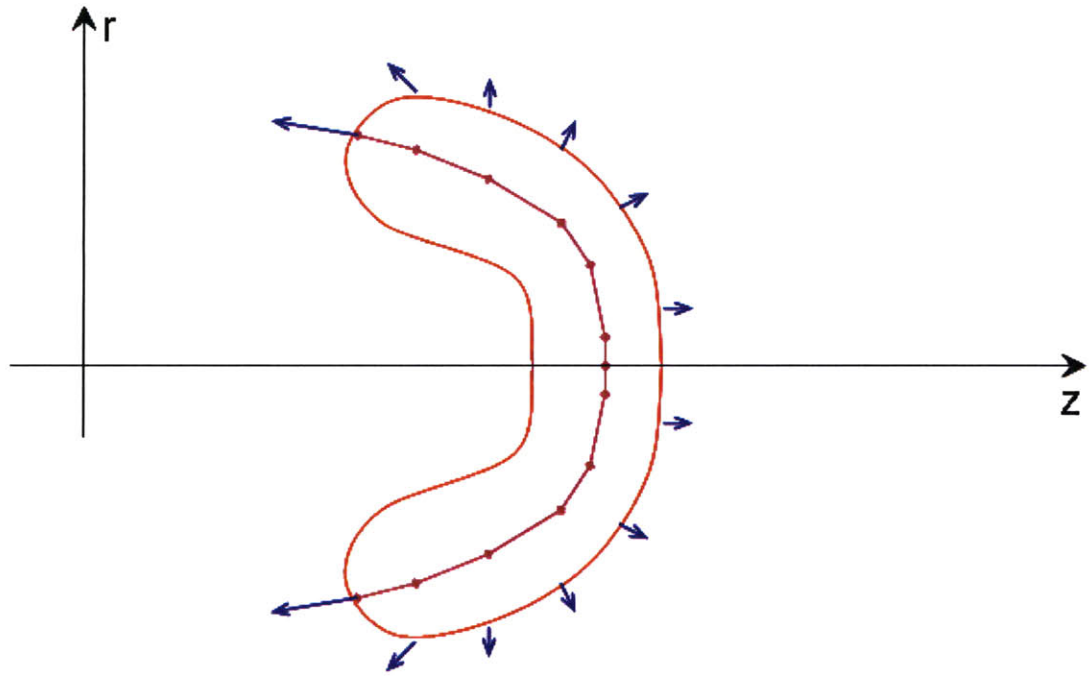


*Figure 2.1.4 : Schematic model of curved plate for sickling RBC.*

To model the elastic stresses, we use a simple linear spring model. Stresses are to be proportional to the difference between the actual length and a reference length "at rest" of the hemoglobin chain. This reference length is to be proportional to the oxygen level in order to characterize oxygen-dependent sickling. Additional parameters to the spring constant set the boundaries of this dynamical model, namely the reference oxygen level below which sickling starts, and the maximal polymer elongation (corresponding to no oxygen). Axial stresses are thus described by the following equations :

$$F_{HbS} = k_{HbS}\left(l_{HbS\_ref}(p_{O_2}) - l_{HbS}\right), \tag{55}$$

$$l_{HbS\_ref}(p_{O_2}) = l_0\left(1 - \left(\left(\frac{l_{HbS\_ref}}{l_0}\right)_{\max} - 1\right)\left(\frac{p_{O_2\_ref} - p_{O_2}}{p_{O_2\_ref}}\right)\right), \tag{56}$$

where $F_{HbS}$ is the total force exerted by the hemoglobin polymers (in Newtons), $k_{HbS}$ is the effective spring constant of the polymer chain (in kg/s$^2$), $l_{HbS}$ is the curvilinear length of the chain, $l_{HbS\_ref}$ is the expected length of the chain for a given oxygen concentration/partial pressure, $l_0$ is the reference length before sickling, corresponding to the oxygen partial pressure $p_{O_2\_ref}$, and $\left(\frac{l_{HbS\_ref}}{l_0}\right)_{\max}$ is the maximal relative elongation of the chain with respect to the reference state.

Since we expect to observe the effects of the chain growth, $k_{HbS}$ should be sufficiently high to counterbalance stresses in the membrane and reshape the RBC. In this study, to emphasize the dependence of polymer growth on oxygen level we will assume that the elongation of HbS polymer chains is basically not stopped by the membrane. We thus set $k_{HbS}$ to an arbitrarily high value (determined by the numerical limits), to essentially keep $l_{HbS}$ and $l_{HbS\_ref}$ equal, and use $\left(\frac{l_{HbS\_ref}}{l_0}\right)_{\max}$ as the main parameter for the sickle model to be determined by experimental data. In other terms, our definition of the spring force becomes simply a dynamical substitute to a fixed polymer length condition, with Equation (56) defining how the polymer chain should elongate. This rough simplification, while being arguable, follows the purpose of keeping our model as simple as possible.

To avoid large local curvatures (formation of a corner), we also consider a localized thickness of the hemoglobin fibers. This corresponds in practice to representing a polymer with multiple strings, to spread out the resulting axial force on the membrane (see Figure 2.1.5).

Lateral stresses exerted by the polymer chain on the RBC membrane use a similar formulation, with the forces defined for each control point of the structure, as acting on the closest membrane point facing it laterally (see Figure 2.1.5) :

$$F_{HbS} = k_{HbS}\left(d_{HbS\_ref}(p_{O_2}) - d_{HbS}\right), \tag{57}$$

$$d_{HbS\_ref}(p_{O_2}) = d_0\left(1 - \left(\left(\frac{d_{HbS\_ref}}{d_0}\right)_{\max} - 1\right)\left(\frac{p_{O_2\_ref} - p_{O_2}}{p_{O_2\_ref}}\right)\right), \tag{58}$$

where $F_{HbS}$ is the lateral force exerted on a point facing laterally one of the polymer control points, $k_{HbS}$ is the same spring constant, $d_{HbS}$ is the actual distance between a control point and its opposing point on the RBC membrane, $d_{HbS\_ref}$ is the expected distance for a given oxygen concentration/partial pressure, $d_0$ is the reference distance before sickling corresponding to the oxygen partial pressure $p_{O_2\_ref}$, and $\left(\frac{d_{HbS\_ref}}{d_0}\right)_{\max}$ is the maximal relative elongation of this lateral distance, with respect to the reference state.

Figure 2.1.5 shows the resulting model, which corresponds in practice to representing the polymer chain as a "tree" of hemoglobin fibers forming along the RBC midline. To simplify the analysis, we will only consider the lateral stresses on the upper (convex) side of the RBC. Since the flow strain rate is much higher near the capillary walls, stresses on the lower (concave) side are not expected to have significant effects on the RBC dynamics (besides reshaping). To fit our linear spring model into an axisymmetric average problem, the resulting forces are to be spread out axysimmetrically.

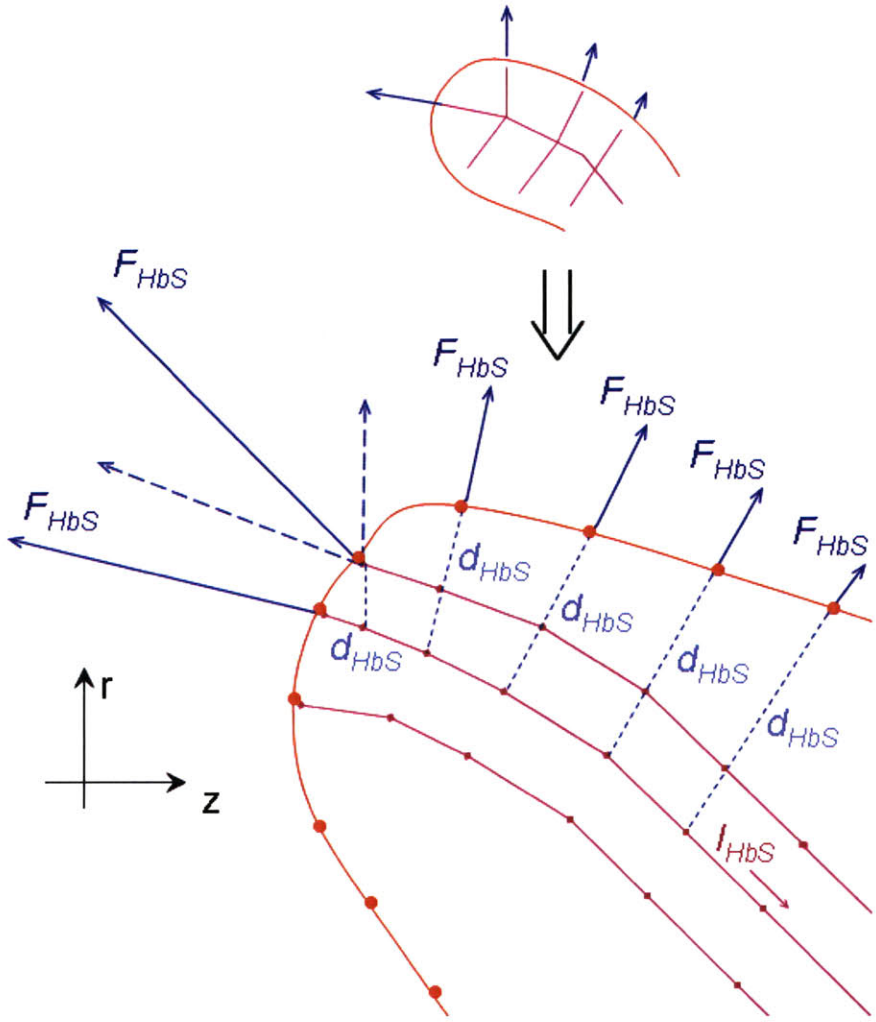


*Figure 2.1.5 : Schematic model of curved plate for sickling RBC (detail).*

As a case study, we set the model constants as follows. $l_0$ and $d_0$ are to be defined by the non-sickle case, using the RBC midline calculated under steady flow conditions (with respect to the moving RBC). $p_{O_2\_ref}$ is set to an upper limit of **95 mmHg**, which corresponds to an assumption of early sickling, at highly oxygenated blood. These 2 hypotheses mean that sickling will start as soon as the RBC arrives in the capillary, with a polymer chain just reaching the size of the RBC when entering the capillary (this fits precisely to our motivation to represent RSCs turning into ISCs). Since the growing polymer chain cannot exert an overall force on the RBC (pushing it down the flow or dragging it), the sum of all forces need to be zero. This physical constraint effectively reduces the definition of $\left(\frac{l_{HbS\_ref}}{l_0}\right)_{\max}$ and $\left(\frac{d_{HbS\_ref}}{d_0}\right)_{\max}$ to one constant (in other terms, lateral forces must

compensate axial forces). The remaining parameter is "tuned" to match a chosen set of experimental data, namely the ratio of apparent viscosity of **1.5** observed for larger vessels, observed in results from Usami and coworkers [62]. The obtained value for $\left(\frac{d_{HbS\_ref}}{d_0}\right)_{\max}$ is approximately **10** when $k_{HbS}$ is set to $\mathbf{5.10^{-5}\ kg/s}$ (the value of $k_{HbS}$ determined to meet numerical limitations is discussed in the Section 2.2). This ratio is evidently an upper bound for the theoretical maximal elongation.

For the sickle cell model, Equations (40) to (54) will still be used. To study separately the impact of the modeled sickling RBC and of the varying parameters due to the disease, we will carry calculations first with the **same values** for **all the physical parameters**. As a supplemental preliminary study, we will then study the effect of the reduced hematocrit in the sickle case, set to **0.25** in accordance with experimental data [85]. Further work is encouraged to examine the impact of other varying parameters, which is expected to be as important as the variation of their relative value roughly suggests. Following the discussion on available experimental data in Section 1.3.2, these parameters include plasma viscosity (increased to $\mathbf{1.7.10^{-3}\ Pa.s}$ in the crisis state), decreased RBC volume and increased cytoplasmic viscosity (due to dehydration), changes in $p_{O_2,50\%}^{Hb}$ and the Hill coefficient $n$ corresponding to the shift in the oxyhemoglobin dissociation curve, and increased shear modulus $K_{sh}$ corresponding to the irreversible reorganization of the RBC membrane structure (other elastic coefficients being potentially affected too). Finally, some physical parameters such as plasma viscosity could be modified to reflect interactions with the endothelial cell layer, although Higgins's work proved it not to be necessary to achieve reversible vessel occlusion [81].

$$\vec{\nabla}\cdot\vec{v} = \frac{1}{r}\frac{\partial}{\partial r}(r\,v_r) + \frac{\partial}{\partial z}v_z = 0, \tag{40}$$

$$\rho\left(\frac{\partial v_r}{\partial t} + v_r\frac{\partial v_r}{\partial r} + v_z\frac{\partial v_r}{\partial z}\right) = -\frac{\partial p}{\partial r} + \mu\left(\frac{1}{r}\frac{\partial}{\partial r}\left(r\frac{\partial v_r}{\partial r}\right) + \frac{\partial^2 v_r}{\partial z^2} - \frac{v_r}{r^2}\right), \tag{41}$$

$$\rho\left(\frac{\partial v_z}{\partial t} + v_r\frac{\partial v_z}{\partial r} + v_z\frac{\partial v_z}{\partial z}\right) = -\frac{\partial p}{\partial z} + \mu\left(\frac{1}{r}\frac{\partial}{\partial r}\left(r\frac{\partial v_z}{\partial r}\right) + \frac{\partial^2 v_z}{\partial z^2}\right), \tag{42}$$

$$\left(\alpha + [Mb]\frac{p^{Mb}_{O_2,50\%}}{(p^{Mb}_{O_2,50\%} + p_{O_2})^2}\right)\left(\frac{\partial p_{O_2}}{\partial t} + v_r\frac{\partial p_{O_2}}{\partial r} + v_z\frac{\partial p_{O_2}}{\partial z}\right) = \left(\alpha\,D + D^{Mb}\,[Mb]\frac{p^{Mb}_{O_2,50\%}}{(p^{Mb}_{O_2,50\%} + p_{O_2})^2}\right)\left(\frac{1}{r}\frac{\partial}{\partial r}\left(r\frac{\partial p_{O_2}}{\partial r}\right) + \frac{\partial^2 p_{O_2}}{\partial z^2}\right)$$
$$+ k^{Hb}\,[Hb]\left(S^{Hb} - \left(1 - S^{Hb}\right)\left(\frac{p_{O_2}}{p^{Hb}_{O_2,50\%}}\right)^n\right) - M\,, \tag{43}$$

$$\frac{\partial S^{Hb}}{\partial t} + v_r\frac{\partial S^{Hb}}{\partial r} + v_z\frac{\partial S^{Hb}}{\partial z} = D^{Hb}\left(\frac{1}{r}\frac{\partial}{\partial r}\left(r\frac{\partial S^{Hb}}{\partial r}\right) + \frac{\partial^2 S^{Hb}}{\partial z^2}\right) - k^{Hb}\left(S^{Hb} - \left(1 - S^{Hb}\right)\left(\frac{p_{O_2}}{p^{Hb}_{O_2,50\%}}\right)^n\right), \tag{44}$$

$$\frac{dF_n}{dA} = -t_s\frac{d\phi}{ds} - t_\theta\frac{\sin\phi}{R} - \frac{1}{R}\frac{d(R\,q_s)}{ds}, \qquad \frac{dF_t}{dA} = \frac{1}{R}\frac{d(R\,t_s)}{ds} - t_\theta\frac{\cos\phi}{R} - q_s\frac{d\phi}{ds}, \tag{50)-(51}$$

$$\bar{t} = \frac{t_s + t_\theta}{2} = \sigma_0 + K_{bu}\left(\frac{ds}{ds_0}\frac{R}{R_0} - 1\right), \tag{45}$$

$$t_d = \frac{t_s - t_\theta}{2} = \frac{K_{sh}}{2}\left(\left(\frac{ds}{ds_0}\right)^2 - \left(\frac{R}{R_0}\right)^2\right) - \frac{B}{2}\left(\frac{d\phi}{ds} - \frac{\sin\phi}{R}\right)\left(\frac{d\phi}{ds} + \frac{\sin\phi}{R} - k_0\right), \tag{46}$$

$$q_s = -B\left(\frac{d^2\phi}{ds^2} + \frac{d}{ds}\left(\frac{\sin\phi}{R}\right)\right). \tag{47}$$

*Figure 2.1.6 : System of equations of the full capillary flow model.*

$$F_{HbS} = k_{HbS}\left(l_{HbS\_ref}(p_{O_2}) - l_{HbS}\right), \qquad l_{HbS\_ref}(p_{O_2}) = l_0\left(1 - \left(\left(\frac{l_{HbS\_ref}}{l_0}\right)_{\max} - 1\right)\left(\frac{p_{O_2\_ref} - p_{O_2}}{p_{O_2\_ref}}\right)\right), \quad (55)\text{-}(56)$$

$$F_{HbS} = k_{HbS}\left(d_{HbS\_ref}(p_{O_2}) - d_{HbS}\right), \qquad d_{HbS\_ref}(p_{O_2}) = d_0\left(1 - \left(\left(\frac{d_{HbS\_ref}}{d_0}\right)_{\max} - 1\right)\left(\frac{p_{O_2\_ref} - p_{O_2}}{p_{O_2\_ref}}\right)\right), \quad (57)\text{-}(58)$$

$$\sum F_{HbS} = 0\,. \quad (59)$$

*Figure 2.1.7 : Additional equations for the sickling RBC model (local axial and lateral forces exerted on the RBC membrane).*

| Geometry | | (Fluid) Dynamics | | Oxygen Transport | | RBC Elastic Membrane | | HbS Elastic Model | |
|---|---|---|---|---|---|---|---|---|---|
| Parameter (units) | Value | Parameter (units) | Value | Parameter (units) | Value | Parameter (units) | Value | Parameter (units) | Value |
| $V_{RBC}$ ($m^3$) | $9.10^{-17}$ | $\rho$ ($kg/m^3$) | 1025 | $\alpha$ ($mol/m^3/mmHg$) | $\sim 1.10^{-3}$...* $\sim 1.51.10^{-3}$ | $k_0$ ($m^{-1}$) | $7.1941.10^5$ | $k_{HbS}$ ($kg/s^2$) | $\infty$ |
| $A_{RBC}$ ($m^2$) | $1.35.10^{-10}$ | $\mu$ (Pa.s) | $1.4.10^{-3}$ * $5.89.10^{-3}$ | $D$ ($m^2/s$) | $\sim 1.10^{-9}$...* $2.41.10^{-9}$ | $\{s_0, ds_0\}$ {m} | $R_w$-case dependent | $\{l_0, d_0\}$ {m} | $R_w$-case dependent |
| $R_w$ (m) | $\geq 2.5.10^{-6}$ $\leq 4.5.10^{-6}$ | | | $M$ ($mol/m^3/s$) | 0... * $6.1321.10^{-3}$ | $\{R_0\}$ {m} | $R_w$-case dependent | $\left(\frac{d_{HbS\_ref}}{d_0}\right)_{\max}$ | <10 |
| $R_I - R_w$ (m) | $0.3.10^{-6}$ | $n$ | 2.2 | $k^{Hb}$ ($s^{-1}$) | 44 | $\sigma_0$ ($kg/s^2$) | $7.10^{-2}$ | $p_{O_2\_ref}$ (mmHg) | 95 |
| $R_T - R_I$ (m) | $0.35.10^{-6}$ | $p^{Hb}_{O_2,50\%}$ (mmHg) | 29.3 | $[Hb]$ ($mol/m^3$) | 0 * 21.099 | $K_{bu}$ ($kg/s^2$) | 0.5 | | |
| $R_K$ (m) | $20.10^{-6}$ | $D^{Hb}$ ($m^2/s$) | $1.3783.10^{-11}$ | $D^{Mb}$ ($m^2/s$) | $6.10^{-11}$ | $K_{sh}$ ($kg/s^2$) | $4.2.10^{-6}$ | | |
| $Hct$ | 0.45 $0.25^s$ | $p^{Mb}_{O_2,50\%}$ (mmHg) | 5.3 | $[Mb]$ ($mol/m^3$) | 0 * 0.4 | $B$ ($kg.m^2/s^2$) | $1.8.10^{-19}$ | | |

*Table 2.1.2 : Summary of physical parameters of the model ($^s$ sickle case - * see also Table 2.1.1).*

Figures 2.1.6 and 2.1.7 summarize the dynamical system of equations for both normal and sickle cases, and Table 2.1.2 lists the parametric values of the physical constants (except for the inlet average velocity, static pressure and oxygen partial pressure). Equations (49) and (54) implicitly complete the system. For normal RBCs, the resulting mathematical problem consists in 11 equations for the 11 unknowns $v_z$, $v_r$, $p$, $p_{O_2}$, $S^{Hb}$, $R(s)$, $Z(s)$, $\phi(s)$, $t_s$, $t_\theta$ and $q_s$. Besides the 2 families of control points $(s_0, R_0)$ defining the membrane in its preferred configuration, the total number of physical parameters is 25 (35 specific parametric values for the 5 layers), and there are 3 fixed boundary values (average velocity, static pressure and oxygen partial pressure). In the sickle case, there are additionally 2 vectors of control points $(l_0, d_0)$ with as many equations, 1 supplemental parametric value for the hematocrit, and 3 new model parameters. The next section defines the solving method retained and the associated numerical parameters.

## 2.2. Numerical model : Immersed Boundary Method

In order to solve the large system of differential equations mentioned in the previous sections, various numerical techniques were first investigated.

Traditional methods use simultaneous solvers with separate formulations for the 5 layers considered, and coupled through boundary conditions. The fluid dynamics equations are usually considered by far the most complex part to solve, and there is considerable literature on various advanced methods. Finite elements methods are a standard technique used to calculate complex flows [138]. A main specificity, and major difficulty of our problem, is to have a deformable boundary corresponding to the RBC membrane. To address this problem, finite elements methods can be applied with structured grids [139], unstructured grids [140], overset grids [141] and other advanced space mapping techniques [142]. Finite volume methods are also an alternative technique [144], using an integral form of the physical equations [143], and having specific advantages since it enforces conservation principles directly at the local scale. In the late 90's, Peskin developed the Immersed Boundary Method (IBM) as a novel alternative which proved to be very well suited to problems involving deformable boundaries with specific mechanics. This method quickly gained popularity among researchers and developers of numerical methods, with the noteworthy variant called the Immersed Interface Method (IIM) [148] [150] [151], and is likely to become a new standard due to its simplicity and ease of use compared to previous methods. While its efficiency was not explicitly compared to other methods for our problem, time considerations and advising by MIT faculty made

it the ideal candidate for numerical implementation. The IBM is explained in detail by Peskin [147], who also discussed the possible degrees of numerical precision [145] [149] and showed some examples of application [146].

### 2.2.1. Application of the IBM and discretization scheme

The IBM consists in solving the fluid dynamics equations in an extended form, to combine the surrounding fluid (here plasma) with the moving boundary containing similar or different fluid (here the RBC membrane). Both fluid dynamics and transport equations are therefore to be generalized to the combined space, and to replace boundary conditions representing the RBC membrane, the boundary forces are to be added into the fluid as a localized force field. In other terms, the 2-D boundary is replaced by an equivalent 3-D, localized force using a Dirac distribution. While the oxygen transport equations are unchanged, the generalized Navier-Stokes equations become :

$$\vec{\nabla}\cdot\vec{v} = \frac{1}{r}\frac{\partial}{\partial r}(r\,v_r) + \frac{\partial}{\partial z}v_z = 0\ , \tag{40}$$

$$\rho\left(\frac{\partial v_r}{\partial t} + v_r\frac{\partial v_r}{\partial r} + v_z\frac{\partial v_r}{\partial z}\right) = -\frac{\partial p}{\partial r} + \mu\left(\frac{1}{r}\frac{\partial}{\partial r}\left(r\frac{\partial v_r}{\partial r}\right) + \frac{\partial^2 v_r}{\partial z^2} - \frac{v_r}{r^2}\right) + f_r\,\delta\left(\begin{pmatrix} z \\ r \end{pmatrix} - \begin{pmatrix} Z(s) \\ R(s) \end{pmatrix}\right)\ , \tag{60}$$

$$\rho\left(\frac{\partial v_z}{\partial t} + v_r\frac{\partial v_z}{\partial r} + v_z\frac{\partial v_z}{\partial z}\right) = -\frac{\partial p}{\partial z} + \mu\left(\frac{1}{r}\frac{\partial}{\partial r}\left(r\frac{\partial v_z}{\partial r}\right) + \frac{\partial^2 v_z}{\partial z^2}\right) + f_z\,\delta\left(\begin{pmatrix} z \\ r \end{pmatrix} - \begin{pmatrix} Z(s) \\ R(s) \end{pmatrix}\right)\ , \tag{61}$$

where $\delta$ is the Dirac distribution mapping the 2-D membrane into the 3-D combined space, and $f_r$ and $f_z$ are the forces per unit area exerted by the RBC membrane on the flow, given in Equations (52) and (53). To solve numerically the generalized system of equations, a spatial discretization scheme is to be applied to $\delta$ in addition to all the field variables, effectively "smearing out" the boundary into the fluid. In the resulting combined space, it is important to note the emergence of discontinuous parameters (viscosity, oxygen diffusion constant, hemoglobin concentration and oxygen solubility constant), which are to be carefully specified as a function of location in the numerical method.

Using the IBM allows considerable simplification of the numerical problem. The 4 regions of space left (blood flow, capillary wall, interstitium and surrounding tissue) are defined by fixed boundaries, which allows us to use a very simple, permanent, structured mesh for each case study. In this simplified framework, the 3 fundamental steps left to define our numerical method are time

discretization, space discretization, and specification of the algorithm procedure and its numerical parameters.

Time discretization for first-order dynamics is typically performed by explicit and implicit methods, the first being in general simpler to implement and the second being more stable. The resulting system is to be solved at each iteration, using typically iterative methods or linearization and Gaussian elimination. We choose to use the second one for simplicity. Because this method is better suited for linear systems, we use a specific implicit method to compromise stability with the non-linear terms. More precisely, in the Navier-Stokes equations all linear terms are to be calculated implicitly (i.e. expressed as their value at the next time step), and all non-linear terms are calculated explicitly (i.e. expressed at the current time step). The resulting time discretization scheme gives the following equations from time step $t$ to time step $t+dt$ :

$$\left.\frac{1}{r}\frac{\partial}{\partial r}(r\,v_r)\right|_{t+dt} + \left.\frac{\partial}{\partial z}v_z\right|_{t+dt} = 0\ , \tag{62}$$

$$\left.\rho\frac{v_r}{dt}\right|_{t+dt} - \mu\left(\frac{1}{r}\frac{\partial}{\partial r}\left(r\frac{\partial v_r}{\partial r}\right) + \frac{\partial^2 v_r}{\partial z^2} - \frac{v_r}{r^2}\right)\Bigg|_{t+dt} + \left.\frac{\partial p}{\partial r}\right|_{t+dt} =$$

$$\rho\left(\frac{v_r}{dt} - v_r\frac{\partial v_r}{\partial r} - v_z\frac{\partial v_r}{\partial z}\right)\Bigg|_t + f_r(s)\,\delta\left(\begin{pmatrix} z \\ r \end{pmatrix} - \begin{pmatrix} Z(s) \\ R(s) \end{pmatrix}\right)\Bigg|_{s(s_0,t)}\ , \tag{63}$$

$$\left.\rho\frac{v_z}{dt}\right|_{t+dt} - \mu\left(\frac{1}{r}\frac{\partial}{\partial r}\left(r\frac{\partial v_z}{\partial r}\right) + \frac{\partial^2 v_z}{\partial z^2}\right)\Bigg|_{t+dt} + \left.\frac{\partial p}{\partial z}\right|_{t+dt} =$$

$$\rho\left(\frac{v_z}{dt} - v_r\frac{\partial v_z}{\partial r} - v_z\frac{\partial v_z}{\partial z}\right)\Bigg|_t + f_z(s)\,\delta\left(\begin{pmatrix} z \\ r \end{pmatrix} - \begin{pmatrix} Z(s) \\ R(s) \end{pmatrix}\right)\Bigg|_{s(s_0,t)}\ . \tag{64}$$

In the oxygen transport equations, a similar discretization scheme is applied, with convective terms expressed explicitly, diffusion terms implicitly (with the exception of the myoglobin-related non-linear term appearing in the factorization), and the remaining (non-linear) kinetic terms calculated explicitly :

$$\left.\frac{p_{O_2}}{dt}\right|_{t+dt} - \left.\frac{\left(\alpha\ D\ +\ D^{Mb}\ [Mb]\frac{p^{Mb}_{O_2,50\%}}{(p^{Mb}_{O_2,50\%}\ +\ p_{O_2})^2}\right)}{\left(\alpha\ +\ [Mb]\frac{p^{Mb}_{O_2,50\%}}{(p^{Mb}_{O_2,50\%}\ +\ p_{O_2})^2}\right)}\right|_t \left.\left(\frac{1}{r}\ \frac{\partial}{\partial r}\left(r\frac{\partial p_{O_2}}{\partial r}\right)\ +\ \frac{\partial^2 p_{O_2}}{\partial z^2}\right)\right|_{t+dt} =$$

$$\left.\left(\frac{p_{O_2}}{dt}\ -\ v_r\frac{\partial p_{O_2}}{\partial r}\ -\ v_z\frac{\partial p_{O_2}}{\partial z}\right)\right|_t + \left.\frac{k^{Hb}\ [Hb]\left(S^{Hb}\ -\ \left(1\ -\ S^{Hb}\right)\left(\frac{p_{O_2}}{p^{Hb}_{O_2,50\%}}\right)^n\right)\ -\ M}{\left(\alpha\ +\ [Mb]\frac{p^{Mb}_{O_2,50\%}}{(p^{Mb}_{O_2,50\%}\ +\ p_{O_2})^2}\right)}\right|_t . \quad (65)$$

$$\left.\frac{S^{Hb}}{dt}\right|_{t+dt} - D^{Hb}\left.\left(\frac{1}{r}\ \frac{\partial}{\partial r}\left(r\frac{\partial S^{Hb}}{\partial r}\right)\ +\ \frac{\partial^2 S^{Hb}}{\partial z^2}\right)\right|_{t+dt} =$$

$$\left.\left(\frac{S^{Hb}}{dt} - v_r\frac{\partial S^{Hb}}{\partial r}\ -\ v_z\frac{\partial S^{Hb}}{\partial z}\right)\right|_t - k^{Hb}\left.\left(S^{Hb}\ -\ \left(1\ -\ S^{Hb}\right)\left(\frac{p_{O_2}}{p^{Hb}_{O_2,50\%}}\right)^n\right)\right|_t . \quad (66)$$

Finally, the RBC membrane position is iterated implicitly, using the calculated velocity field :

$$Z(s)\big|_{t+dt} = v_z\big(Z(s),R(s)\big)\big|_{t+dt}\,dt\ , \quad (67)$$

$$R(s)\big|_{t+dt} = v_r\big(Z(s),R(s)\big)\big|_{t+dt}\,dt\ . \quad (68)$$

Spatial discretization is performed using a finite difference scheme, with a simple cylindrical mesh of regularly placed points (i.e. a rectangular mesh when projected in 2-D). As shown in Figure 2.2.1, all the field variables are expressed at the same points with the exception of the static pressure, placed on an out-of-phase grid (staggered mesh) to express discretized pressure gradients naturally and avoid possible numerical issues (due to the central difference scheme). First-order central differences are used to replace the various space differentials :

$$\frac{\partial A}{\partial z}(z_i,r_j) \rightarrow \frac{A_{i+1,j} - A_{i-1,j}}{2\,dz}\ ,\ \frac{\partial A}{\partial r}(z_i,r_j) \rightarrow \frac{A_{i,j+1} - A_{i,j-1}}{2\,dr}\ , \quad (69)\text{-}(70)$$

$$\frac{\partial^2 A}{\partial z^2}(z_i,r_j) \rightarrow \frac{A_{i+1,j} + A_{i-1,j} - 2A_{i,j}}{dz^2}\ ,\ \frac{\partial^2 A}{\partial r^2}(z_i,r_j) \rightarrow \frac{A_{i,j+1} + A_{i,j-1} - 2A_{i,j}}{dr^2}\ , \quad (71)\text{-}(72)$$

$$\frac{\partial p}{\partial z}(z_i,r_j) \rightarrow \frac{p_{i+1/2,j+1/2} - p_{i-1/2,j+1/2} + p_{i+1/2,j-1/2} - p_{i-1/2,j-1/2}}{2\,dz}\ , \quad (73)$$

$$\frac{\partial p}{\partial r}(z_i, r_j) \rightarrow \frac{p_{i+1/2,j+1/2} - p_{i+1/2,j-1/2} + p_{i-1/2,j+1/2} - p_{i-1/2,j-1/2}}{2\,dr}, \tag{74}$$

where $i$ and $j$ are the indices of the 2-D discretized space grid points, $z_i$ and $r_j$ are the corresponding coordinates, $dz$ and $dr$ represent the spatial distance between two neighbor points in the main directions, $A_{i,j}$ represents any field variable except static pressure (velocity components, oxygen partial pressure, oxyhemoglobin saturation) at the location $(z_i, r_j)$, and $p_{i+1/2,j+1/2}$ is the static pressure on the staggered mesh. The resulting discretized system of equations is very large and of little interest to our discussion, hence its full expression is left to the reader.

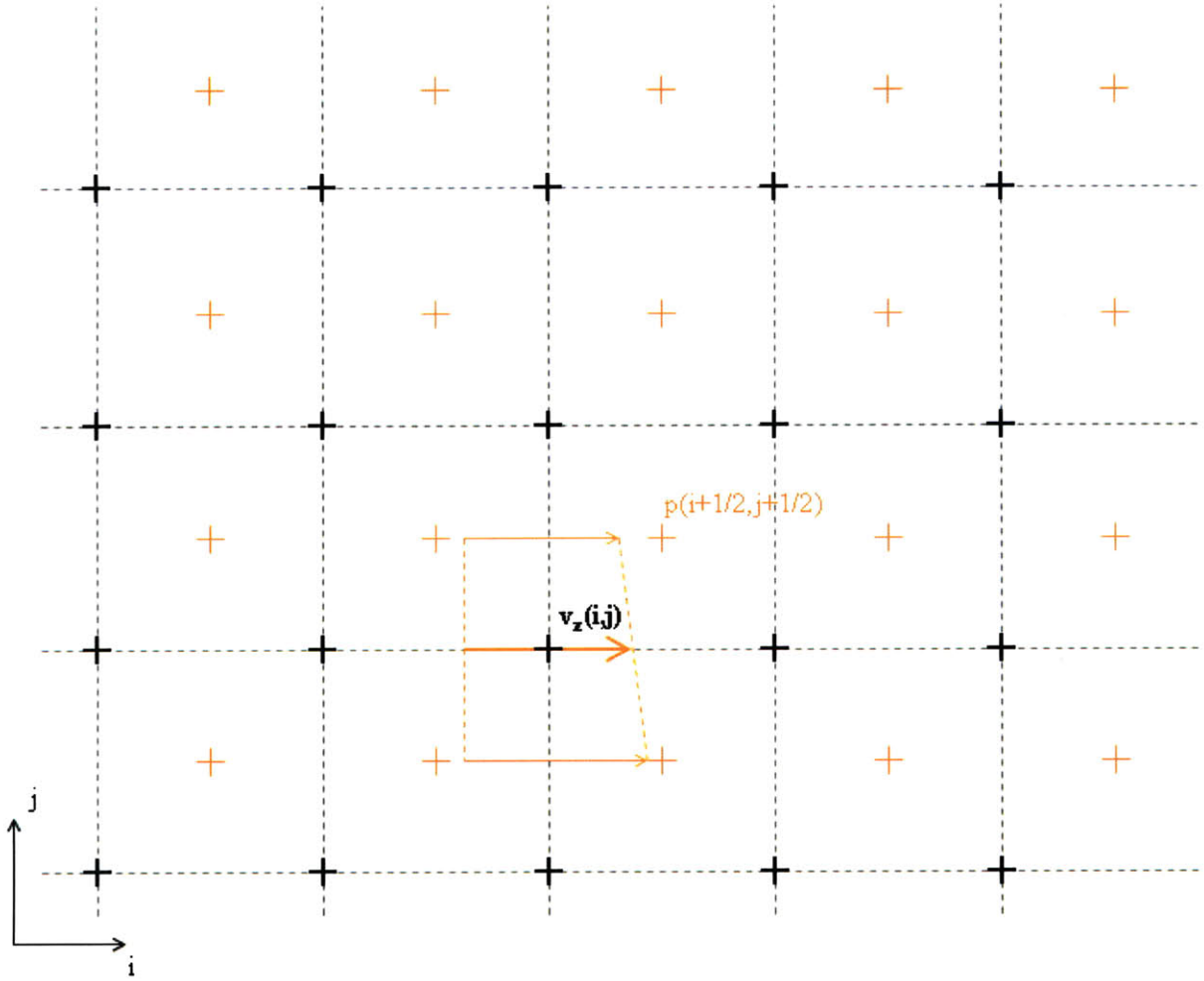


*Figure 2.2.1 : Spatial discretization with staggered mesh and interpolated pressure gradients.*

The RBC membrane is discretized into cylindrical segments represented in 2-D by the family of points $(s_k)$ (see Figure 2.2.2). The obtained polygonal shape is used to calculate membrane stresses, using the discretized radii $R_k$, segment lengths between two points $ds_{k+1/2}$, and corresponding angles $\phi_{k+1/2}$. The multiple derivatives of $\phi$ needed at the control points $(s_k)$ are determined by a combination of first-order central differences and (linearly interpolated) averaging :

$$\cos\phi_{k+1/2} = \frac{R_{k+1} - R_k}{ds_{k+1/2}} \;,\; \phi(s_k) \;\rightarrow\; \frac{\phi_{k+1/2}\, ds_{k-1/2} + \phi_{k-1/2}\, ds_{k+1/2}}{ds_{k-1/2} + ds_{k+1/2}} \;, \tag{75)-(76}$$

$$\frac{d\phi}{ds}(s_k) \;\rightarrow\; 2\frac{\phi_{k+1/2} - \phi_{k-1/2}}{ds_{k+1/2} + ds_{k-1/2}} \;, \tag{77}$$

$$\frac{d^2\phi_{k+1/2}}{ds_{k+1/2}^2} = \frac{\frac{d\phi}{ds}(s_{k+1}) - \frac{d\phi}{ds}(s_k)}{ds_{k+1/2}} \;,\; \frac{d^2\phi}{ds^2}(s_k) \;\rightarrow\; \frac{\frac{d^2\phi_{k+1/2}}{ds_{k+1/2}^2} ds_{k-1/2} + \frac{d^2\phi_{k-1/2}}{ds_{k-1/2}^2} ds_{k+1/2}}{ds_{k-1/2} + ds_{k+1/2}} \;, \tag{78)-(79}$$

$$\frac{d^3\phi}{ds^3}(s_k) \;\rightarrow\; 2\frac{\frac{d^2\phi_{k+1/2}}{ds_{k+1/2}^2} - \frac{d^2\phi_{k-1/2}}{ds_{k-1/2}^2}}{ds_{k+1/2} + ds_{k-1/2}} \;, \tag{80}$$

$$s_{0,k} = s_k(s_0, t=0) \;,\; k_0(s_k) = \frac{d\phi}{ds}(s_{0,k}) + \frac{\sin\phi(s_{0,k})}{R_k} \;. \tag{81)-(82}$$

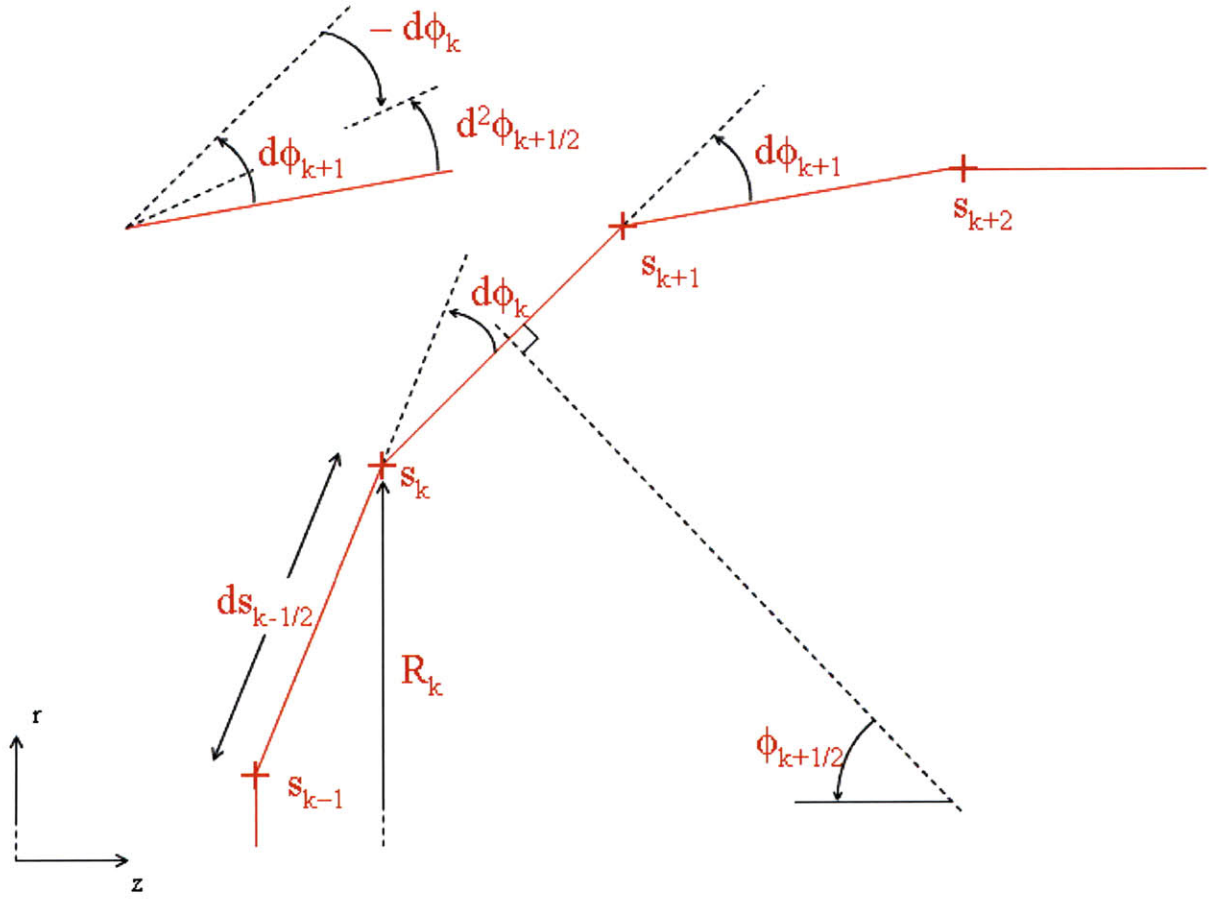


*Figure 2.2.2 : RBC membrane discretization, and discrete derivatives of $\phi$.*

The resulting stresses on the membrane are also obtained with a combination of centered differences and averaging :

$$\bar{t}(s_k) \;\rightarrow\; \sigma_0 \;+\; K_{bu}\left(\left(\frac{\frac{ds_{k+1/2}}{ds_{0,k+1/2}}\,ds_{k-1/2}+\frac{ds_{k-1/2}}{ds_{0,k-1/2}}\,ds_{k+1/2}}{ds_{k-1/2}\;+\;ds_{k+1/2}}\right)\frac{R_k}{R_{0,k}}\;-\;1\right), \tag{83}$$

$$\frac{d\bar{t}}{ds}(s_k) \;\rightarrow\; K_{bu}\left(\begin{array}{l}\left(2\,\dfrac{\frac{ds_{k+1/2}}{ds_{0,k+1/2}}-\frac{ds_{k-1/2}}{ds_{0,k-1/2}}}{ds_{k+1/2}\;+\;ds_{k-1/2}}\right)\dfrac{R_k}{R_{0,k}} \\ \quad+\left(\dfrac{\frac{ds_{k+1/2}}{ds_{0,k+1/2}}\,ds_{k-1/2}+\frac{ds_{k-1/2}}{ds_{0,k-1/2}}\,ds_{k+1/2}}{ds_{k-1/2}\;+\;ds_{k+1/2}}\right)\left(2\,\dfrac{\frac{R_{k+1}+R_k}{R_{0,k+1}+R_{0,k}}-\frac{R_k+R_{k-1}}{R_{0,k}+R_{0,k-1}}}{ds_{k+1/2}\;+\;ds_{k-1/2}}\right)\end{array}\right), \tag{84}$$

$$t_d(s_k) \rightarrow \frac{K_{sh}}{2}\left(\left(\frac{\frac{ds_{k+1/2}}{ds_{o,k+1/2}}ds_{k-1/2}+\frac{ds_{k-1/2}}{ds_{o,k-1/2}}ds_{k+1/2}}{ds_{k-1/2}+ds_{k+1/2}}\right)^2-\left(\frac{R_k}{R_{0,k}}\right)^2\right)$$

$$-\frac{B}{2}\left(\frac{d\phi}{ds}(s_k)-\frac{\sin\phi(s_k)}{R_k}\right)\left(\frac{d\phi}{ds}(s_k)+\frac{\sin\phi(s_k)}{R_k}-k_0(s_k)\right), \quad (85)$$

$$\frac{dt_d}{ds}(s_k) \rightarrow \frac{K_{sh}}{2}\left(\left(2\frac{\left(\frac{ds_{k+1/2}}{ds_{o,k+1/2}}\right)^2-\left(\frac{ds_{k-1/2}}{ds_{o,k-1/2}}\right)^2}{ds_{k+1/2}+ds_{k-1/2}}\right)-\left(2\frac{\left(\frac{R_{k+1}+R_k}{R_{0,k+1}+R_{0,k}}\right)^2-\left(\frac{R_k+R_{k-1}}{R_{0,k}+R_{0,k-1}}\right)^2}{ds_{k+1/2}+ds_{k-1/2}}\right)\right)$$

$$-\frac{B}{2}\left(\frac{d^2\phi}{ds^2}(s_k)-\left(2\frac{\frac{\sin\phi_{k+1/2}}{R_{k+1}+R_k}-\frac{\sin\phi_{k-1/2}}{R_k+R_{k-1}}}{ds_{k+1/2}+ds_{k-1/2}}\right)\right)\left(\frac{d\phi}{ds}(s_k)+\frac{\sin\phi(s_k)}{R_k}-k_0(s_k)\right)$$

$$-\frac{B}{2}\left(\frac{d\phi}{ds}(s_k)-\frac{\sin\phi(s_k)}{R_k}\right)\left(\frac{d^2\phi}{ds^2}(s_k)+\left(2\frac{\frac{\sin\phi_{k+1/2}}{R_{k+1}+R_k}-\frac{\sin\phi_{k-1/2}}{R_k+R_{k-1}}}{ds_{k+1/2}+ds_{k-1/2}}\right)\right), \quad (86)$$

$$q_s(s_k) \rightarrow -B\left(\frac{d^2\phi}{ds^2}(s_k)+2\frac{\frac{\sin\phi_{k+1/2}}{R_{k+1}+R_k}-\frac{\sin\phi_{k-1/2}}{R_k+R_{k-1}}}{ds_{k+1/2}+ds_{k-1/2}}\right), \quad (87)$$

$$\frac{dq_s}{ds}(s_k) \rightarrow -B\left(\frac{d^3\phi}{ds^3}(s_k)+\frac{\frac{\cos\phi_{k+1/2}}{R_{k+1}+R_k}\left(\frac{d\phi}{ds}(s_{k+1})+\frac{d\phi}{ds}(s_k)\right)-4\frac{\sin\phi_{k+1/2}\cos\phi_{k+1/2}}{(R_{k+1}+R_k)^2}-\frac{\cos\phi_{k-1/2}}{R_k+R_{k-1}}\left(\frac{d\phi}{ds}(s_k)+\frac{d\phi}{ds}(s_{k-1})\right)+4\frac{\sin\phi_{k-1/2}\cos\phi_{k-1/2}}{(R_k+R_{k-1})^2}}{ds_{k+1/2}+ds_{k-1/2}}\right)$$

(88)

which allows the resulting forces to be calculated at each point on the discretized RBC membrane :

$$\frac{dF_n}{dA}(s_k) = -t_s(s_k)\frac{d\phi}{ds}(s_k)-t_\theta(s_k)\frac{\sin\phi(s_k)}{R_k}-\frac{dq_s}{ds}(s_k)-\frac{q_s(s_k)}{R_k}\cos\phi(s_k), \quad (89)$$

$$\frac{dF_t}{dA}(s_k) = \frac{dt_s}{ds}(s_k) + \frac{t_s(s_k)}{R_k}\cos\phi(s_k) - t_\theta \frac{\cos\phi(s_k)}{R_k} - q_s(s_k)\frac{d\phi}{ds}(s_k), \quad (90)$$

and in cylindrical coordinates :

$$f_r(s_k) = \frac{dF_n}{dA}(s_k)\sin\phi(s_k) + \frac{dF_t}{dA}(s_k)\cos\phi(s_k), \quad (91)$$

$$f_z(s_k) = -\frac{dF_n}{dA}(s_k)\cos\phi(s_k) + \frac{dF_t}{dA}(s_k)\sin\phi(s_k). \quad (92)$$

Finally, we use a discretized Dirac distribution inspired by Peskin's work [147]. In 2 dimensions, the forces per unit area are first integrated on the RBC membrane surface they represent (see Equation (93)). The resulting point forces are effectively distributed among the 16 closest mesh points using a cosine bell function (see Figure 2.2.3). The discretization in cylindrical coordinates is similar to Peskin's formulation in the z-direction, and is modified in the r-direction to fulfill Peskin's postulates (in particular, the postulate that the force is split evenly on each side of the membrane point after integration – the torque identity (6.5) as defined by Peskin [147]) :

$$\delta\left(\begin{pmatrix} z_i \\ r_j \end{pmatrix} - \begin{pmatrix} Z(s_k) \\ R(s_k) \end{pmatrix}\right) = \delta_z(z_i, Z(s_k))\,\delta_r^2(r_j, R(s_k))\,\pi\left(\frac{ds_{k-1/2}\,(R_{k-1}+3R_k) + ds_{k+1/2}\,(3R_k+R_{k+1})}{4}\right), \quad (93)$$

$$\delta_z(z_i, Z(s_k)) = \frac{1}{4\,dz}\left(1 + \cos\left(\pi\,\frac{z_i - Z(s_k)}{2\,dz}\right)\right), \qquad |z_i - Z(s_k)| \le 2\,dz, \quad (94)$$

$$\delta_r^2(r_j, R(s_k)) = \frac{1}{8\,\pi\,r_j\,dr}\left(1 + \cos\left(\pi\,\frac{r_j - R(s_k)}{2\,dr}\right)\right), \quad |r_j - R(s_k)| \le 2\,dr, \quad (95)$$

Note that Equation (95) needs to be modified near the centerline. A useful alternative is :

$$\delta_r^2(r_j, R(s_k)) = \frac{1}{8\,\pi\,R(s_k)\,dr}\left(1 + \cos\left(\pi\,\frac{r_j - R(s_k)}{2\,dr}\right)\right), \quad |r_j - R(s_k)| \le 2\,dr, \quad (95b)$$

which can be used for the radial component to distribute RBC forces evenly on points of higher and lower r-coordinate (the original force on the RBC membrane being considered homogenous per unit area, this formulation is more appropriate for the r-component). Also, for the points where $R(s_k) < dr$ the discrete value of $\delta_r^2$ is normalized specifically to take into account symmetric radial terms and the Dirac distribution overlapping.

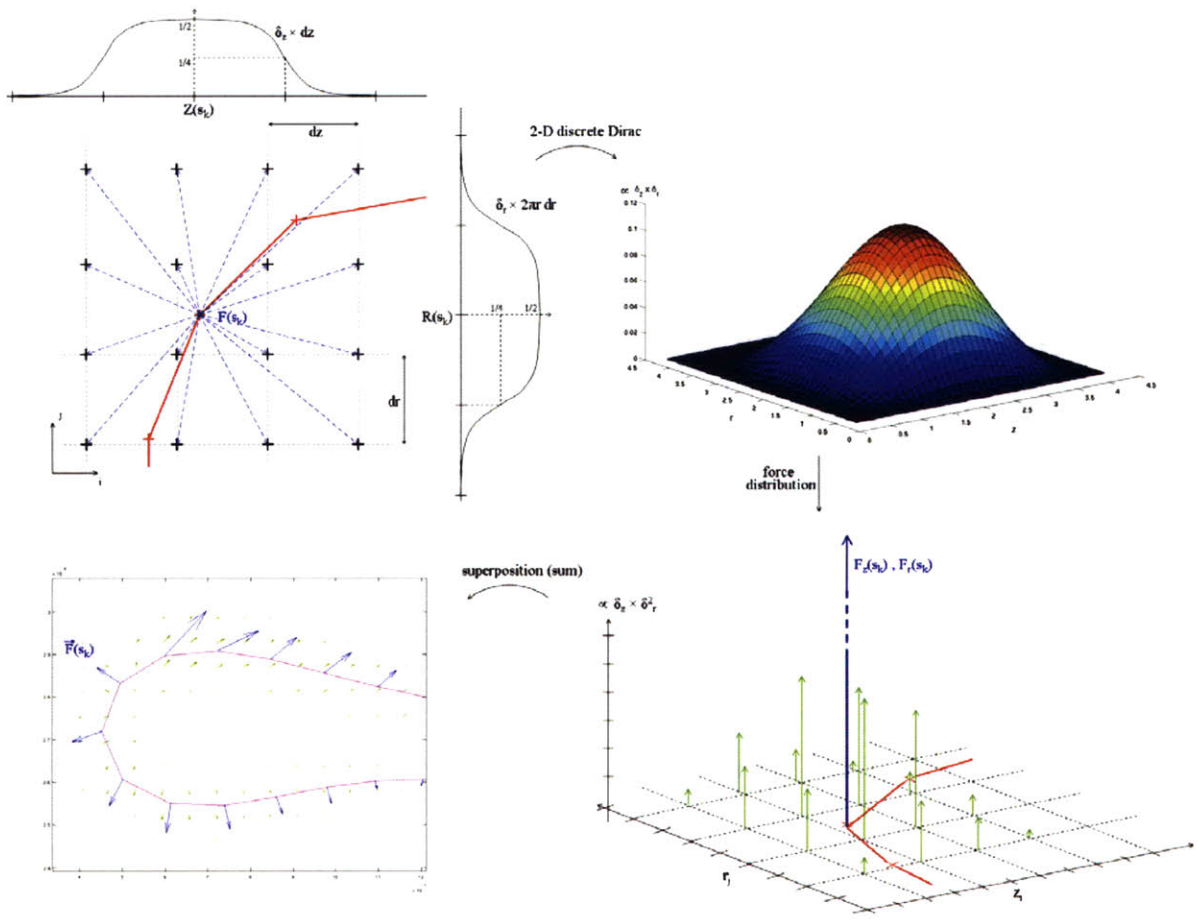


*Figure 2.2.3 : Immersed Boundary Method applied to the discretized RBC membrane (in red).*

The RBC velocity at the membrane points (needed in Equations (67)-(68)) is interpolated using the same discretized Dirac functions. This constitutes the implicit "feedback" from the flow to the RBC membrane position.

In the sickle case, the RBC midline formula was determined as a compromise between extreme simplicity and subjective appreciation of the result. The 2 basic control points of the sickling hemoglobin polymer were set to the RBC midpoint on the axis of symmetry, and the point on the RBC membrane with the lowest z-coordinate or "furthest RBC point downstream". These 2 points separate the RBC membrane in 2 pieces, called "upper" and "lower" sides of the RBC membrane. The first attempt to determine a RBC midline was simply a curvilinear average between the 2 pieces (see Figure 2.2.4). However the result proved to follow poorly the membrane shape near the second basic point, as the point sampling was sparser on the upper side than on the lower side. To enhance the result, a couple of improvements were tested on the sampling of the RBC control points on the lower surface. The use of linear, hyperbolic, then double-hyperbolic sampling formulas gave

significant visual improvements (see Figures 2.2.5, 2.2.6 and 2.2.7), and the latter one was retained for our model. To give the polymerized structure an effective reference thickness, 2 more series of control points were determined, placed at a lateral distance based on local discretization of the RBC (see Figure 2.2.8). The resulting sets of control points were used to apply Equations (55)-(59), with the resultant forces added to the forces exerted on the RBC membrane at each point $s_k$.

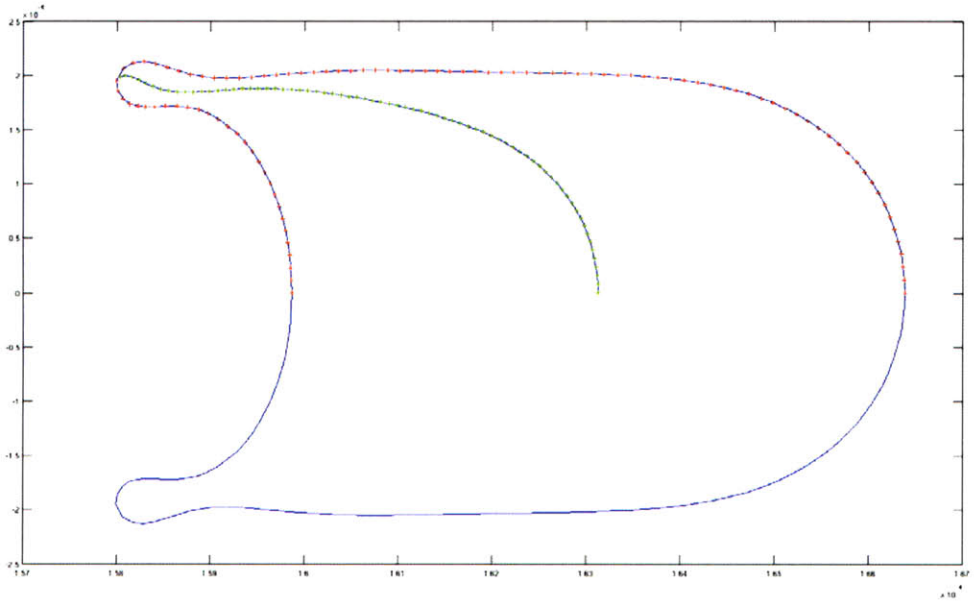

*Figure 2.2.4 : RBC midline calculation (homogeneous sampling - Note:only r>0 is plotted).*

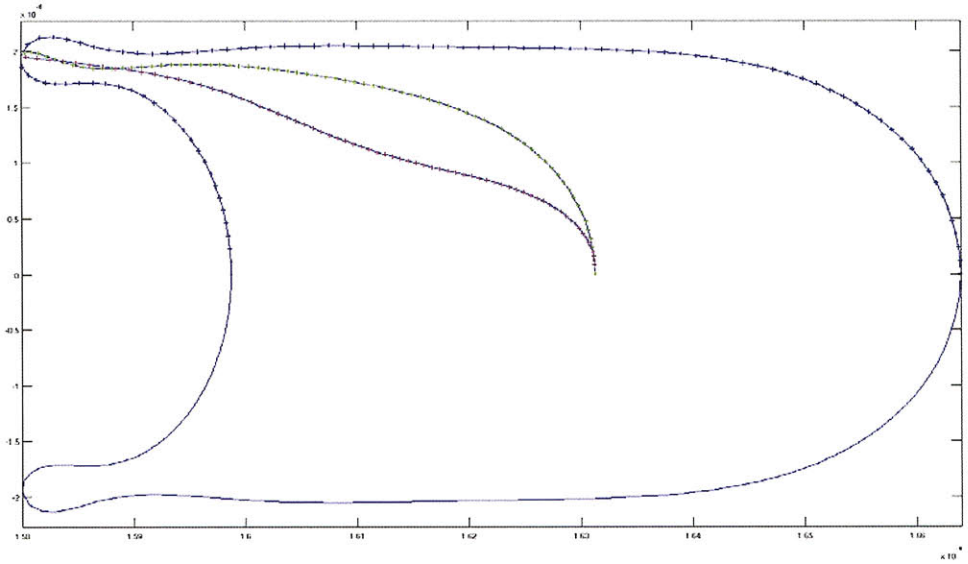

*Figure 2.2.5 : RBC midline calculation (green:homogeneous sampling, purple:linear sampling).*

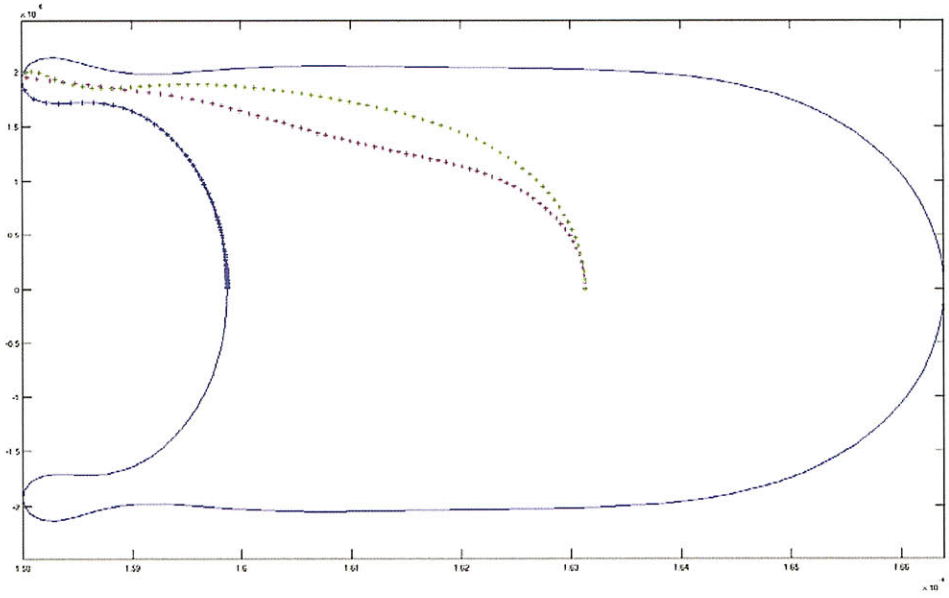

*Figure 2.2.6 : RBC midline calculation (green:homogeneous sampling, purple:hyperbolic sampling).*

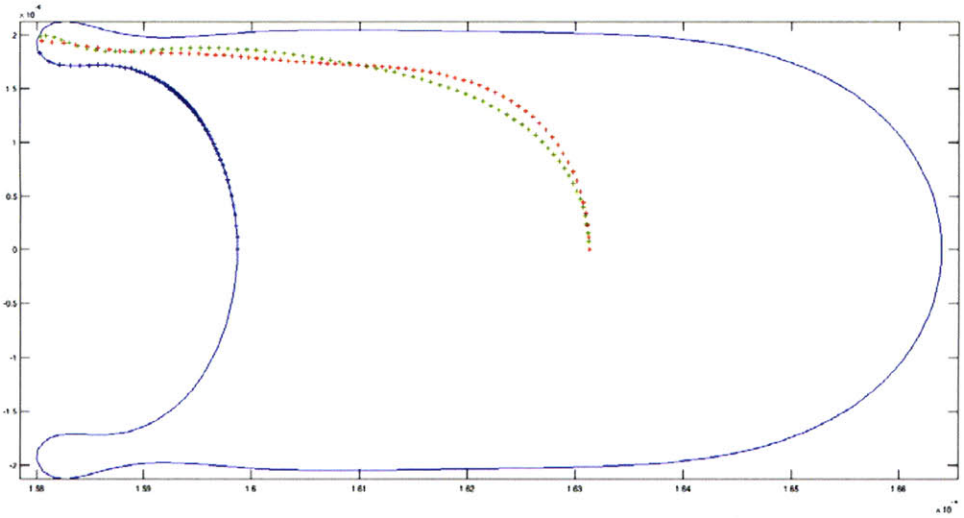

*Figure 2.2.7 : RBC midline calculation (green:homogeneous sampling, red:double-hyperbolic sampling).*

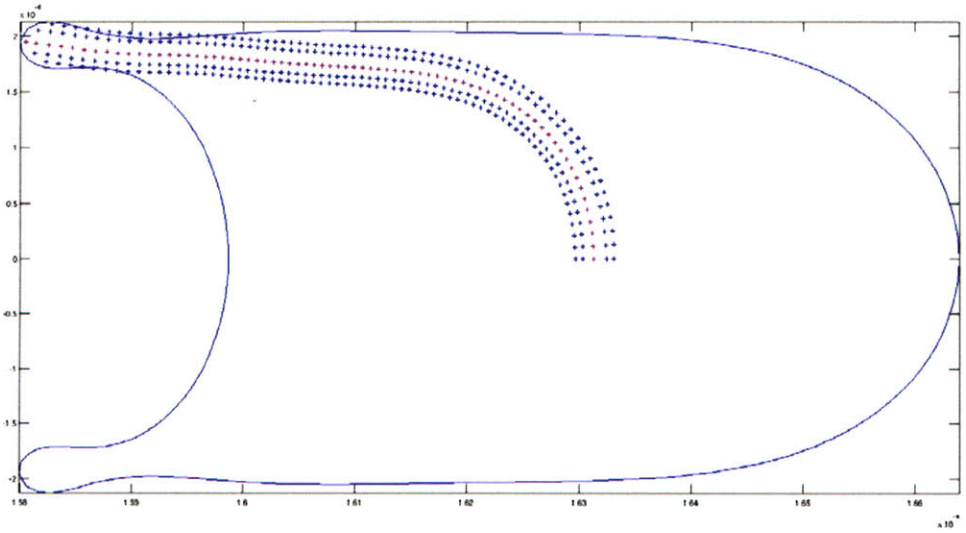

*Figure 2.2.8 : HbS modeled polymer structure (Note:a potential double-thickness layer is shown for illustration).*

### 2.2.2. Numerical procedure, parametric adjustments, and limitations of the method

The resulting discrete system of equations is a sparse linear system that can be written as :

$$A_t = \begin{pmatrix} v_z \\ v_r \\ p \\ p_{O_2} \\ S^{Hb} \end{pmatrix}_{\{z_i, r_j\}} (t) , \tag{96}$$

$$M\, A_{t+dt} = B(A_t) , \tag{97}$$

where $A_t$ is the state vector of the system at time $t$, $M$ is the rigidity matrix of the system, comprising all the linear terms expressed implicitly, and $B(A_t)$ is the second term. This system is solved at each iteration using Gaussian elimination in Matlab® (backslash "\" operator). Note that, since the oxygen convection terms are non-linear terms (therefore put in $B(A_t)$), $M$ is diagonal by blocks, and Equation (96) can be split in 2 sub-systems, for the fluid dynamics and the oxygen transfer respectively.

The numerical procedure consists in iterating these steps :

1) using the current RBC position, calculate RBC membrane stresses (Equations (75)-(92)),

2) calculate the resulting RBC membrane forces on the fluid mesh (Equations (93)-(95b)),

3) calculate the second term $B(A_t)$ and the rigidity matrix $M$ on the discrete mesh (Equations (62)-(66), (69)-(74)),

4) solve the system for the state vector at the next time iteration $A_{t+dt}$,

5) calculate the new RBC position (Equations (67)-(68)).

Some "tweaks" can be easily added to this numerical scheme, such as non-dimensionalization and adaptive time step, and also some "hard" numerical procedures, for example to enforce global RBC volume conservation after a large number of iterations (compensating numerical leaks). Other considerations on improving the numerical method are left to further work (e.g. iterative methods based on trapezoid rule and higher-order Runge-Kutta methods, n-point finite difference schemes, boundary integral methods, lattice-Boltzman methods, partial linearization of nonlinear terms...). Also, determination of the RBC stresses based on its approximate shape can use higher-order interpolation schemes such as rational splines [152] [153] [154].

Numerical parameters vary depending on the case studies, with typically 100 to 200 points defining the RBC shape and 40 to 65 vertical divisions of the capillary vessel (and other vertical and horizontal meshing such that mesh size is as homogeneous and square as possible). Finally, the time step is set to be always smaller than the mesh size divided by the flow velocity. Given our case studies $dt$ was set for all our calculations to $\mathbf{1.45555.10^{-5}}$ **s**. Certain RBC membrane stresses may need a smaller time step to be properly implemented, but would considerably slow down calculations. Instead, decision was taken to effectively reduce $K_{bu}$ to $\mathbf{1.10^{-4}\ kg/s^2}$ and set $k_{HbS}$ to $\mathbf{5.10^{-5}\ kg/s^2}$ to ensure numerical stability without significant changes in the results (RBC surface area remaining effectively quasi-constant, always within 2% in all our results). Convergence was based on a determined total number of iterations, corresponding for the worst case to a maximal change in relative positions of RBC control points of less than 1%, for a time equivalent to traveling at least 2 spatial periods. From the observed asymptotic trends and due to the numerical precision, we roughly estimated a global precision of around 2% for all spatial variables, and at most 5% for the synthetic variables (such as apparent viscosity). For more details or to ask for a copy of the code used in this work, please contact flefloch@alum.mit.edu.

Peskin discussed in details the limitations and issues of the Immersed Boundary Method in his publications [145] [146] [147] [149]. One important difficulty we encountered was the relation between mesh size and RBC discretization : if RBC points are too close, the calculated stresses on the RBC membrane do not lead to sufficient "feedback" from the flow, and may result in the RBC membrane folding onto itself (due only to this numerical phenomenon). Inversely, if RBC points are too far apart, the distributed forces on the flow grid are not connected, and may result in local flow vortices and instability. As a consequence, the resolution chosen for the RBC membrane (200 points) imposed very tight restrictions on the mesh precision. Varying geometries (e.g. varying capillary sizes or hematocrit) were also subject to recalculations of the most appropriate mesh dimensions, to obtain stable RBC local dynamics. For this resolution, full calculations on one case until reaching steady state lasted about 5 days on an Intel Core i7-965 processor (3.2 GHz). With longer calculation times, improvements in terms of precision and range of situations or parametric values are clearly possible, and the 12 Gb of RAM should allow for an increase in variable space of at least a factor 5 in each of the 2 dimensions. The use of a compiled code (Fortran or C/C++) is also to be considered for future extensive use, despite longer development times.

## 2.3. Validation of the simulation model

The designed model is now to be validated with results from previous models and experiments, before further examination of the results.

As a qualitative assessment, the obtained RBC shapes under steady flow are first examined. Figure 2.3.1 shows our results compared to RBC micrographs obtained by Secomb, for a capillary vessel of radius 3.5 μm [46]. The superposition of our results with the observed RBC shapes shows a remarkably good fit. Figure 2.3.2 also shows a fairly good agreement of our results with Secomb's simulation model [100].

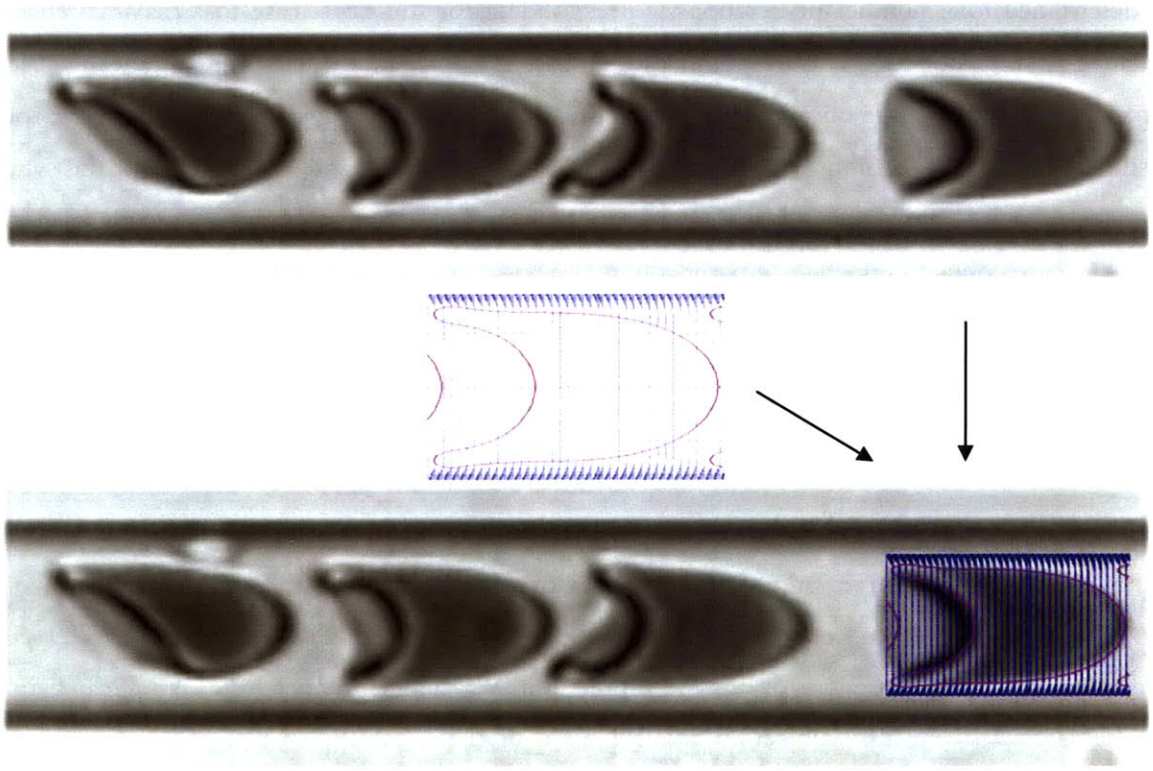

*Figure 2.3.1 : Comparison of obtained RBC shapes with Secomb's micrographs [46].*

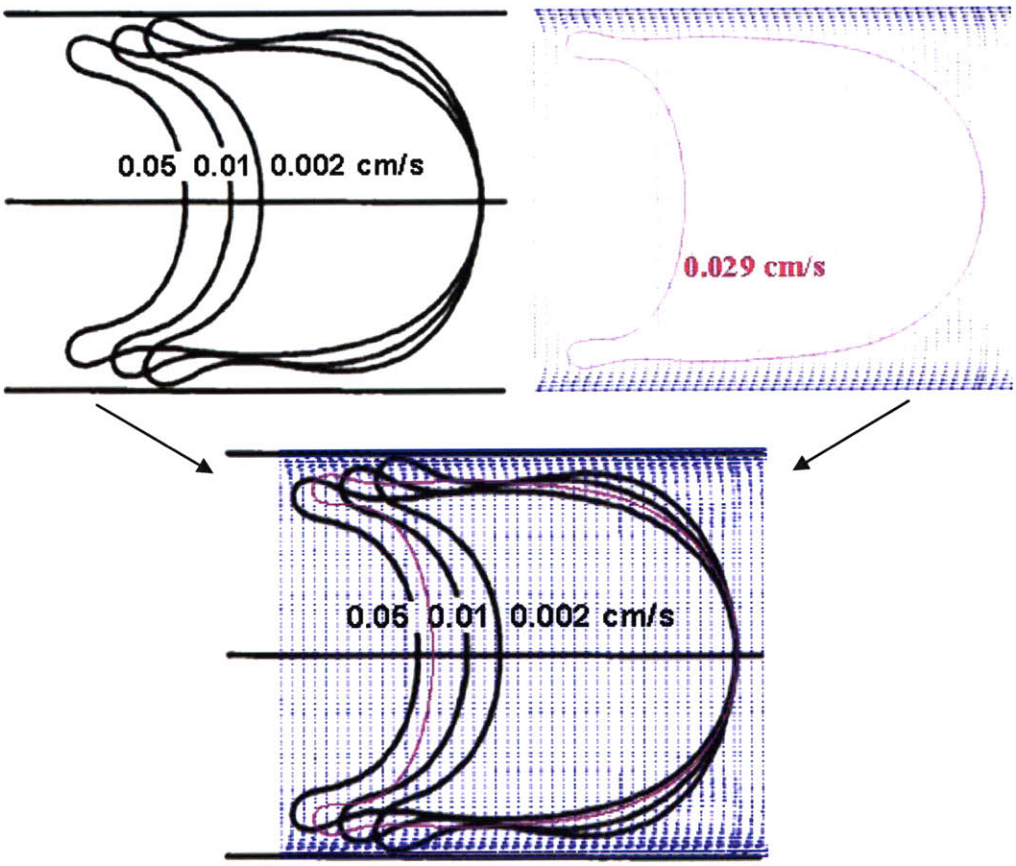


*Figure 2.3.2 : Comparison of obtained RBC shapes with Secomb's model (R=3μm)* [100].

On Figure 2.3.3 we compare our results with literature data. Measurements of the apparent viscosity (or whole blood viscosity, showing the overall resistance of RBCs and plasma) are reported by Goldsmith and coworkers in the shaded area [35]. We observe that the inversion of the Fåhraeus-Lindqvist effect at near-minimal capillary radii corresponds to our case study range, where RBCs tend to flow individually along the centerline. We see that our data slightly overestimates the apparent viscosity. The reason here is that we use a low flow velocity (0.25 m/s) for all the cases reported, corresponding to the lower end of capillary sizes (leftmost point on our plot). In reality blood velocity is known to increase with vessel size (see Figure 1.3.1), and Figure 2.3.4 shows adjusted results based on a velocity of 0.5 m/s corresponding to the higher capillary vessel size (rightmost point). Since the exact relation between vessel size and blood velocity is unknown, we were unable to determine exactly where the intermediate points should be, but from Figures 2.3.3 and 2.3.4 it seems that we would fit fairly well the upper side of Goldsmith's curve.

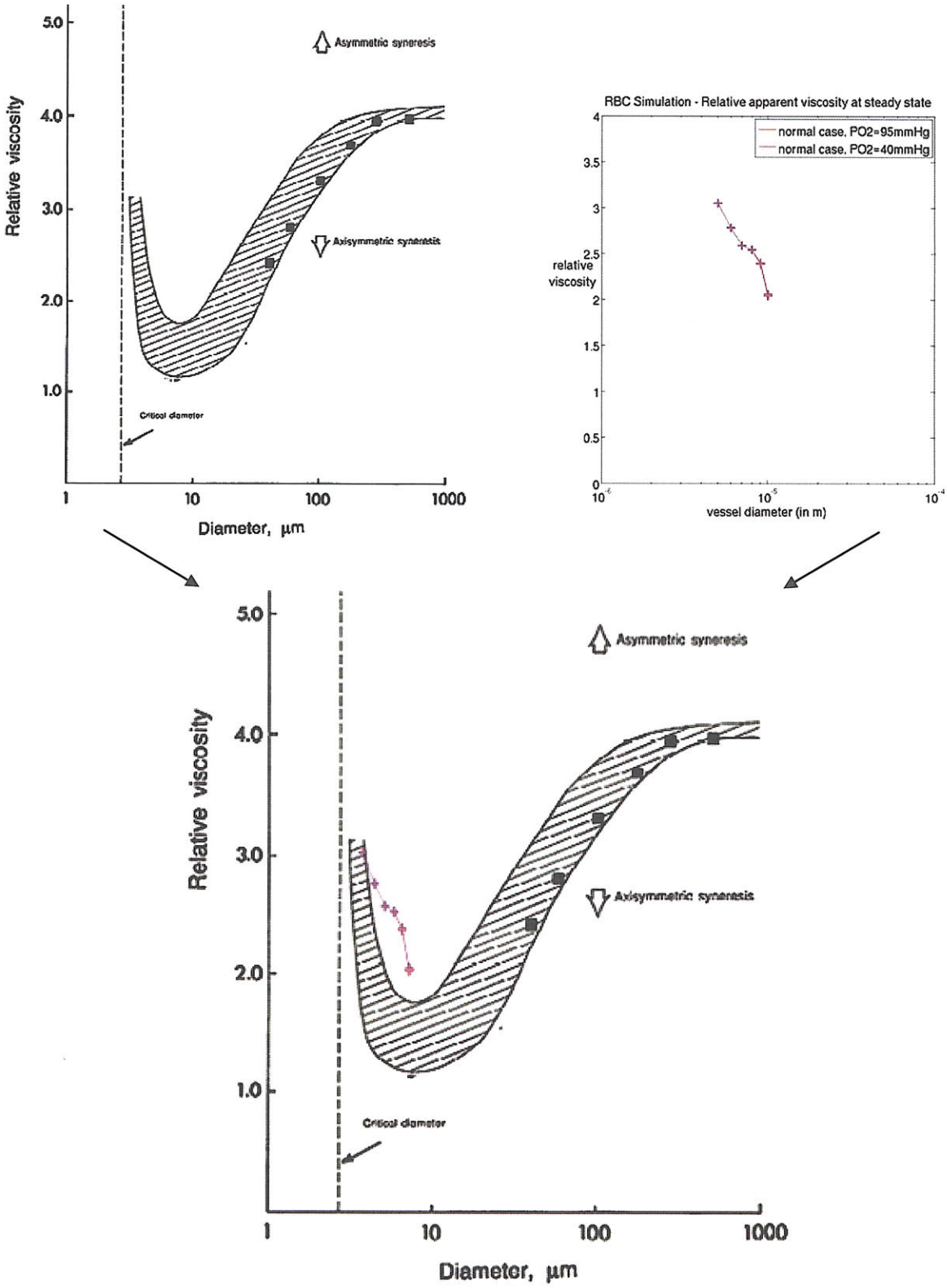


*Figure 2.3.3 : Relative viscosity vs. vessel size (left: literature data [35]; right: our results).*

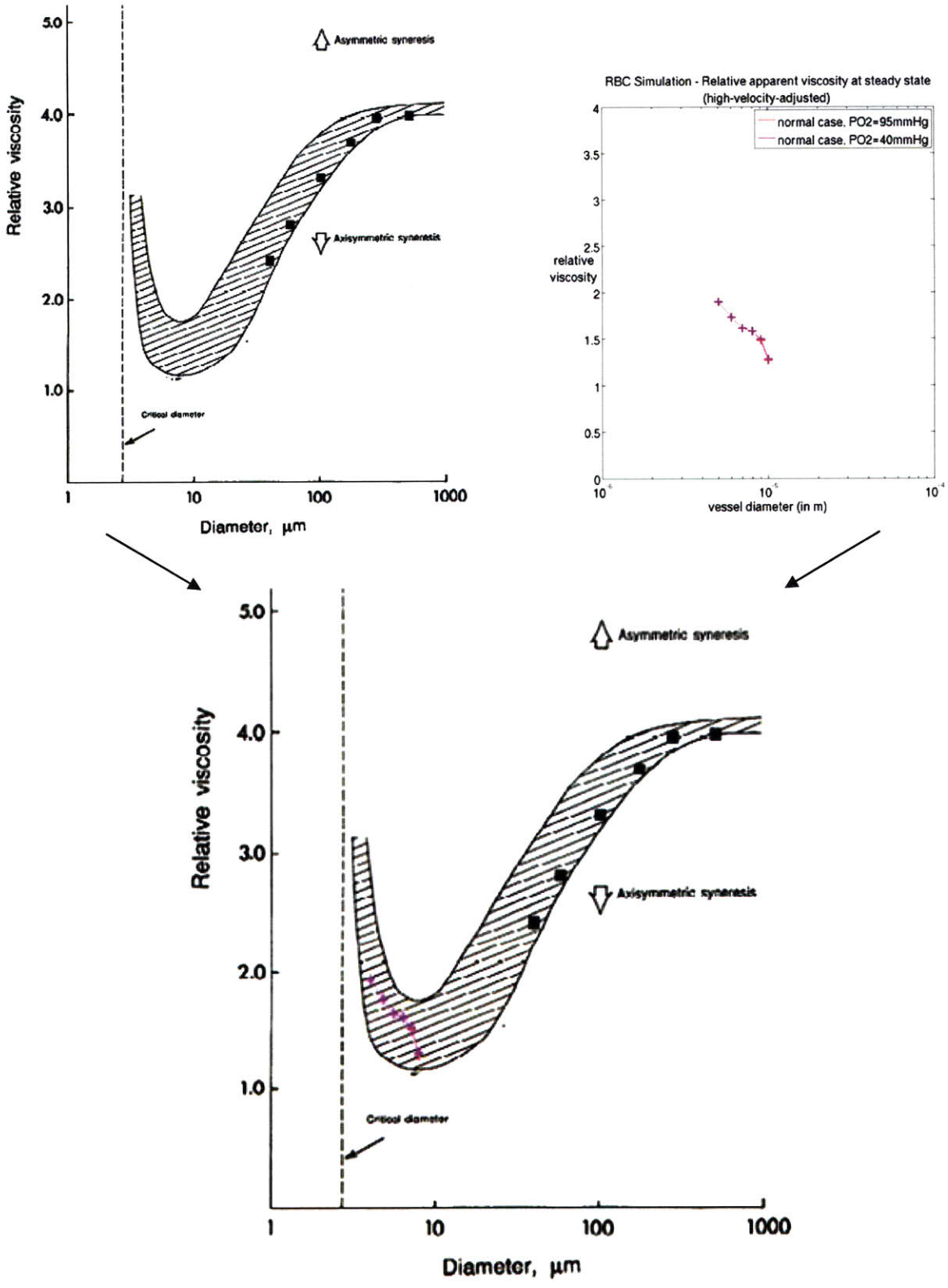


*Figure 2.3.4 : Relative viscosity vs. vessel size (left: literature data [35]; right: our results) – adjusted velocity for higher capillary vessel sizes.*

Comparison of our data with results from Secomb and coworkers [100] is presented in Figures 2.3.5 and 2.3.6. Secomb used the apparent intrinsic viscosity here, defined as $\frac{1}{Hct}\left(\frac{\mu_{app}}{\mu}-1\right)$. On Figure 2.3.5 we see that a direct comparison suggests that we overestimate the apparent viscosity. However, Secomb's work was based on a value of plasma viscosity of 1 centipoise ($1.10^{-3}$ Pa.s). Figure 2.3.6 shows adjusted results to take this plasma viscosity into account, using a simple linear extrapolation. The adjusted data points now slightly underestimate the apparent viscosity, which is probably due to the linear extrapolation. The trends however are in good agreement with Secomb's data.

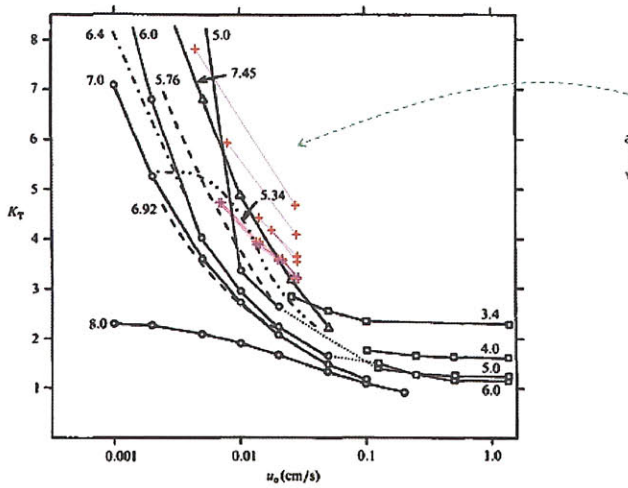


Variation of $K_T$ with cell velocity $u_0$: comparison of present study with other theoretical and experimental studies. Vessel diameter in μm is shown on each curve. Theoretical results: □, lubrication model including shear elasticity but neglecting bending; ○, lubrication model including both shear and bending elasticity; △, finite-element results of Tözeren & Skalak (1980). Experimental results: – – – –, results of Lee & Fung (1969) using macroscopic model cells; ·· –·· – ··, results of Lingard (1979) using human red blood cells; · –· –· –, results of Driessen *et al.* (1984) using rat red blood cells.

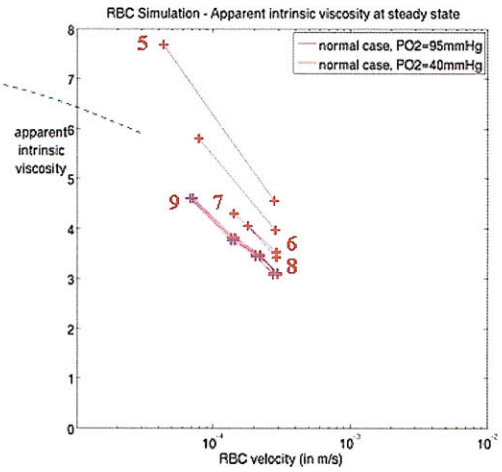


*Figure 2.3.5 : Apparent intrinsic viscosity vs. RBC velocity (left: Secomb et al. [100]; right: our results).*

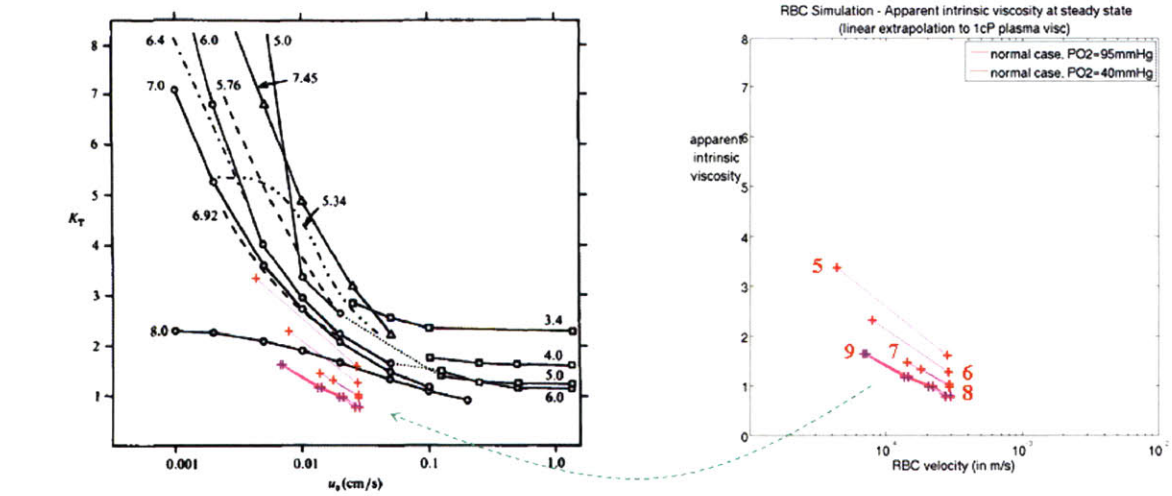


**Variation of $K_T$ with cell velocity $u_0$: comparison of present study with other theoretical and experimental studies. Vessel diameter in μm is shown on each curve. Theoretical results: □, lubrication model including shear elasticity but neglecting bending; ○, lubrication model including both shear and bending elasticity; △, finite-element results of Tözeren & Skalak (1980). Experimental results: – – – –, results of Lee & Fung (1969) using macroscopic model cells; · · –· · –· ·, results of Lingard (1979) using human red blood cells; · –· · –· ·, results of Driessen *et al.* (1984) using rat red blood cells.**

*Figure 2.3.6 : Apparent intrinsic viscosity vs. RBC velocity – extrapolation for plasma viscosity of 1 centipoise (left: Secomb et al. [100]; right: our results).*

The measurements from Chien, Usami and Bertles (seen in Figure 1.3.3) cannot be compared to our simulations directly : not only were the conditions very different (viscometer imposing a Couette-like shear flow), but also the shear rates. Measured at the capillary wall, they evolve between 200 and 1000 $s^{-1}$, which is clearly out of the range of the measurements from Usami et al. Figure 2.3.7 shows that our results, however, are expected to be compatible with their experimental observations, with again observation of the inversion of the Fåhraeus-Lindqvist effect.

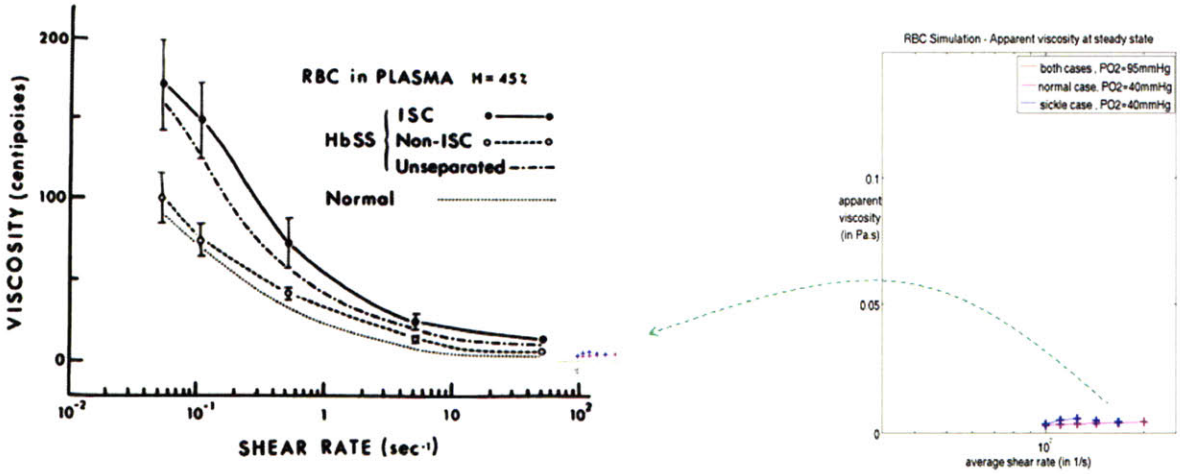


*Figure 2.3.7 : Apparent viscosity vs. shear rates (left: experimental data [62]; right: our results).*

Curves obtained experimentally by Mackie and Hochmut have also been investigated, looking at the resulting apparent viscosity. The concentration used for RBC hemoglobin in our simulations is 34 g/l (or 340 kg/m$^3$), but the viscosities obtained in Mackie and Hochmut's results correspond to pure hemoglobin solutions so that absolute values cannot really be compared directly. Nevertheless, we can observe on Figure 2.3.8 comparable trends in our results, with the characteristic rise in the case of sickle cells.

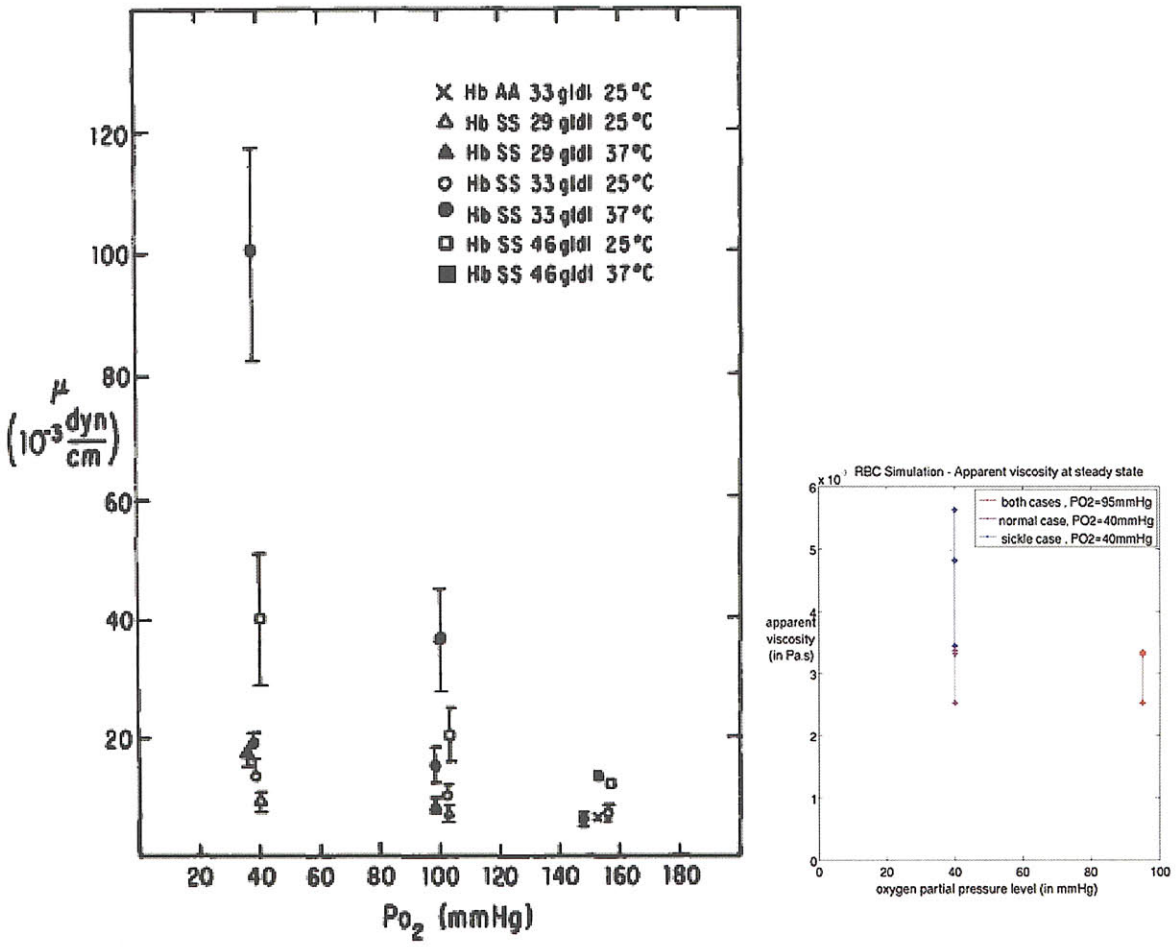


*Figure 2.3.8 : Viscosity vs. oxygen level (left: literature data [70]; right: our results, Hb concentration is 34 g/dl, $R_w$ = 4.5 μm).*

Comparison of our results with Higgins's clogging and unclogging time scales for sickle blood seems also inappropriate at this point. As seen in Higgins's results and supporting videos (available online at http://www.pnas.org/content/suppl/2007/12/19/0707122105.DC1), the microfluidic

device used in Higgins's experiment deals with large channels (7 mm to 30 mm) where RBCs do not flow individually, and with larger time scales (tens to thousands of seconds compared with tens of milliseconds in our simulations). The onset of vessel occlusion in Higgins's experiment is evidently specific to his device size, and would need a model of a different scale (dynamical models for larger vessels and taking into account RBC interactions exist, but are yet to be completed with a sickle cell model).

Lipowsky and coworkers also provided some experimental data of sickle cell blood, reported in Table 2.3.1 below [69]. As we see, for an average vessel diameter of 10 μm the measured RBC velocity is around 0.72 mm/s, which is fairly high compared to the existing models we reviewed. Unfortunately the technique used did not provide measurement of any pressure gradient, which prevents us from comparing it to our simulation data. It is important to stress, however, that this research suggests the possible availability of complete measurements in vivo in a near future.

***Resting and Hyperemic Hemodynamic Characteristics in Nailfold Capillaries***

| Subject | No. capillaries | $T_{skin}$ | Diameter | $V_{rbc}$ | $Q_{rbc}$ | $V_{pk}/V_{rbc}$ | $T_{pk}$ | $T_{p50}$ | $N_{50}/N$ |
|---|---|---|---|---|---|---|---|---|---|
| | | °C | μm | mm/s | nl/s | | s | s | |
| HbAA controls ($n$ = 14) | 90 | 31.5±0.27 | 9.7±0.30 | 0.71±0.04 | 0.058±0.0043 | 1.95±0.07 | 39.6±5.2 | 55.7±4.8 | 0.47 |
| HbSS crisis-free ($n$ = 20) | 202 | 32.8±0.18 | 10.0±0.17 | 0.72±0.03 | 0.061±0.004 | 2.05±0.05 | 35.9±2.9 | 63.8±3.9 | 0.61 |
| HbSS crisis ($n$ = 10) | 46 | 32.2±0.38 | 10.6±0.31 | 0.98±0.06 | 0.088±0.006 | 1.76±0.08 | 55.6±7.0 | 84.7±8.8 | 0.39 |
| $t$ test: SS crisis-free vs. SS crisis | | NS | NS | $P < 0.001$ | $P < 0.001$ | $P < 0.01$ | $P < 0.01$ | $P < 0.05$ | |

Values are means±SE; see Figs. 6 and 7 for SD. $T_{skin}$, skin temperature; Dia, capillary diameter; $V_{rbc}$, control red cell velocity; $Q_{rbc}$, estimated control volumetric flow rate; $V_{pk}$, peak red cell velocity during reactive hyperemia; $T_{pk}$, time to attain peak rbc velocity during reactive hyperemia; $T_{p50}$, time to repay 50% of flow debt incurred during no-flow state; $N_{50}/N$, fraction of capillaries which repay 50% of flow debt incurred during no-flow.

*Table 2.3.1 : Measured characteristics of sickle cell blood (Lipowsky et al. [69]).*

Finally, considering the drop in oxygen partial pressure between the ends of the capillary vessels from approximately 95 mmHg to 40 mmHg, we can estimate the total capillary length across a model organ. Averaging the oxygen partial pressure gradients, we obtain approximately a range from $4.10^{-4}$ to $1.4.10^{-3}$ m, which is in agreement with the order of magnitude given in Table 1.3.1 ($1.10^{-3}$ m) (see Figure 3.1.15).

## 2.4. Conclusions on the proposed model

This section completes the presentation of the physical and numerical modeling. We have now defined a model for the blood microcirculation, included a model describing sickle cell disease, implemented a numerical solver for the system of equations, and validated some of our results with experimental and simulation data from various sources. In particular, our proposed model for sickle cells has shown trends in good agreement with experimental data, which allows us to consider its use for further study of the disease. The following sections will now present more detailed results of our simulations, using this model.

# 3. Insights on blood microcirculation and sickle cell disease

This chapter presents a thorough analysis of the results produced by our model, for a comprehensive set of variations of a few parameters. After presenting the case studies used, we first present our original findings for normal RBCs and review some main parametric trends of capillary blood flow. Secondly, we present results of our sickling RBC model and analyze the simulated flow behavior. Based on these original results and our improved understanding of sickle blood dynamics, we were able to determine a set of analytical quantities to best describe affected blood properties. Finally, we conclude on the new perspectives unveiled by this study, and its effect on developing an analytical, simulation-based, sickle cell treatment strategy.

## 3.1. Presentation of a few case studies

We propose now to perform a comprehensive study of RBC dynamics, focusing on comparisons between normal and sickle cells. As a pilot study, we look at results of simulated blood flow for series of typically varying parameters. In each series of calculations, 3 cases will correspond to the high oxygen partial pressure end (95 mmHg), the low oxygen partial pressure end (40 mmHg) for normal cells, and the low oxygen partial pressure end (40 mmHg) for sickle cells. The high oxygenation level corresponds to both normal and sickle cells as they give identical results. The first series of calculations will constitute baseline cases with a vessel radius of 4.5 μm and a hematocrit of 0.45. The sickle case will have 2 baselines corresponding to the same normal case, depending on the fixed boundary condition being either the same total blood inflow, or the same pressure gradient along the capillary vessel. In the following series of calculations, we will examine the effects of a lower inlet velocity, then of a radius varying between 2.5 μm and 5.0 μm in increments of 0.5 μm. In order to encompass the diversity of situations, the series with varying radii will be obtained with the same fixed average velocity at inlet, and then with the same pressure gradient for all cases. The former situation is to reflect possible variations along a capillary vessel length, while the latter illustrates differences that can be observed between vessels in a parallel alignment, such as across an organ. Finally, we will show the effects of a reduced hematocrit of 0.25, typically encountered in sickle cell patients. The obtained series of results will allow us to analyze general flow characteristics, present some key features of blood microcirculation through synthetic quantities, compare oxygen

delivery performance, and characterize the aggravated state in the sickle cell case. Table 3.1.1 summarizes the case studies listed above. $\bar{v}_{in}$ is the reference velocity, 0.25 mm/s, and $\overline{\left(\frac{dp}{dz}\right)}$ is set to the corresponding pressure gradient for the baseline case with normal cells (case 1a), i.e. approximately $3.25.10^5$ Pa/m. The simulation results corresponding to the constant velocity cases (series 3), and constant pressure gradient cases (series 4), were used to validate the model in the previous chapter.

| Case (Series) | Capillary Radius (μm) | Oxygen Partial Pressure Level (mmHg) | Normal/Sickle Cells | Fixed Boundary Conditions | Hematocrit |
|---|---|---|---|---|---|
| 1a (baseline) | 4.5 | 95 | both | $\bar{v}_{in}, \overline{\left(\frac{dp}{dz}\right)}$ | 0.45 |
| 1b (baseline) | 4.5 | 40 | normal | $\bar{v}_{in}, \overline{\left(\frac{dp}{dz}\right)}$ | 0.45 |
| 1c (baseline) | 4.5 | 40 | sickle | $\bar{v}_{in}, \overline{\left(\frac{dp}{dz}\right)}$ | 0.45 |
| 2a | 4.5 | 95 | both | $\bar{v}_{in}, \frac{3\bar{v}_{in}}{4}, \frac{\bar{v}_{in}}{2}, \frac{\bar{v}_{in}}{4}$ | 0.45 |
| 2b | 4.5 | 40 | normal | $\bar{v}_{in}, \frac{3\bar{v}_{in}}{4}, \frac{\bar{v}_{in}}{2}, \frac{\bar{v}_{in}}{4}$ | 0.45 |
| 2c | 4.5 | 40 | sickle | $\bar{v}_{in}, \frac{3\bar{v}_{in}}{4}, \frac{\bar{v}_{in}}{2}, \frac{\bar{v}_{in}}{4}$ | 0.45 |
| 3a | 2.5, 3.0, 3.5, 4.0, 4.5, 5.0 | 95 | both | $\bar{v}_{in}$ | 0.45 |
| 3b | 2.5, 3.0, 3.5, 4.0, 4.5, 5.0 | 40 | normal | $\bar{v}_{in}$ | 0.45 |
| 3c | 2.5, 3.0, 3.5, 4.0, 4.5, 5.0 | 40 | sickle | $\bar{v}_{in}$ | 0.45 |
| 4a | 2.5, 3.0, 3.5, 4.0, 4.5, 5.0 | 95 | both | $\overline{\left(\frac{dp}{dz}\right)}$ | 0.45 |
| 4b | 2.5, 3.0, 3.5, 4.0, 4.5, 5.0 | 40 | normal | $\overline{\left(\frac{dp}{dz}\right)}$ | 0.45 |
| 4c | 2.5, 3.0, 3.5, 4.0, 4.5, 5.0 | 40 | sickle | $\overline{\left(\frac{dp}{dz}\right)}$ | 0.45 |
| 5a | 4.5 | 95 | both | $\overline{\left(\frac{dp}{dz}\right)}$ | 0.45, 0.35, 0.25 |
| 5b | 4.5 | 40 | normal | $\overline{\left(\frac{dp}{dz}\right)}$ | 0.45, 0.35, 0.25 |
| 5c | 4.5 | 40 | sickle | $\overline{\left(\frac{dp}{dz}\right)}$ | 0.45, 0.35, 0.25 |

*Table 3.1.1 : Summary of case studies.*

## 3.2. Parametric study of the dynamics of Red Blood Cells

The results provided by our case studies allow us to demonstrate and compare several trends. In particular, the preliminary study presented in this chapter will focus on analyzing the effects of :
-varying vessel sizes, with constant blood flow (case series 3),
-varying vessel sizes, with constant pressure gradient (case series 4),
-constant vessel size, with varying blood flow (case series 2),
-constant vessel size, with varying hematocrit at constant pressure gradient (case series 5).
Our findings will be presented in detail for all of the above variations, and considering the 2 different oxygen levels prescribed (cases series "a" and "b"). The results of our modeled sickling cells (case series "c") will be discussed later in Section 3.3.

Our first observation concerns qualitative aspects of the RBCs under different conditions. Figure 3.2.1 shows the various asymptotic shapes reached at steady state conditions, for different vessel sizes (to improve visibility, velocity vectors in blue are represented in the relative frame moving with the RBC). Not only do we observe the expected "squeezing" of RBCs similar to Secomb's analysis, but also that, depending on whether velocity or pressure gradient is constant, the resulting shape changes significantly differ. In fact, at constant pressure gradient the velocity decreases with decreasing vessel radius since the RBCs obstruct more and more the flow. At the cases of lower radii, the obtained RBC shapes are less squeezed than when the velocity is kept constant. The squeezing of RBCs explains the shear-thinning property of blood in capillary vessels (increasing resistance to flow with increasing shear rate), which matches the trend observed experimentally in the region of reversed Fåhraeus-Lindqvist effect. From our comparison of cases 3 and 4, the increase of blood resistance to flow is expected to be stronger at constant pressure gradient (case series 4). Otherwise, we observe the formation of vortices as the RBCs get further apart when the vessel radius decreases, which suggest possible additional losses and increased resistance to flow. Since for normal RBCs there is no coupling between oxygen transport and fluid dynamics, series "a" and "b" give exactly the same results here.

(3a)
$R_w$ = 5.0 μm

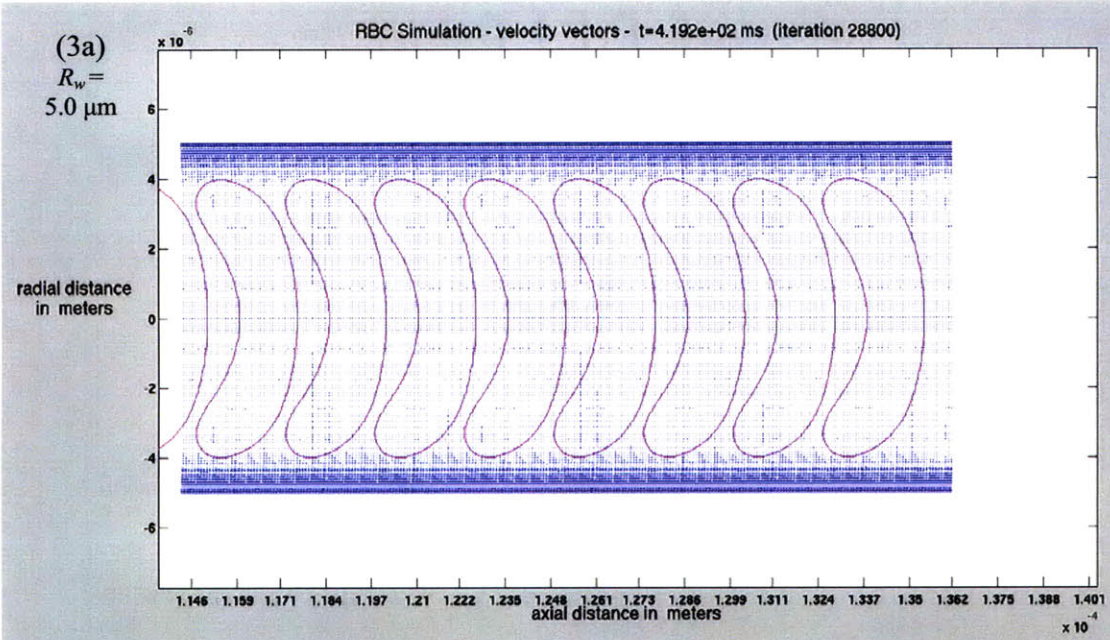


(4a)
$R_w$ = 5.0 μm

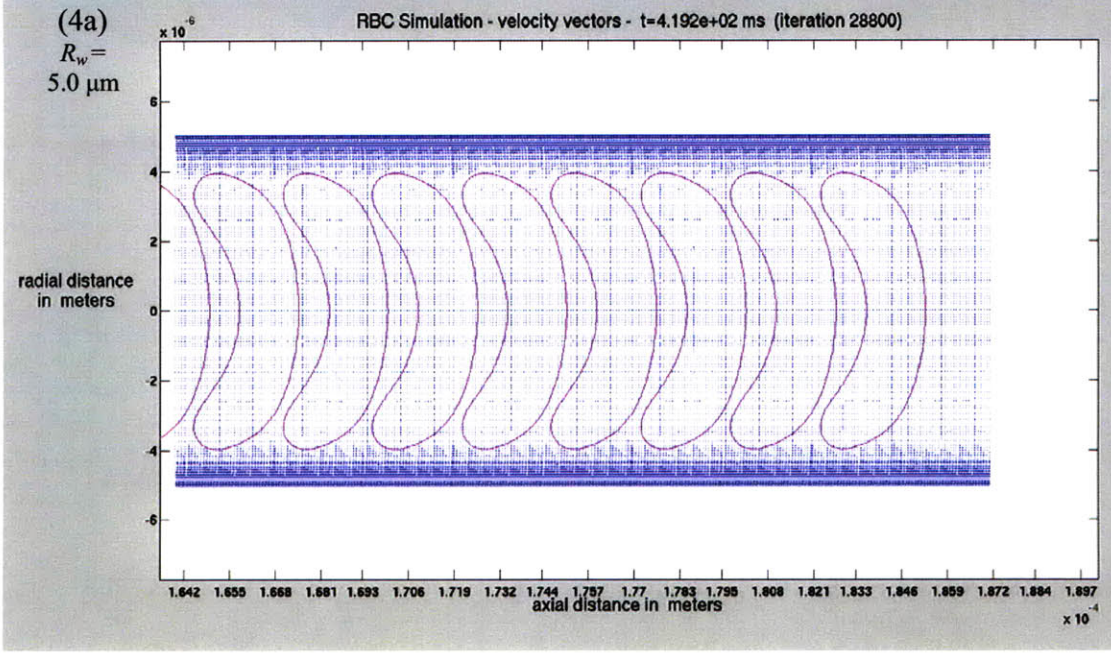

(3a)
$R_w$=
4.5 μm

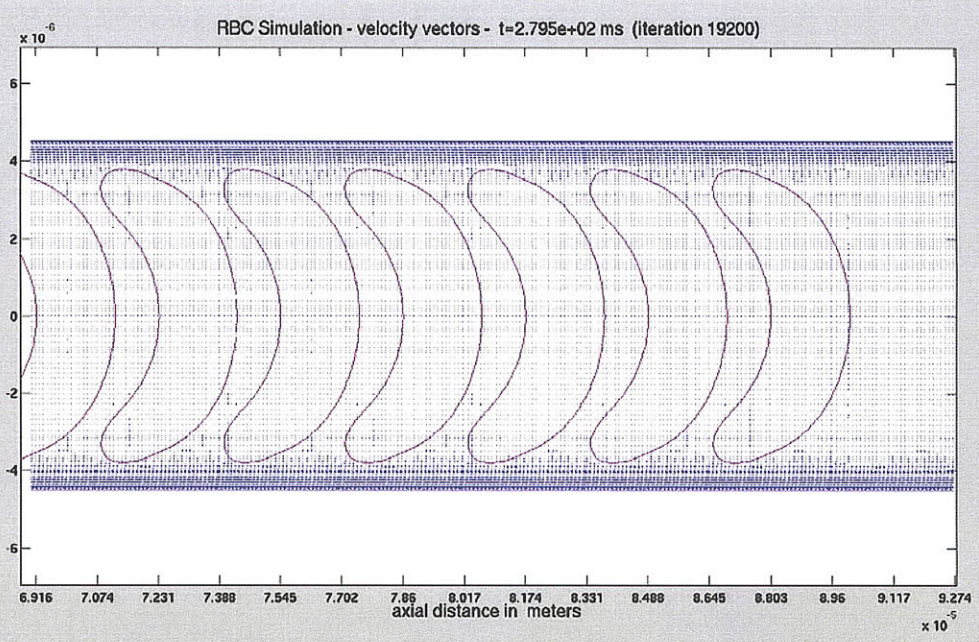


(4a)
$R_w$=
4.5 μm

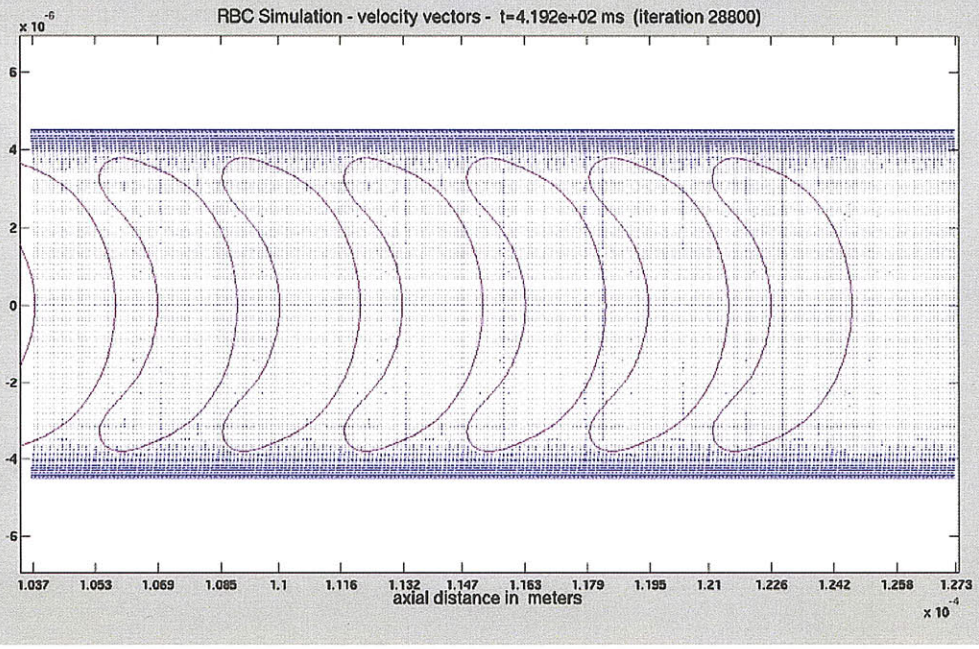

(3a)
$R_w$ = 4.0 μm

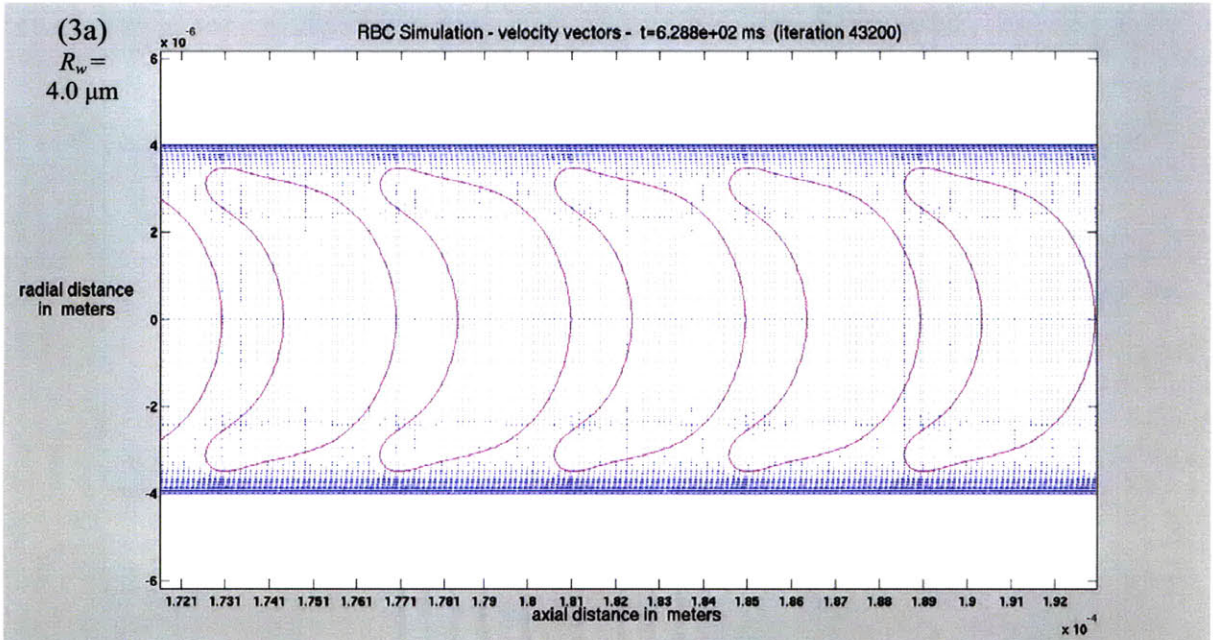


(4a)
$R_w$ = 4.0 μm

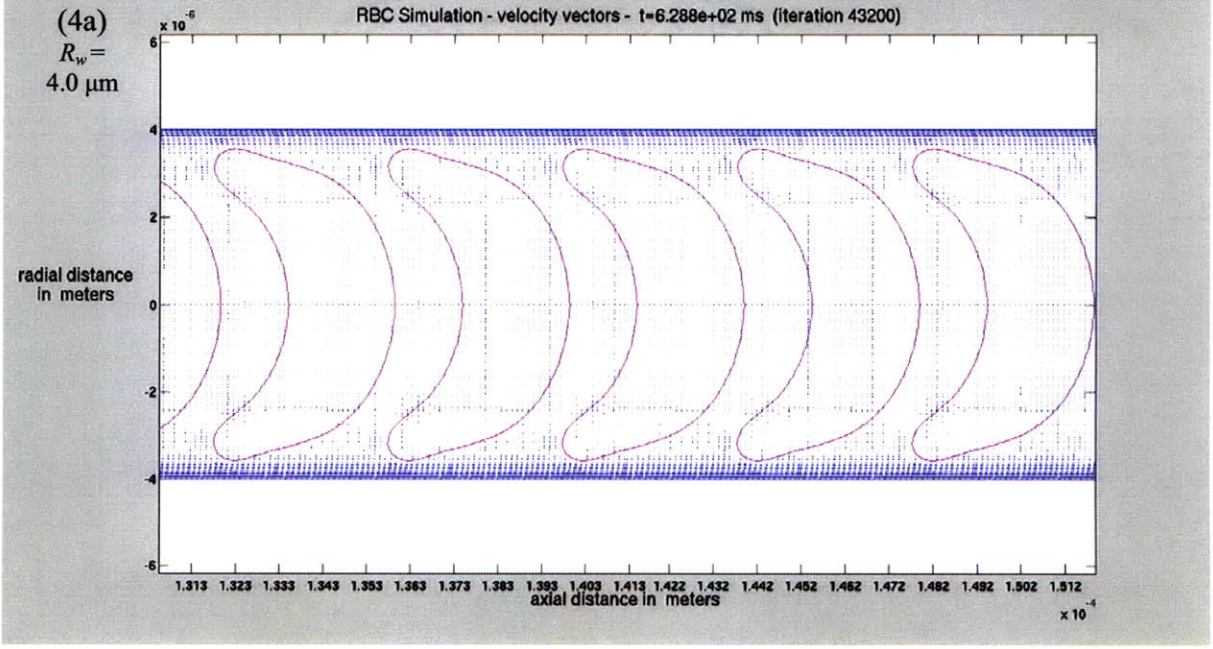

(3a)
$R_w$ = 3.5 μm

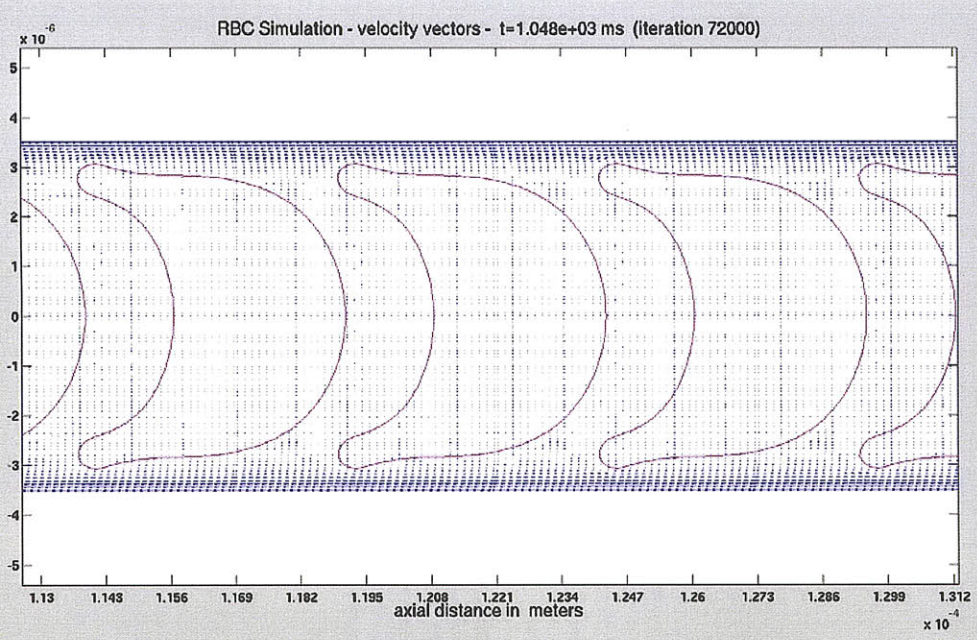


(4a)
$R_w$ = 3.5 μm

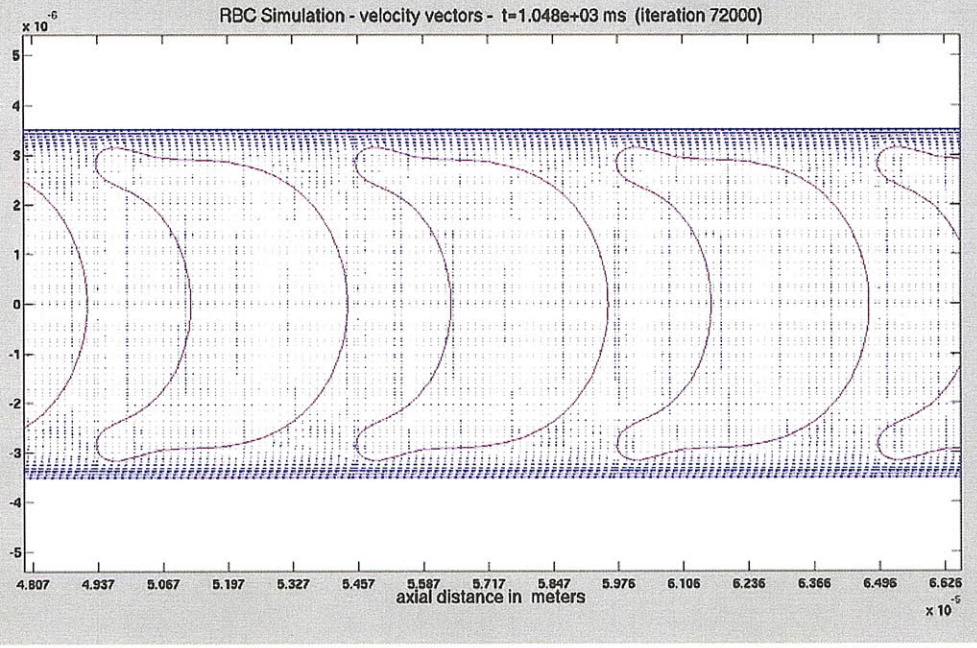

(3a)
$R_w$ = 3.0 μm

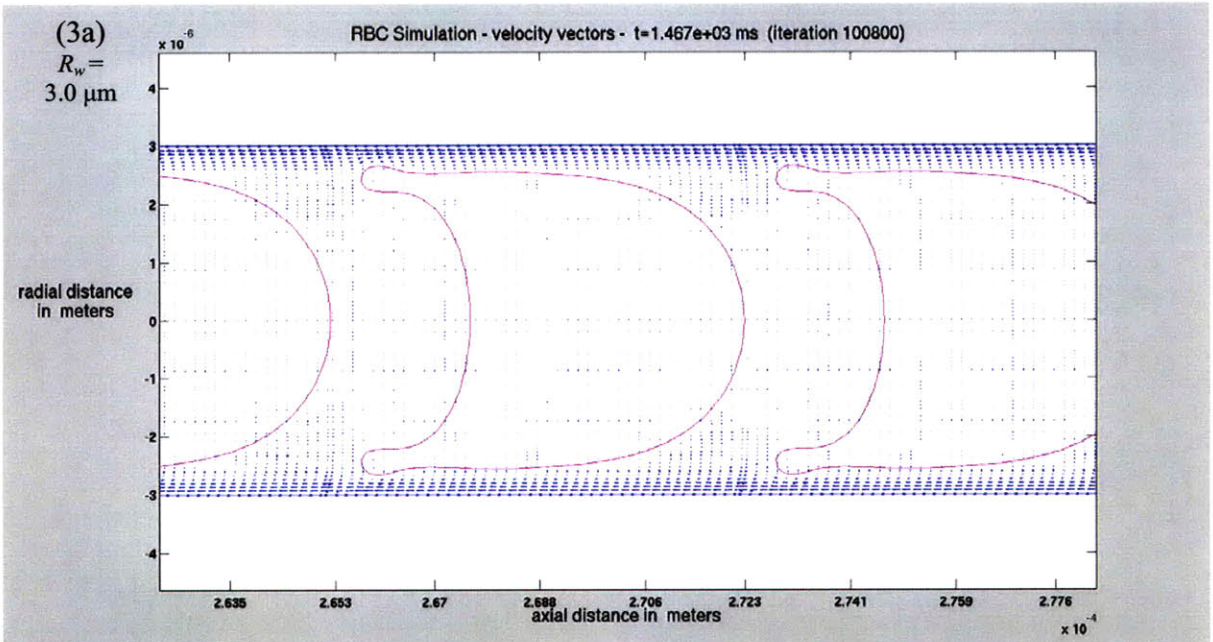


(4a)
$R_w$ = 3.0 μm

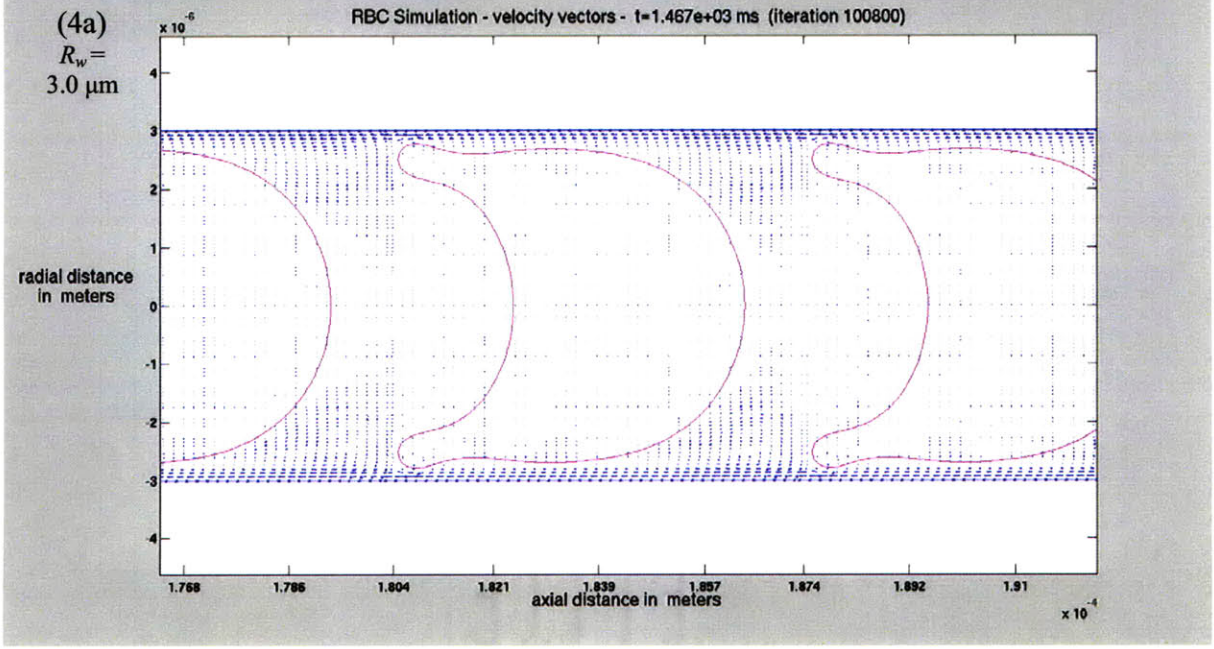

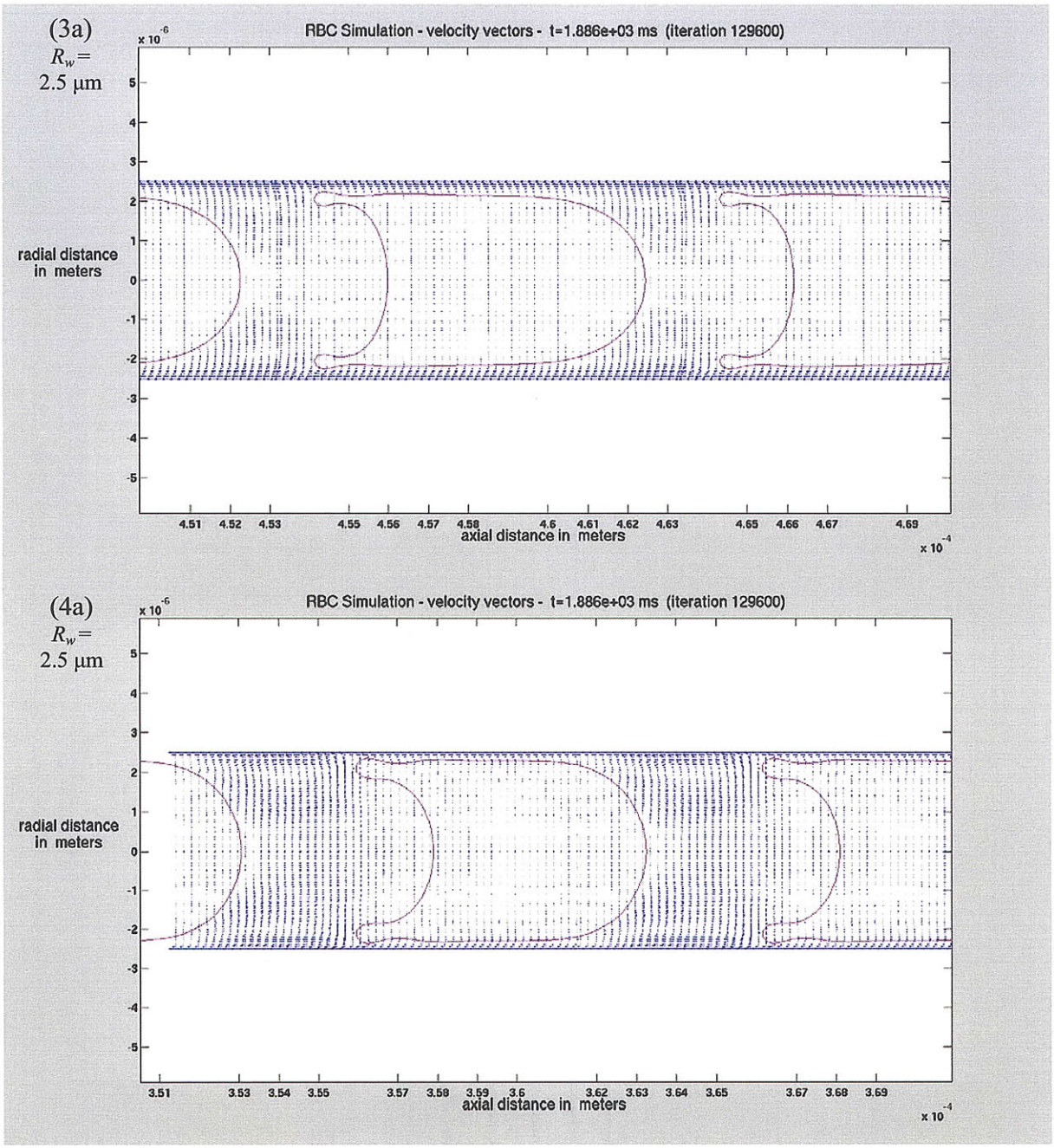


*Figure 3.2.1 : RBC asymptotic shapes for varying radii (cases are indicated at the top left).*

Figure 3.2.2 shows the curves of apparent viscosity of whole blood as a function of vessel size. The different results for cases 3 and 4 prove that the apparent viscosity depends at least on 2 case variables : vessel size, and flow velocity or pressure gradient. This feature illustrates the difficulty of reconciling simulations with experimental data, as the velocity function of vessel size remains unknown and does not seem to ever have been addressed. Figure 3.2.3 and Figure 3.2.4 represent

RBC velocity and discharge hematocrit for the same cases. RBC velocity and hematocrit reflect both changes in flow velocity (giving larger variations in cases 4), and changes of the lubrication layer (which increases with vessel size). Comparison of Figures 3.2.2, 3.2.3 and 3.2.4 shows quantatively how cases 3 and 4 lead to different results, and how cases "a" and "b" lead to the same results as oxygen transfer is not coupled to fluid dynamics (plots are superposed). We observe that RBC velocities are always higher than the average flow, due to their alignment on the centerline, which is consistent with the notion of higher discharge hematocrit than actual vessel hematocrit, known as the Fåhraeus effect. As cases 4 keep the pressure gradient constant, flow velocities are lower than in the cases 3 for the lower vessel sizes, and lead to higher apparent viscosities. Interestingly, we find a correlation between apparent viscosity and discharge hematocrit that seems to fit all the cases (see Figure 3.2.5). This striking result was observed experimentally by Pries and coworkers at larger vessel sizes, and here presents an inverted trend for vessels of capillary radius less than 5 μm [36].

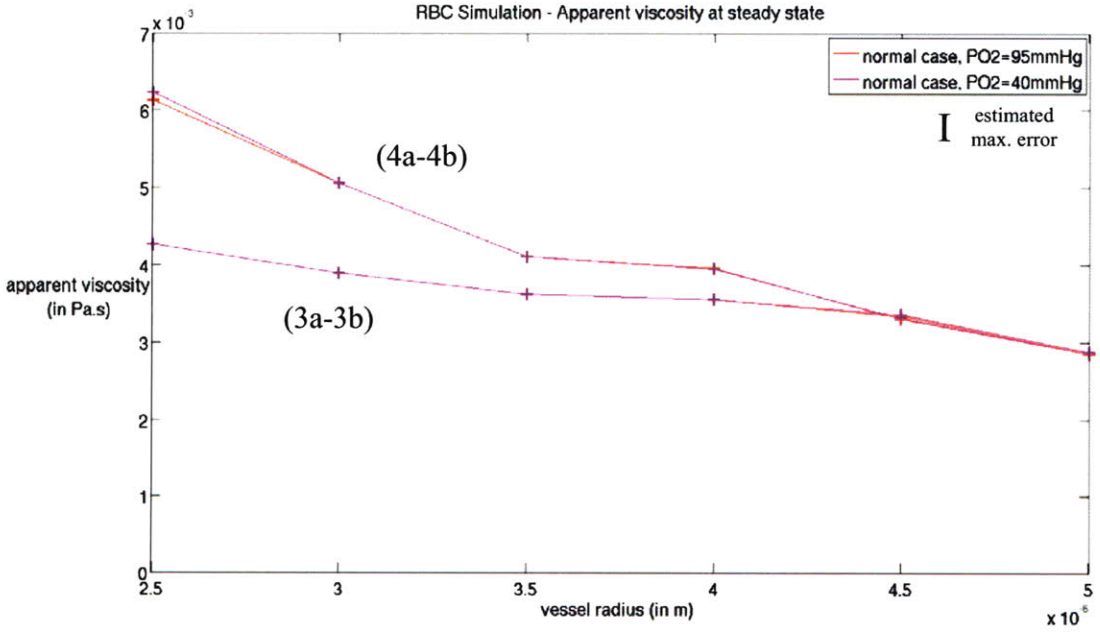


*Figure 3.2.2 : Apparent viscosity vs. vessel size.*

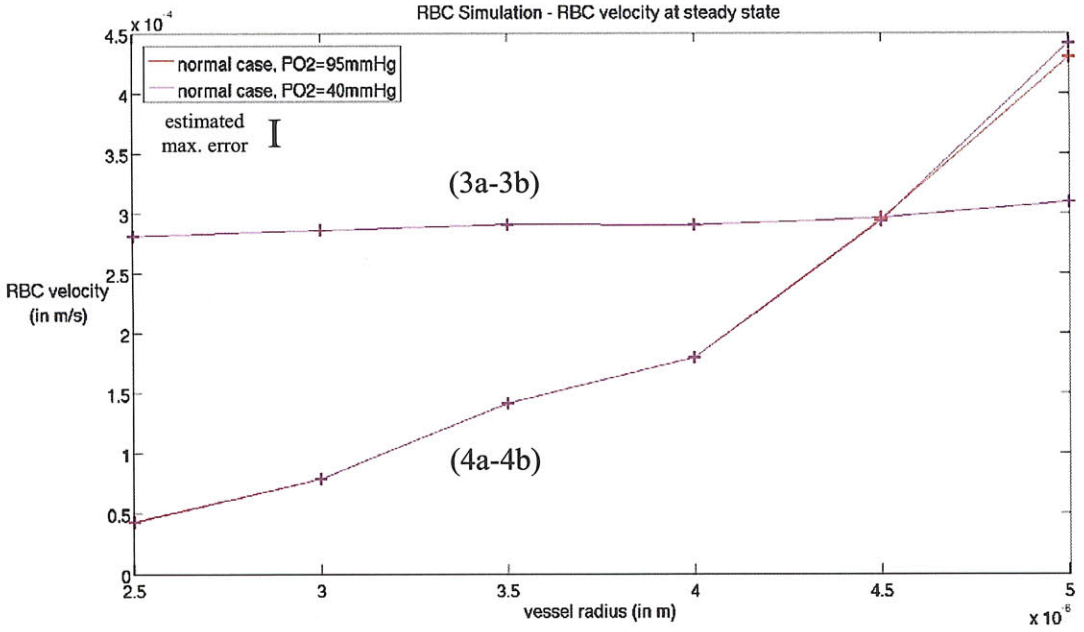


*Figure 3.2.3 : RBC velocity vs. vessel size.*

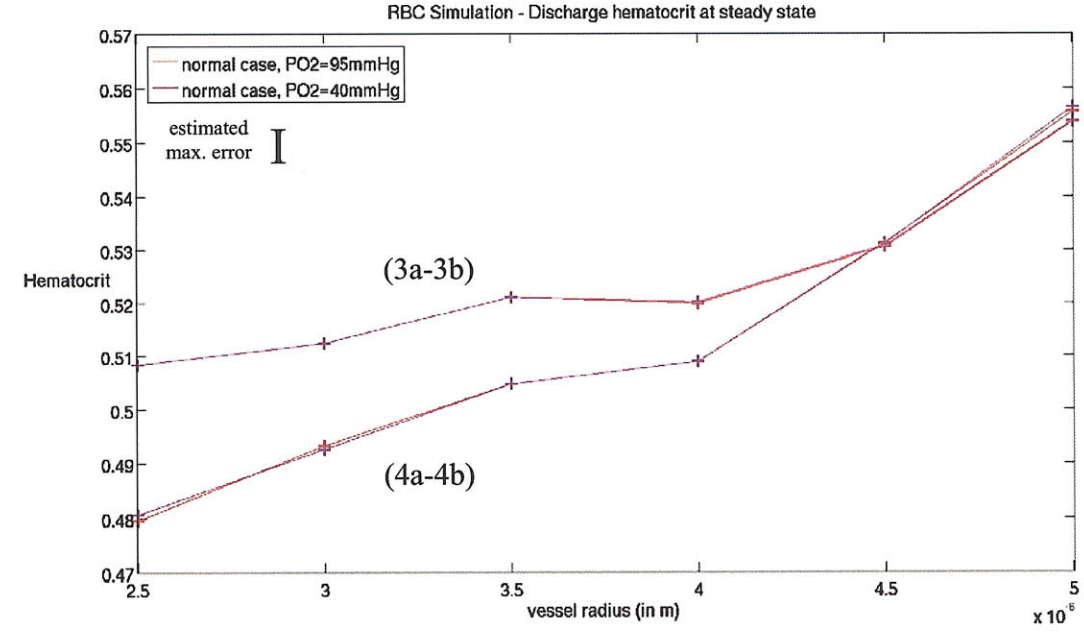


*Figure 3.2.4 : Discharge hematocrit vs. vessel size.*

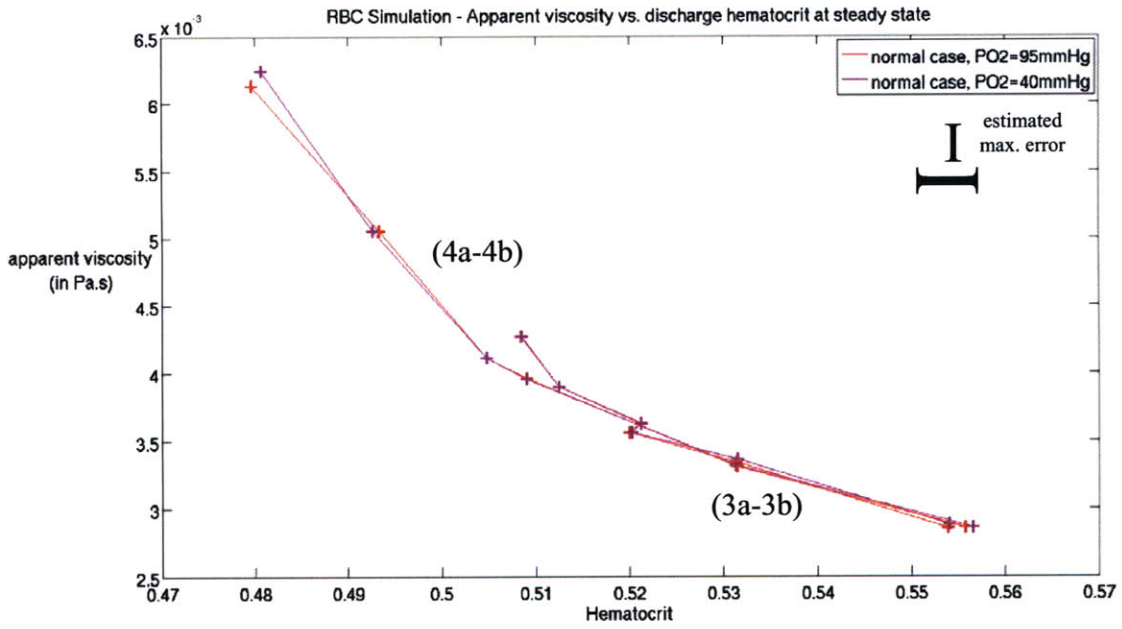


*Figure 3.2.5 : Apparent viscosity vs. discharge hematocrit.*

Oxygen transport is a separate problem for normal RBCs. Its characteristics are directly dependent on the flow features, but do not produce any dynamical effects. Hence while the observed previous trends gave the same results for cases labeled "a" and "b", oxygen transport results will differ for those cases. Figure 3.2.6 shows the steady state oxygen profiles for cases 3a, 3b and 4a. The profiles for cases 4b follows the expected combined trends from decreased oxygen level (3a to 3b) and reduced velocity under constant pressure gradient (3a to 4a). On Figure 3.2.6 we see that oxygen profiles follow RBC membrane contours in the vessel, showing that convection is the main mechanism of transfer locally, followed by lateral diffusion across the streamlines. We see here how oxygen transported by RBCs imposing a "plug flow" is more efficient than if it were transported freely in blood plasma (the diffusion gradients are greater in the plasma and at the capillary wall). We see also that even in low oxygen conditions, convection still dominates oxygen transfer, although more signs of lateral transfer appear within the RBCs (diffusion visible in the 3b cases). The higher velocities of cases 3a compared to 4a result in higher concentration gradients that are visible across the vessel and in the surrounding tissue (contours are less steep). In cases 3b, the lower oxygen level also results in higher gradients and more diffusion across the surrounding tissue. Figure 3.2.7 shows the resulting oxygen drops per unit length along the capillary, for all cases 3a, 4a, 3b and 4b. In Figure 3.2.8 the same data is represented as equivalent capillary length to have oxygen partial pressure drop from 95 mmHg to 40 mmHg. We note that :

(1)- as already observed in Figure 3.2.6, higher oxygen levels lead to higher transfer to the surrounding tissue (since consumption is the same, it means that more oxygen gets transferred from the hemoglobin to the myoglobin, used as local storage).

(2)- calculations of the corresponding capillary length to have oxygen drop from 95 mmHg to 40 mmHg gives a precise range and quite good estimation of the effective capillary length where oxygen is exchanged, here about $1.10^{-3}$ m.

(3)- the 95 mmHg case allows us to observe a peak of oxygen consumption, which seems surprisingly independent of whether blood flow velocity or pressure gradient is constant, at a radius between 3.5 μm and 4.0 μm. This shows two competing effects. Large vessels prevent good oxygen transfer because of an increased distance between RBC hemoglobin and the capillary wall, while small vessels seems to suffer from the oxygen-deprived bolus flow, an inconstant oxygen supply and of course a smaller external vessel area. This last effect is emphasized for the lower oxygen level cases, where the peak of maximal oxygen delivery seems to be at a larger vessel size, here out of range.

(4)- the peak of oxygen consumption is more important for cases 4 than cases 3 at 95 mmHg, which shows the greater emergence of this peak for variable flow velocities. This means that the optimality of vessel size would be more emphasized in a network of vessels than in a single vessel of varying diameter. In the case 4 at 95 mmHg, the oxygen transfer even gets below the 40 mmHg case for vessel sizes greater than 10 μm.

(3a)
$R_w$ = 5.0 μm

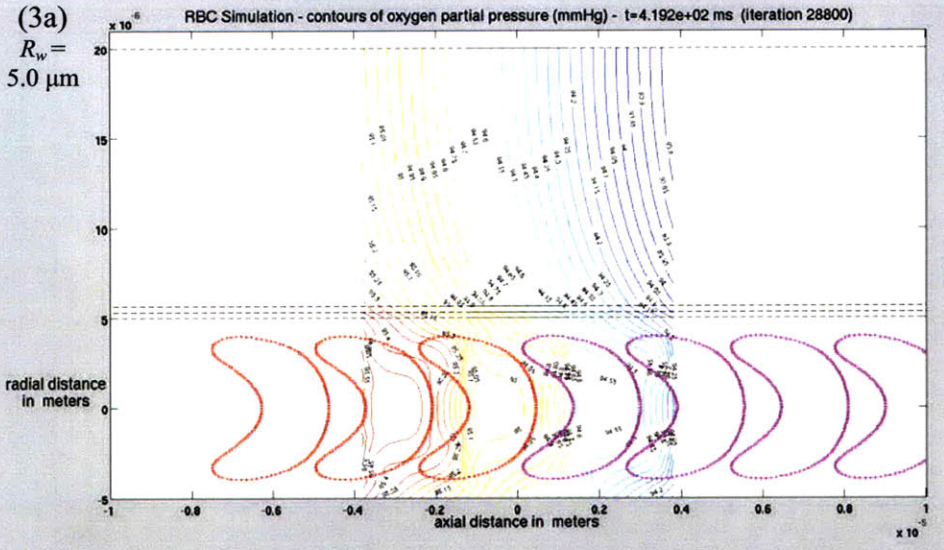


(4a)
$R_w$ = 5.0 μm

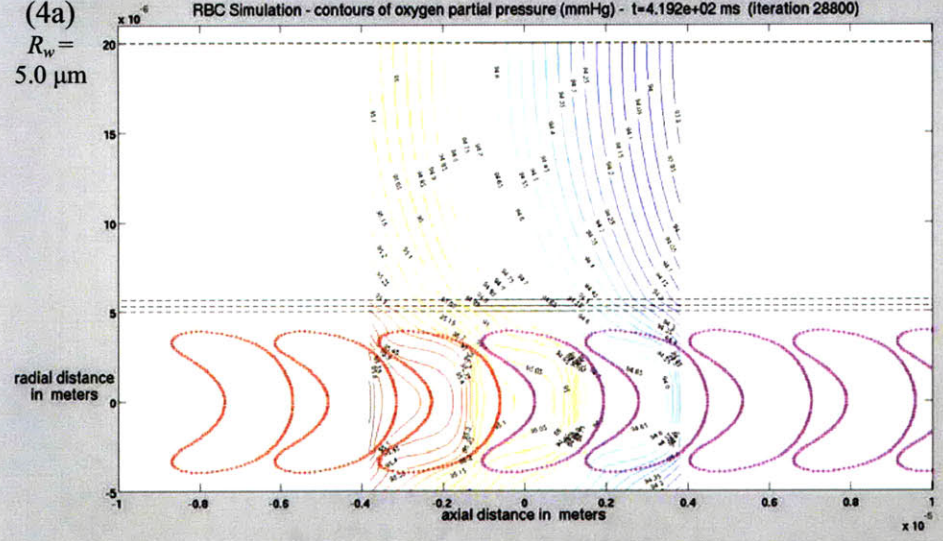


(3b)
$R_w$ = 5.0 μm

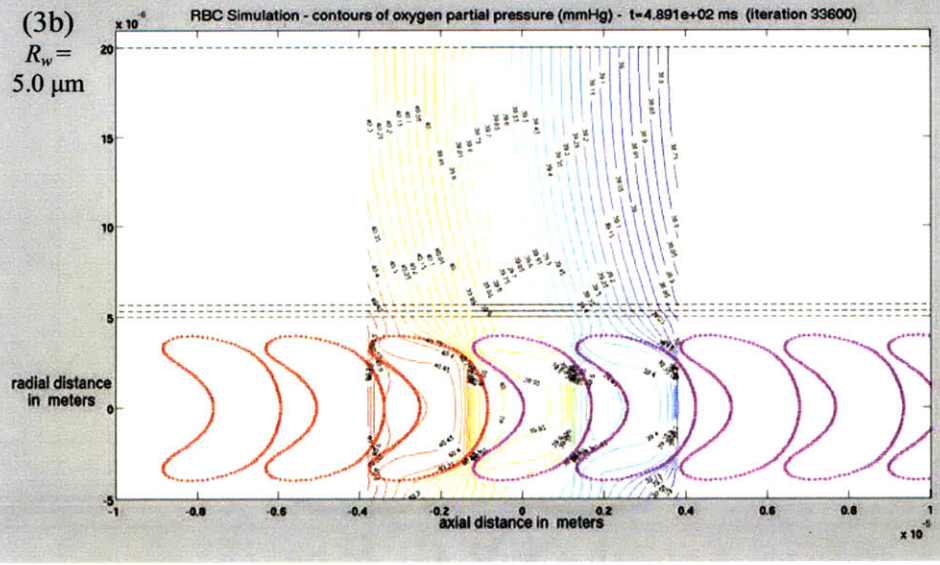

(3a)
$R_w$ = 4.5 μm

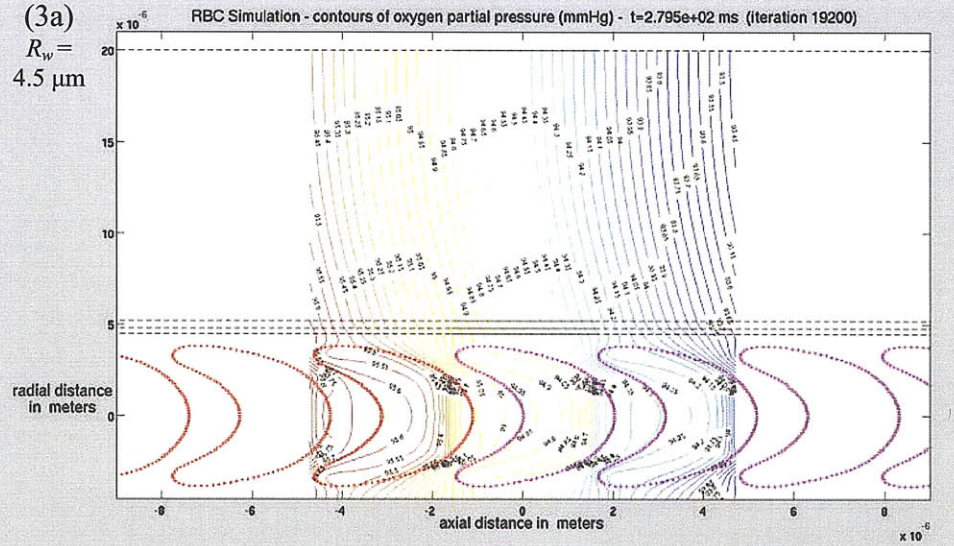


(4a)
$R_w$ = 4.5 μm

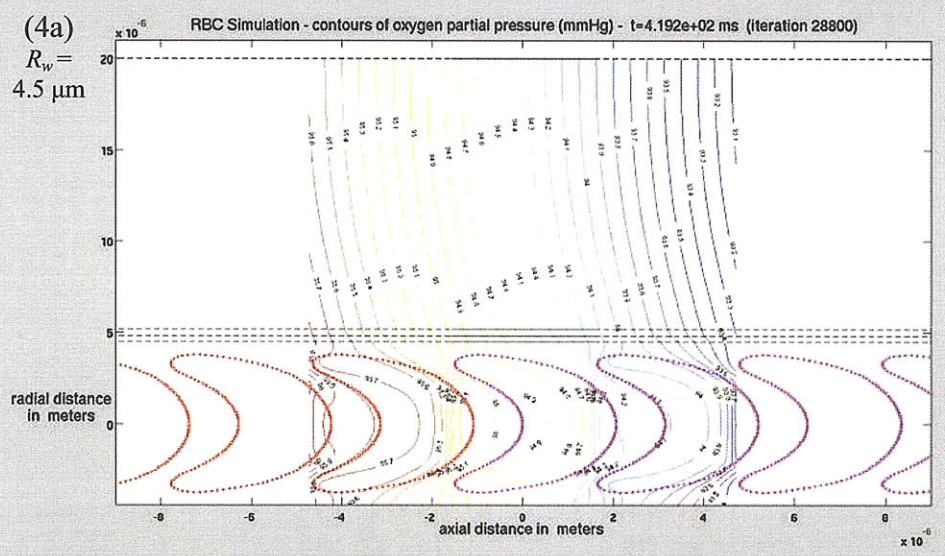


(3b)
$R_w$ = 4.5 μm

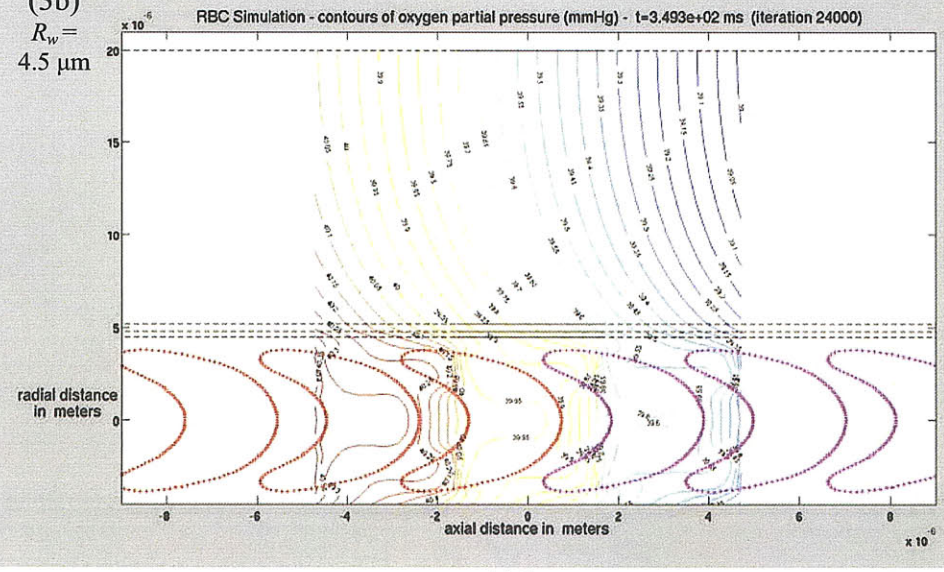

(3a)
$R_w$ = 4.0 μm

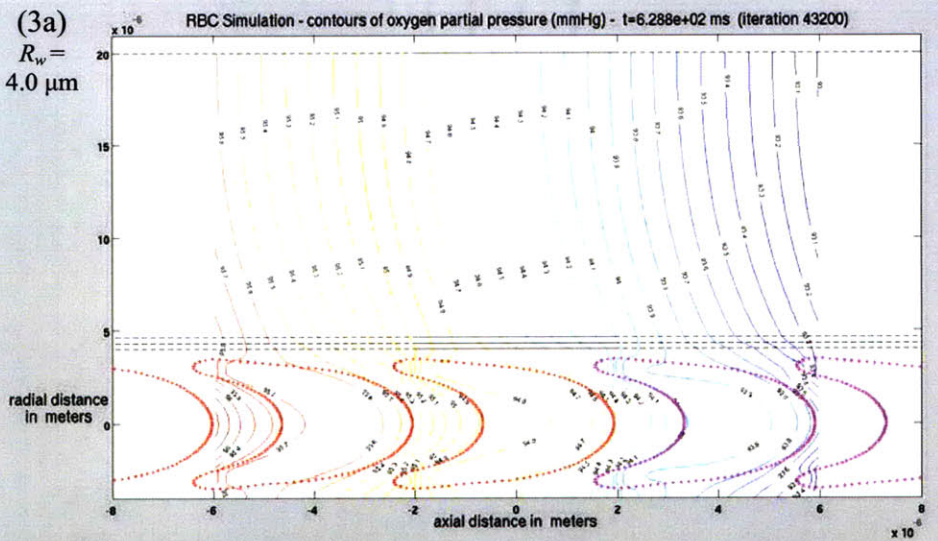


(4a)
$R_w$ = 4.0 μm

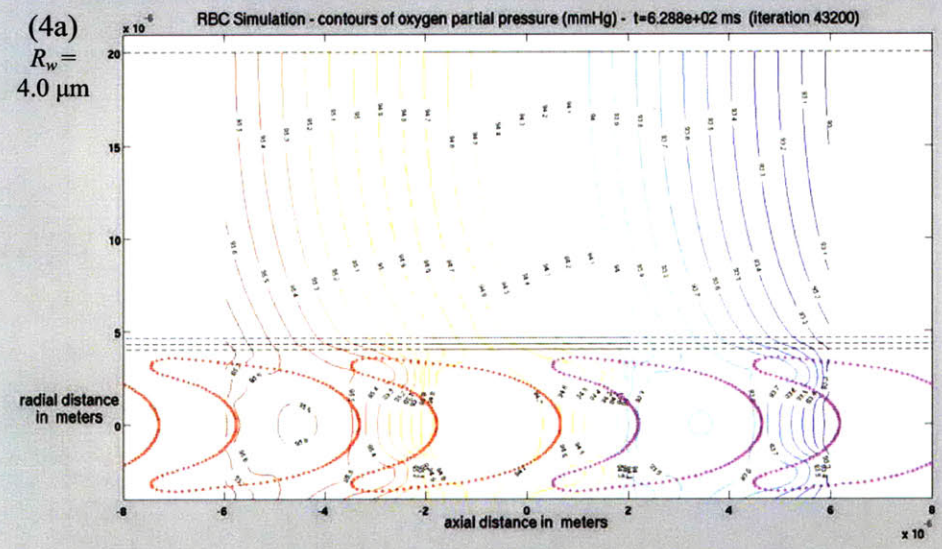


(3b)
$R_w$ = 4.0 μm

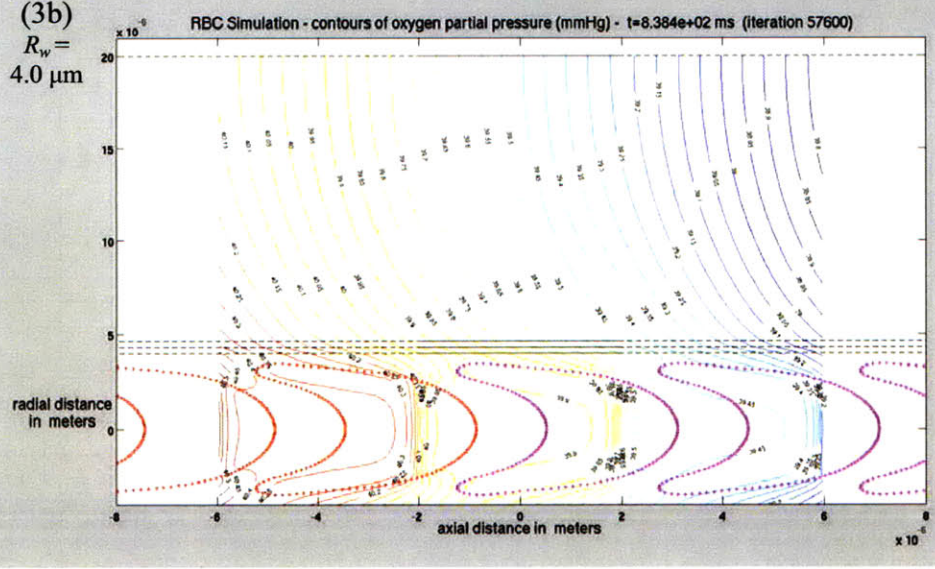

(3a)
$R_w$ = 3.5 μm

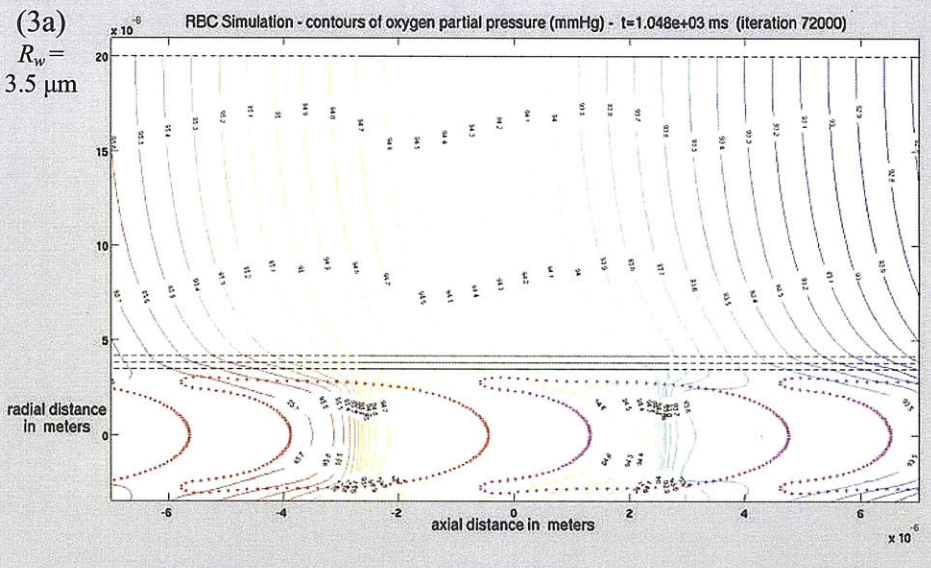


(4a)
$R_w$ = 3.5 μm

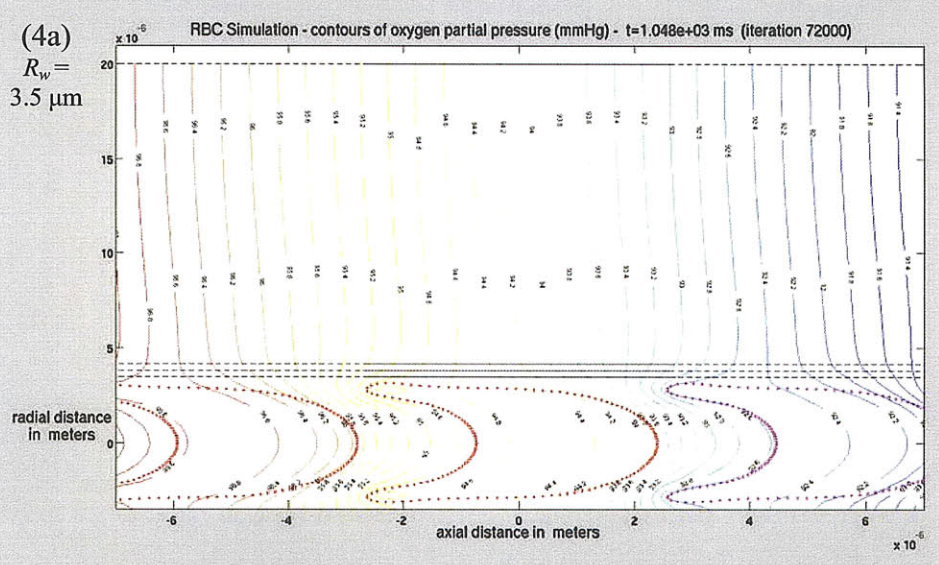


(3b)
$R_w$ = 3.5 μm

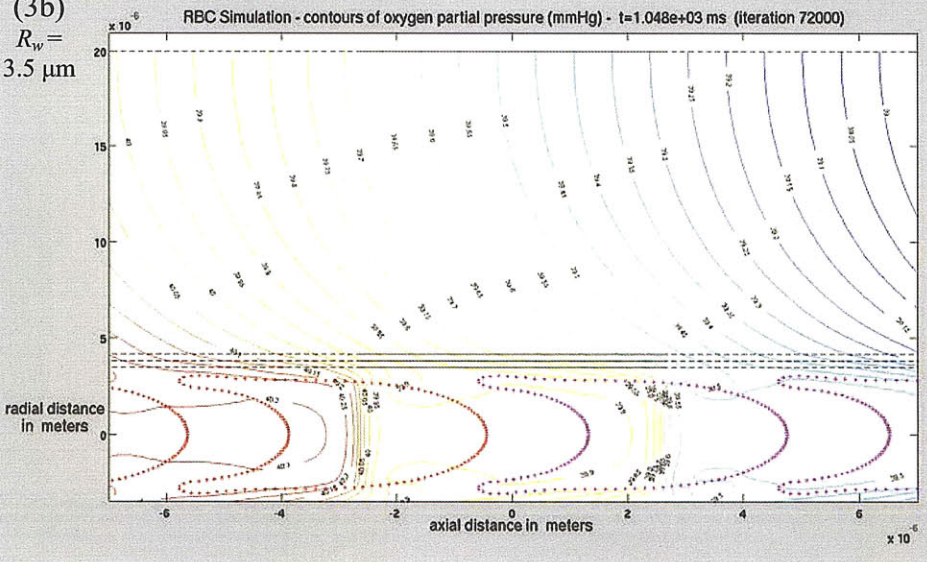

(3a)
$R_w$ = 3.0 μm

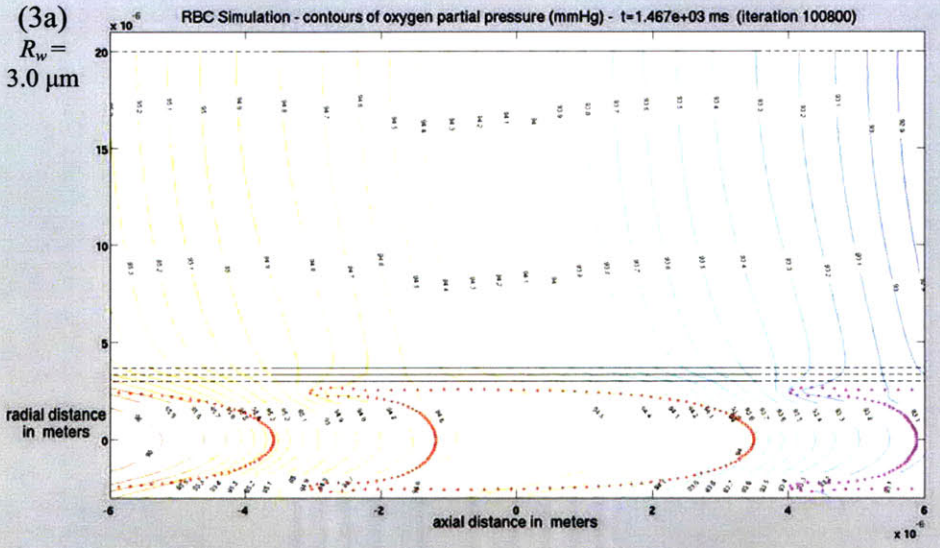


(4a)
$R_w$ = 3.0 μm

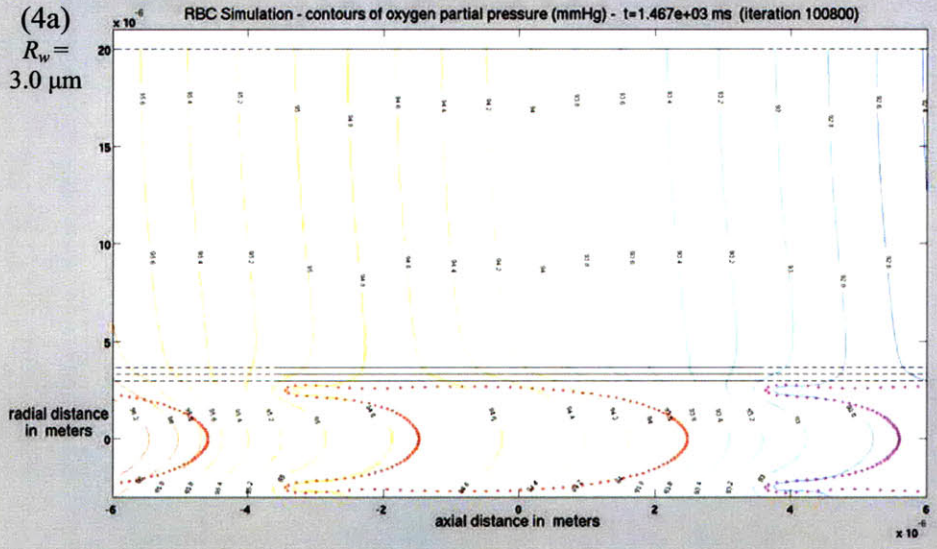


(3b)
$R_w$ = 3.0 μm

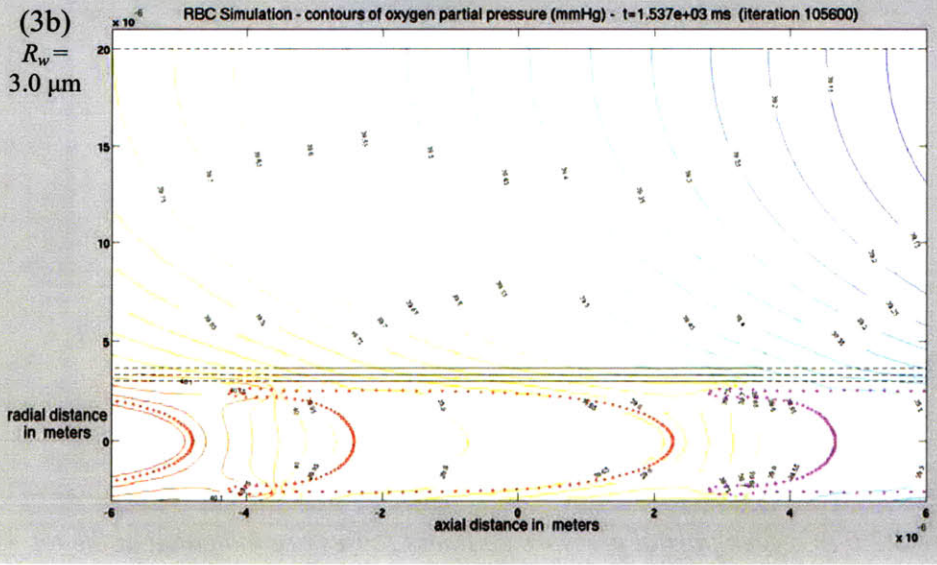

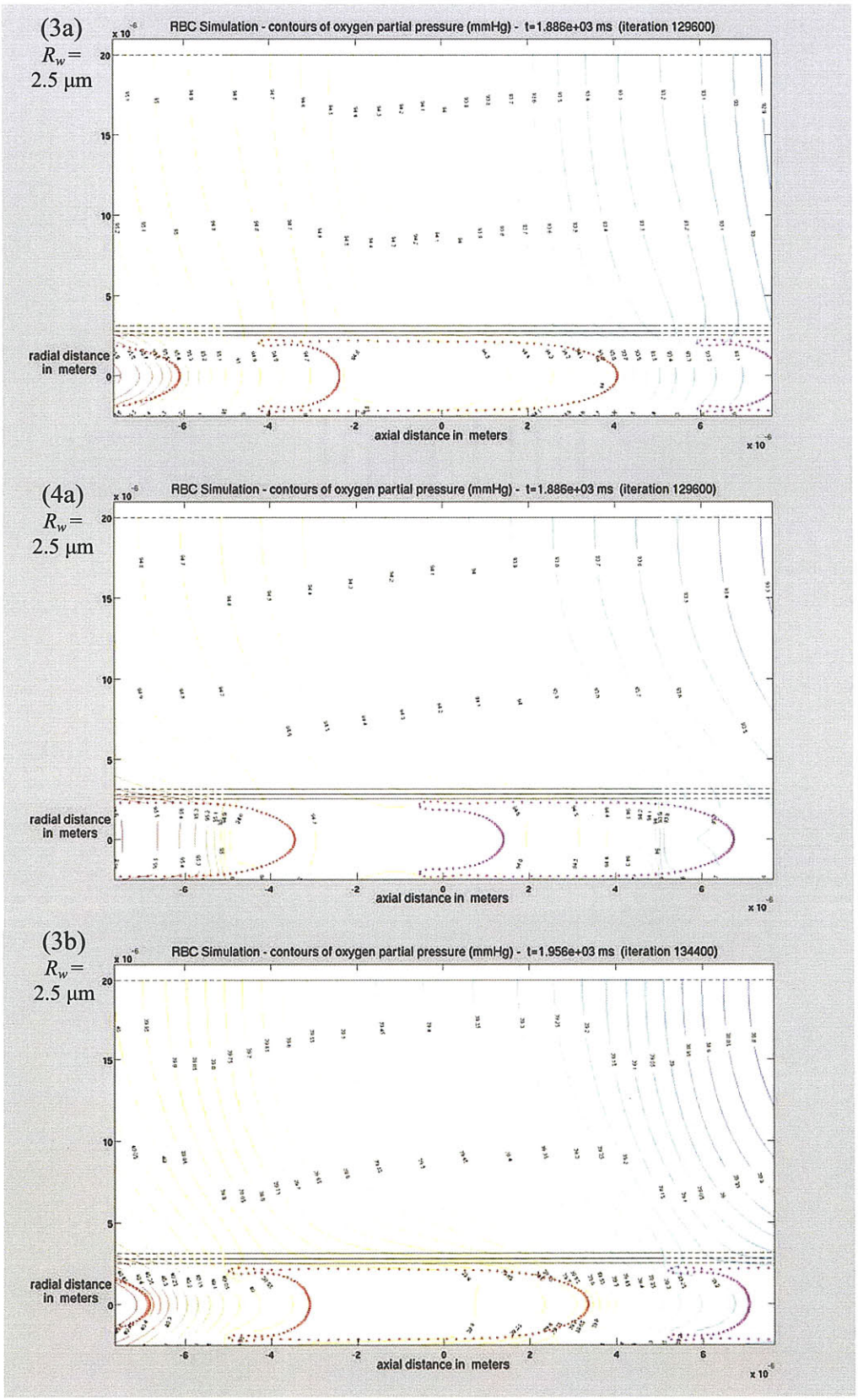


*Figure 3.2.6 : Oxygen partial pressure contours (cases are indicated at the top left).*

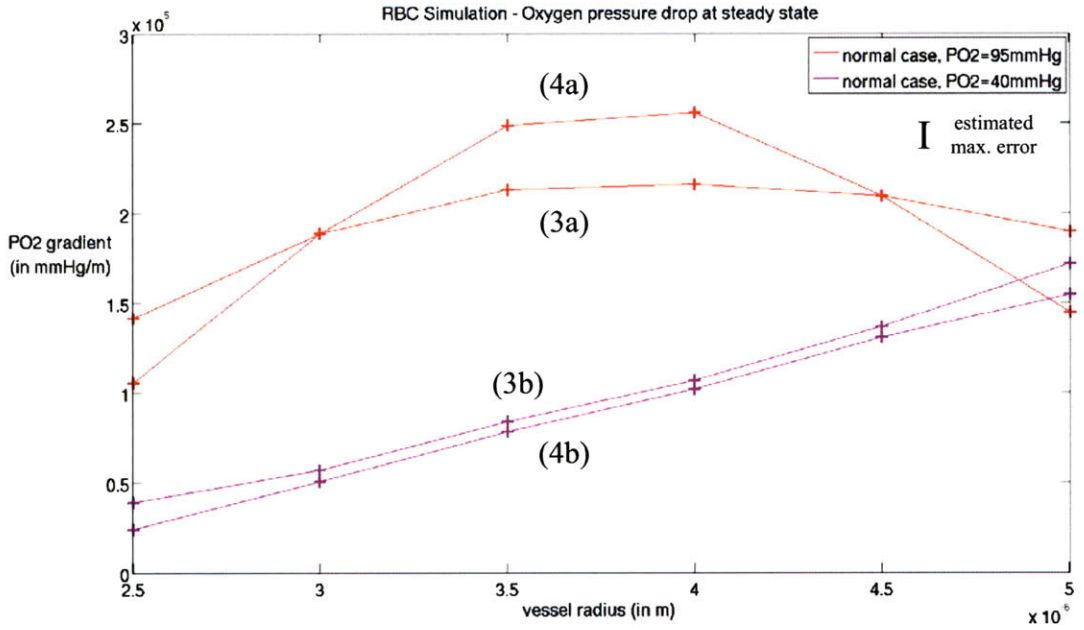


*Figure 3.2.7 : Oxygen partial pressure gradient vs. vessel size.*

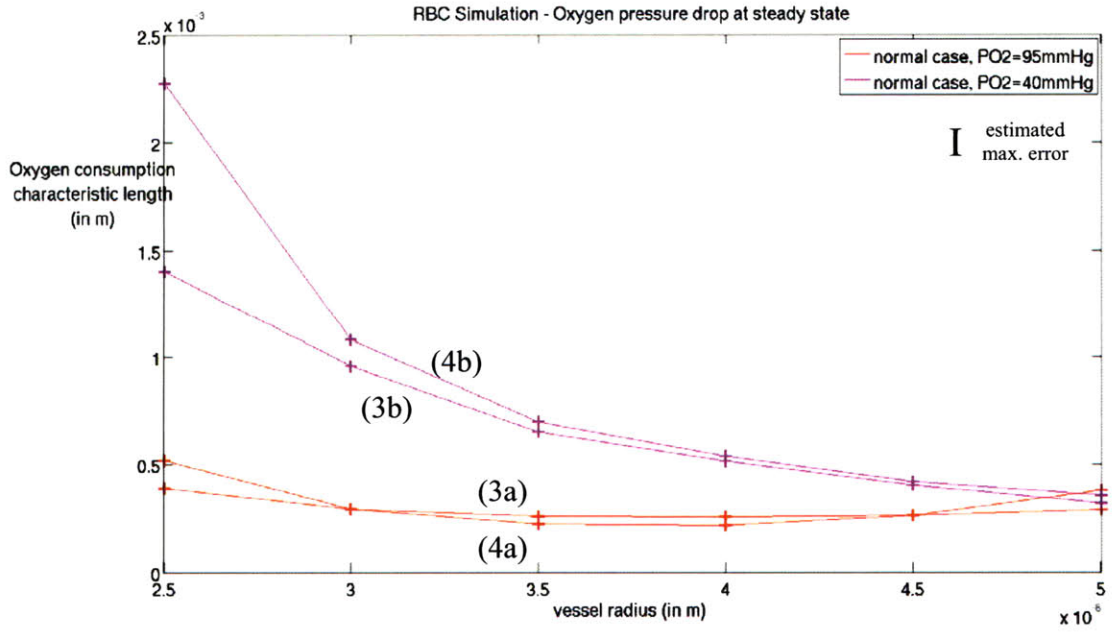


*Figure 3.2.8 : Oxygen partial pressure gradient vs. vessel size (equivalent vessel length).*

Case 2 is used to emphasize the previous observations for varying flow velocities. The resulting curves showing blood dynamics are presented in Figures 3.2.9, 3.2.10, 3.2.11 and 3.2.12. Figure 3.2.9 supports directly our claim that the apparent viscosity generally decreases with increasing blood flow (shear thinning or pseudoplastic behavior). Figure 3.2.10 shows also that RBC velocity correlates well with average blood velocity for the cases where $R_w$ = 4.5 μm. As a direct consequence, the discharge hematocrit also increases with increasing blood flow (see Figure 3.2.11). Figure 3.2.12 is found to follow the same behavior as Figure 3.2.5, with apparent viscosity and discharge hematocrit located on the same curve for all cases.

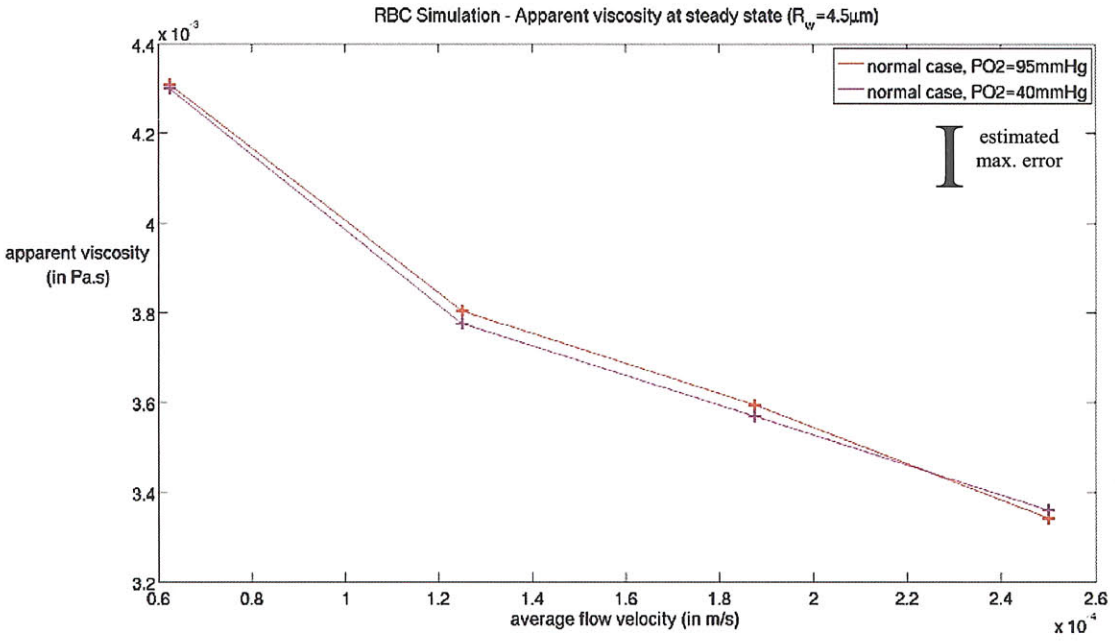


*Figure 3.2.9 : Viscosity vs. average flow velocity.*

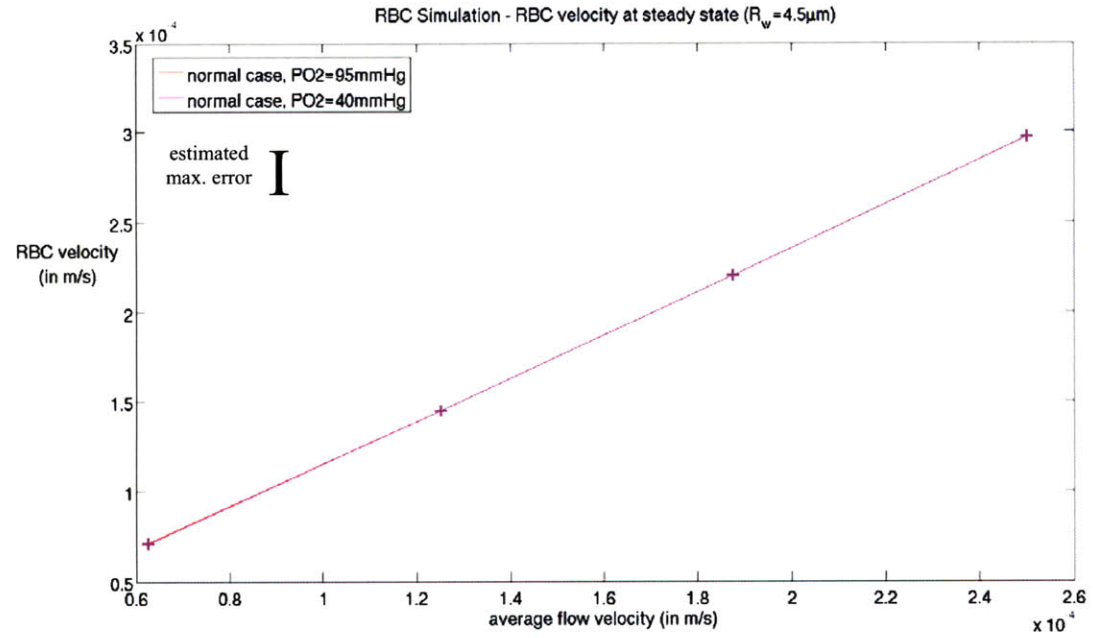


*Figure 3.2.10 : RBC velocity vs. average flow velocity.*

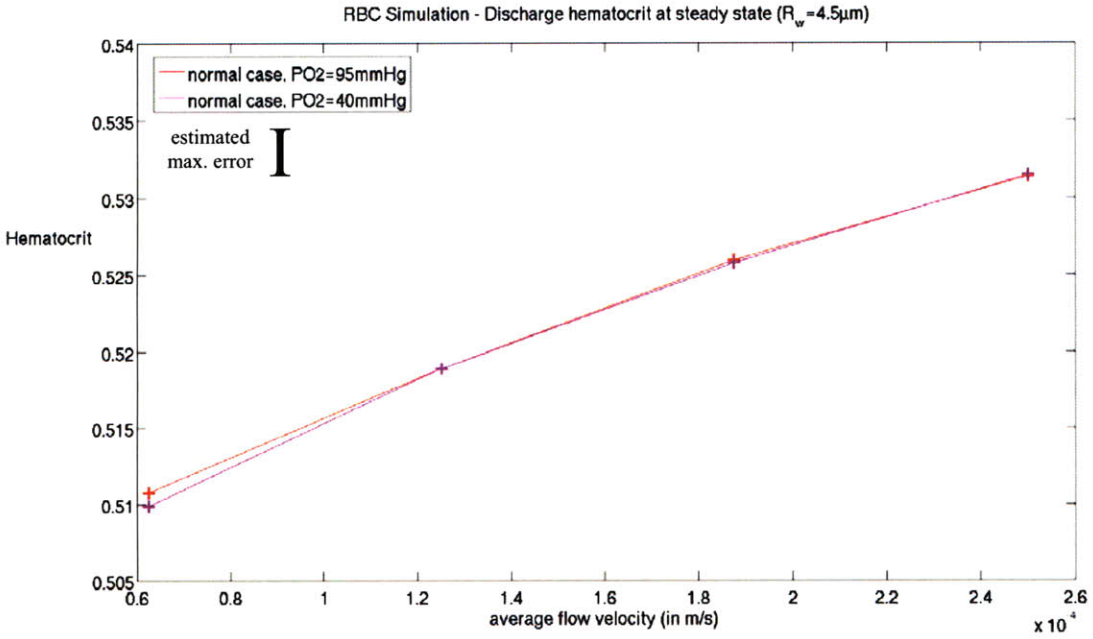


*Figure 3.2.11 : Discharge hematocrit vs. average flow velocity.*

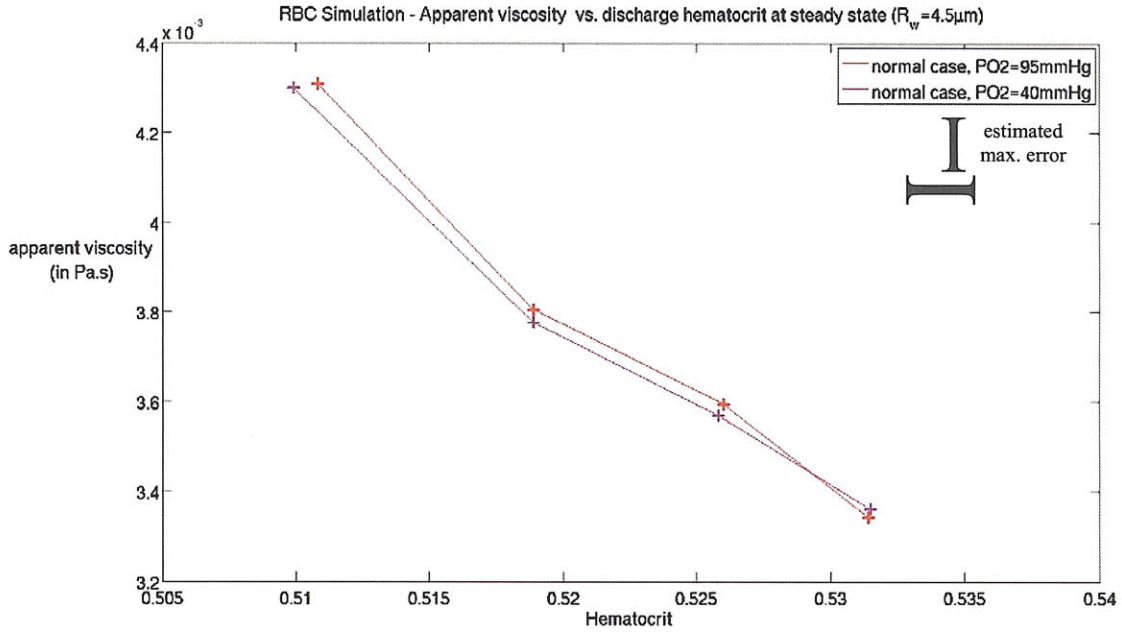


*Figure 3.2.12 : Viscosity vs. discharge hematocrit.*

The oxygen transfer results for case 2 are shown in Figures 3.2.13 and 3.2.14. We notice that oxygen transfer clearly decreases with increasing flow velocity for an oxygenation level corresponding to $p_{O_2,in}$ = 95 mmHg. This trend disappears almost completely at $p_{O_2,in}$ = 40 mmHg, however, as the limits of oxygen supply capabilities are reached and oxygen release and diffusion become limiting factors (as opposed to blood flow). Below the velocity of $2.5.10^{-4}$ m/s, oxygen supply is found to remain quasi-constant at the venous end of the capillary, suggesting in vivo an effective lack of oxygen supplied to the tissue, and illustrating the direct relation between ischemia (restriction in blood supply) and hypoxia (shortage of oxygen).

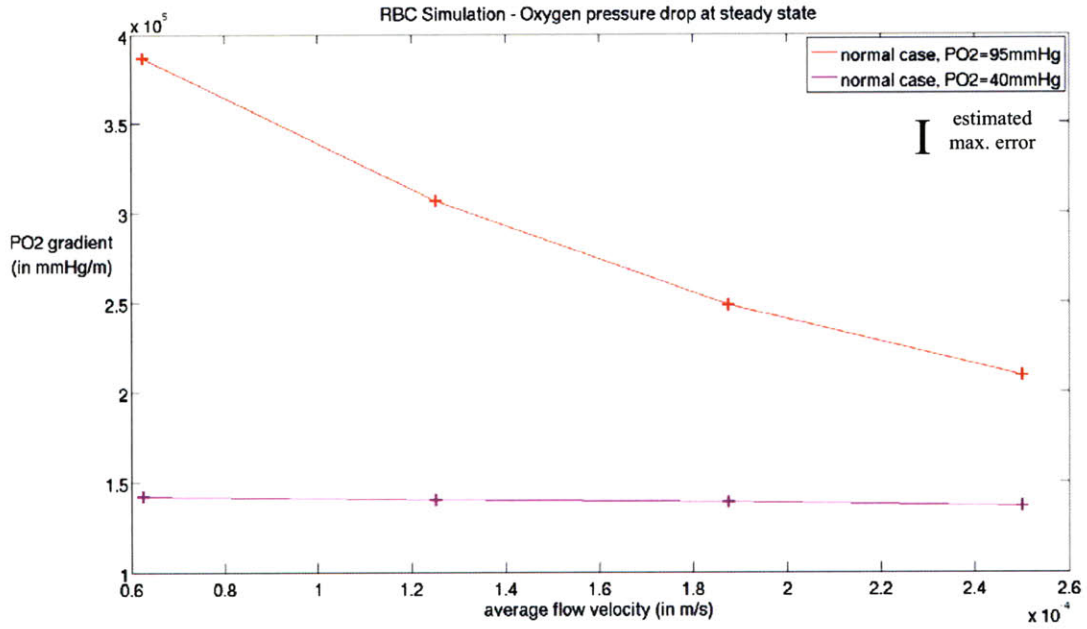


*Figure 3.2.13 : Oxygen partial pressure gradient vs. average flow velocity.*

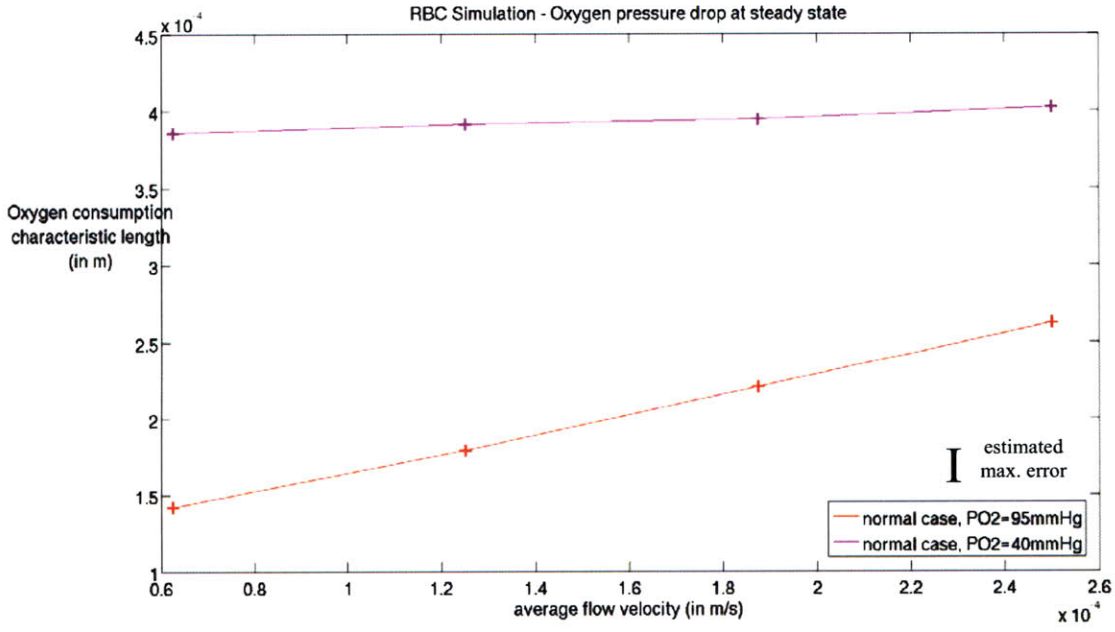


*Figure 3.2.14 : Oxygen partial pressure gradient vs. average flow velocity (equiv. vessel length).*

To identify the effects of reduced hematocrit, cases 5a and 5b are presented in the following figures for a vessel hematocrit of 0.45 and 0.25. Firstly, Figure 3.2.15 shows the resulting blood flow,

compared to the case of hematocrit 0.45. We see that a lower hematocrit results not only in more spaced RBCs, but also in a different configuration, where the cells are more squeezed and more RBC volume is confined around the centerline. The lubrication flow between the RBCs and the capillary wall also seems to have a larger width, which shows how more stresses are supported by each RBC on average.

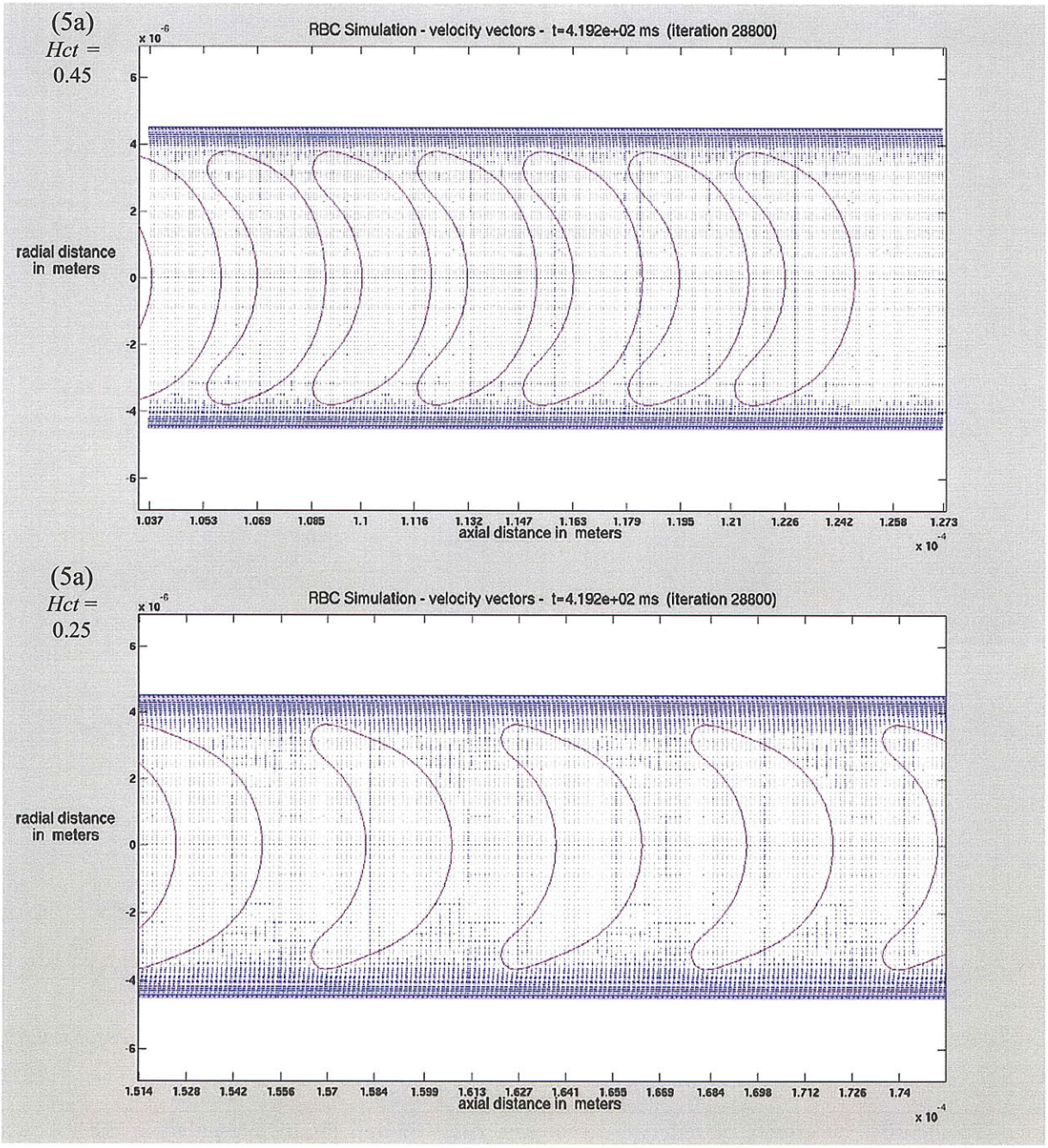


*Figure 3.2.15 : Comparison of normal and low hematocrit blood flows.*

Figures 3.2.16, 3.2.17 and 3.2.18 show the resulting changes in dynamics. We see on Figures 3.2.16 and 3.2.17 how a drop in hematocrit from 0.45 to 0.25 leads to a drop of about 25% in apparent viscosity, and an increase of about 37% in RBC velocity, with the same pressure gradient along the capillary. Figure 3.2.18 shows that relative to the vessel hematocrit, the new cases still fit remarkably well the apparent viscosity vs. discharge hematocrit curve obtained for cases 3 and 4.

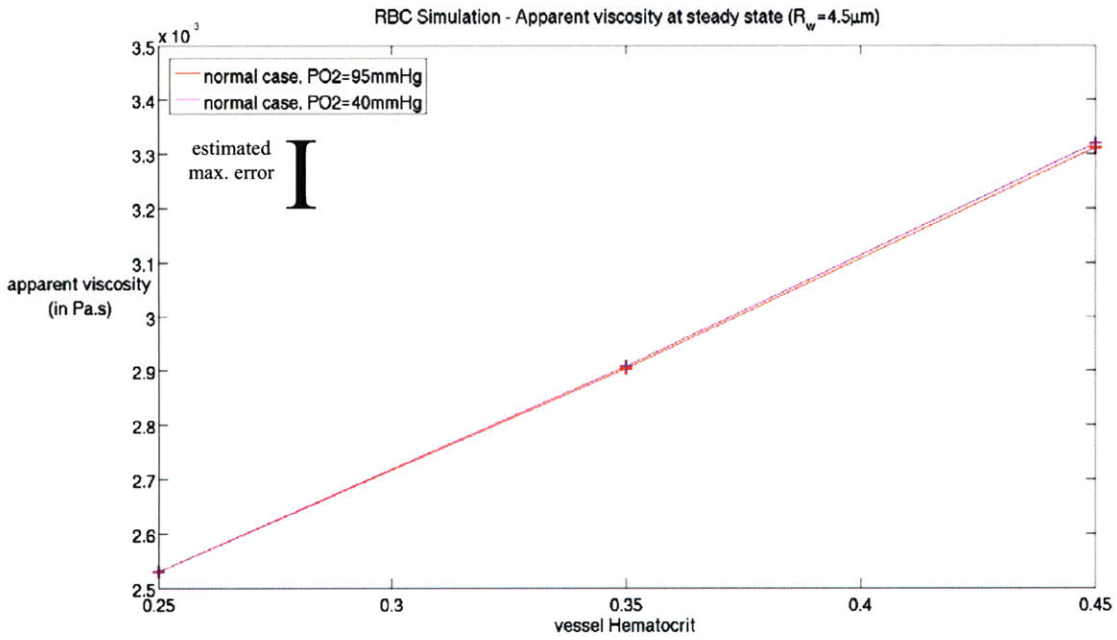


*Figure 3.2.16 : Viscosity vs. vessel hematocrit.*

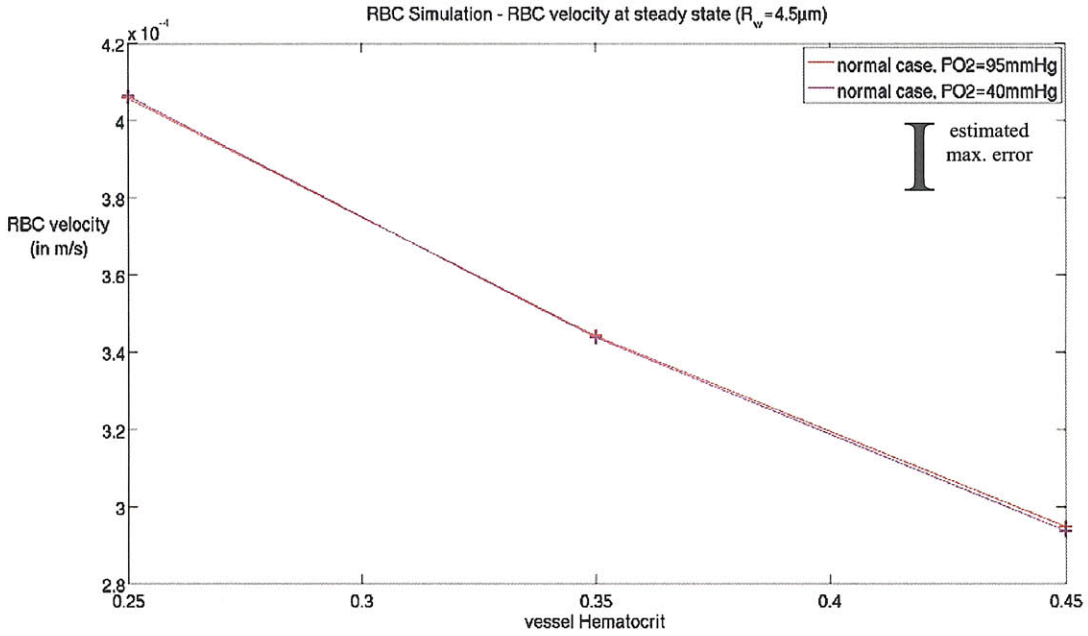


*Figure 3.2.17 : RBC velocity vs. vessel hematocrit.*

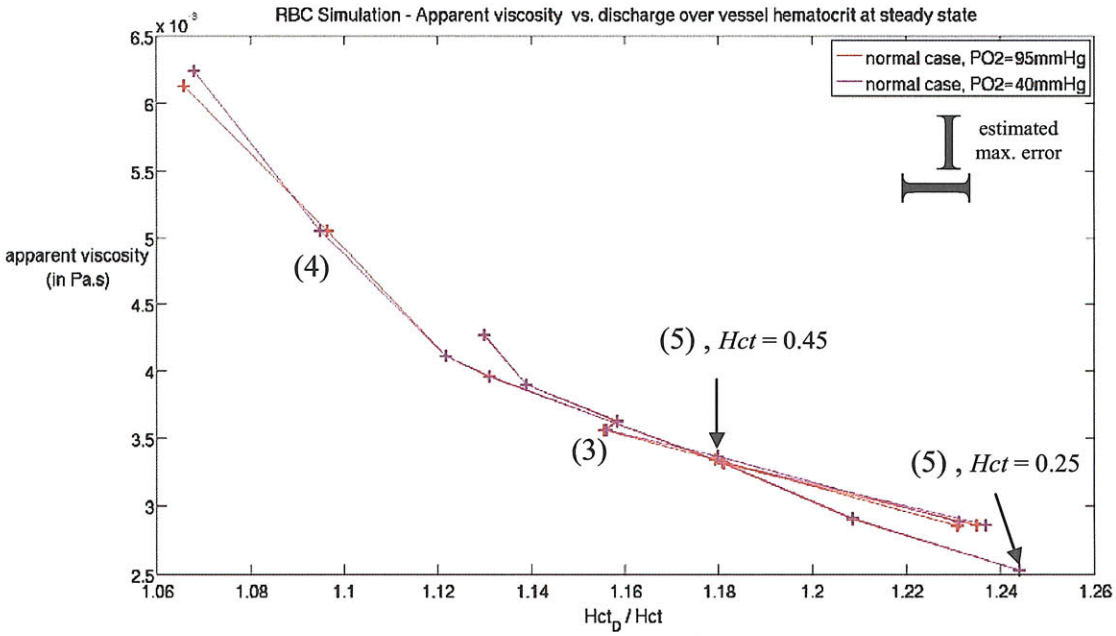


*Figure 3.2.18 : Viscosity vs. hematocrit ratio.*

Figures 3.2.19 and 3.2.20 show the oxygen transfer performance profiles. We see that the lower hematocrit levels lead to a significant decrease in oxygen delivery performance (– 21%), mainly due

to the lack of oxygen supply, even though blood flow is increased. This shows once again the direct relation between ischemia (restriction in blood supply) and hypoxia (shortage of oxygen).

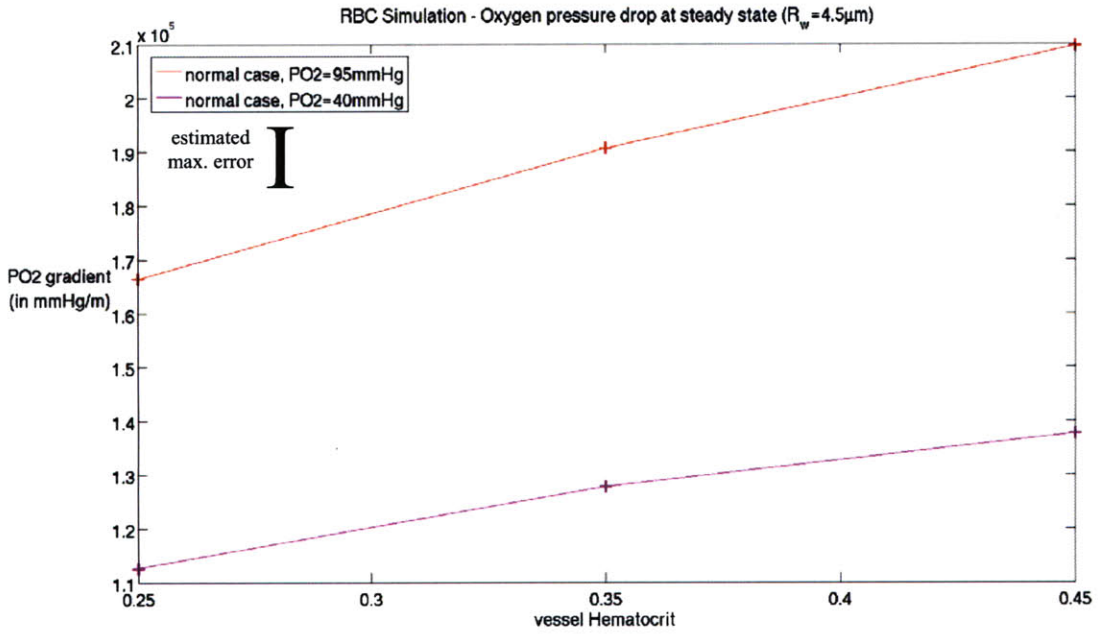


*Figure 3.2.19 : Oxygen partial pressure gradient vs. vessel hematocrit.*

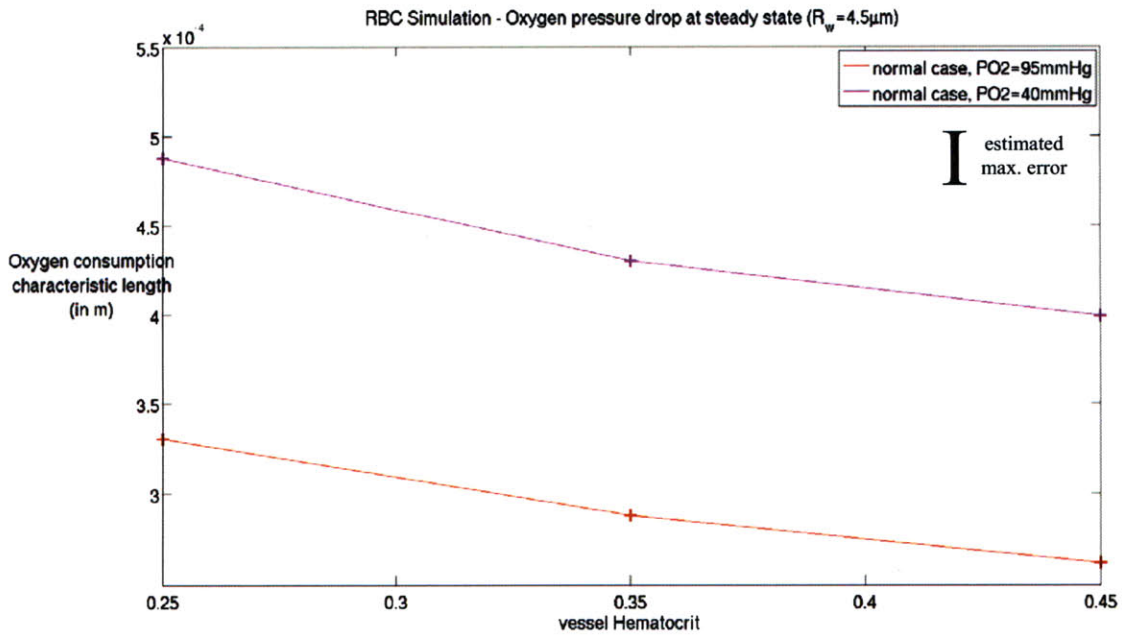


*Figure 3.2.20 : Oxygen partial pressure gradient vs. vessel hematocrit (equivalent vessel length).*

Table 3.2.1 recaps qualitatively the main features of normal blood flow observed in the proposed parametric study. The physical explanations are proposed to explain the trends observed :

(1)- variable vessel radii at constant velocity and hematocrit reflect local changes along a capillary vessel. Since RBCs restrict viscous friction to the lubrication layer, it is expected that larger vessel sizes correspond to lower resistance to the flow and slightly higher RBC velocity relative to the total flow. While at smaller vessel sizes oxygen delivery is limited by diffusion, at larger vessel sizes and at 95 mmHg of oxygen partial pressure convection is the limiting phenomenon.

(2)- variable vessel radii at constant pressure gradient and hematocrit reflect variable vessel size for capillary vessels arranged in parallel. Here the characteristics of the flow follow similar trends as the previous case, amplified by the variations of total blood flow.

(3)- variations of total flow correspond to changes in blood supply, such as possibly due to hyper- and hypotension. Increased blood flow is naturally expected to increase the elastic stresses in RBCs, allowing them to flow faster, with a lower resistance to flowing. At a vessel size corresponding to convection-limited oxygen transfer for a level of 95 mmHg of oxygen, increases in flow velocity decrease the transfer as stiffer diffusion profiles emerge. On the other hand, at 40 mmHg, the diffusion-limited oxygen transfer is very slightly improved by increasing blood flow.

(4)- variations of hematocrit at constant pressure gradient illustrates how the presence of RBCs affect the flow under the same discharge constraints. At higher hematocrit levels the RBCs form trains of cells that can bear the shear stresses and resist blood flow very efficiently, which leads naturally to increased apparent viscosity and decreased RBC velocity. Oxygen transfer is also directly related to the absolute concentration of oxygen carriers (hemoglobin), and increases with the hematocrit.

the wall. Figure 3.3.2 shows the same results as Figure 3.3.1 at a constant pressure gradient (cases 4c and 4a/4b). As we see, under low velocity flow the sickling RBC shape deteriorates considerably and may obstruct the flow very differently. For vessel sizes below $R_w$ = 4 μm our algorithm leads to form secondary "corners", as the polymerizing structure starts to fold onto itself. Without even considering reorganization of the polymerized hemoglobin, we have already an illustration of how sickled cells may come to completely obstruct the flow, even at the individual level. Also, for vessel sizes below $R_w$ = 3.5 μm the resulting RBC is found to reach computational limits, as it gets as close as one numerical cell from the capillary wall. In the following analysis, we will therefore mention these last results with caution (unconnected points and/or dashed lines).

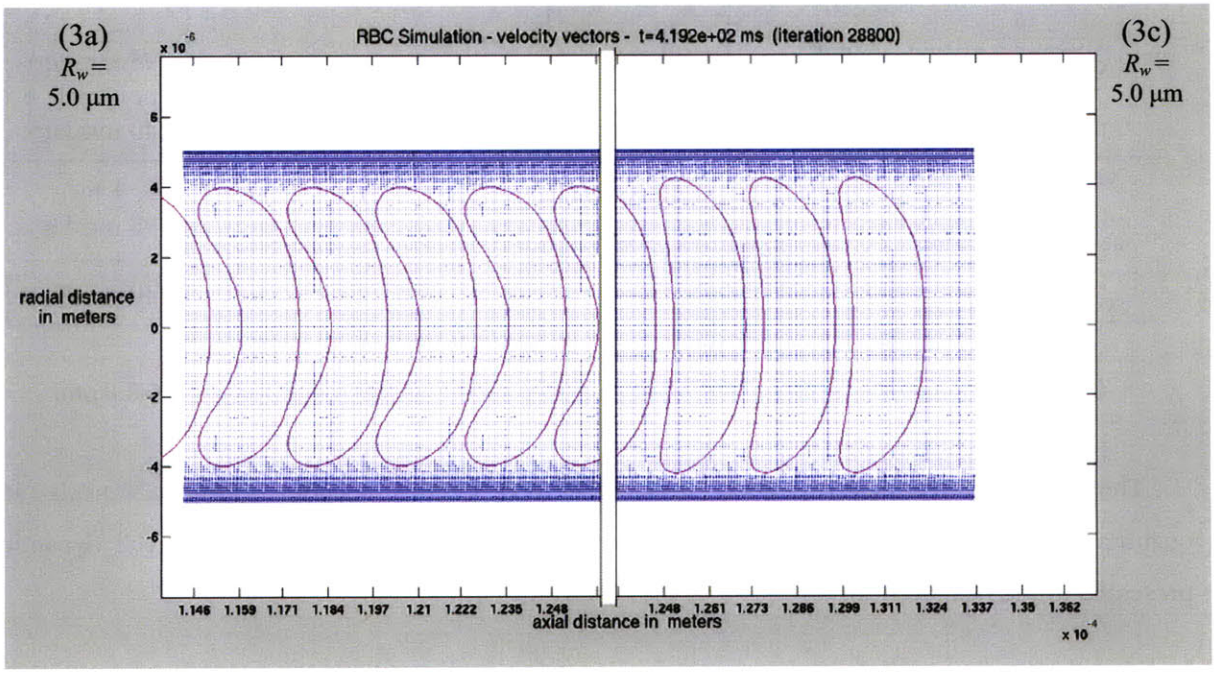

the wall. Figure 3.3.2 shows the same results as Figure 3.3.1 at a constant pressure gradient (cases 4c and 4a/4b). As we see, under low velocity flow the sickling RBC shape deteriorates considerably and may obstruct the flow very differently. For vessel sizes below $R_w$ = 4 μm our algorithm leads to form secondary "corners", as the polymerizing structure starts to fold onto itself. Without even considering reorganization of the polymerized hemoglobin, we have already an illustration of how sickled cells may come to completely obstruct the flow, even at the individual level. Also, for vessel sizes below $R_w$ = 3.5 μm the resulting RBC is found to reach computational limits, as it gets as close as one numerical cell from the capillary wall. In the following analysis, we will therefore mention these last results with caution (unconnected points and/or dashed lines).

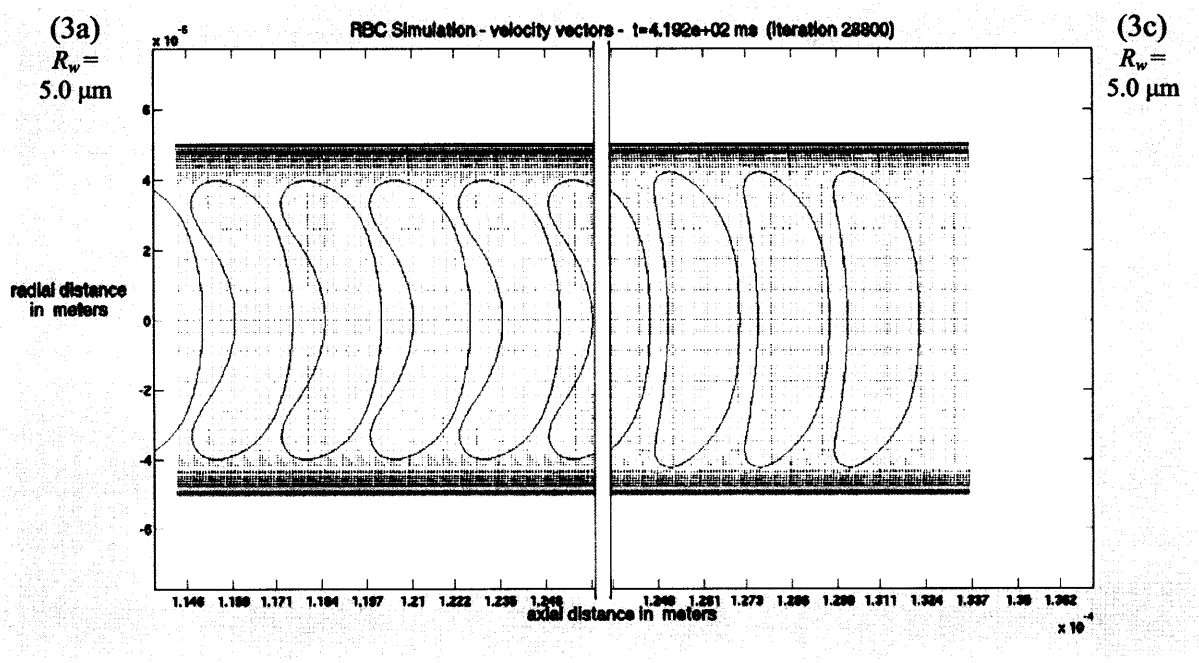

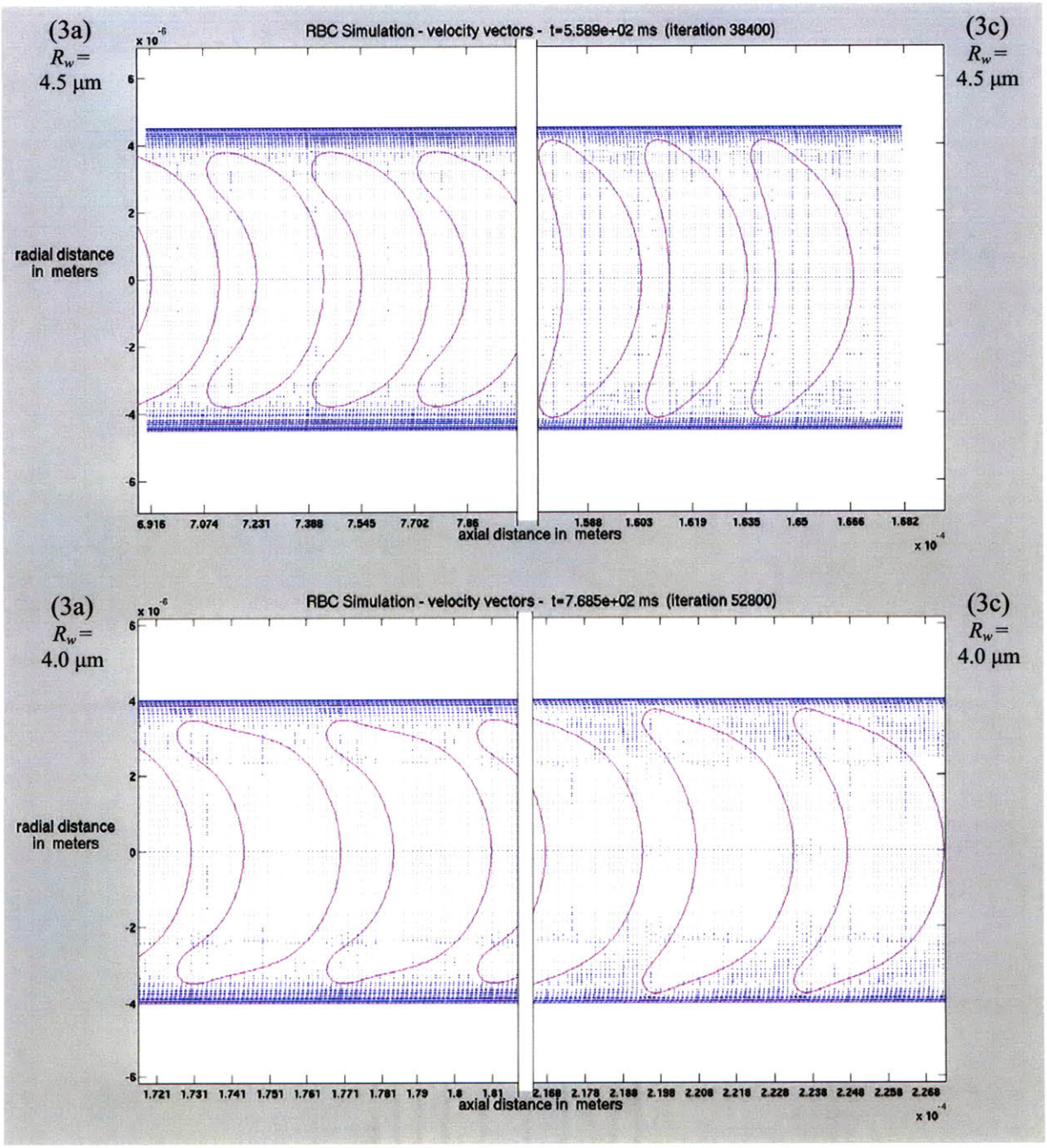
(3a)
$R_w$ = 4.5 μm
RBC Simulation - velocity vectors - t=5.589e+02 ms (iteration 38400)
(3c)
$R_w$ = 4.5 μm
radial distance in meters
axial distance in meters
(3a)
$R_w$ = 4.0 μm
RBC Simulation - velocity vectors - t=7.685e+02 ms (iteration 52800)
(3c)
$R_w$ = 4.0 μm
radial distance in meters
axial distance in meters

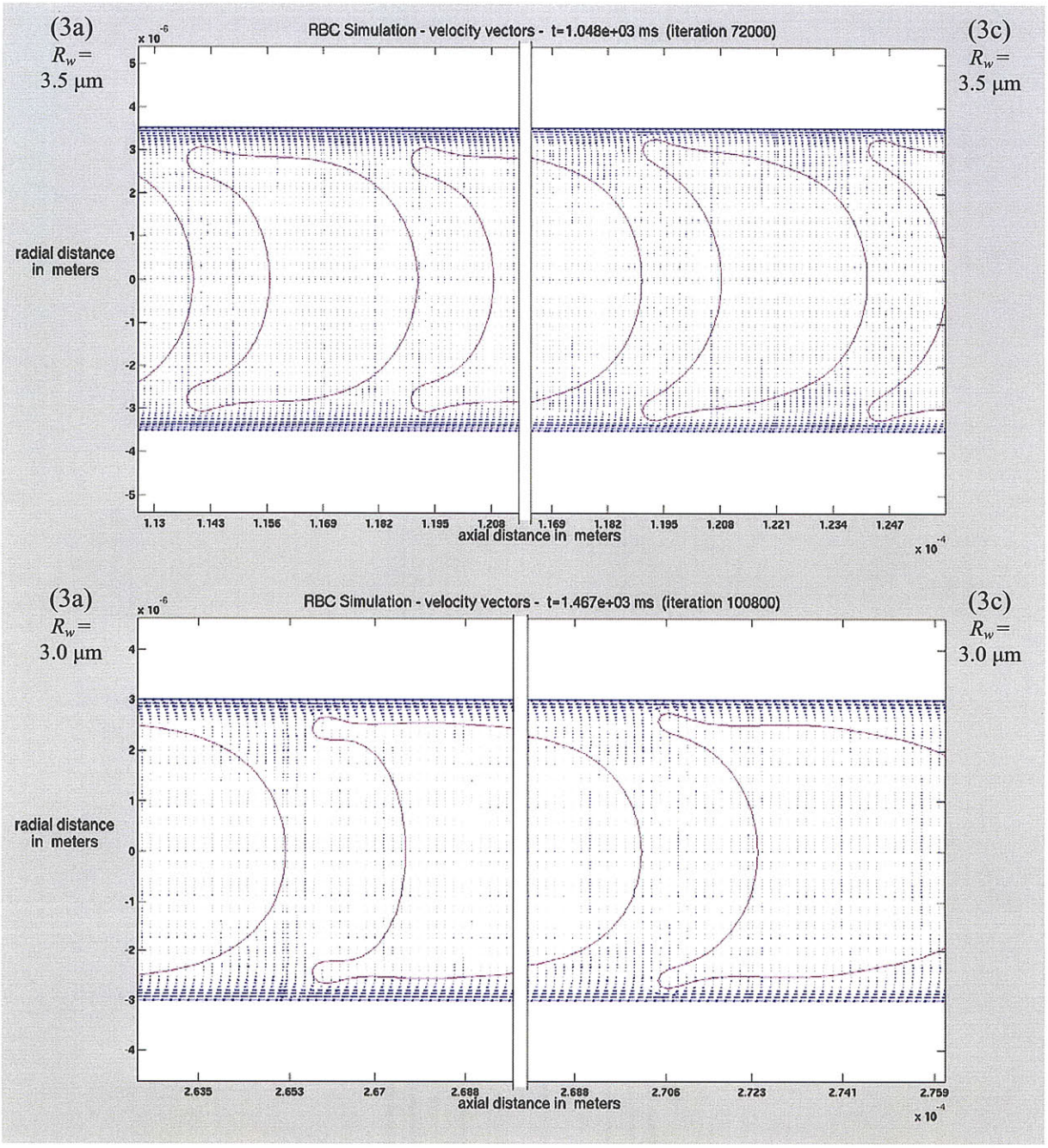


*Figure 3.3.1 : Compared steady state RBC shapes (left: normal ; right: sickle).*

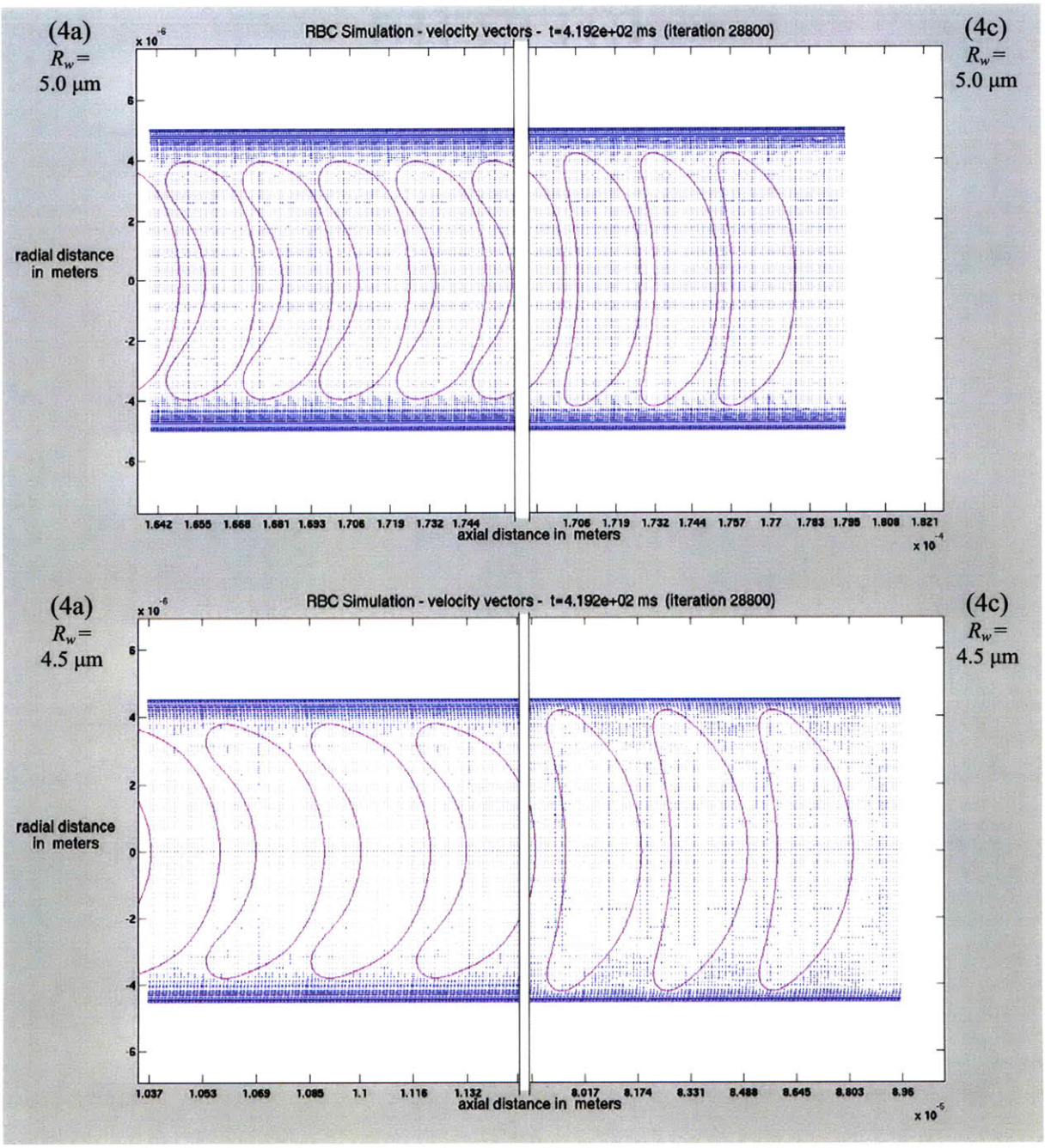
(4a)
$R_w$=
5.0 μm
RBC Simulation - velocity vectors - t=4.192e+02 ms (iteration 28800)
(4c)
$R_w$=
5.0 μm
radial distance
in meters
x 10^-6
6
4
2
0
-2
-4
-6
1.642 1.655 1.668 1.681 1.693 1.706 1.719 1.732 1.744
1.706 1.719 1.732 1.744 1.757 1.77 1.783 1.795 1.808 1.821
axial distance in meters
x 10^-4
(4a)
$R_w$=
4.5 μm
RBC Simulation - velocity vectors - t=4.192e+02 ms (iteration 28800)
(4c)
$R_w$=
4.5 μm
radial distance
in meters
x 10^-6
6
4
2
0
-2
-4
-6
1.037 1.053 1.069 1.085 1.1 1.116 1.132
8.017 8.174 8.331 8.488 8.645 8.803 8.96
axial distance in meters
x 10^-5

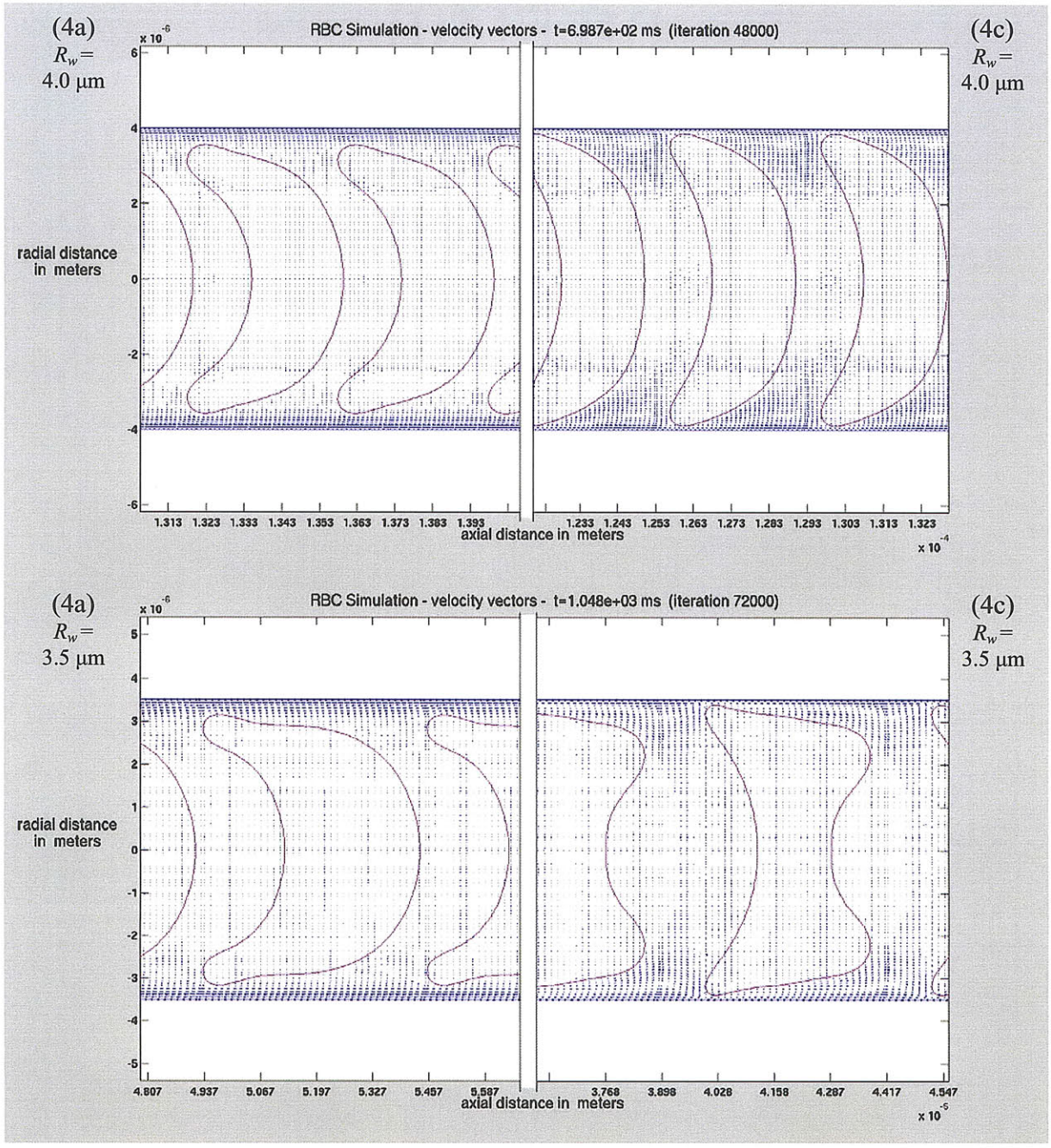
(4a)
$R_w$= 4.0 μm
RBC Simulation - velocity vectors - t=6.987e+02 ms (iteration 48000)
(4c)
$R_w$= 4.0 μm
radial distance in meters
axial distance in meters
(4a)
$R_w$= 3.5 μm
RBC Simulation - velocity vectors - t=1.048e+03 ms (iteration 72000)
(4c)
$R_w$= 3.5 μm
radial distance in meters
axial distance in meters

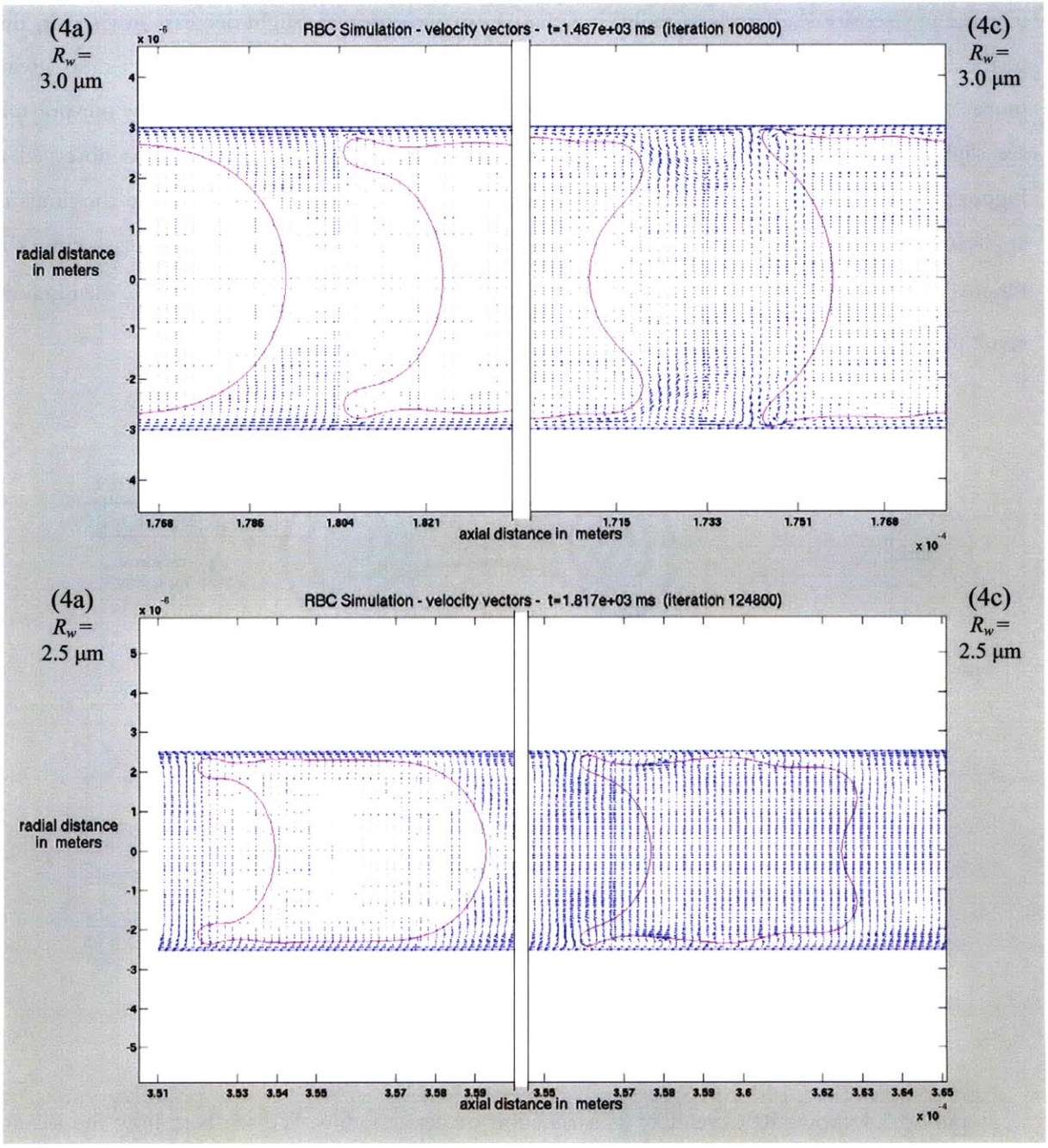


*Figure 3.3.2 : Compared steady state RBC shapes (left: normal ; right: sickle).*

Figure 3.3.3 shows the apparent viscosity as a function of vessel size. As expected, we see for all cases a significant increase in viscosity in the sickle case. In the case of constant velocity, between the radii of 4 μm and 5 μm the apparent viscosity is always about 1.5 times higher than normal blood, which follows the experimental observations of Chien, Usami and Bertles [62] and validates the use of this value to set the baseline case. In the case of constant pressure gradient, we also observe a large

increase in viscosity. At vessels of radius less than 4 μm, we observe a slight decrease in viscosity due to the fact that the RBC gets squeezed and gets forced into a shape of smaller aspect ratio, giving more "space" for the hemoglobin polymer to stretch (i.e. the lateral forces generated by our polymer are slightly less important) We observe also secondary folding features in case 4 as observed in Figure 3.3.2,. Since the obtained shapes become arguable, and are likely to go beyond the limits of application of our model, we report these data points as dashed parts of the sickle case curves in Figure 3.3.3. In the case (4c) for $R_w$ = 3 μm, although the result is numerically arguable, the obtained result may be interpreted as an upper bound for the resistance to the flow.

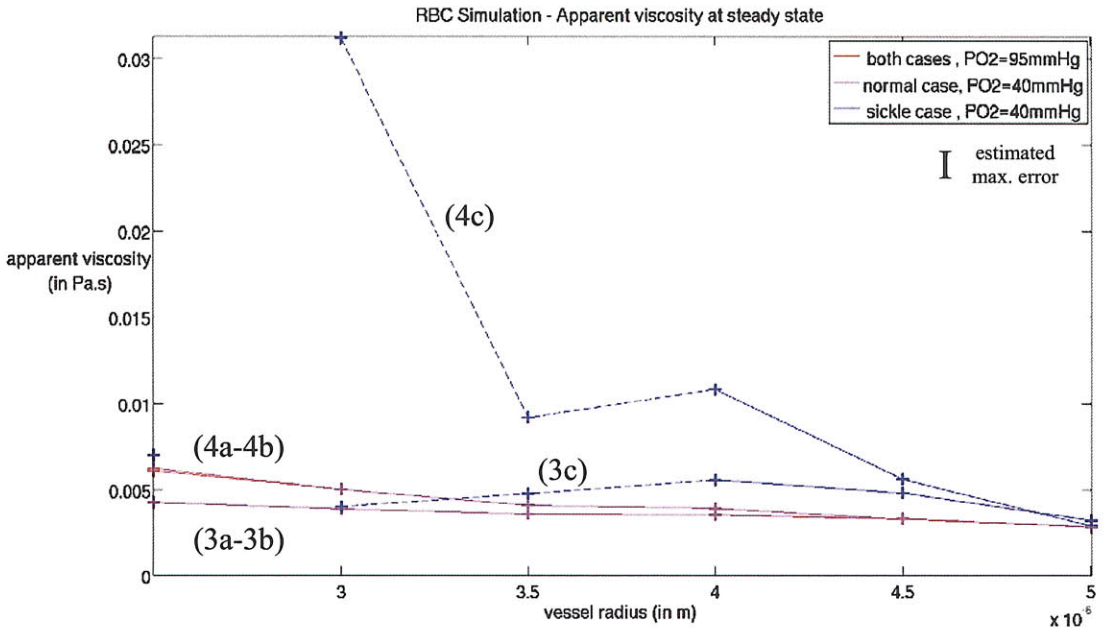


*Figure 3.3.3 : Apparent viscosity vs. vessel size.*

Figure 3.3.4 shows RBC velocity as a function of vessel radius. We see here how the sickling results in significant decreases in RBC velocity, even in the case of imposed flow velocity. This is easily understood by the decrease of the lubrication layer between RBC and capillary wall. In the constant pressure gradient cases (4), for vessel sizes between 3.5 μm and 4.5 μm, the RBC velocity decrease represents 50% to 70% of the value for normal blood cells. Figure 3.3.4 illustrates the "vicious cycle" described previously by Berger. Sickling RBCs resist more and more the flow as they deoxygenate, which in turn makes them slow down, lose more oxygen, sickle more, and so on until the RBC vessels get blocked.

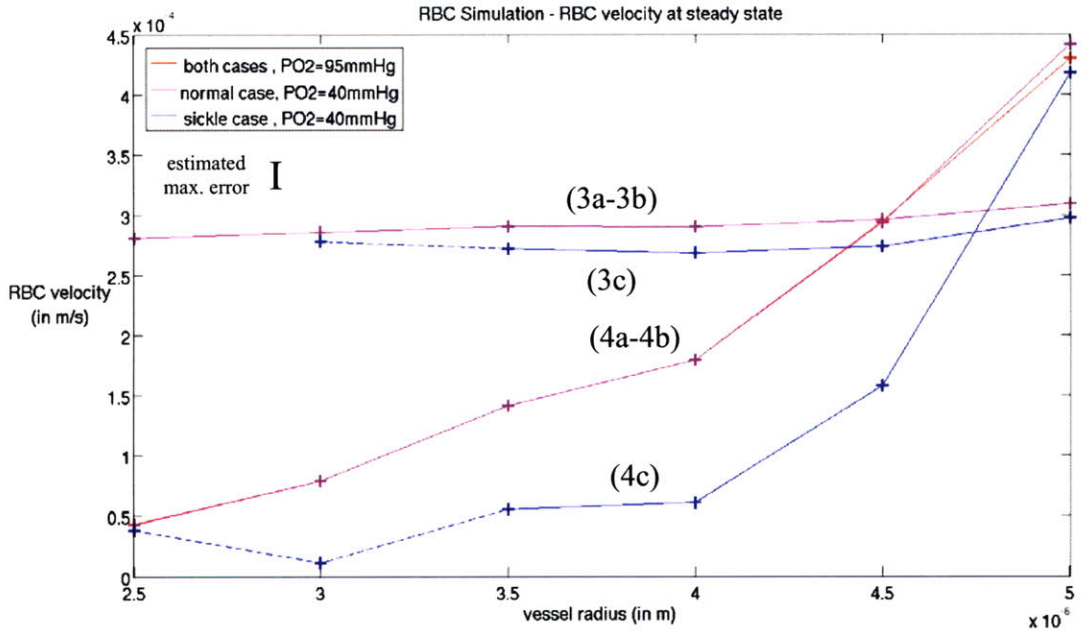


*Figure 3.3.4 : RBC velocity vs. vessel size.*

Figure 3.3.5 shows the discharge hematocrit as a function of vessel size. The decreased RBC velocity in the sickle cases observed previously leads to a significant reduction in flowing hematocrit. For vessel sizes below 4 μm, we notice that the shape changes shown previously lead to less stresses from the hemoglobin polymer, and may decrease this effect.

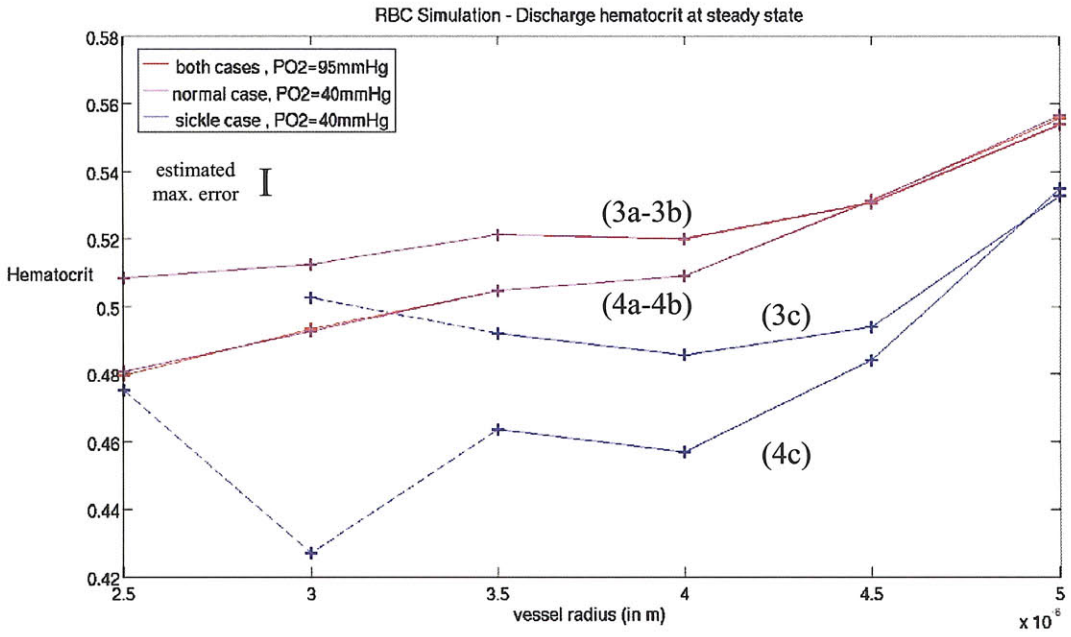


*Figure 3.3.5 : Discharge hematocrit vs. vessel size.*

Figure 3.3.6 shows the apparent viscosity as a function of discharge hematocrit. We observe here a quasi-perfect correlation between the two variables along one curve, for all cases 3 and 4. The relationship between apparent viscosity and discharge hematocrit is therefore a purely hydrodynamic behavior of our model, independent of the sickling characteristics of RBCs. All the changes in resistance to blood flow are directly related to how much the RBC obstructs the flow and how fast cells flow compared to the total blood flow. Interestingly, even the most arguable sickle cases leading to deformed RBCs fit very well on the curve, as does the case 4c with $R_w$ = 3 μm (point far on the upper left side).

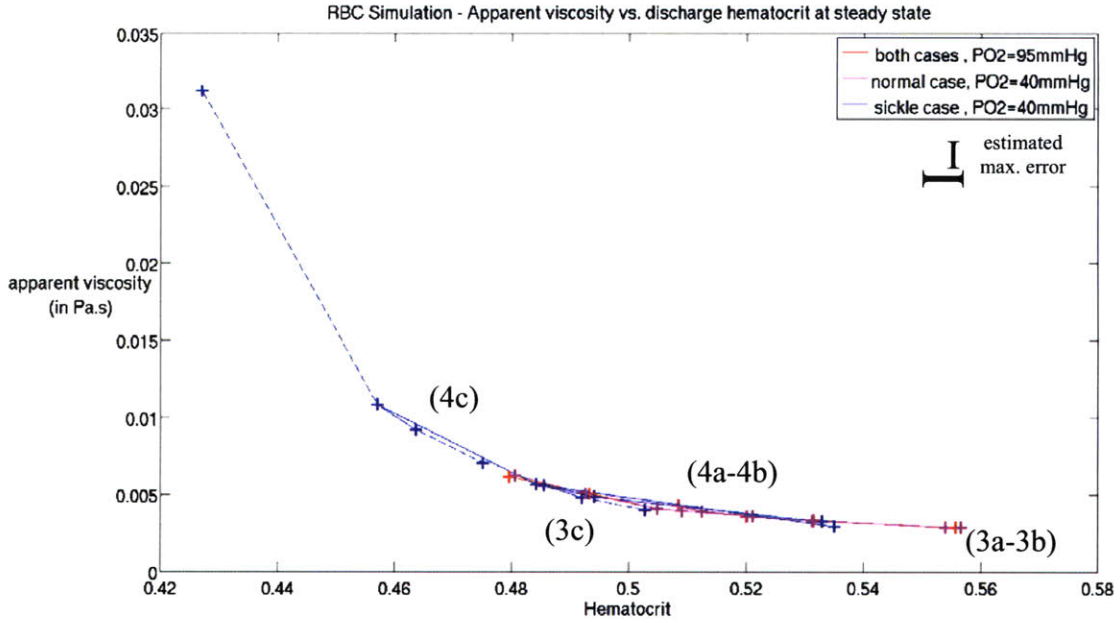


*Figure 3.3.6 : Apparent viscosity vs. discharge hematocrit.*

Comparison between oxygen profiles between cases 3b and 3c is shown in Figure 3.3.7, and between cases 4b and 4c in Figure 3.3.8. We see that for all cases sickling RBCs lead to a stretching of the contour plots, indicating the lower RBC velocity, increased diffusion in comparison, and overall less effective oxygen transfer to the surrounding tissue. Since the sickling RBCs are closer to the capillary wall, they are more likely to transfer oxygen closer to the capillary walls, and the oxygen profiles are therefore steeper. On the other hand, oxygen delivery becomes less homogeneous with higher-oxygen regions at the sickling RBC corners, creating distorted oxygen profiles likely to transport oxygen less efficiently (this is particularly visible on Figure 3.3.7 for $R_w$ = 4.0 μm). Diffusion is increased here, but not homogeneously and since convection is reduced (RBC velocity is lower), the overall oxygen transfer is reduced compared to normal cases.

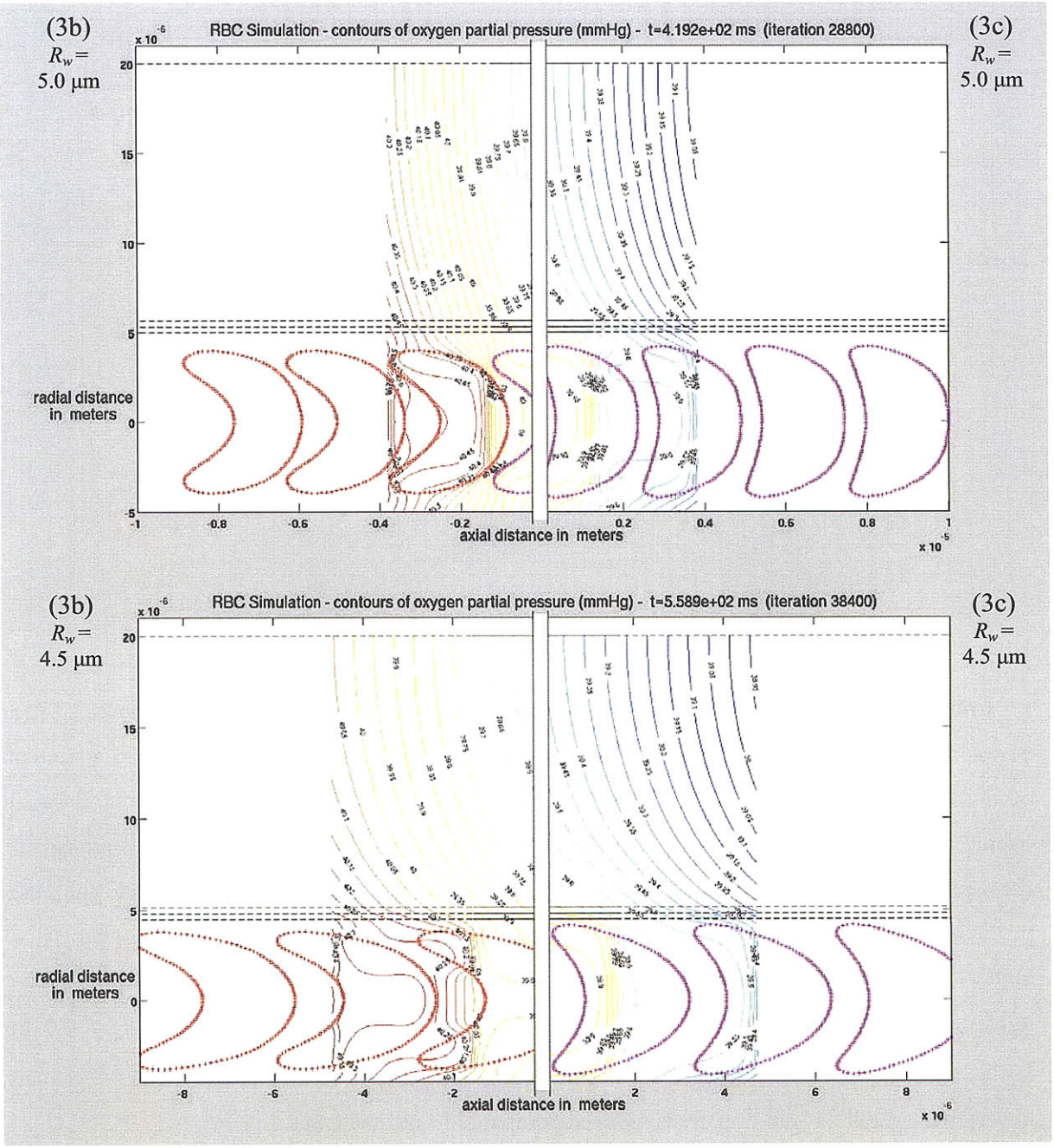
(3b)
$R_w$=
5.0 μm
RBC Simulation - contours of oxygen partial pressure (mmHg) - t=4.192e+02 ms (iteration 28800)
(3c)
$R_w$=
5.0 μm
radial distance
in meters
axial distance in meters
(3b)
$R_w$=
4.5 μm
RBC Simulation - contours of oxygen partial pressure (mmHg) - t=5.589e+02 ms (iteration 38400)
(3c)
$R_w$=
4.5 μm
radial distance
in meters
axial distance in meters

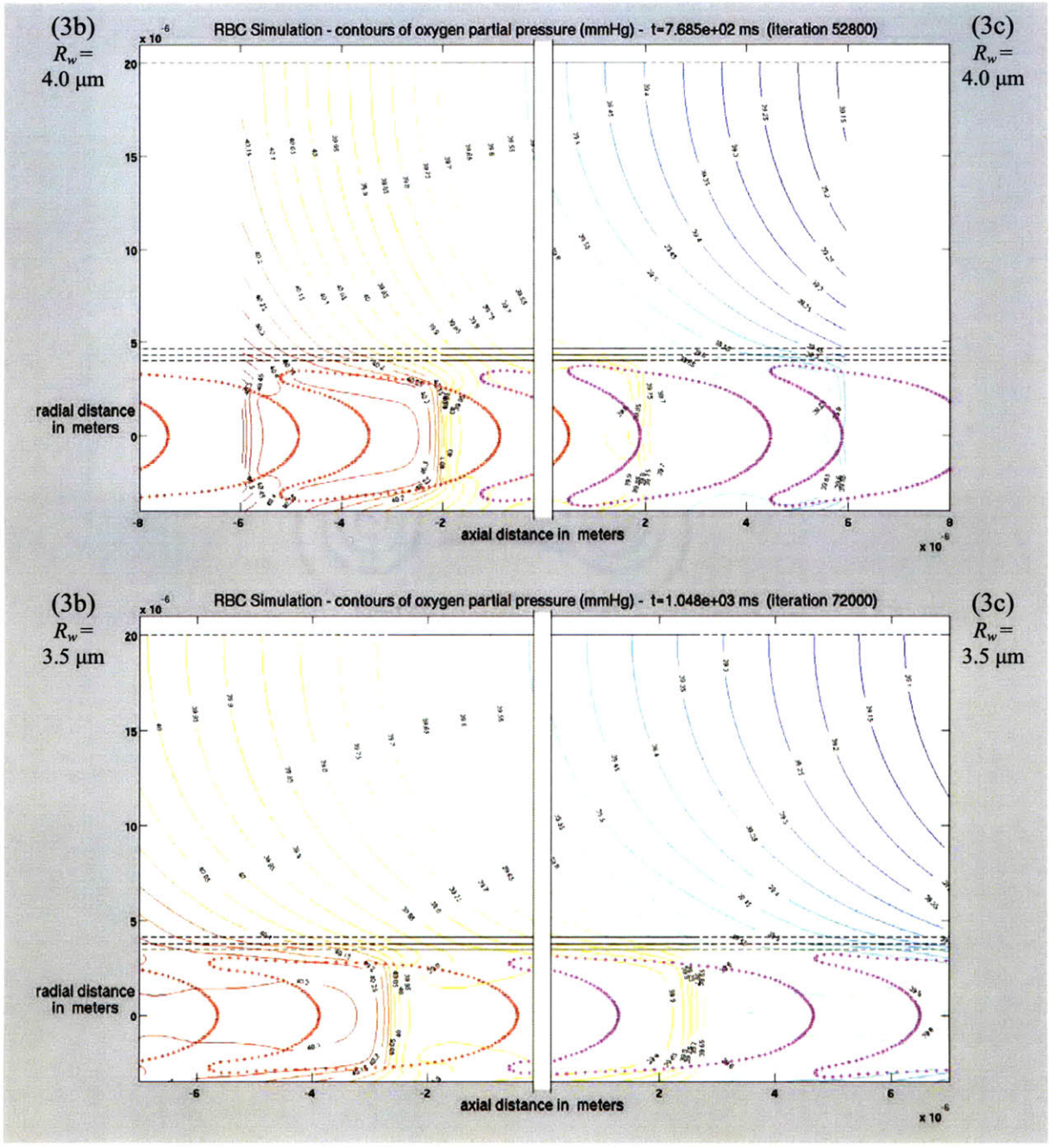
(3b)
$R_w$ = 4.0 μm
RBC Simulation - contours of oxygen partial pressure (mmHg) - t=7.685e+02 ms (iteration 52800)
(3c)
$R_w$ = 4.0 μm
radial distance in meters
axial distance in meters
(3b)
$R_w$ = 3.5 μm
RBC Simulation - contours of oxygen partial pressure (mmHg) - t=1.048e+03 ms (iteration 72000)
(3c)
$R_w$ = 3.5 μm
radial distance in meters
axial distance in meters

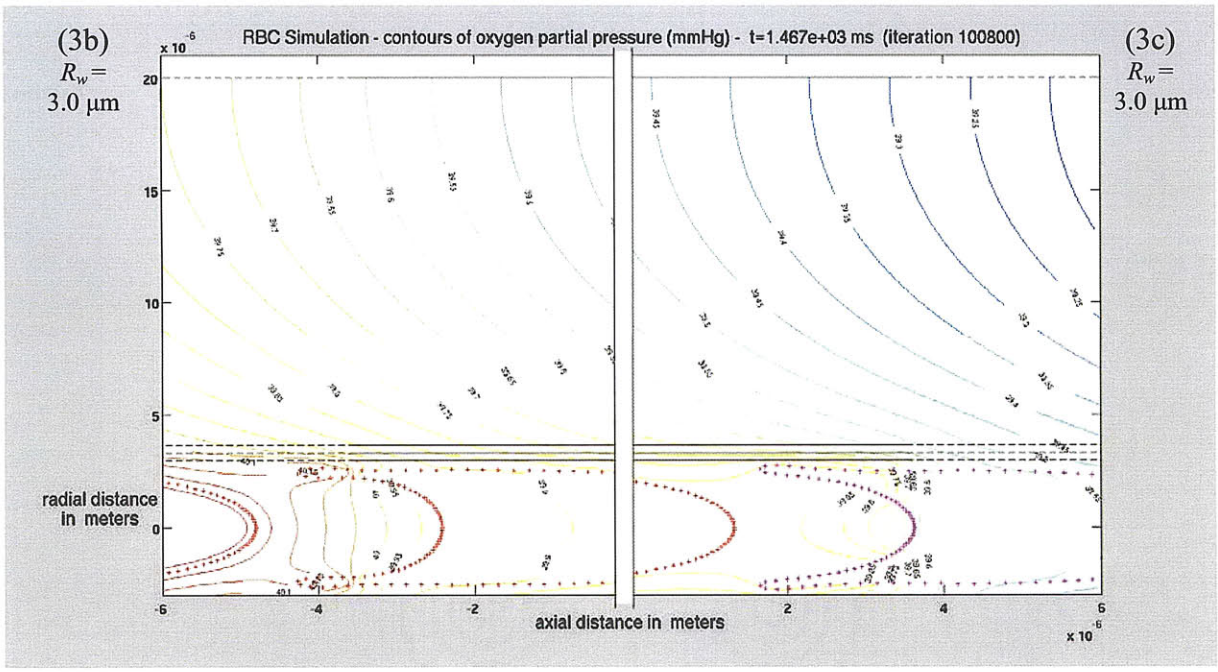


*Figure 3.3.7 : Comparison of oxygen partial pressure levels (left: normal ; right: sickle).*

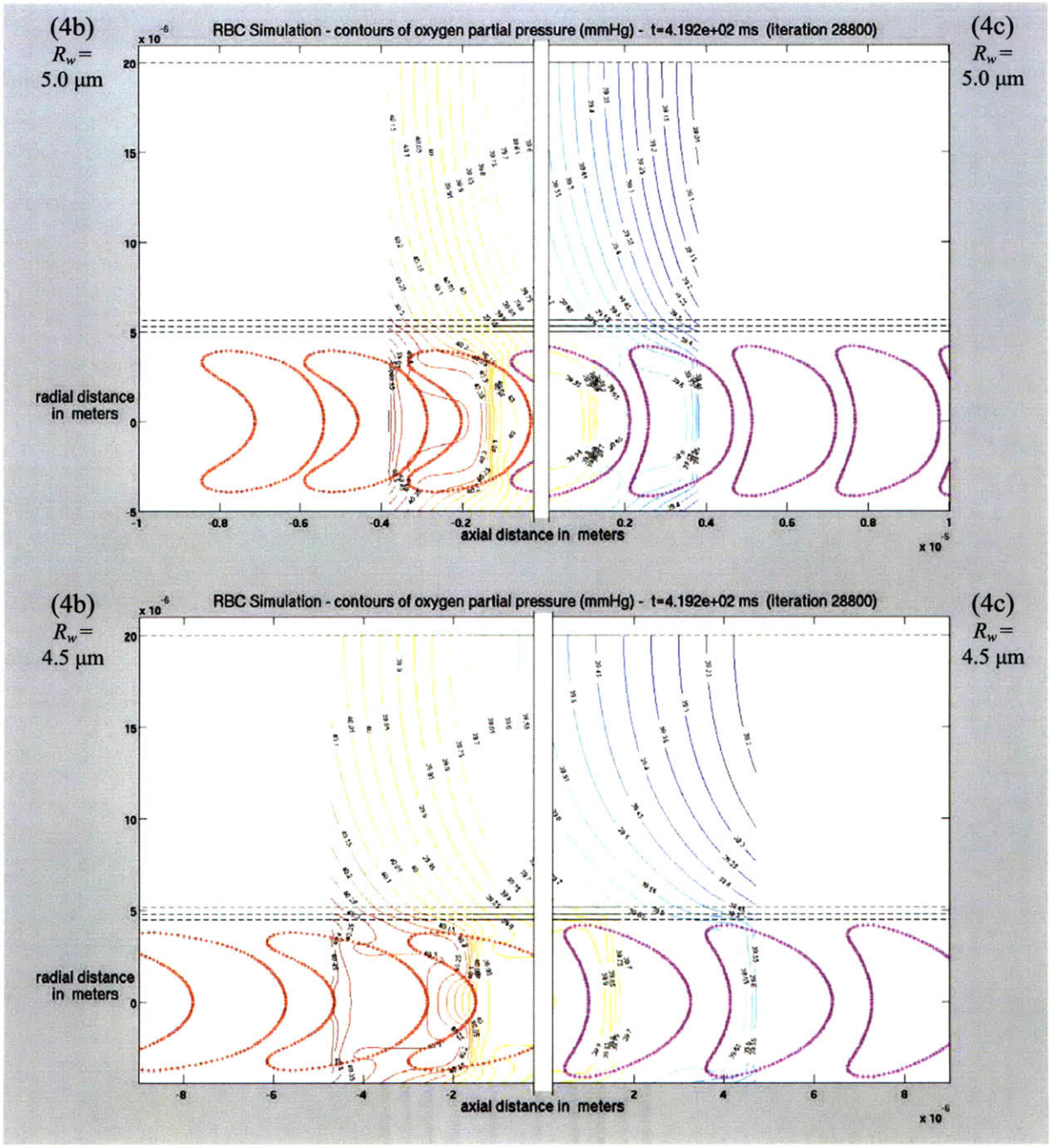
(4b)
$R_w$ = 5.0 μm
RBC Simulation - contours of oxygen partial pressure (mmHg) - t=4.192e+02 ms (iteration 28800)
(4c)
$R_w$ = 5.0 μm
radial distance in meters
axial distance in meters
(4b)
$R_w$ = 4.5 μm
RBC Simulation - contours of oxygen partial pressure (mmHg) - t=4.192e+02 ms (iteration 28800)
(4c)
$R_w$ = 4.5 μm
radial distance in meters
axial distance in meters

(4b)
$R_w$ = 4.0 μm

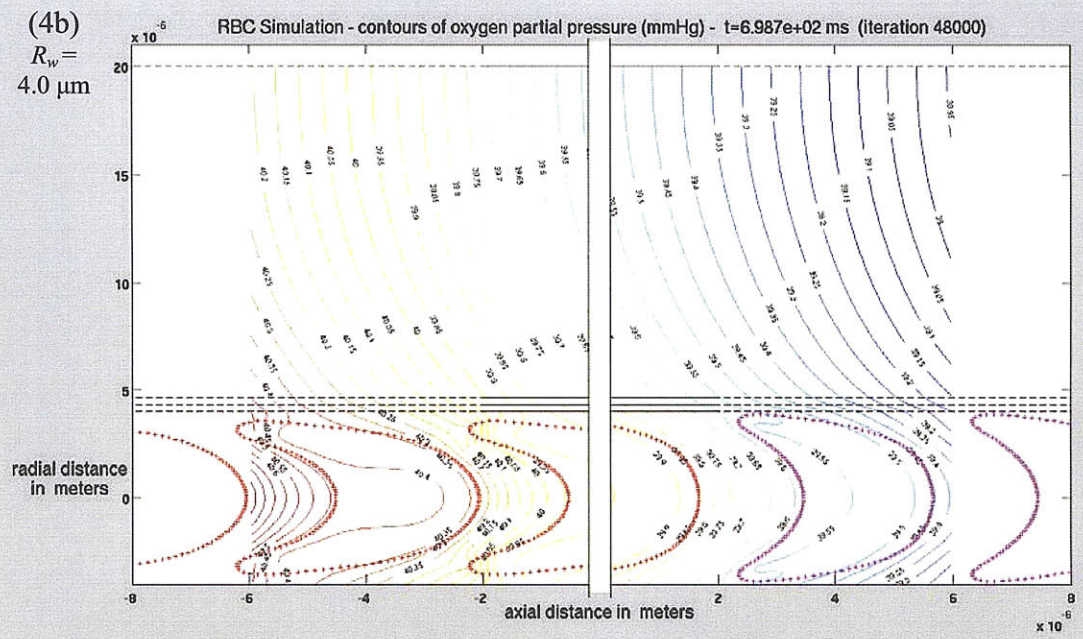


(4c)
$R_w$ = 4.0 μm

(4b)
$R_w$ = 3.5 μm

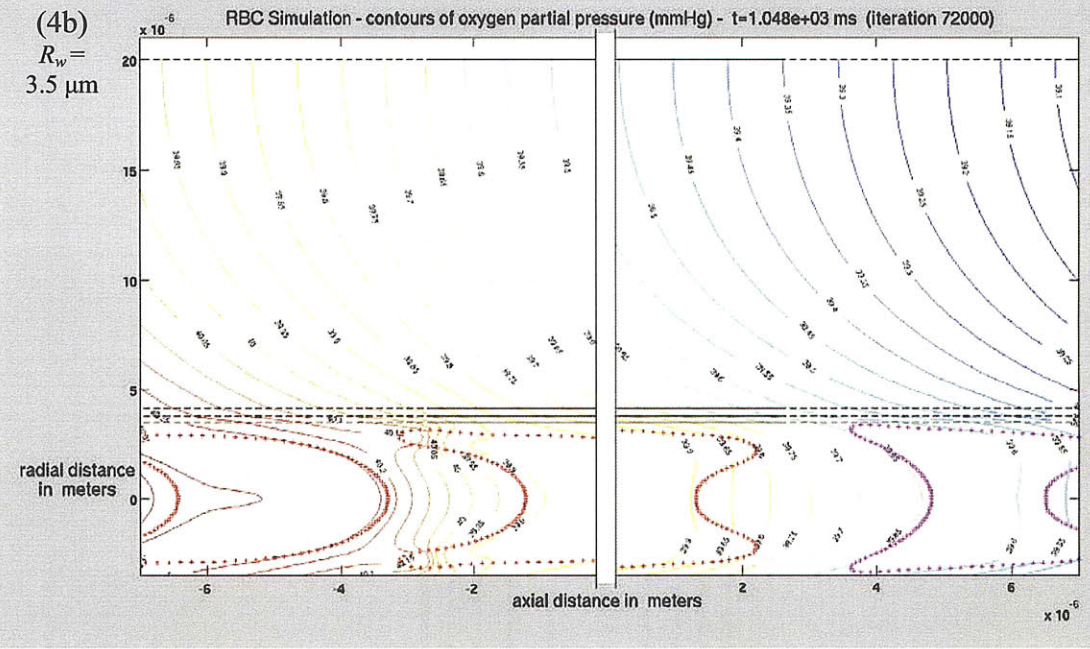


(4c)
$R_w$ = 3.5 μm

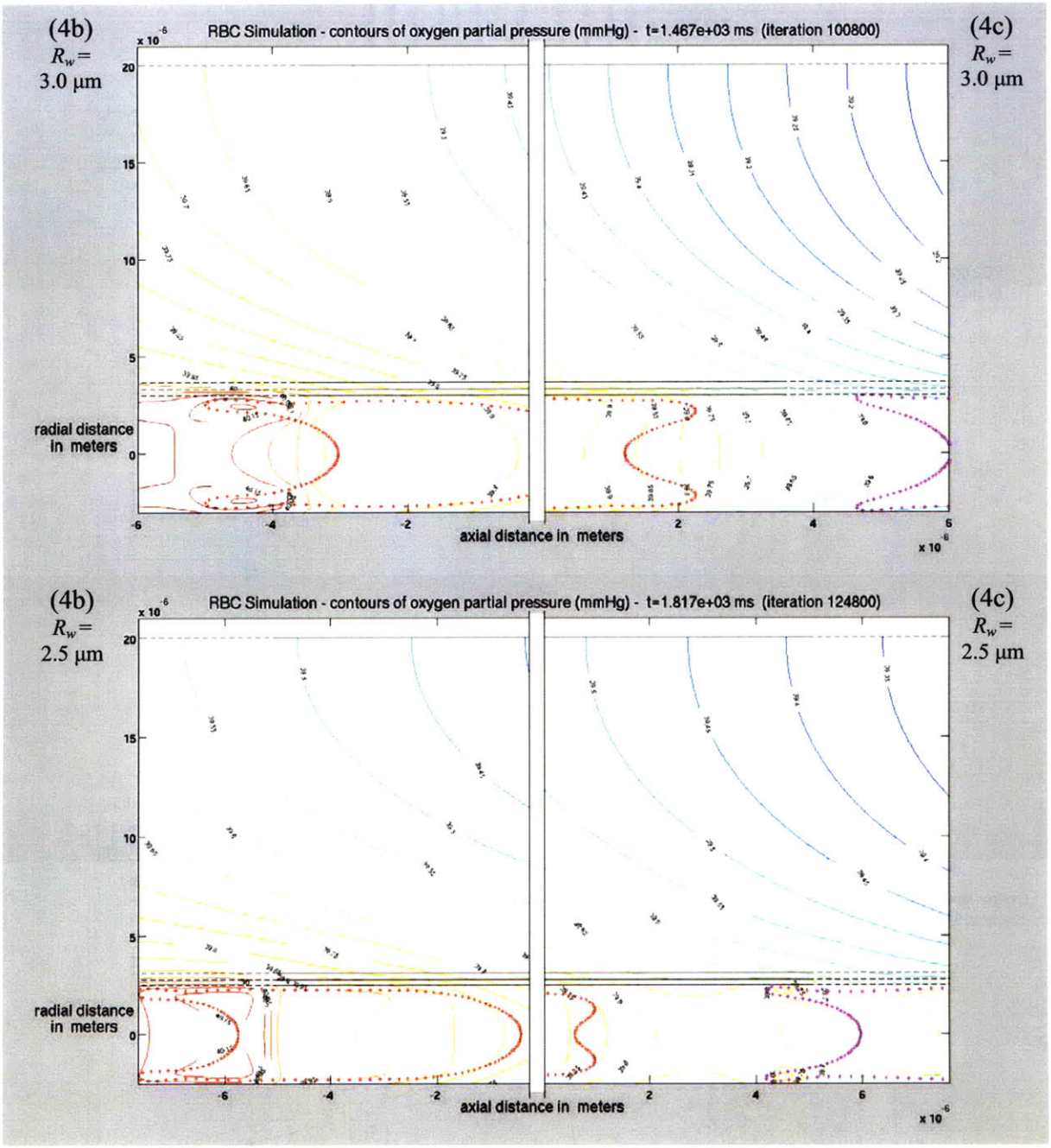


*Figure 3.3.8 : Comparison of oxygen partial pressure levels (left: normal ; right: sickle).*

Figure 3.3.9 and Figure 3.3.10 show the oxygen partial pressure gradients for the sickle cases. We see here quantitatively how sickled cells lead to lower oxygen gradients. The oxygen delivery, compared between normal and sickle cases at 40 mmHg (cases "b" and "c"), at radius 5 μm drops from about $1.7.10^5$ mmHg/m to $1.4.10^5$ mmHg/m (– 18%), and at radius 3.5 μm from about $0.75.10^5$ mmHg/m to $0.5.10^5$ mmHg/m (– 33%).

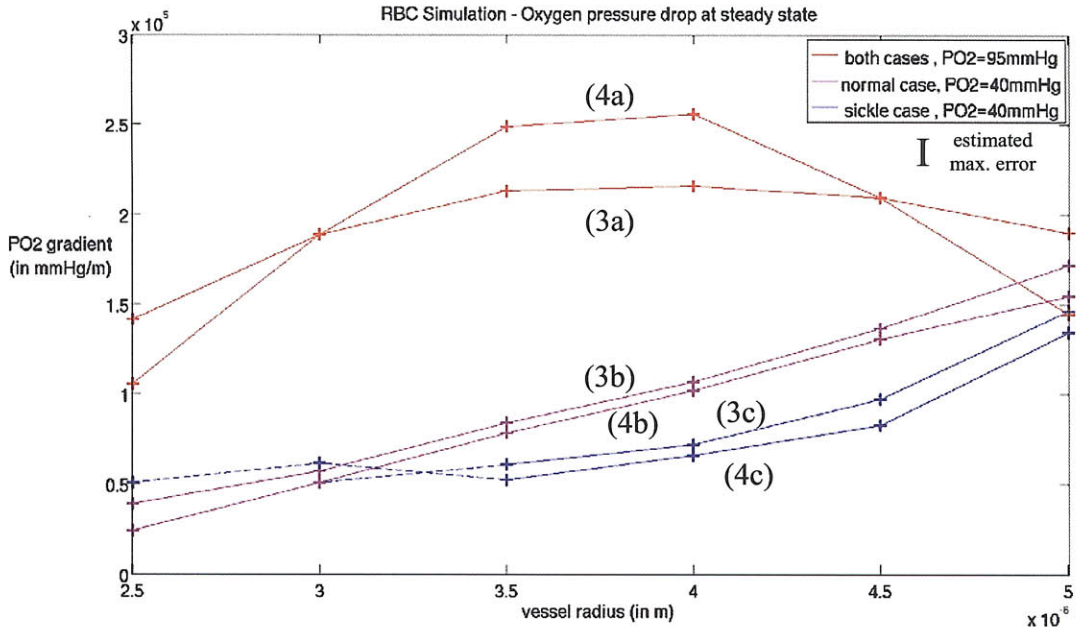


*Figure 3.3.9 : Oxygen partial pressure gradient vs. vessel size.*

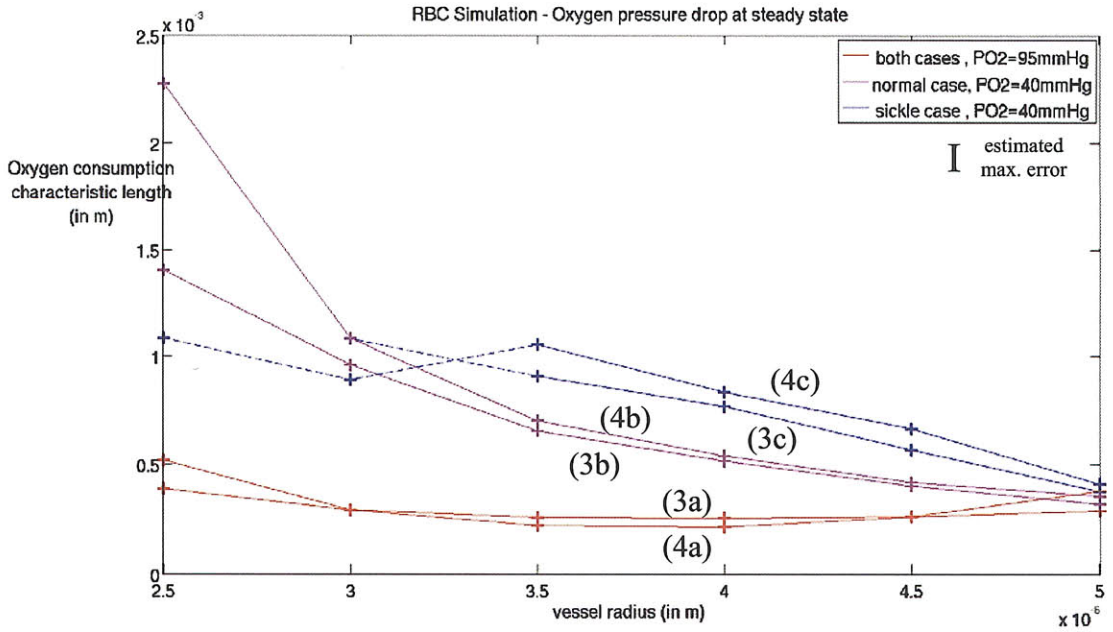


*Figure 3.3.10 : Oxygen partial pressure gradient vs. vessel size (equivalent vessel length).*

Figures 3.3.11, 3.3.12, 3.3.13 and 3.3.14 show the analysis of RBC dynamics for case 2 including the sickle cell model. We observe that :

(1)- the apparent viscosity of blood is considerably increased in the sickle case, for all the flow velocities considered. With a vessel radius $R_w$ = 4.5 μm, the ratio of viscosities between the normal and sickle case is also found to decrease a little with decreasing flow velocities, from 1.5 at $\overline{v}_{in}$ = $2.5.10^{-4}$ m/s, to approximately 1.25 at $\overline{v}_{in}$ = $6.25.10^{-5}$ m/s.

(2)- RBC velocity remains fairly well correlated with average flow velocity, with a small relative difference at the parametric values considered. Sickle cases lead to a slight decrease in the RBC velocity for all cases.

(3)- the discharge hematocrit is found to be significantly reduced in the sickle case, which is obviously due to the reduced lubrication layer. The reduction in hematocrit value goes approximately from 0.03 at $\overline{v}_{in}$ = $2.5.10^{-4}$ m/s, to 0.02 at $\overline{v}_{in}$ = $6.25.10^{-5}$ m/s.

(4)- the relationship between viscosity and discharge hematocrit remains unchanged, and follows the same curve as observed for cases 3 and 4. Sickle cases have both a higher apparent viscosity and discharge hematocrit.

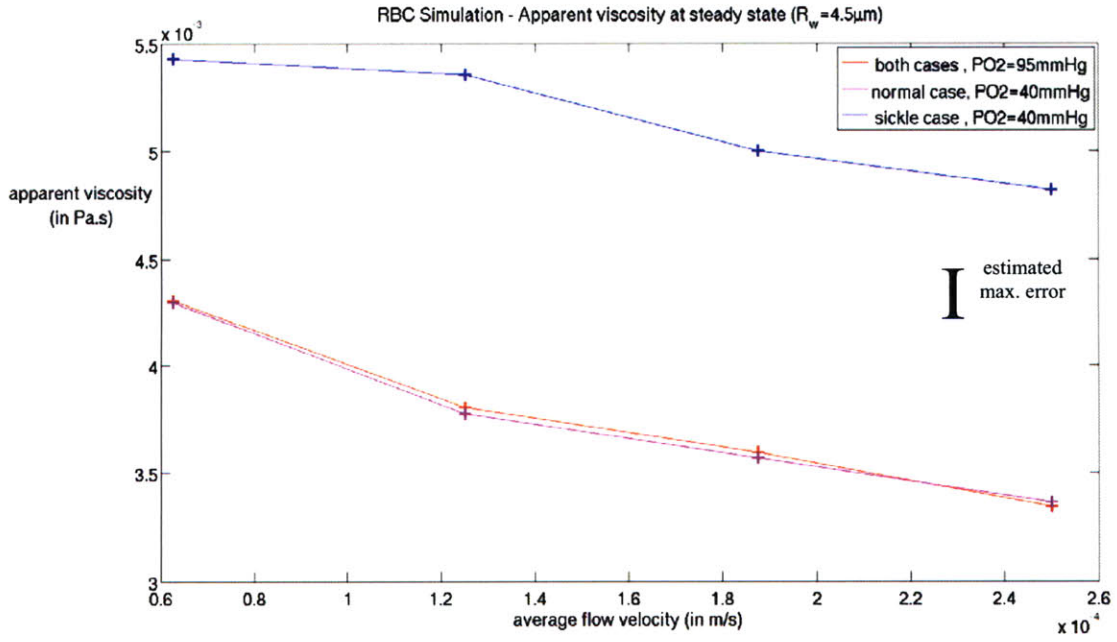


*Figure 3.3.11 : Viscosity vs. average flow velocity.*

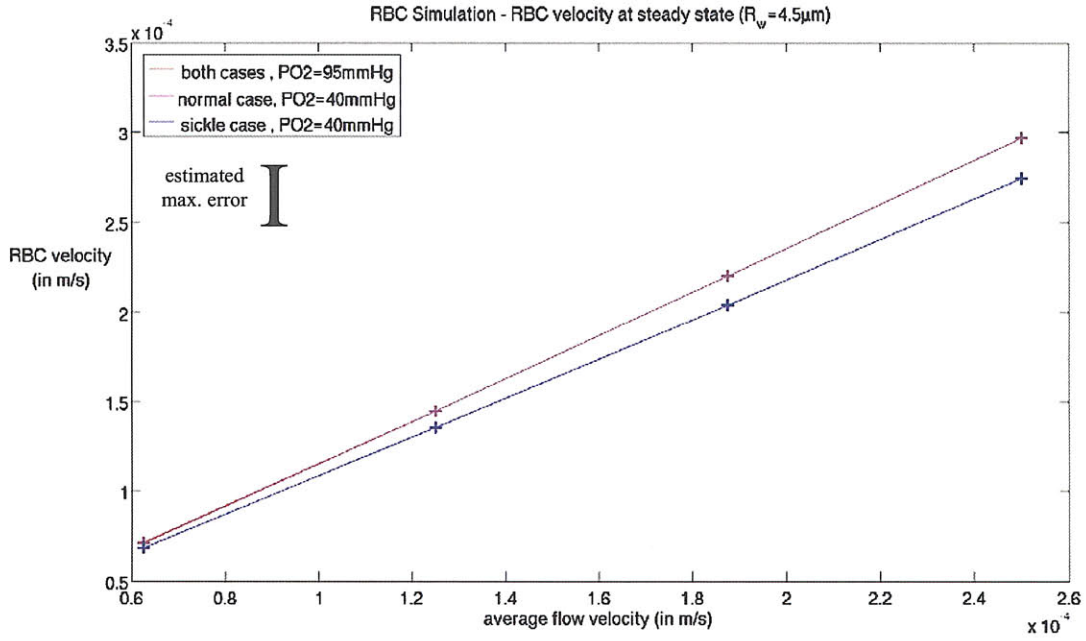


*Figure 3.3.12 : RBC velocity vs. average flow velocity.*

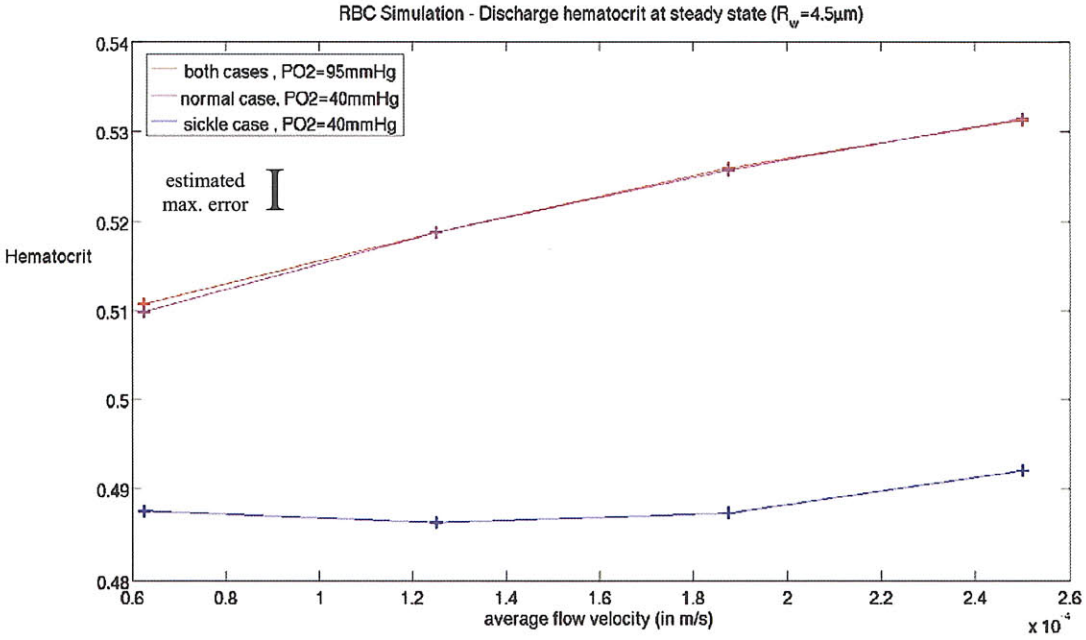


*Figure 3.3.13 : Discharge hematocrit vs. average flow velocity.*

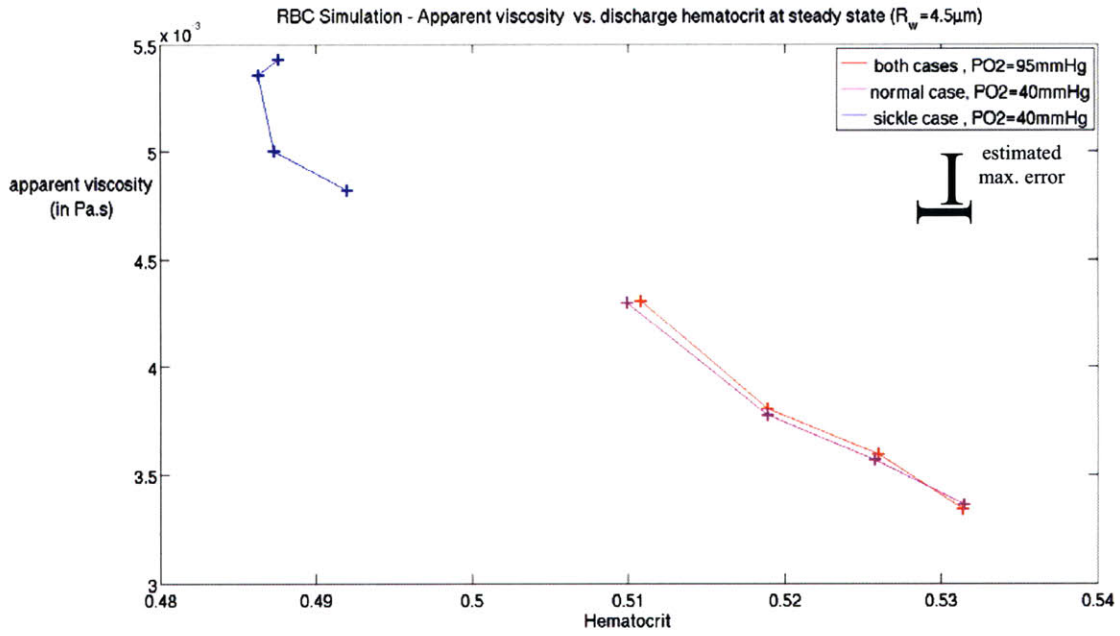


*Figure 3.3.14 : Viscosity vs. discharge hematocrit.*

Figures 3.3.15 and 3.3.16 present the analysis of oxygen delivery for the same case. Our results show how sickling RBCs have worse oxygen transfer performance than normal cells. Especially at a low oxygen level of $p_{O_2,in}$ = 40 mmHg, the already diffusion-limited oxygen transport to the surrounding tissue is even more reduced by sickling.

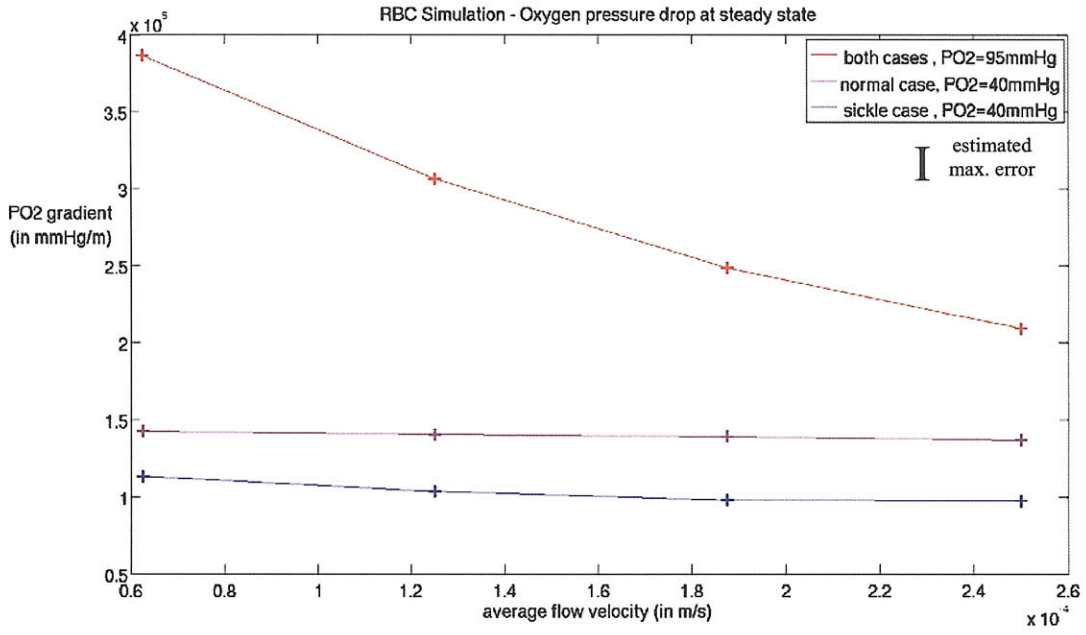


*Figure 3.3.15 : Oxygen partial pressure gradient vs. average flow velocity.*

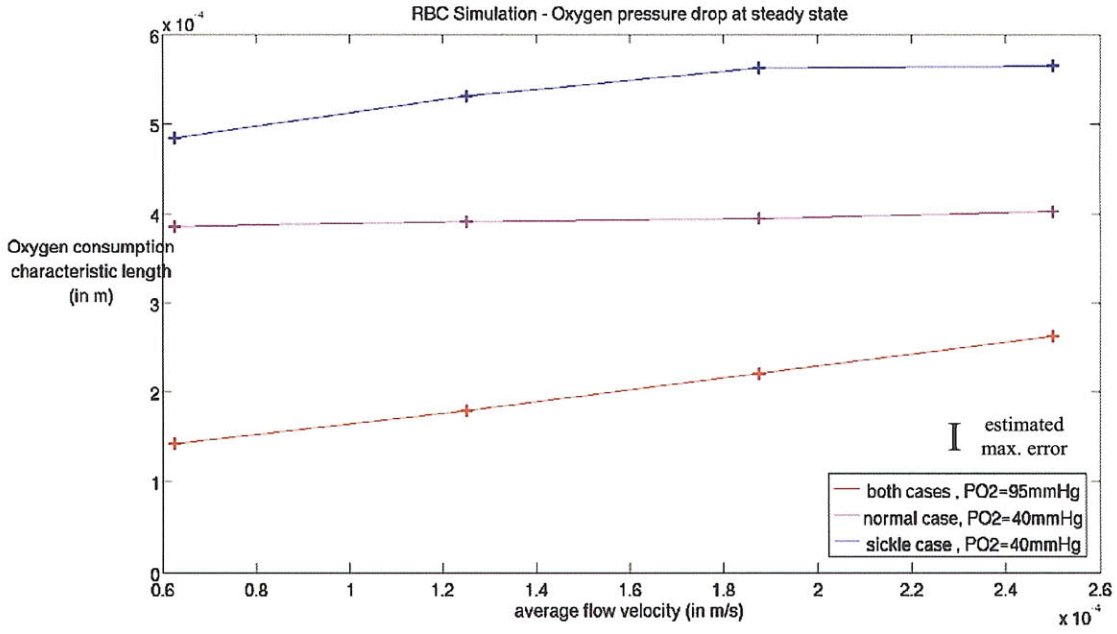


*Figure 3.3.16 : Oxygen partial pressure gradient vs. average flow velocity (equiv. vessel length).*

Figure 3.3.17 presents results for the sickle case under low hematocrit. We observe a similar deformation at a hematocrit 0.25 than at 0.45, with a RBC stretching towards the capillary walls. Like

the normal case, sickle cells are more stretched along the flow in the low hematocrit case, which is again due to more flow stress supported by each cell.

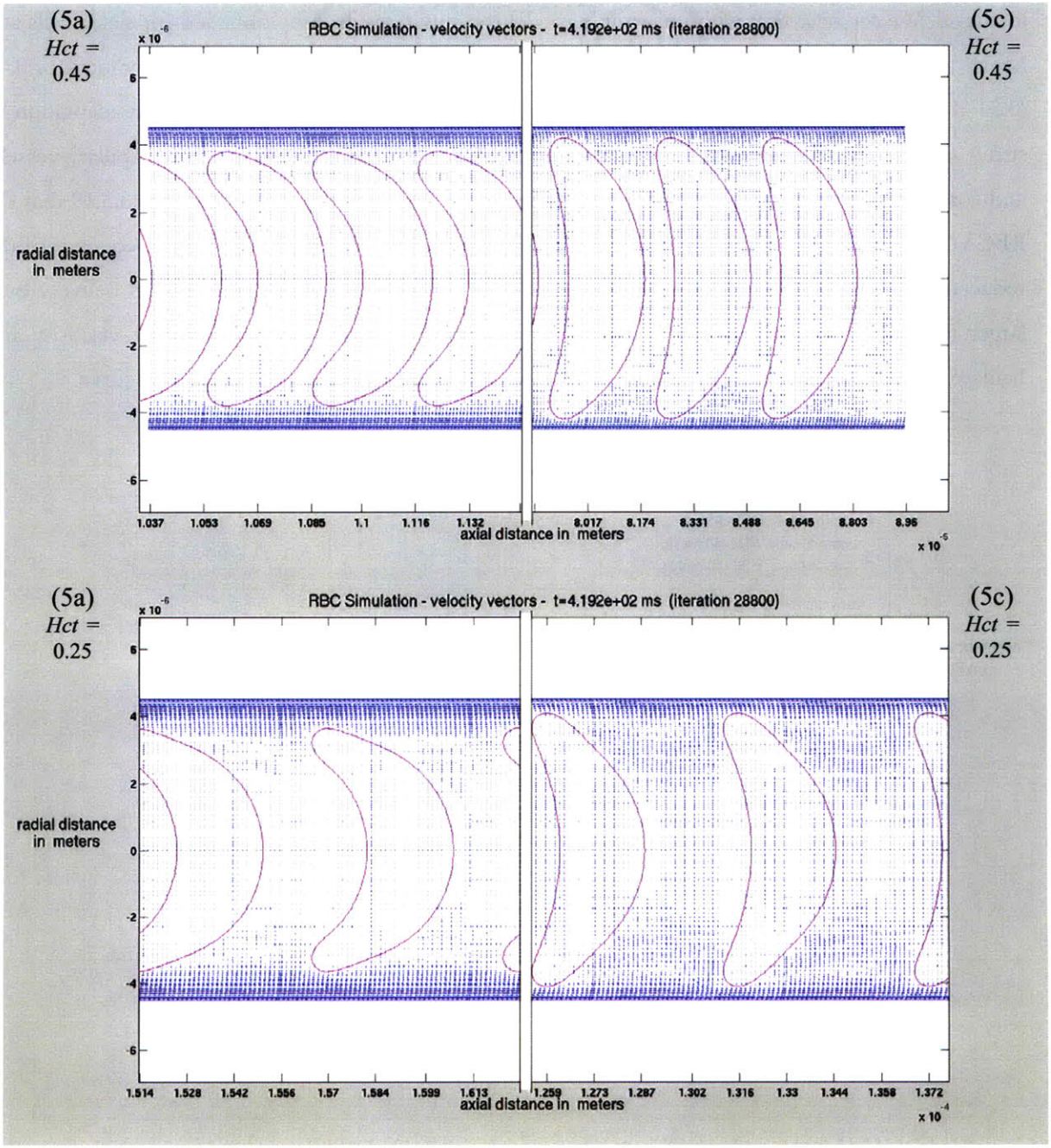


*Figure 3.3.17 : Comparison of normal and low hematocrit blood flow for the sickle cases.*

Figures 3.3.18, 3.3.19 and 3.3.20 show the dynamical analysis of sickle cells for the 2 different hematocrit levels. We see in Figure 3.3.18 how the reduced hematocrit leads again to a reduced

apparent viscosity. The obtained result is believed to explain the relation between low hematocrit and the deteriorated RBC structure : sickling RBCs lead to a high resistance to the flow per cell, which reduces the RBC lifespan and/or production so much that the effective hematocrit decreases to a low level. We see here that with our simple model the apparent viscosity obtained for sickle cells at a hematocrit of 0.25 ($3.44.10^{-3}$ Pa.s), is very close to the value for normal blood at a hematocrit of 0.45 ($3.31.10^{-3}$ Pa.s). This striking result strongly supports the hypothesis of a physiological adaptation to stiffer sickle cells, in order to maintain an "acceptable" resistance to the flow in the capillary vessels, and correspond to a sustainable cardiac pulse pressure. Comparably, we see on Figure 3.3.19 that the RBC velocity at steady state is also increased at low hematocrit. This not only is a consequence of the reduced viscosity, but is also bears the advantage of compensating the lower oxygen delivery by a larger inflow. Figure 3.3.20 shows that the physiological relation between apparent viscosity and hematocrit ratio is still verified, as all the points of all the cases studied fit on the same curve.

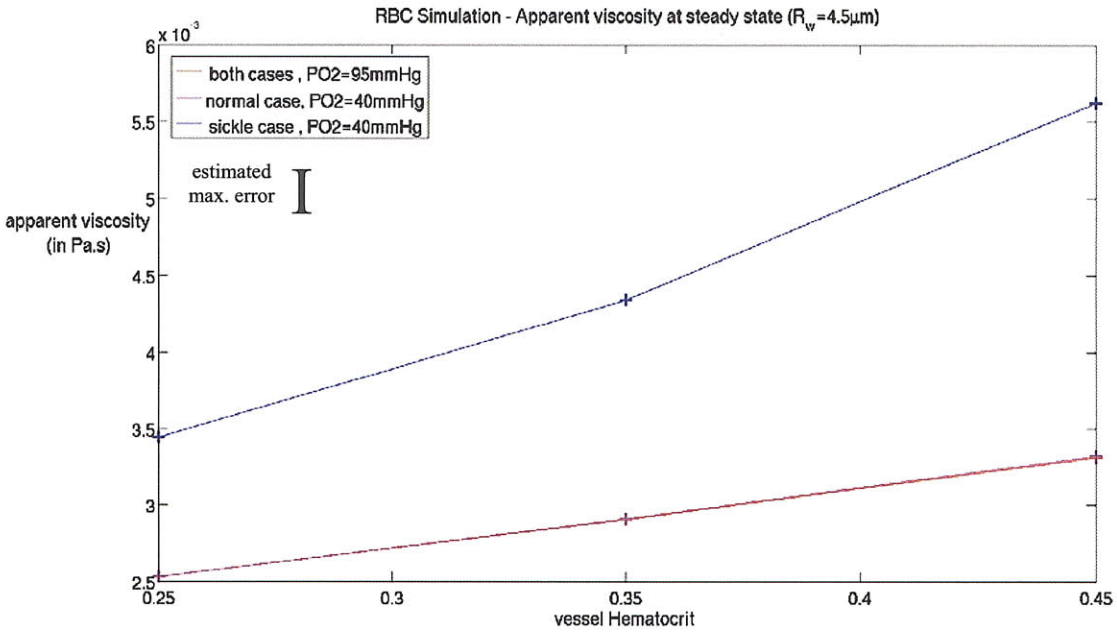


*Figure 3.3.18 : Viscosity vs. vessel hematocrit.*

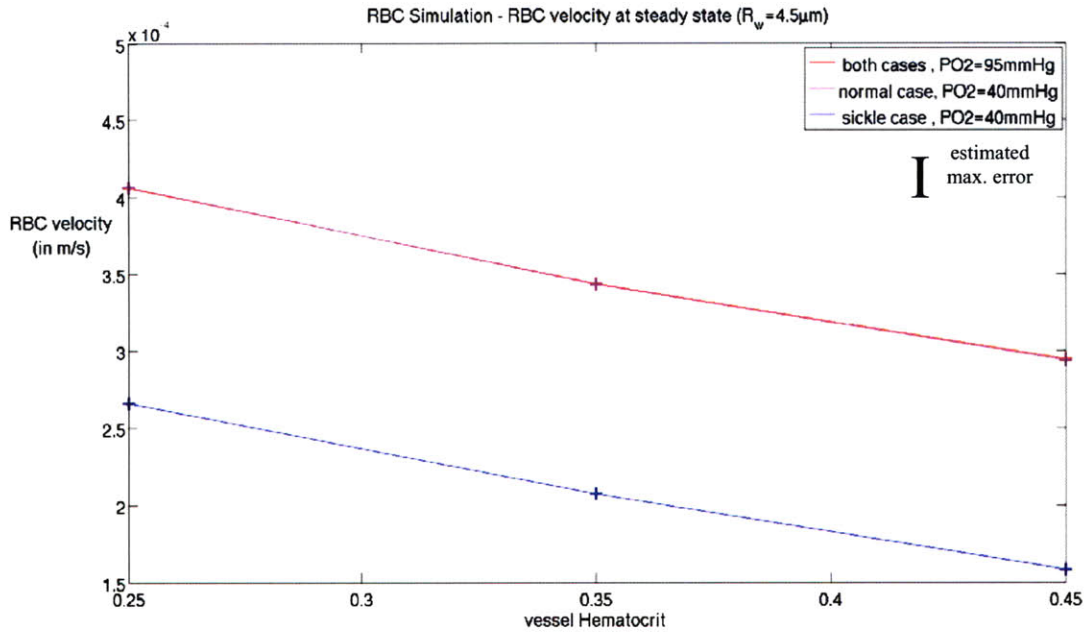


*Figure 3.3.19 : RBC velocity vs. vessel hematocrit.*

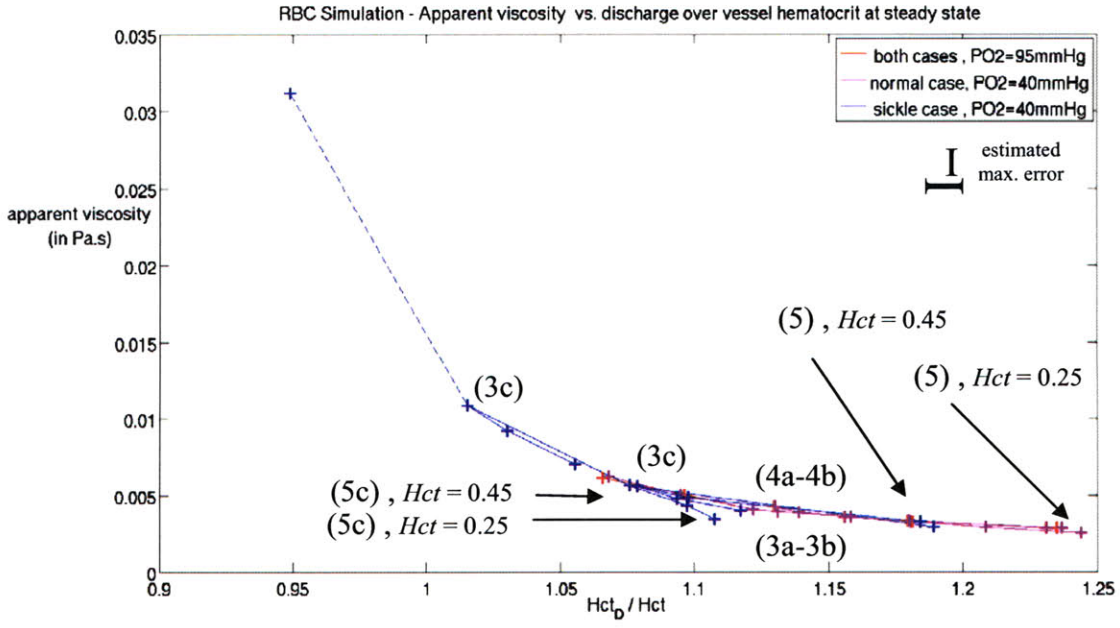


*Figure 3.3.20 : Viscosity vs. hematocrit ratio.*

Finally, Figures 3.3.21 and 3.3.22 show the oxygen performance comparisons. We find that unlike the normal cases, in the sickle case the reduced hematocrit considerably deteriorates the

oxygen delivery. Despite the increase in RBC velocity, oxygen transfer remains really low, and gets even much lower than all the normal cases. This result successfully reflects the anemic state of sickle cell patients, and shows how, despite the dynamical adaptation to sickle cells, oxygen delivery cannot be assured at normal levels. Since at lower hematocrit the blood oxygenation is expected to be lower than normal at the capillary start, we see how this essentially results in both a shift of oxygen levels (and gradients) to lower values, and poor delivery in surrounding tissues.

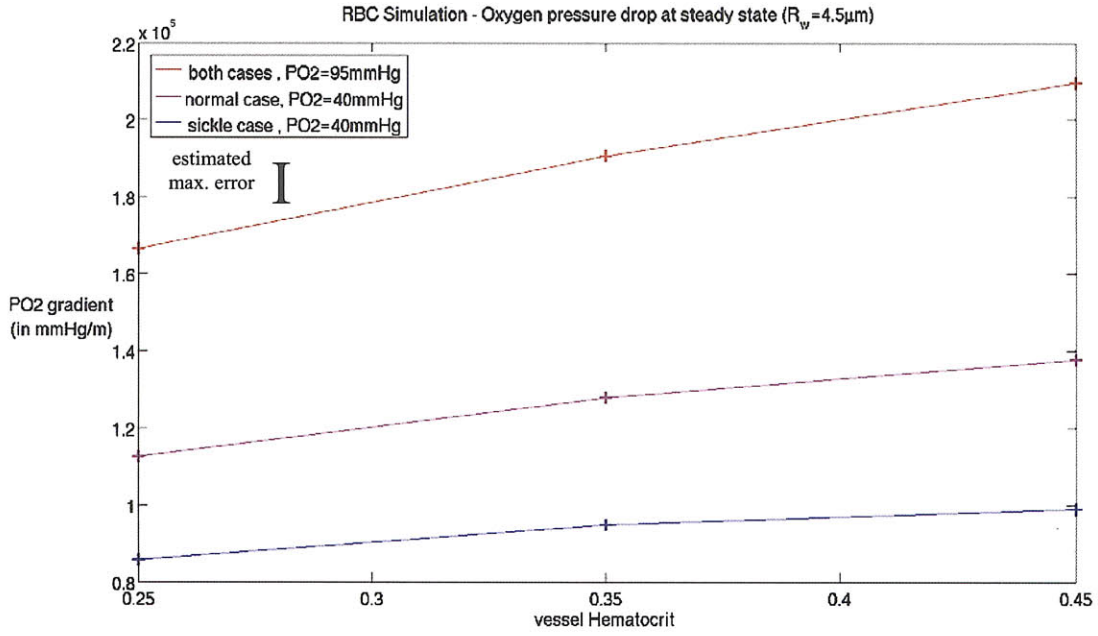


*Figure 3.3.21 : Oxygen partial pressure gradient vs. vessel hematocrit.*

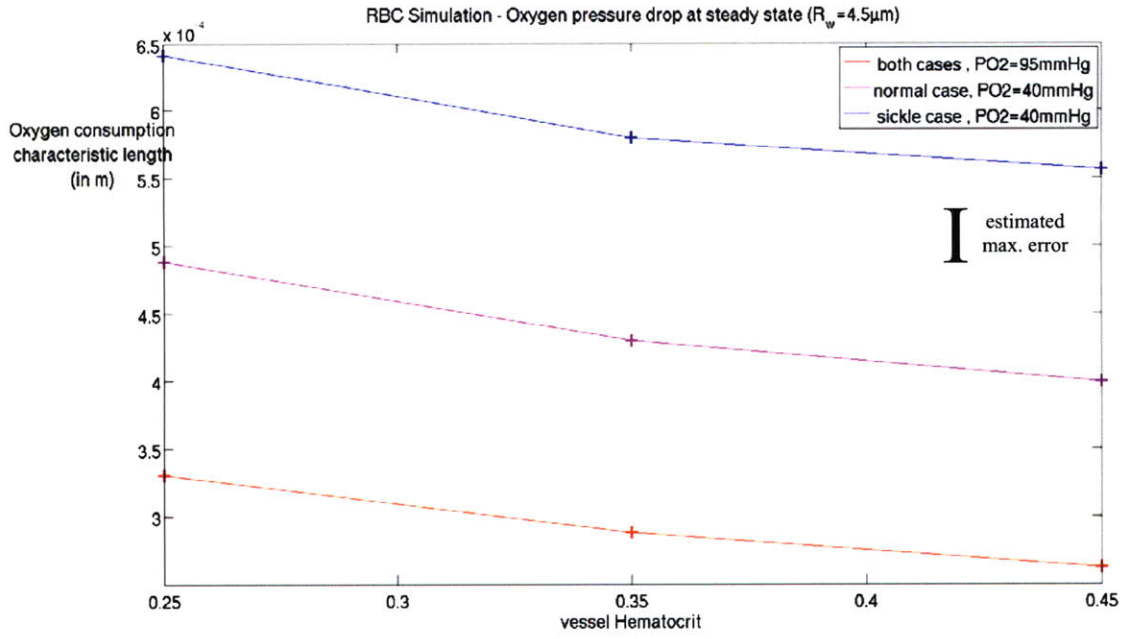


*Figure 3.3.22 : Oxygen partial pressure gradient vs. vessel hematocrit (equivalent vessel length).*

Table 3.3.1 summarizes the influence factors for the sickle cases. We see that besides the case of low hematocrit, these variations are essentially the same than for normal RBCs, although the levels are different. This illustrates how in the sickle case the dynamics follow generally the same parametric behavior, with a system operating at different conditions leading to the state of anemia. Because of the adapted dynamics in sickle cell disease at low hematocrit level, blood clogging is therefore expected to be particularly rare and acute, and preceded by a seemingly "normal" blood flow. The main indication of increased risks of vascular occlusion remains associated with the increased proximity of the RBCs with the capillary walls.

| Effect of increasing… | | on apparent viscosity $\mu_{app}$ | on RBC velocity $v_{RBC}$ | on discharge hematocrit $Hct_D$ | on oxygen transfer $\overline{\left(\frac{dp_{O_2}}{dz}\right)}$ |
|---|---|---|---|---|---|
| Vessel radius, at cst $\bar{v}_{in}$ and vessel hematocrit | $R_w\Big\|_{\bar{v}_{in},Hct}$ | – – | + | ++ | + (40 mmHg) |
| Vessel radius, at cst $\overline{\left(\frac{dp}{dz}\right)}$ and vessel hematocrit | $R_w\Big\|_{\overline{\left(\frac{dp}{dz}\right)},Hct}$ | – – – | +++ | +++ | + (40 mmHg) |
| $\bar{v}_{in}$, at cst vessel radius and vessel hematocrit | $\bar{v}_{in}\Big\|_{R_w,Hct}$ | – – | +++ | +++ | very small + (40 mmHg) |
| Vessel hematocrit, at cst $\overline{\left(\frac{dp}{dz}\right)}$ and vessel radius | $Hct\Big\|_{R_w,\overline{\left(\frac{dp}{dz}\right)}}$ | ++ | – – | +++ | +++ (40 mmHg) |

*Table 3.3.1 : Influence factors of the blood microcirculation – sickle case (vessel radius range : 2.5-5.0 µm).*

The simulation results presented in this section successfully show both qualitatively and quantitatively the consequences of sickle cell disease. We have demonstrated that our dynamical model allows a precise estimation of the changes in flow resistance and oxygen delivery performance, for a large variety of parametric values corresponding to either variable physiological conditions (such as vessel size) or disease characteristics (such as hematocrit level).

## 3.4. Synthesis of the simulation results, limits of the model and unveiled perspectives towards a systematic study of therapeutic opportunities

This study successfully identified some major features of sickle cell disease. From the few cases presented in Table 3.1.1, abnormal flow characteristics were determined precisely :

-the sickle model successfully reproduced the sickling RBC phenomenon. The current range of application covers the capillary radii from approximately 3.5 µm to 5.0 µm for a flow velocity of 0.25

mm/s. Lower velocities can reduce this range of application in the lower radii end (but changes in numerical parameters may overcome this difficulty).

-abnormal flow characteristics were clearly reported as increased apparent viscosity of blood for the whole range of vessel sizes at constant hematocrit level, with some variation depending on the cases. This increase correlated perfectly with the decrease of discharge hematocrit.

-oxygen delivery performance was compared for all the cases. Abnormal oxygen delivery in the sickle case was assessed quantitatively and was showed also to be correlated with the decrease of discharge hematocrit.

-the combination of sickle characteristics with a reduced hematocrit of 0.25 successfully showed how abnormal blood flow is likely to be compensated dynamically by the organism, leading to seemingly normal dynamics and the characteristic unpredictability of sickle cell crises due to sudden vessel occlusion. However, this still results in greatly affected oxygen delivery performance. The model designed predicts successfully both influences of the 2 stages leading to serious permanent anemia (i.e. due to sickling and due to low hematocrit).

The results presented here constitute a crucial step to advance towards larger-scale parametric studies. Based on our detailed analysis, we can now reformulate the problematic of sickle cell disease in terms of 2 major consequences observed. The increased apparent viscosity synthesizes the dynamical effects, while the decreased oxygen partial pressure gradient captures the gravity of the state of anemia. It is with these 2 quantities that we now propose to analyze quantitatively the effects of therapeutical directions. The work presented in the next chapter is based on this conclusion.

# 4. Identification and assessment of therapeutic opportunities

This chapter presents synthetically a large-scale, systematic analysis of a selected set of parametric variations that would constitute therapeutic opportunities. We will first explain our selection of target parameters in this study. Secondly, we will show and analyze for each case the results of our simulations. Finally, we will conclude by a discussion on the found therapeutic opportunities, and how these results can help to devise new directions for medical research.

## 4.1. Sickle cell treatment strategy

As mentioned in chapter 2, the full system of equations used in our model contains 38 parameters, excluding sickle cell models and numerical parameters. At this point these could all constitute potential targets for therapeutical research. We propose to analyze the effects of existing or alternative therapies through reasonable variations of these parameters in our model. Our study is to be restricted to the parameters whose variations are perceived as realistic options for a near future, considering the current state of availability of pharmaceutical treatments or short-term developments in medical research.

### 4.1.1. Excluded parameters

Oxygen solubility, binding and dissociation constants regroup 11 parameters : $\alpha$ (oxygen solubility – 5 values), $k^{Hb}$ (kinetic dissociation rate constant of oxyhemoglobin), $n$ (Hill coefficient), $p^{Hb}_{O_2,50\%}$ (equilibrium oxygen partial pressure at 50% saturation of hemoglobin), and $p^{Mb}_{O_2,50\%}$ (equilibrium oxygen partial pressure at 50% saturation of myoglobin), to which are added $D^{Hb}$ (diffusivity of hemoglobin) and $D^{Mb}$ (diffusivity of myoglobin). We believe at this point that changes among these parameters would be either ineffective or undoable. Oxygen solubility can only be changed through pressure or temperature unless blood composition is affected, which does not seem to be a valid option as of today. And while changing the pressure can have more direct effects on the flow and will be discussed later, changing blood temperature does not look either like a realistic option. An increase in the kinetic dissociation rate constant is not expected to produce significant

changes, as our analysis showed that it was never a limiting factor of oxygen transport. The remaining parameters seem to be deeply associated with the chemical processes of oxygen binding to hemoglobin and myoglobin, and we have found no research grounds to support possible enhancements of oxygen release.

Mechanical elastic constants associated with the RBC membrane regroup 5 parameters : $\sigma_0$ (membrane tension at rest), $K_{bu}$ (2-D bulk modulus), $K_{sh}$ (shear modulus), $B$ (bending modulus), and $k_0$ (curvature at rest). Changing these parameters seems unrealistic at this point, since it would concern the membrane structure at the molecular level, and not only raise questions about how to do it, but also about all the other functions of the RBC membrane that may be affected. Also, no research was found on a possible implementation of such changes.

Excluded geometrical parameters regroup 5 parameters : $R_K$ (radius of the Krogh cylinder model of oxygen transport), $R_T - R_I$ (thickness of the interstitium), $R_I - R_w$ (thickness of the capillary wall), $V_{RBC}$ (RBC volume), and $A_{RBC}$ (RBC surface area). Changes to the model geometry could be achieved in theory by promoting vessel growth (angiogenesis) within an organ, effectively making the capillary network more dense. VEGF-based treatments for example could constitute a therapeutical option for research. However, increasing the vascularization is also likely to increase the risks of vessel occlusion and sickle cell crises, especially as it would decrease the flow in each vessel. In vivo changes of the geometry of the interstitium and capillary wall do not seem applicable either. As for the RBC geometry, the only known process of volume change is regulated by osmotic pressure, but departing from a normal osmotic equilibrium would undeniably be very adventurous.

To the previous group of parameters we should add that changing initial RBC dimensions through the set of variables $\{s_0, ds_0\}$ and $\{R_0\}$ follows the same arguments against changing $V_{RBC}$ and $A_{RBC}$, and are unlikely to constitute a therapeutical objective.

Finally, the local concentrations of hemoglobin, $[Hb]$, and myoglobin, $[Mb]$ are also not considered of therapeutical interest. No research has been found to demonstrate the feasibility of "packing" more hemoglobin inside a RBC. The underlying reason is probably that the natural concentration of hemoglobin is already relatively high within the RBC. Alternatives such as hemoglobin carriers outside the RBC will be discussed later. Myoglobin is also at a relatively high concentration in muscular tissue, which is likely to limit any possible treatment (promotion of myoglobin production is likely to simply result in increased muscular volume, not concentration).

### 4.1.2. Parameters independent of any permanent therapeutical action (uncontrollable)

Parameters related to oxygen consumption, $M_w$ (in the capillary wall), and $M_t$ (in the muscular tissue), reflect essentially normal metabolism and physical activity, which is not really controllable as such by medical treatments and constitute rather external factors imposed on the rheology, and are therefore excluded from our study.

The oxygen level at capillary entrance, $p_{O_2\,in}$ (95mmHg), is also not considered as a potential target in our study : while increasing the level of oxygen is possible with oxygen masks and hyperbaric oxygen therapy, it is more considered here as a temporary measure used for emergency treatment. Both treatments, under permanent use, are also subject to a large range of secondary effects from nausea and vertigo to oxygen toxicity (or oxygen poisoning), potentially resulting in major damages to cells and the central nervous system. Reduced exposure on a regular basis may constitute an alternative [95], although the improvement may only be transient [86]. Further research on the possible benefits and drawbacks could definitely allow us to address this possibility as a potential therapeutical target. Interestingly, the same type of study may be used to address the adverse effects of an impaired air ventilation (such as due to pulmonary infections, or obesity), and prolonged exposure to low-pressurized environments, such as in altitude or space.

### 4.1.3. Therapeutical targets retained, working hypotheses and possible implementations

The 12 remaining parameters are $R_w$ (capillary vessel radius), $\overline{v}_{in}$ (average inlet velocity), $\overline{\left(\frac{dp}{dz}\right)}$ (average pressure gradient between 2 RBCs), $Hct$ (vessel hematocrit), $\mu$ (plasma/cytoplasm viscosity), $D$ (oxygen diffusion constant – 5 values), and $\rho$ (blood density).

Acting on capillary vessel size comes directly from our previous analysis : since sickling RBCs tend to obstruct more blood flow, we will consider dilating capillary vessels as a first option for therapeutical treatment. Vasodilating drugs exist currently to achieve vessel size augmentation, although the absence of smooth muscle in the small capillaries does not make it appropriate for such vessels, and suggests a need for research for alternative techniques. The main drawbacks of a

vasodilating treatment are connected to hypotension symptoms, reduction of blood flow potentially leading to coagulation and formation of peripheral blood clots, and compensation by the heart through pulse acceleration. Also, avoiding exposure to cold environments is desirable to prevent vasoconstriction.

Increasing blood flow was also researched as a way to enhance sickle cell disease, taking advantage of the blood shear thinning properties. Cardiotonic drugs such as digitalis, Common Inotropic and Cardiotonic Drugs (CICDs), or even caffeine, can be used effectively to increase cardiac output. Platelet antiaggregants would reinforce the effects of such drugs by decreasing plasma viscosity (hence facilitating increase in velocity instead of increase in blood pressure). However, undesired effects may result from pulse acceleration (tachycardia), and a reaction of the organism leading to vasodilatation, in order to compensate an increased peripheral blood viscosity.

Increasing pressure levels in the organism is very similar to increasing blood flow, since it implies also a stimulating action on the heart. Again, we hypothesize here positive effects from "forcing" the RBCs to flow down the capillaries. Cardiotonics without platelet antiaggregants are a possible implementation, to increase cardiac output, but not reduce blood viscosity to obtain lower flow for the same pressure level. Again, major issues may rise at the cardiac level due to pulse acceleration, but also in the peripheral circulation due to the abnormal high pressure (organ damages in the brain, the lungs, and other hypertension symptoms).

Increasing the hematocrit was a hypothesis formulated to compensate directly the poor oxygen delivery performance, especially starting from the low hematocrit of 0.25 in sickle cell patients. Here a large variety of implementations exist, such as EPO injections. However when the hematocrit goes beyond normal levels (polycythemia), risks of occlusion may become very important. Platelet antiaggregants and anticoagulant drugs may decrease the risks, but only up to a certain level.

Decreasing the viscosity of blood plasma or cytoplasm directly is also a very interesting idea that we would like to explore to reduce the resistance of whole blood. For simplicity, we will restrict our study to varying plasma viscosity, since it is expected to be both easier to implement, and more consequential. Here as mentioned earlier platelet antiaggregants would be a possible implementation that we consider, keeping in mind the limits associated with these drugs. Also, avoiding dehydration is known to favor a lower plasma viscosity.

To act on the low oxygen delivery performance of sickle cell patients, we also propose to examine possible action on oxygen diffusion constants. The opportunity of improving oxygen transport is supported by recent research on free oxygen carriers, such as free plasma hemoglobin presented in the work of Vadapalli, Goldman and Popel [108]. As the most plausible implementation,

our study will focus on increasing diffusivity of blood plasma only, as an implicit model for such therapies, and ignore variations of diffusivity in other regions.

Finally, we propose to examine the possible effects of changes in blood density. Although the implementation is highly questionable, we hypothesize that diuretic therapies or other methods favoring water retention or elimination may lead to such changes in blood density.

Table 4.1.1 recaps the list of target parameters selected, effectively reduced to 7 parametric studies.

| Parameter | idea | how ? | comments/secondary effects |
|---|---|---|---|
| $R_w$ | increase | vasodilating drugs | hypotension, peripheral clots, pulse acceleration |
| $\bar{v}_{in}$ | increase | cardiotonics (digitalis, caffeine) + platelet antiaggregants | pulse acceleration, vasodilatation |
| $\overline{\left(\frac{dp}{dz}\right)}$ | increase | cardiotonics (digitalis, caffeine) | pulse acceleration, organ damage (brain, lung) |
| $Hct$ | increase | EPO (+ platelet antiaggregants + anticoagulants) | peripheral clots, polycythemia if too high |
| $\mu_p$ | decrease | platelet antiaggregants | very few adverse effects |
| $D_p$ | increase | plasma oxygen carriers | relatively recent research |
| $\rho$ | decrease | diuretic action ? blood supplements ? | range of variation is relatively small |

*Table 4.1.1 : target parameters for sickle cell treatment strategy.*

It is important to note that, although most of the drugs cited are generally used to **restore** a normal state, we are here considering their theoretical use to **depart** from a normal state, with the idea to compensate sickle cell dynamics by another mechanism. One must keep in mind that, since we are not advising a typical use of these drugs, the organism may not only respond unexpectedly to

such constraints, but also react against therapeutical implementations and enforce the natural physiological regulation of the body functions.

For our simulations, we note that $\bar{v}_{in}$ and $\overline{\left(\frac{dp}{dz}\right)}$ cannot be changed independently at a constant vessel radius, but only at a varying radius. Therefore, the 7 proposed parametric studies of potential therapeutical targets will consist in :

- varying $\bar{v}_{in}$, at constant $R_w$, $Hct$, $\mu_p$, $D_p$ and $\rho$. The proposed values are **0.0625 mm/s**, **0.125 mm/s**, **0.1875 mm/s**, and **0.25 mm/s** (velocities higher than 0.25 mm/s were numerically more unstable, so we chose to do our analysis starting at lower velocities).

- varying $R_w$, at constant $\bar{v}_{in}$, $Hct$, $\mu_p$, $D_p$ and $\rho$. The capillary radii examined are the same as in the previous chapter, i.e. **2.5 µm**, **3.0 µm**, **3.5 µm**, **4.0 µm**, **4.5 µm**, and **5.0 µm**. To give an idea of the relevance of these values, one can note that for our set parameters (in particular RBC volume and surface area), the minimal radius possible for RBCs to be able to flow down a capillary vessel is 1.4227 µm, and the maximal theoretical radius to maintain RBCs aligned on the centerline under no flow is 6.6348 µm at hematocrit 0.45, and 8.9015 µm at hematocrit 0.25.

- varying $R_w$, at constant $\overline{\left(\frac{dp}{dz}\right)}$, $Hct$, $\mu_p$, $D_p$ and $\rho$. We use the same values of capillary size as above.

- varying $Hct$, at constant $R_w$, $\overline{\left(\frac{dp}{dz}\right)}$, $\mu_p$, $D_p$ and $\rho$. The hematocrit will take the values **0.25**, **0.35**, **0.45**, and **0.55** as representative cases.

- varying $\mu_p$, at constant $R_w$, $\overline{\left(\frac{dp}{dz}\right)}$, $Hct$, $D_p$ and $\rho$. The work of Laogun et al. [65] shows that in sickle cell patients undergoing crises, $\mu_p$ can raise from $1.4.10^{-3}$ Pa.s to $1.7.10^{-3}$ Pa.s. We will therefore consider as a reasonable set of values **$1.1.10^{-3}$ Pa.s**, **$1.4.10^{-3}$ Pa.s**, and **$1.7.10^{-3}$ Pa.s** ($1.1.10^{-3}$ Pa.s being our hypothesized improvement opportunity).

- varying $D_p$, at constant $R_w$, $\overline{\left(\frac{dp}{dz}\right)}$, $Hct$, $\mu_p$ and $\rho$. Published work by Menchaca et al. [45] suggests a possible improvement of 30% of oxygen diffusive transfer, so that we will consider values of **$1.7.10^{-9}$ m²/s**, **$2.4.10^{-9}$ m²/s**, and **$3.1.10^{-9}$ m²/s** to illustrate the range of possible values ($3.1.10^{-9}$ m²/s being the hypothesized improvement opportunity).

- varying $\rho$, at constant $R_w$, $\overline{\left(\frac{dp}{dz}\right)}$, $Hct$, $\mu_p$ and $D_p$. Since the density of cytoplasm is about 10% higher than that of plasma (1125 kg/m$^3$ instead of 1025 kg/m$^3$), we hypothesize a characteristic range of accessible values from **925 kg/m$^3$**, to **1125 kg/m$^3$**, and include again the reference **1025 kg/m$^3$**.

These case studies will be denoted A through H (including the baseline). For each of them, our analysis will compare the cases of RBCs at 95 mmHg, normal RBCs at 40 mmHg, and sickle cells at 40 mmHg. We will focus exclusively on the effects of parametric changes on both **apparent viscosity**, and **oxygen consumption characteristic length** (equivalent length at a given oxygen partial pressure gradient, to decrease the level from 95 mmHg to 40 mmHg).

## 4.2. Simulation results, and comparative analysis of therapeutical hypotheses

In order to appropriately estimate and compare the benefits of each parametric variation, we will represent the results with the same synthetic curve, showing explicitly the tradeoff between oxygen consumption and apparent viscosity of the calculated flow. Since we have cases at constant velocity and constant pressure gradient, we set 2 baseline cases corresponding to either $\bar{v}_{in}$ = 0.25 m/s or $\overline{\left(\frac{dp}{dz}\right)}$ = 3.25.10$^5$ Pa/m, and $R_w$ = 4.5 μm, $Hct$ = 0.45, $\mu_p$ = 1.4.10$^{-3}$ Pa.s, $D_p$ = 2.4.10$^{-9}$ m$^2$/s and $\rho$ = 1025 kg/m$^3$ (see Table 4.2.1). Together with whole blood apparent viscosity, oxygen consumption is represented by the equivalent capillary length, calculated to get from 95 mmHg to 40 mmHg at the partial pressure gradient obtained by our simulations. Figure 4.2.1 shows the results for the 2 baseline cases.

| $R_w$ | $\bar{v}_{in}$ | $\overline{\left(\frac{dp}{dz}\right)}$ | $Hct$ | $\mu_p$ | $D_p$ | $\rho$ |
|---|---|---|---|---|---|---|
| 4.5 μm | 0.25 m/s | 3.25.10$^5$ Pa/m | 0.45 | 1.4.10$^{-3}$ Pa.s | 2.4.10$^{-9}$ m$^2$/s | 1025 kg/m$^3$ |

*Table 4.2.1 : baseline values of the target parameters.*

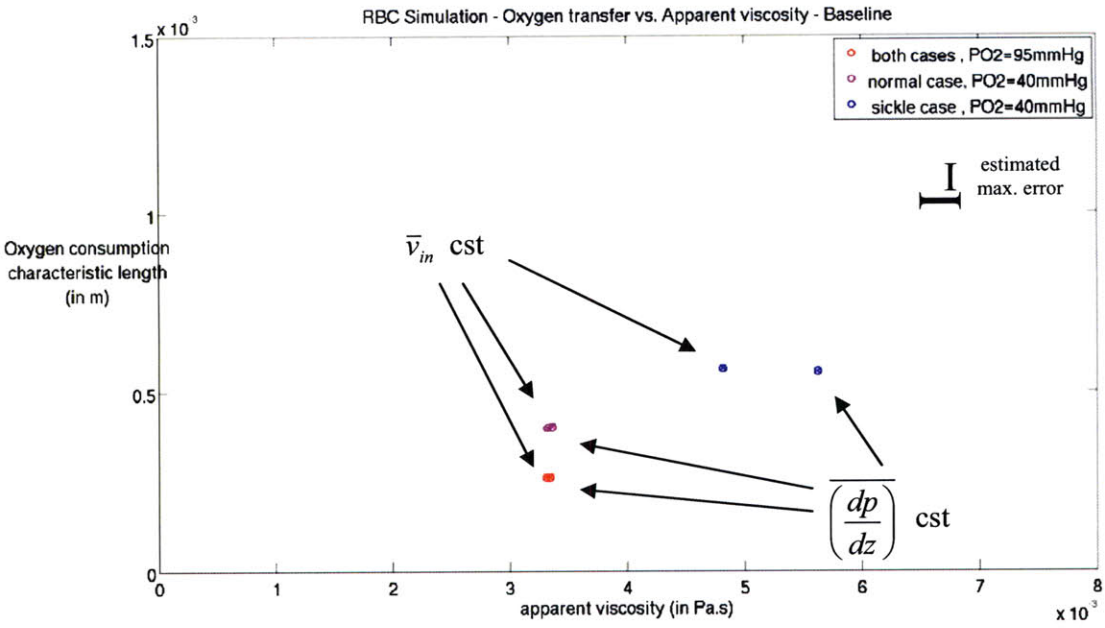


*Figure 4.2.1 : baseline cases (A).*

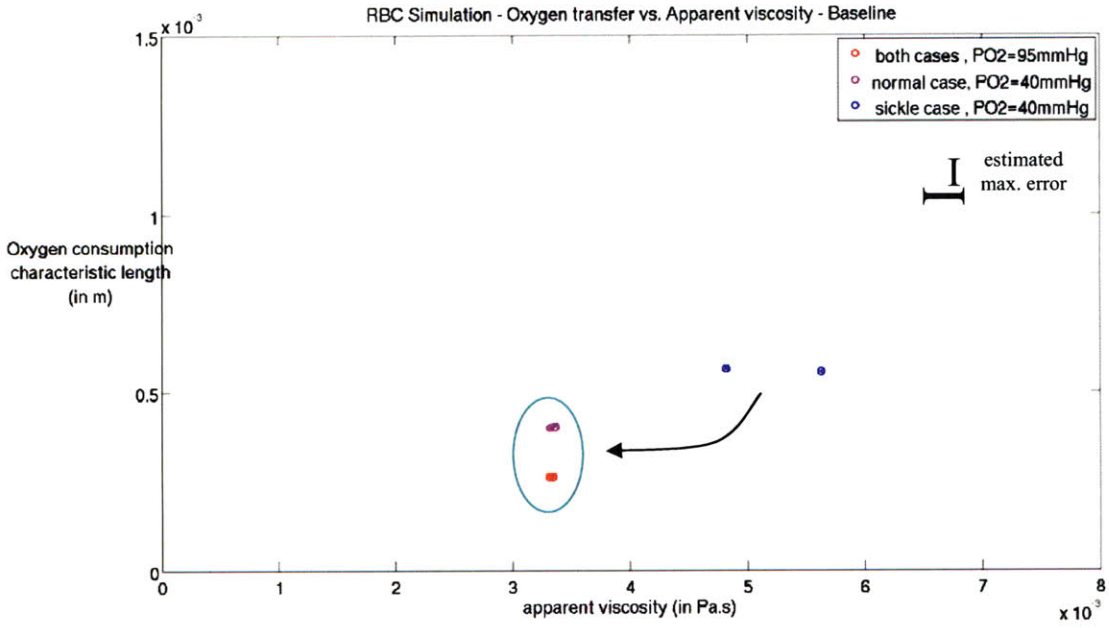


*Figure 4.2.2 : baseline cases (A) : schematic of therapeutical objective.*

As we see on Figure 4.2.1, the problematic of sickle cell disease can be summarized in our context, as follows : the potential therapies we want to assess by simulations will focus on both bringing back apparent viscosity to levels corresponding to the normal cases (about $3.3.10^{-3}$ Pa.s), and improving oxygen delivery to bring back the characteristic length to a normal value (about 0.4 mm, which is to be interpreted as the "effective" capillary length of oxygen absorption predicted by our model). Figure 4.2.2 illustrates this double objective.

Figure 4.2.3 shows the theoretical results obtained after changes in the inlet velocity $\overline{v}_{in}$, corresponding to the first proposed parametric study (B). Our simulations show that varying inflow does not seem to be able to both improve blood dynamics and oxygen delivery of low-oxygenated sickle blood : while increasing velocity decreases the apparent viscosity, it penalizes oxygen delivery as the RBCs get further from the capillary walls. RBCs flowing faster may improve oxygen transfer by convection, but it is largely overcome by the penalty on oxygen diffusion due to the larger gap between RBCs and capillary. Inversely, decreasing velocity improves oxygen transfer but deteriorates greatly the dynamics.

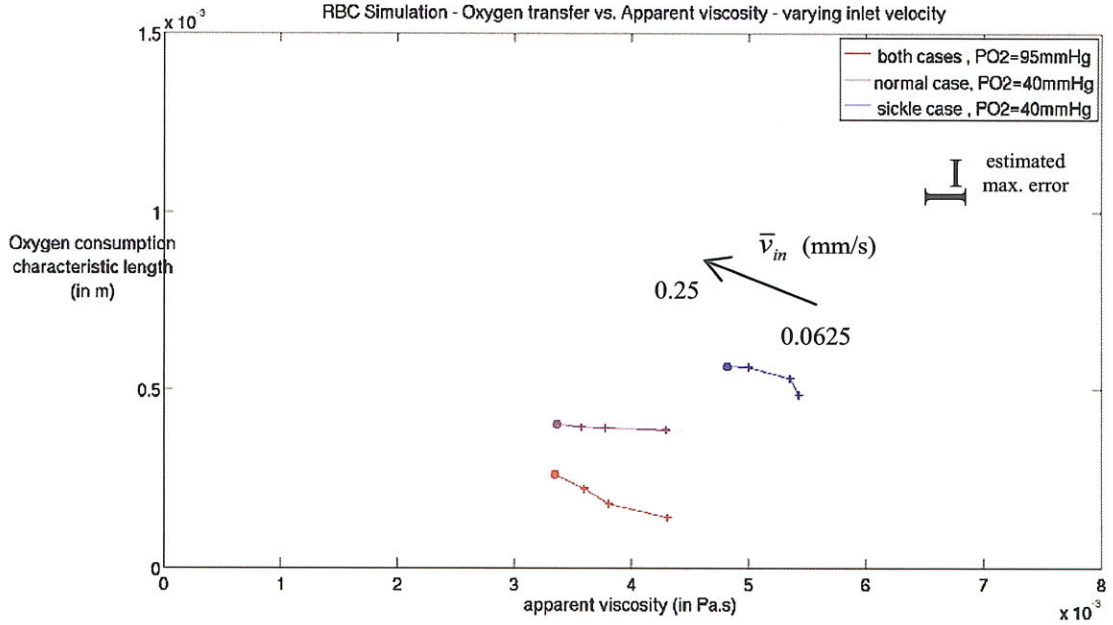


*Figure 4.2.3 : case study B : variable inflow.*

Figure 4.2.4 shows the potential effects of increasing vessel size at constant inlet velocity. As we see here, there is a clear opportunity for improvement of both dynamics and oxygen delivery. In particular, we notice that for sickle blood at 40 mmHg, increasing the radius from the baseline case, $R_w$ = 4.5 μm, to $R_w$ = 5 μm, brings both apparent viscosity and oxygen consumption characteristic length below the calculated values of normal blood at the same oxygen level. The dashed part of the blue curve indicates questionable results due to secondary folding of the sickled cells.

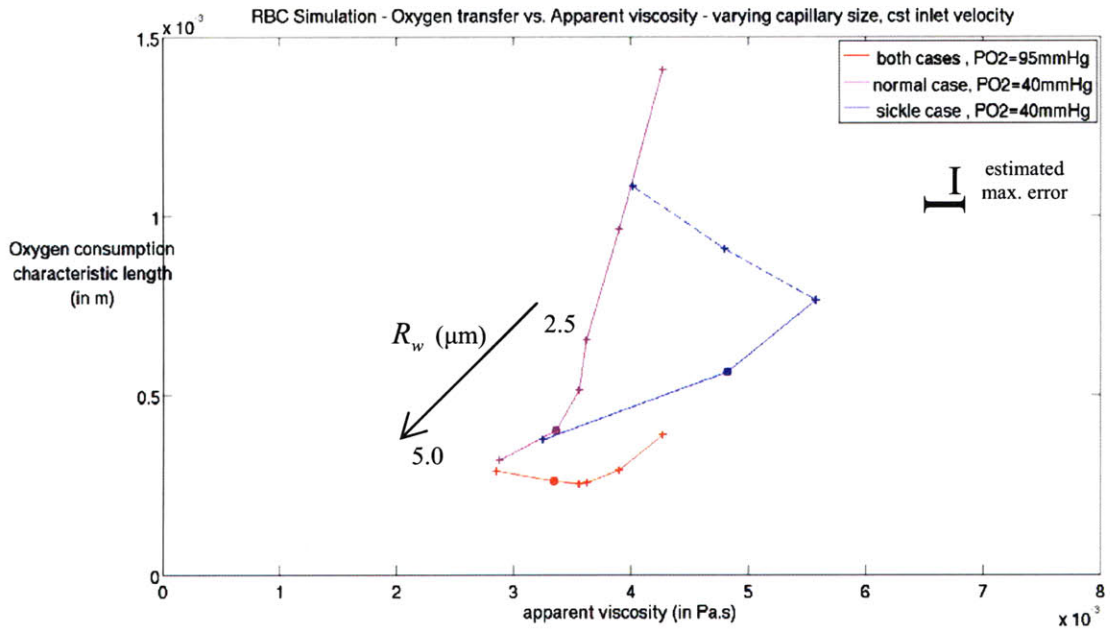


*Figure 4.2.4 : case study C : variable radius, constant inflow.*

Figure 4.2.5 shows comparatively the same vessel size variations as Figure 4.2.4, but at constant pressure gradient across the cases. As we see, there is again a great opportunity for improvement of both blood dynamics and oxygen delivery. Moreover, we see that the change between $R_w$ = 4.5 μm and $R_w$ = 5 μm, leads to a greater relative decrease in apparent viscosity than in case study C. The improvement of oxygen delivery performance is slightly smaller (oxygen consumption characteristic length reaches 0.41 mm), but still very close to the value of normal blood at 40 mmHg (0.40 mm). At $R_w$ = 5 μm, the sickle case results in blue get very close to the normal cases, suggesting a quasi-normal behavior of sickle blood with an acceptable oxygen performance.

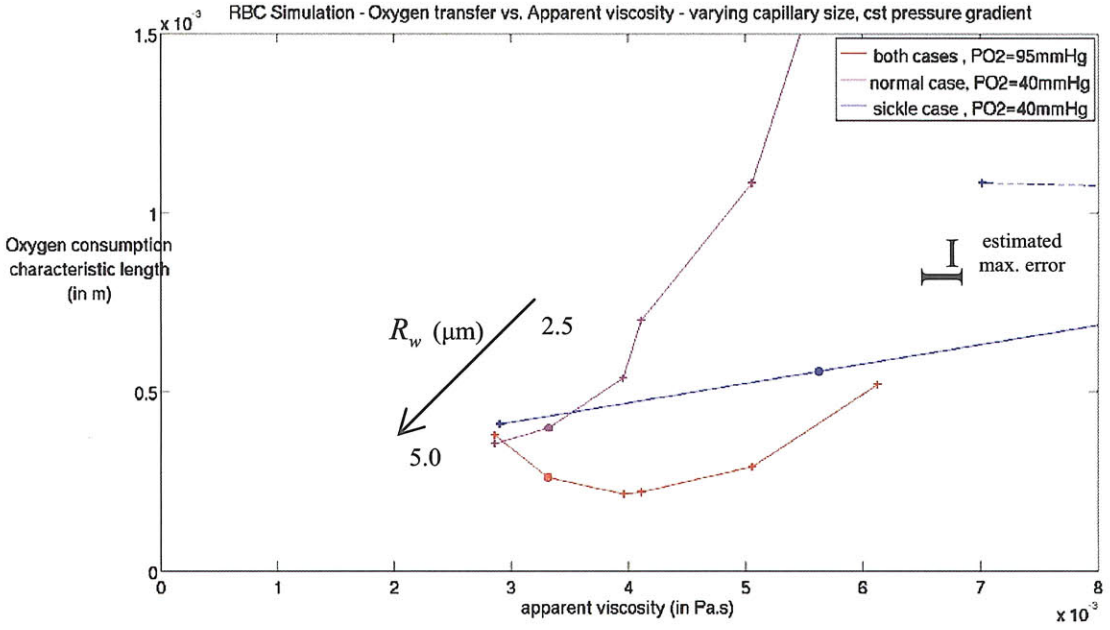


*Figure 4.2.5 : case study D : variable radius, constant pressure gradient.*

Figure 4.2.6 shows the potential effects of enforcing different values of blood hematocrit. The curve representing low-oxygenated sickle blood (in blue) shows how varying hematocrit would not be efficient. While increasing the hematocrit is shown to improve oxygen delivery, the impact on apparent viscosity is terrible. We notice that, in accordance with our conclusions in Chapter 3, the low hematocrit of sickle cell patients, 0.25, seems to result from a natural bias, favoring normal blood dynamics over reduced oxygen delivery. Keeping this result in mind, we can hypothesize therapeutic strategies combining this natural behavior with another induced parametric variation. This would lead to possible benefits in 2 ways. One idea would be to research a potential therapy that would mainly improve oxygen delivery, assuming that the hematocrit regulation would be enforced by the organism in order to maintain the apparent viscosity to a normal level. The other idea would be to research a potential therapy that would reduce greatly the apparent viscosity (i.e. below normal levels), and expect the organism to regulate the hematocrit back towards 0.45, or even maybe higher levels, to restore a normal apparent viscosity, with an eventual benefit in oxygen delivery. As an example put to the test, the results of case study B present a very similar curve to that of variable hematocrit, so that very little improvement would be expected from any combination of the 2 parametric variations.

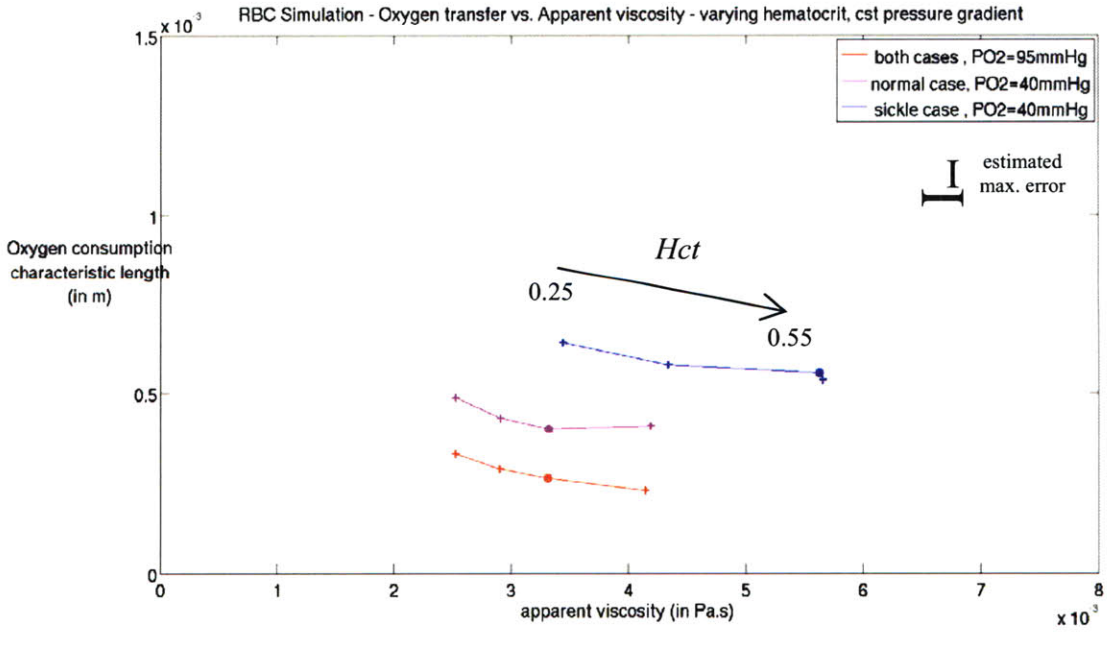


*Figure 4.2.6 : case study E : variable vessel hematocrit.*

Figure 4.2.7 shows the results of variations in plasma viscosity. As expected, decreasing plasma viscosity acts directly on decreasing whole blood viscosity, even though it brings it down only half-way towards the value of normal blood. Unfortunately, we also see that the oxygen consumption characteristic length increases a little when plasma viscosity decreases, which effectively means worsening the state of anemia. In light of the results of case study E, it may be possible to consider the success of a therapy based on combining reduced plasma viscosity with hematocrit regulation. One of the main challenges of such a therapy would reside in being able to reduce considerably the plasma viscosity, by extrapolation about twice as much as we hypothesized for the lowest value (in other terms plasma viscosity would have to be decreased to $0.5.10^{-3}$ Pa.s, which is below water at body temperature, $0.7.10^{-3}$ Pa.s...). Even though this result does not seem to be accessible, it is important however to keep in mind, that even a partial improvement of the disease remains an opportunity worth being considered for therapeutical research.

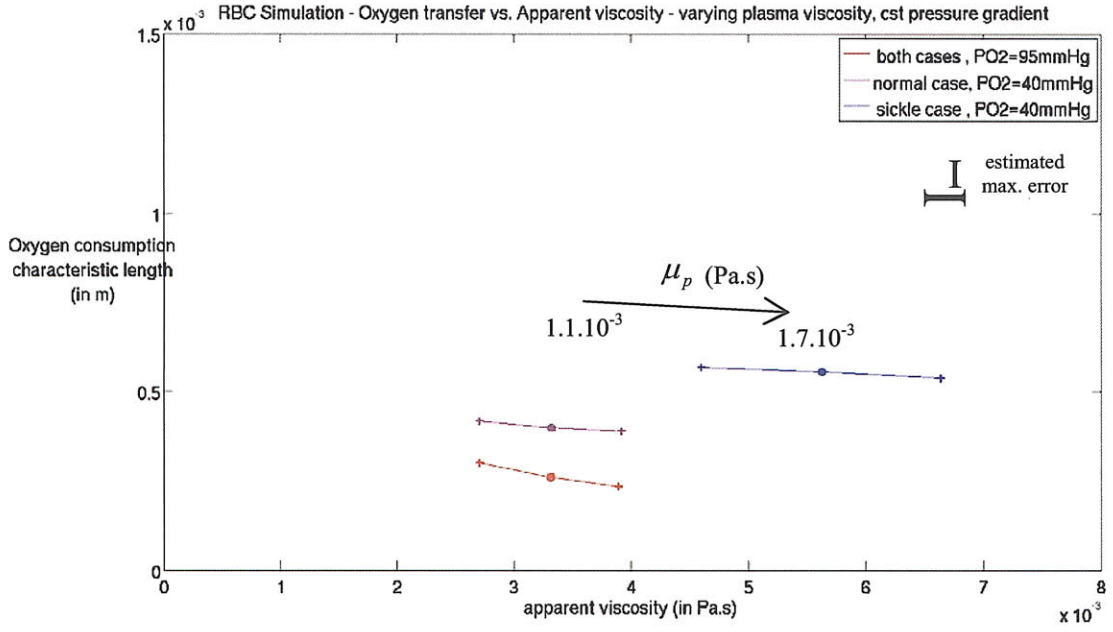


*Figure 4.2.7 : case study F : variable plasma viscosity.*

Figure 4.2.8 shows the potential benefits from changing the effective oxygen diffusion constant in the blood plasma. We see here that our estimated window for improvement of oxygen diffusion, up to about 30%, can decrease the oxygen consumption characteristic length from 0.56 mm to 0.44 mm, which is very close to the value of our baseline case for normal low-oxygenated blood (0.40 mm). However no significant change of the apparent viscosity was observed.

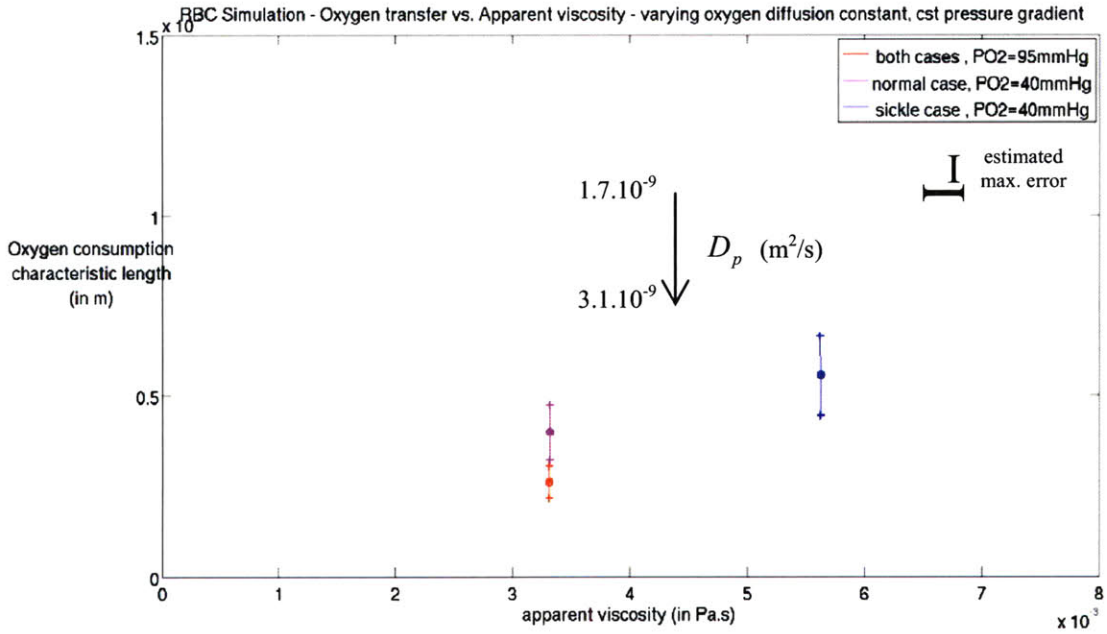


*Figure 4.2.8 : case study G : variable oxygen diffusion constant in blood plasma.*

Following our results for case study G, we extrapolated the impact of varying oxygen diffusion constant for low-oxygenated, sickle blood at a hematocrit of 0.25. Figure 4.2.9 shows these results in addition to case study G. We see now that not only the oxygen performance becomes nearly that of normal blood, but also the apparent viscosity, down from $5.63.10^{-3}$ Pa.s to $3.45.10^{-3}$ Pa.s (to be compared with the calculated value in the baseline case for normal low-oxygenated blood, $3.32.10^{-3}$ Pa.s).

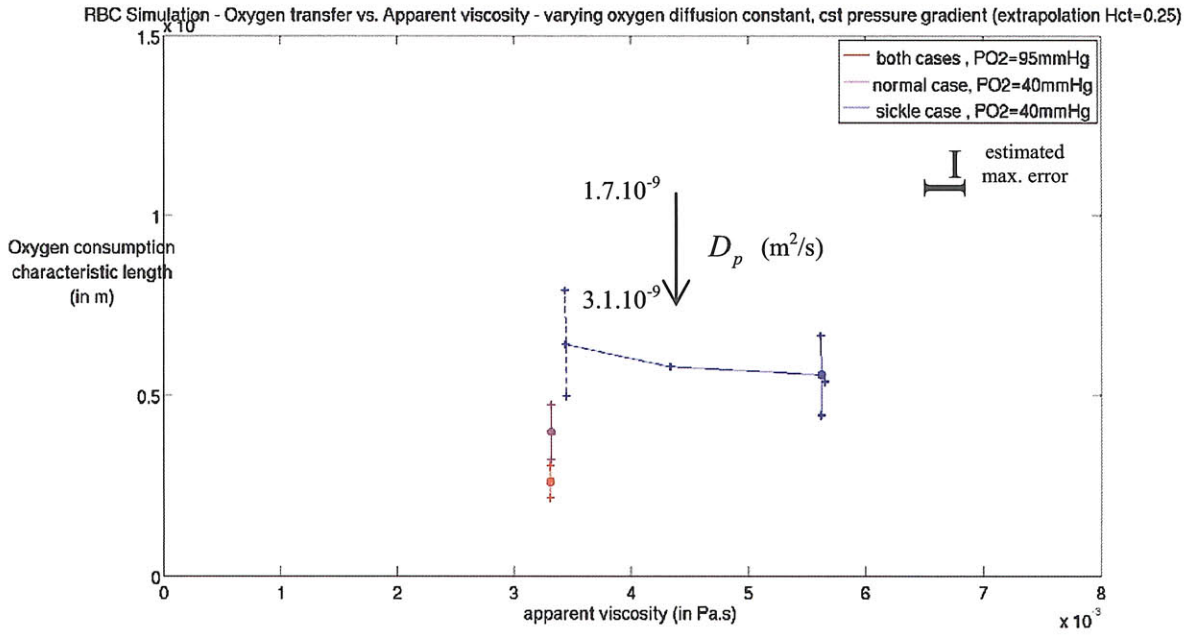


*Figure 4.2.9 : case study G : variable oxygen diffusion constant in blood plasma (with dashed points as extrapolation of the case Hct = 0.25).*

Finally, Figure 4.2.10 shows the results of case study H, where we vary blood density. As we see, the small relative variation of blood density does not lead to any appreciable change, neither in apparent viscosity, nor in oxygen delivery performance. In fact, the changes obtained end up well below the estimated precision of our simulations.

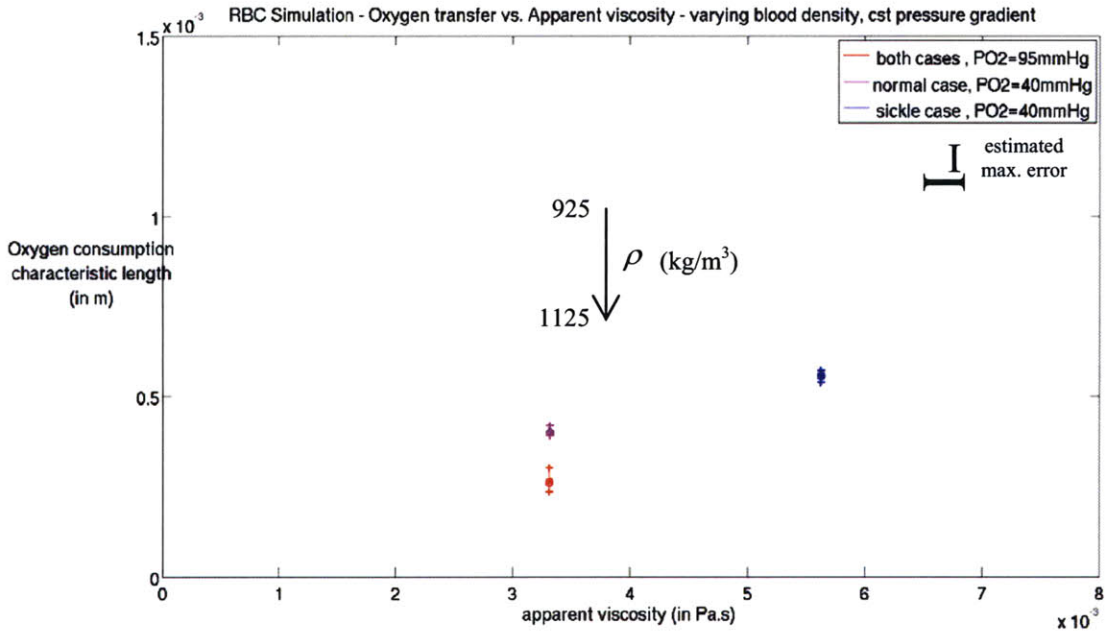


*Figure 4.2.10 : case study H : variable blood density.*

## 4.3. Conclusions on potential directions for medical research

Table 4.3.1 recaps the results obtained in the proposed study of potential therapeutical targets. Our research has demonstrated with the current model, the existence of 2 potential therapeutic opportunities accessible by a single parametric variation. The first positive result is related to an enlargement of capillary vessel size, where we have showed the considerable impact on both blood dynamics and oxygen delivery. Although the feasibility remains highly arguable, this result constitutes a very powerful direction for medical research. The second positive result is related to an increase in the effective oxygen diffusion constant, which combined with the low hematocrit of sickle cell patients constitutes an original research hypothesis to treat sickle cell disease. This important result

strongly supports further research on free oxygen carriers in blood plasma as a possible new therapy for sickle cell disease. Finally, our simulation results suggested that decreasing plasma viscosity may be a possible third option for improvement, although apparently limited in extent.

| Parameter | idea | efficient target ? | comments |
|---|---|---|---|
| $R_w$ | increase | Yes | better at constant pressure gradient (= within organ) than at constant inflow (=along capillary) |
| $\bar{v}_{in}$ | increase | No | decreases apparent viscosity, but deteriorates oxygen transfer |
| $\overline{\left(\frac{dp}{dz}\right)}$ | increase | | |
| $Hct$ | increase | No | improves oxygen transfer, but increases apparent viscosity |
| $\mu_p$ | decrease | Maybe | decreases apparent viscosity, and oxygen delivery may be partially restored by the organism (hematocrit compensation) |
| $D_p$ | increase | Yes | improves greatly the state of anemia, and is likely to be a happy combination with a low hematocrit level |
| $\rho$ | decrease | No | very limited effects, at a high risk |

*Table 4.3.1 : Conclusions of the case studies on potential therapeutical targets.*

# 5. Conclusions

## 5.1. Doctoral contribution

The doctoral work presented in this thesis has successfully :

- defined a rigorous model for blood dynamics in the microcirculation. This model not only gathers the most recent and most detailed theoretical description of blood dynamics and oxygen transport, but is also designed to be able to address specific issues that require the combination of **fluid dynamics**, **RBC membrane mechanics** and **oxygen convection, diffusion and consumption**. The resulting number of physical parameters has offered possible implementations of a large variety of scenarios and comparative studies.

- designed a comprehensive model for sickle cell disease. This model is based on an original modeling of the sickling mechanism, taking advantage of recent progress made in understanding the molecular growth of sickle hemoglobin (HbS) polymers. This innovative model has allowed a systematic assessment of the abnormal characteristics of blood flow, with a strong emphasis on the physical causes and the chain mechanism leading to impaired blood properties.

- used simulation results to improve our knowledge of blood microcirculation and sickle cell disease. In particular, we have successfully demonstrated the quantitative influence of some parameters reflecting a variety of physiological situations. Among the many observations, we were able to report the evidence of a maximum of oxygen transport with respect to varying vessel sizes. We also identified clearly the consequences of a reduced hematocrit among sickle cell patients, being beneficial to the apparent viscosity, but aggravating oxygen delivery performance. The modified dynamics of sickle blood at low hematocrit strongly support the hypothesis of a natural adaptation to sickling RBCs, and provide also a rational explanation to the unpredictability of sickle cell crises. Sickle cell anemia has thus been quantitatively related to its combined causes, sickling RBCs and reduced blood hematocrit. Finally, from our improved understanding has emerged a concise problematic to address potential therapies for sickle cell disease. To provide a quantitative

assessment of potential therapeutical targets, our methodology proposed to focus on the measured impact of induced parametric changes on both apparent viscosity and oxygen delivery performance.

- identified and assessed therapeutic directions for the treatment of sickle cell disease. The opportunity of further research on specific therapeutical targets was established, based on available medical implementations, on the simulated effects on blood dynamics and oxygen delivery, and on possible compensatory mechanisms by the organism (i.e. the adaptation of hematocrit to regulate blood viscosity).

This research has unveiled the possibilities of novel medical research based on large-scale numerical simulations and systematic analysis of parametric variations, and intends to pave the way for the development of innovative therapeutic directions.

## 5.2. Future steps for sickle cell research, determination of risk factors for crises

In light of our results, the need for further research has emerged in a few directions. Firstly, experimental research is obviously needed to complement our results. Not only would we benefit from getting more information about the disease, and refining our model, but also from being able to verify our hypotheses, our predictions and conclusions. Direct measurements of quantities such as apparent viscosity in capillary-sized vessels, whether in vitro or in vivo, is an example of data where very little documentation was found for sickle cell disease. On the other hand, more details about the mechanisms of hemoglobin polymerization would also improve our model, allow us to estimate more directly the model spring constants and length function of the HbS polymer, or even suggest larger model improvements, such as a direct implementation of Ferrone's model.

The second research opportunity is clearly to use our results to identify risk factors for crises. With medical research showing the driving factors of sickle cell crises, the current model could be used to identify possible correlations between the risk of crises and blood dynamics. For example, the occurrence of crises could be compared to how close to the capillary wall the RBCs end up in our model, for varying physiological situations. Then, modern techniques to visualize blood flow in real time could be used to measure various quantities such as blood velocity in a sickle cell patient, and our model would participate in the elaboration of simple diagnostic tools. This would be a first

step to potentially provide successful monitoring of physical activity, blood composition and other physiological factors as many indicators of risk probabilities of vessel occlusion. To extend this field of research, we could also look at situations involving physical activity and reduced oxygenation from the lungs (such as in low-pressurized environments).

A third research opportunity resides in using numerical simulations to predict the effects of existing or upcoming therapies. For example, a recent paper suggested possible improvements in the condition of sickle cell patients from the combination of EPO with hydroxyurea [94]. An appropriate numerical model could help us here in understanding better the mixed interactions between such drugs and sickle blood, determine the optimal proportions and measure the possible drawbacks.

## 5.3. Simulation model as an analytical tool : extension of parametric studies, integration in larger models

Finally, we hope that our work can contribute to the development of other blood research topics.

Firstly, further work is expected to address more complex descriptions of blood flow (converging-diverging channels, asymmetric time-dependent flow, bifurcations, ...). Various research publications address these issues separately, and can be already used to grow our model.

Recent bioengineering models have found a large echo in the field of cardiovascular diseases and artificial heart engineering. On the other end models of the microcirculation have also expanded recently, and our work is intended to participate in the development of this area. Through the study of blood dynamics in vessel networks, and the development of organ-specific models, the cardiovascular and microcirculation research fields are eventually expected to meet and allow a complete modeling of blood circulation. With this perspective in mind, our work emphasizes the possibilities of large multi-variable studies, to successfully reproduce, interpret and predict various physiological observations, for both natural and induced situations, with the possibilities of a complete global assessment of the blood circulation.

The inclusion of the problematic of oxygen delivery, and its exploitation to achieve specific research purposes, can be generalized to any substance subject to blood distribution and regulation, with considerable impact on medical research. Our work not only showed the investigation of a particular research problem, but also the design of a whole methodology to approach research topics involving blood transport. In this context, similarly-designed blood simulation models are to be used

not only to improve our understanding, but also to help redefine research objectives in very specific terms, and use synthetic quantitative methods for systematic assessment of research hypotheses.

Last but not least, our work could be used to address directly other blood diseases with minor changes. This includes investigation of other RBCs abnormalities, in size (anisocytosis, macrocytosis, microcytosis), in shape (acanthrocytes, echinocytes, elliptocytes, keratocytes, spherocytes, spicules, leptocytes a.k.a. target cells, dacrocytes a.k.a. teardrop cells, RBC rouleaux), or in intracellular structure (normoblasts a.k.a. nucleated cells, reticulocytes, siderocytes, basophilic stippling, Heinz bodies, Cabot's rings). This includes also dynamics of normal and abnormal white blood cells. Last but not least, recent findings have shown evidence of abnormal RBC dynamics among patients infected with malaria [47], which therefore constitutes another potential topic for future research.

# Appendix A : Oxygen dissociation curves

The 2 main proteins binding oxygen in the human body are hemoglobin and myoglobin. Despite their similar function, they have indeed very different binding properties. Myoglobin is a globular protein (globin) containing a non-protein heme group (which binds oxygen through an iron ion), whereas hemoglobin is an assembly of 4 globin subunits, each having its own heme group. Oxygen binding to a hemoglobin tetramer comes with conformational changes, which are significantly improving the binding capability of the other empty sites. Therefore, the binding of oxygen to hemoglobin is characteristic of "cooperative binding", while myoglobin is not.

These properties are reflected in the oxygen dissociation equations and profiles of myoglobin and hemoglobin.

The binding of oxygen to myoglobin is chemically represented by the following reaction :

$$Mb + O_2 \rightleftarrows MbO_2$$

Using the law of mass action and assuming dilute solutions (to use concentrations instead of activities), the equilibrium expression is :

$$K_{Mb} = \frac{[MbO_2]}{[Mb]\,[O_2]}, \tag{A.1}$$

where $[O_2]$, $[Mb]$, $[MbO_2]$ are respectively the concentrations of free oxygen, unbound myoglobin and bound myoglobin, and $K_{Mb}$ is the reaction equilibrium constant, mainly dependent on temperature and pH. Substituting in Equation (A.1) the unbound myoglobin by the total (bound and unbound) myoglobin $[Mb]_{tot}$, we can rewrite equilibrium as :

$$[MbO_2] = [Mb]_{tot}\,\frac{K_{Mb}\,[O_2]}{1 + K_{Mb}\,[O_2]}. \tag{A.2}$$

Then defining the myoglobin saturation $S^{Mb}$ as the ratio of bound myoglobin to total myoglobin, Equation (A.2) becomes :

$$S^{Mb} = \frac{K_{Mb}\,[O_2]}{1 + K_{Mb}\,[O_2]}, \tag{A.3}$$

which is the Hill equation applied to myoglobin, (non-cooperative binding form). Using Henry's law for a dilute solution of oxygen, $[O_2] = \alpha\, p_{O_2}$ with $\alpha$ the solubility constant, and replacing the constants with the partial pressure at 50% saturation, Equation (A.2) becomes :

$$S^{Mb} = \frac{p_{O_2}}{p^{Mb}_{O_2,50\%} + p_{O_2}}, \tag{A.4}$$

where $p^{Mb}_{O_2,50\%} = (K_{Mb}\,\alpha)^{-1}$.

Similarly, the binding of oxygen to hemoglobin is represented by the following equation :

$$Hb_4 + 4\,O_2 \rightleftarrows Hb_4O_8$$

Note that this assumes that all oxygen molecules would bind together, and neglects the presence of all intermediate compounds. Using the law of mass action, the equilibrium expression is :

$$K_{Hb} = \frac{[Hb_4O_8]}{[Hb_4]\,[O_2]^4}, \tag{A.5}$$

where $[O_2]$, $[Hb_4]$, $[Hb_4O_8]$ are respectively the concentrations of free oxygen, unbound hemoglobin and bound hemoglobin, and $K_{Hb}$ is the reaction equilibrium constant, mainly dependent on temperature, pH, and also on concentration of some interfering molecules such as $CO_2$, $CO$ and some compounds produced in the erythrocytes (such as the 2,3-DPG organophosphate). Substituting in Equation (A.5) the unbound hemoglobin by the total (bound and unbound) hemoglobin $[Hb]_{tot}$, we get :

$$[Hb_4O_8] = [Hb]_{tot}\,\frac{K_{Hb}\,[O_2]^4}{1 + K_{Hb}\,[O_2]^4}. \tag{A.6}$$

Then defining the hemoglobin saturation $S^{Hb}$ as the ratio of bound hemoglobin to total hemoglobin, Equation (A.6) becomes :

$$S^{Hb} = \frac{K_{Hb}\,[O_2]^4}{1 + K_{Hb}\,[O_2]^4}, \tag{A.7}$$

which is the Hill equation applied to hemoglobin, (cooperative binding form). In Equation (A.7) the Hill coefficient is 4, which assumes an elementary binding mechanism where the 4 oxygen molecules bind simultaneously to hemoglobin, and leads to the associated increased propensity to bind (cooperativity). However, the assumption of all oxygen molecules binding together (infinite cooperativity) is never matched (intermediate compounds exist), and moreover the equilibrium

constants are different for the α- and the β-globins binding to oxygen. Experimental data has shown that the effective Hill coefficient of the oxyhemoglobin dissociation profile was significantly lower than 4, about 2.2 at the temperature and pH of human body [108]. Using Henry's law and introducing the equilibrium partial pressure at 50% saturation, Equation (A.7) becomes :

$$S^{Hb} = \frac{{p_{O_2}}^n}{{p_{O_2,50\%}^{Hb}}^n + {p_{O_2}}^n}, \tag{A.8}$$

where $n$ is the effective Hill coefficient, and $p_{O_2,50\%}^{Hb} = (K_{Hb}\ \alpha)^{-n}$.

The oxygen dissociation curves are shown in Figure A.1 (Note : the constants used there slightly differ from our model). The myoglobin curve is hyperbolic, while the hemoglobin curve is sigmoidal. Among factors known to influence the dissociation curve, temperature shifts it upwards, pH downwards (which is known as the Bohr effect), and 2,3-DPG concentration shifts it upwards. More complex empirical models exist, such as Kelman's equation, with extensions to include temperature, pH and other factors (Source : http://www.ventworld.com/resources/oxydisso/dissoc.html).

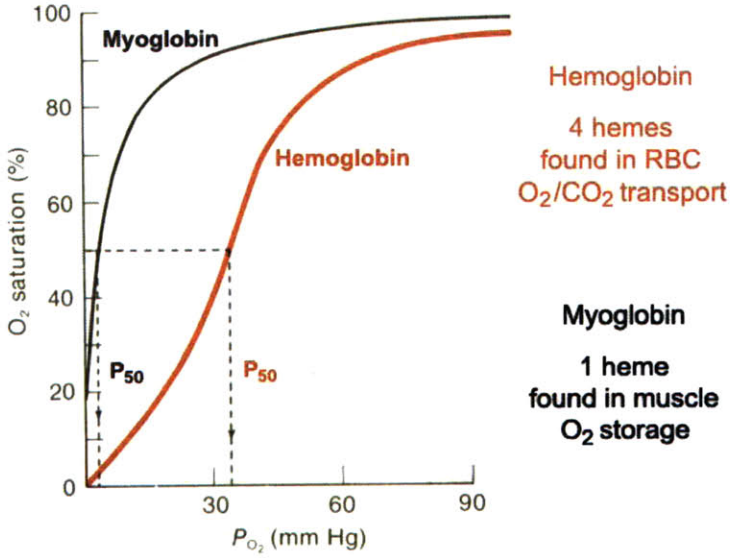


*Figure A.1 : Hemoglobin and myoglobin dissociation curves (source:http://www.colorado.edu/intphys/Class/IPHY3430-200).*

In the case of sickle hemoglobin, experimental data shows a rightward shift of the profile, as presented by Berger and King [123]. Figure A.2 shows this shift, which Berger has related to a simple change in $p_{O_2,50\%}^{Hb}$ from about 25 mmHg to 40 mmHg ($n$ is also closer to 3).

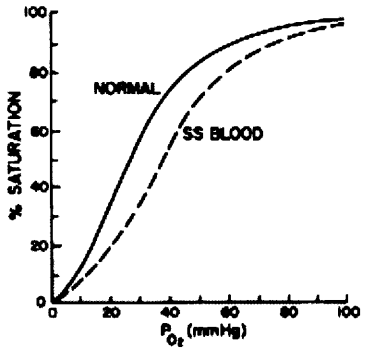


Oxygen dissociation curves of human normal hemoglobin and hemoglobin from individuals with sickle-cell anemia.

*Figure A.2 : Sickle hemoglobin dissociation curve (from Berger and King [123]).*

# Appendix B-1 : Derivation of the generalized constitutive equations – fluid dynamics

The dimensions of interest of our research (~μm) are appropriate to use classical continuum mechanics throughout this work. In this context blood plasma and cytoplasm are to be described with fluid mechanics, starting with the generalized Navier-Stokes equation :

$$\frac{\partial \rho}{\partial t} + \vec{v}\cdot\vec{\nabla}\rho + \rho\,\vec{\nabla}\cdot\vec{v} = 0\,, \tag{B.1}$$

$$\rho\left(\frac{\partial \vec{v}}{\partial t} + (\vec{v}\cdot\vec{\nabla})\vec{v}\right) = \vec{\nabla}\cdot\overline{\overline{T}} + \rho\,\vec{g} + \vec{f}_b\,\delta\left(\vec{r} - \vec{X}_b\right), \tag{B.2}$$

where $\rho(\vec{r},t)$ is the fluid density, $\vec{v}(\vec{r},t)$ is the velocity vector, $\vec{\nabla}$ the del operator (spatial vector differential), $\vec{g}(\vec{r},t)$ the total body force per unit mass, $\overline{\overline{T}}(\vec{r},t)$ the total stress tensor in the fluid (force per unit surface), $\vec{f}_b(\vec{X}_b)$ the total force per unit surface at the fluid boundary, whose surface is defined by $\vec{X}_b(\vec{s}_b,t)$ and parameterized by $\vec{s}_b$, and $\delta$ is a 1-dimensional Dirac distribution. In our case body forces are essentially gravitation (Lorentz electromagnetic forces are ignored since we ignore ionic activity). Examination of the Froude number further justifies ignoring gravitation. Also, the very low Mach number justifies assuming the fluid incompressible, i.e. of constant density (see dimensional analysis in Appendix C). Equations (B.1) and (B.2) thus become :

$$\vec{\nabla}\cdot\vec{v} = 0\,, \tag{B.3}$$

$$\rho\left(\frac{\partial \vec{v}}{\partial t} + (\vec{v}\cdot\vec{\nabla})\vec{v}\right) = \vec{\nabla}\cdot\overline{\overline{T}} + \vec{f}_b\,\delta\left(\vec{r} - \vec{X}_b\right). \tag{B.4}$$

The stress tensor is usually first split in isotropic and deviatoric (traceless) tensors. The trace of the stress tensor is the mean normal (volumetric) stress, whose opposite number is commonly referred to as the mechanical pressure $p_M$ :

$$\overline{\overline{T}} = -\,p_M\,\overline{\overline{I}} + \overline{\overline{T_D}}\,, \tag{B.5}$$

$$\vec{\nabla}\cdot\overline{\overline{T}} = -\,\vec{\nabla}p_M + \vec{\nabla}\cdot\overline{\overline{T_D}}\,, \tag{B.6}$$

where $\overline{\overline{I}}$ is the identity tensor. With the tensor double dot product notation, a mathematical way to express $p_M$ and $\overline{\overline{T_D}}$ is :

$$p_M = -\overline{\overline{T}} : \overline{\overline{I}} \,, \tag{B.7}$$

$$\overline{\overline{T_D}} = \overline{\overline{T}} - \left(\overline{\overline{T}} : \overline{\overline{I}}\right) \overline{\overline{I}} \,. \tag{B.8}$$

The common assumption of Newtonian fluid corresponds to 3 hypotheses. The first hypothesis are that stresses departing from equilibrium (static fluid at rest) are caused by strain rates only, to which they are linearly proportional (this differs noticeably from elastic behavior, typical of solids, where stresses are usually associated with the strain tensor). Assuming that the fluid at rest is characterized by only normal, isotropic thermodynamic forces, this leads to express the stress tensor alternatively as the sum of a hydrostatic pressure tensor and a viscous stress tensor :

$$\overline{\overline{T}} = -p\,\overline{\overline{I}} + \overline{\overline{T_V}} \,, \tag{B.7}$$

$$\vec{\nabla} \cdot \overline{\overline{T}} = -\vec{\nabla} p + \vec{\nabla} \cdot \overline{\overline{T_V}} \,, \tag{B.8}$$

where the thermodynamic pressure $p$ is only a function of temperature and density, while $\overline{\overline{T_V}}$ is a linear function of the strain rate tensor (in fact, $p$ is the resultant of stresses associated with thermal velocities, which are not accounted for as velocity components in continuum mechanics). The second and third hypotheses are that fluid stresses are isotropic, i.e. independent of rotation of the coordinate system, and that only the symmetric part of the strain rate tensor causes stress (the anti-symmetric part corresponds to fluid rotation). The 3 hypotheses of Newtonian fluid reduce $\overline{\overline{T_V}}$ to a simple expression involving only 2 parameters :

$$\overline{\overline{T_V}} = \lambda \left(\overline{\overline{\varepsilon}} : \overline{\overline{I}}\right) \overline{\overline{I}} + 2\,\mu\,\overline{\overline{\varepsilon}} \,, \tag{B.9}$$

$$\overline{\overline{\varepsilon}} = \frac{1}{2}\left(\vec{\nabla}\vec{v} + (\vec{\nabla}\vec{v})^T\right), \tag{B.10}$$

where $\lambda$ and $\mu$ are scalar constants that depend mainly on the temperature, $\overline{\overline{\varepsilon}}$ is the symmetric strain rate tensor, and $\overline{\overline{\varepsilon}} : \overline{\overline{I}}$ is the trace of the strain rate tensor (double dot product with the identity tensor). $\overline{\overline{T_V}}$ is usually reorganized in its normal stress component (diagonal terms) and shear stress component (no diagonal terms). Because the viscous stress tensor is isotropic, the normal stress components are all equal, and the shear stress can be expressed as a deviatoric term :

$$\overline{\overline{T_V}} = \left(\lambda + \frac{2}{3}\mu\right)\left(\overline{\overline{\varepsilon}} : \overline{\overline{I}}\right)\overline{\overline{I}} + 2\,\mu\left(\overline{\overline{\varepsilon}} - \frac{1}{3}\left(\overline{\overline{\varepsilon}} : \overline{\overline{I}}\right)\overline{\overline{I}}\right), \tag{B.11}$$

or using $\overline{\overline{\varepsilon}} : \overline{\overline{I}} = \vec{\nabla}\cdot\vec{v}$ and substituting $\lambda$ for $\mu_b = \lambda + \frac{2}{3}\mu$ :

$$\overline{\overline{T_V}} = \mu_b\left(\vec{\nabla}\cdot\vec{v}\right)\overline{\overline{I}} + 2\,\mu\left(\overline{\overline{\varepsilon}} - \frac{1}{3}\left(\vec{\nabla}\cdot\vec{v}\right)\overline{\overline{I}}\right). \tag{B.12}$$

We have now decomposed the viscous stress $\overline{\overline{T_V}}$ with a mean normal stress and a shear deviatoric term (shear means no diagonal term). Therefore we can identify for a Newtonian fluid the second term (shear stress tensor) with the deviatoric tensor $\overline{\overline{T_D}}$, and relate mechanical and thermodynamic pressure :

$$p_M = p - \mu_b\left(\vec{\nabla}\cdot\vec{v}\right). \tag{B.13}$$

The general form of the Navier-Stokes equations for a Newtonian fluid is therefore :

$$\frac{\partial\rho}{\partial t} + \vec{v}\cdot\vec{\nabla}\rho + \rho\,\vec{\nabla}\cdot\vec{v} = 0\,, \tag{B.1}$$

$$\rho\left(\frac{\partial\vec{v}}{\partial t} + (\vec{v}\cdot\vec{\nabla})\vec{v}\right) = -\vec{\nabla}p + \vec{\nabla}\left[\left(\mu_b - \frac{2}{3}\mu\right)\left(\vec{\nabla}\cdot\vec{v}\right)\right] + \vec{\nabla}\cdot\left(2\mu\,\overline{\overline{\varepsilon}}\right) + \vec{f}_b\,\delta\left(\vec{r} - \vec{X}_b\right), \tag{B.14}$$

where $\mu$ and $\mu_b$ are commonly called the dynamic (shear) viscosity and bulk viscosity. The bulk viscosity is generally small compared to the dynamic viscosity (see Appendix C). However, if we assume incompressibility and constant viscosity coefficients (or constant temperature), we get :

$$\vec{\nabla}\cdot\vec{v} = 0\,, \tag{B.3}$$

$$\rho\left(\frac{\partial\vec{v}}{\partial t} + (\vec{v}\cdot\vec{\nabla})\vec{v}\right) = -\vec{\nabla}p + \mu\,\nabla^2\vec{v} + \vec{f}_b\,\delta\left(\vec{r} - \vec{X}_b\right), \tag{B.15}$$

where we have used $\vec{\nabla}\cdot\overline{\overline{\varepsilon}} = \frac{1}{2}\left(\nabla^2\vec{v} + \vec{\nabla}\left(\vec{\nabla}\cdot\vec{v}\right)\right)$. Note that, expressed separately inside and outside the RBC, Equations (B.15) can be written without the last term, which becomes a boundary condition.

# Appendix B-2 : Derivation of the generalized constitutive equations – oxygen transport

In the context of classical continuum mechanics, oxygen transport is characterized by the general scalar transport equations :

$$\frac{\partial c}{\partial t} + \vec{\nabla} \cdot \vec{N} = R \,, \tag{B.16}$$

$$\vec{N} = c\vec{v} + \vec{J} \,, \tag{B.17}$$

where $c(\vec{r},t)$ is the oxygen concentration in moles per unit volume, $\vec{N}$ is the local oxygen flux vector, $R$ is the rate of (algebraic) production of free oxygen, $\vec{v}$ is the velocity vector, and $\vec{J}$ is the local diffusion flux (there is no other known source of flux for oxygen, which differs from transport equations applied to other quantities like energy, which can be subject to radiative transfer for example). The diffusion flux is expressed using Fick's law of diffusion :

$$\vec{J} = - D \vec{\nabla} c \,, \tag{B.18}$$

where $D$ is the diffusion constant or diffusivity, which depends on various factors such as temperature, density, or chemical composition of the fluid. Assuming constant temperature and density (see Appendix C for dimensional analysis), we limit the possible values of $D$ to the different regions of our capillary flow model, and assume that each of these values is constant. Therefore the transport equation simplifies to :

$$\frac{\partial c}{\partial t} + \vec{\nabla} \cdot (c\vec{v}) = D \nabla^2 c + R \,, \tag{B.19}$$

The production/consumption of free oxygen is of 3 sorts in our case. First, a pure consumption rate is hypothesized in some regions, with a constant rate $M$. Secondly, free oxygen binds and is released by hemoglobin proteins in the RBCs. This is characterized by the law of mass action derived from the oxyhemoglobin dissociation reaction :

$$Hb_4 + 4\, O_2 \rightleftarrows Hb_4O_8$$

$$R^{Hb} = \left.\frac{\partial c}{\partial t}\right|_{chem}^{Hb} = 4\, k_{-1}^{Hb} [Hb_4O_8] - 4\, k_1^{Hb} [Hb_4]\, c^4 \,, \tag{B.20}$$

where $k_1^{Hb}$ and $k_{-1}^{Hb}$ are the kinetic reaction rate constants of the forward and backward reactions, and $[Hb_4]$ and $[Hb_4O_8]$ are respectively the concentration of unbound hemoglobin and (bound) oxyhemoglobin. Note that for simplicity, we assume for now that all oxygen molecules bind together at once (infinite cooperativity). Substituting $[Hb_4]$ by the total (bound and unbound) hemoglobin concentration $[Hb_4]_{tot}$, and defining the oxyhemoglobin saturation $S^{Hb}$, we get :

$$[Hb_4] = [Hb_4]_{tot} - [Hb_4O_8] , \tag{B.21}$$

$$S^{Hb} = \frac{[Hb_4O_8]}{[Hb_4]_{tot}} , \tag{B.22}$$

$$R^{Hb} = \left.\frac{\partial c}{\partial t}\right|_{chem}^{Hb} = [Hb_4]_{tot} \left(4\ k_{-1}^{Hb}\ S^{Hb} - 4\ k_1^{Hb}\ (1 - S^{Hb})\ c^4\right) , \tag{B.23}$$

Substituting the second reaction constant, Equation (B.23) can be reformulated :

$$c_{50\%}^{Hb} = \left(\frac{k_{-1}^{Hb}}{k_1^{Hb}}\right) , \tag{B.24}$$

$$R^{Hb} = \left.\frac{\partial c}{\partial t}\right|_{chem}^{Hb} = 4\ k_{-1}^{Hb}\ [Hb_4]_{tot} \left(S^{Hb} - (1 - S^{Hb}) \left(\frac{c}{c_{50\%}^{Hb}}\right)^4\right) , \tag{B.25}$$

where $c_{50\%}^{Hb}$ is the equilibrium oxygen concentration at 50% saturation. Since the concentration of oxyhemoglobin is implicitly expressed in the resulting equation through $S^{Hb}$, we need to add a transport equation to determine $S^{Hb}(\vec{r},t)$ :

$$\frac{\partial S^{Hb}}{\partial t} + \vec{\nabla}\cdot(S^{Hb}\vec{v}) = D^{Hb}\ \nabla^2 S^{Hb} - \frac{R^{Hb}}{4\ [Hb_4]_{tot}} , \tag{B.26}$$

where $D^{Hb}$ is the diffusivity of oxyhemoglobin, and its production rate was determined using the same reaction. Finally, introducing the total hemoglobin concentration in terms of moles of protein subunits per volume, $[Hb]$, Equations (B.25) and (B.26) become :

$$R^{Hb} = \left.\frac{\partial c}{\partial t}\right|_{chem}^{Hb} = k_{-1}^{Hb}\ [Hb] \left(S^{Hb} - (1 - S^{Hb}) \left(\frac{c}{c_{50\%}^{Hb}}\right)^4\right) , \tag{B.27}$$

$$\frac{\partial S^{Hb}}{\partial t} + \vec{\nabla}\cdot(S^{Hb}\vec{v}) = D^{Hb}\ \nabla^2 S^{Hb} - \frac{R^{Hb}}{[Hb]} . \tag{B.28}$$

At equilibrium, the rate of production of oxygen is zero, leading to the familiar result represented in the oxyhemoglobin dissociation curve (See Appendix A).

At this point, the assumption of infinite cooperativity needs to be addressed. Experimental data shows that intermediate components cannot be totally ignored, so that our simple reaction does not really qualify as "elementary" to apply the law of mass action, and that a more complex group of intermediate reactions would need to be taken into account to be more accurate. To resolve this problem, experimental data is used to determine the Hill coefficient to replace the exponent 4 at equilibrium (see Appendix A). The resulting semi-empirical model gives :

$$R^{Hb} = \left.\frac{\partial c}{\partial t}\right|_{chem}^{Hb} = k_{-1}^{Hb}\,[Hb]\left(S^{Hb} - (1 - S^{Hb})\left(\frac{c}{c_{50\%}^{Hb}}\right)^{n}\right), \tag{B.29}$$

where the Hill coefficient $n$ is approximately equal to 2.2 (and close to 3 for sickle hemoglobin).

Finally, free oxygen is bound and released by myoglobin in the muscular tissue. The binding reaction of myoglobin is very similar to the one of hemoglobin, except that only one molecule of oxygen binds each protein :

$$Mb + O_2 \rightleftarrows MbO_2$$

Deriving the rate of oxygen production in a similar manner to the case of hemoglobin, we obtain with similar notations:

$$R^{Mb} = \left.\frac{\partial c}{\partial t}\right|_{chem}^{Mb} = k_{-1}^{Mb}\,[Mb]\left(S^{Mb} - (1 - S^{Mb})\left(\frac{c}{c_{50\%}^{Mb}}\right)\right). \tag{B.30}$$

$$\frac{\partial S^{Mb}}{\partial t} + \vec{\nabla}\cdot(S^{Mb}\vec{v}) = D^{Mb}\,\nabla^2 S^{Mb} - \frac{R^{Mb}}{[Mb]}. \tag{B.31}$$

However, the oxy-myoglobin dissociation rate constant is much higher than for the hemoglobin (see Appendix C), which allows us to assume local equilibrium of oxygen with the myoglobin. This corresponds to :

$$S^{Mb} = \frac{c}{c_{50\%}^{Mb} + c}, \tag{B.32}$$

Combining now Equations (B.19), (B.28), (B.29), (B.30) and (B.31), we obtain :

$$\frac{\partial c}{\partial t} + \vec{\nabla}\cdot(c\vec{v}) = D\,\nabla^2 c + k_{-1}^{Hb}\,[Hb]\left(S^{Hb} - (1 - S^{Hb})\left(\frac{c}{c_{50\%}^{Hb}}\right)^{n}\right)$$

$$+ k_{-1}^{Mb}\,[Mb]\left(S^{Mb} - (1 - S^{Mb})\left(\frac{c}{c_{50\%}^{Mb}}\right)\right) + M, \tag{B.33}$$

$$\frac{\partial S^{Hb}}{\partial t} + \vec{\nabla}\cdot(S^{Hb}\vec{v}) = D^{Hb}\nabla^2 S^{Hb} - k_{-1}^{Hb}\left(S^{Hb} - (1 - S^{Hb})\left(\frac{c}{c_{50\%}^{Hb}}\right)^n\right), \quad \text{(B.34)}$$

$$[Mb]\left(\frac{\partial S^{Mb}}{\partial t} + \vec{\nabla}\cdot(S^{Mb}\vec{v})\right) = D^{Mb}[Mb]\nabla^2 S^{Mb} - k_{-1}^{Mb}[Mb]\left(S^{Mb} - (1 - S^{Mb})\left(\frac{c}{c_{50\%}^{Mb}}\right)\right). \quad \text{(B.35)}$$

Deriving from Equation (B.32) :

$$dS^{Mb} = \frac{c_{50\%}^{Mb}}{(c_{50\%}^{Mb} + c)^2}\, dc\,, \quad \text{(B.36)}$$

and substituting Equation (B.36) in (B.35), then summing it with (B.33), we finally get the generalized system of equations for oxygen transport :

$$\left(1 + [Mb]\frac{c_{50\%}^{Mb}}{(c_{50\%}^{Mb} + c)^2}\right)\left(\frac{\partial c}{\partial t} + \vec{\nabla}\cdot(c\vec{v})\right) = \left(D + D^{Mb}[Mb]\frac{c_{50\%}^{Mb}}{(c_{50\%}^{Mb} + c)^2}\right)\nabla^2 c$$

$$+ k_{-1}^{Hb}[Hb]\left(S^{Hb} - (1 - S^{Hb})\left(\frac{c}{c_{50\%}^{Hb}}\right)^n\right) + M\,, \quad \text{(B.37)}$$

$$\frac{\partial S^{Hb}}{\partial t} + \vec{\nabla}\cdot(S^{Hb}\vec{v}) = D^{Hb}\nabla^2 S^{Hb} - k_{-1}^{Hb}\left(S^{Hb} - (1 - S^{Hb})\left(\frac{c}{c_{50\%}^{Hb}}\right)^n\right), \quad \text{(B.34)}$$

To complete this derivation, we introduce Henry's law to convert oxygen concentration to partial pressure (which has the additional property of being continuous across an infinitely thin membrane) :

$$c = \alpha\, p_{O_2}\,, \quad \text{(B.38)}$$

where $\alpha$ is the solubility constant of oxygen, and $p_{O_2}(\vec{r},t)$ is the partial pressure of oxygen. Assuming also flow incompressibility (see justification in Appendix C), substitution of variables gives eventually :

$$\left(\alpha + [Mb]\frac{p_{O_2,50\%}^{Mb}}{(p_{O_2,50\%}^{Mb} + p_{O_2})^2}\right)\left(\frac{\partial p_{O_2}}{\partial t} + \vec{v}\cdot\vec{\nabla}p_{O_2}\right) = \left(\alpha D + D^{Mb}[Mb]\frac{p_{O_2,50\%}^{Mb}}{(p_{O_2,50\%}^{Mb} + p_{O_2})^2}\right)\nabla^2 p_{O_2}$$

$$+ k_{-1}^{Hb}[Hb]\left(S^{Hb} - (1 - S^{Hb})\left(\frac{p_{O_2}}{p_{O_2,50\%}^{Hb}}\right)^n\right) + M\,, \quad \text{(B.39)}$$

$$\frac{\partial S^{Hb}}{\partial t} + \vec{v}\cdot\vec{\nabla}S^{Hb} = D^{Hb}\,\nabla^2 S^{Hb} - k_{-1}^{Hb}\left(S^{Hb} - (1 - S^{Hb})\left(\frac{p_{O_2}}{p_{O_2,50\%}^{Hb}}\right)^n\right), \tag{B.40}$$

where $p_{O_2,50\%}^{Mb}$ and $p_{O_2,50\%}^{Hb}$ are the equivalent partial pressures of oxygen at 50% saturation of myoglobin and hemoglobin, respectively.

# Appendix B-3 : Derivation of the generalized constitutive equations – membrane mechanics

In this appendix we derive the constitutive equations for the RBC membrane. For simplicity, we assume an axisymmetric configuration and will use cylindrical coordinates. The membrane is to be modeled as a 2-D elastic solid, subject to surface tensions, bending moments and shear stresses. Figure B.1 recalls some definitions and orientation conventions used throughout this thesis.

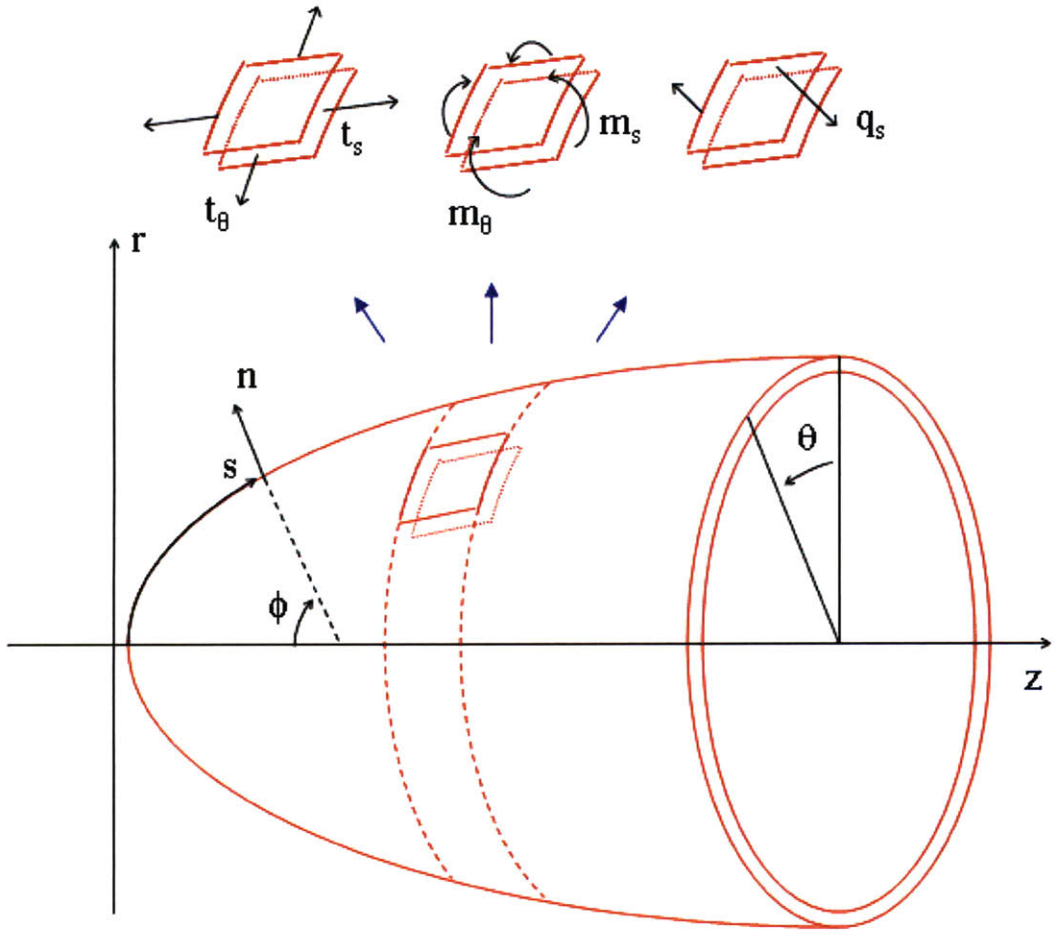


*Figure B.1 : Curvilinear coordinates for axisymmetric RBC membrane and membrane stresses convention (model of superposed leaflets).*

Because of axisymmetry, the membrane surface is parameterized with only one curvilinear variable $s$. Any point on the surface is defined by a minimum-stress configuration with a position

"at rest" $s_0$, so that $s$ is a function of $s_0$ and $t$ : $s = s(s_0,t)$. To replace the membrane stresses within the surrounding plasma and cytoplasm, we use in addition to the cylindrical coordinates $(z,r,\theta)$ the local angle of the normal to the surface to the axis to symmetry, $\phi(s)$. Denoting the radius of the membrane at a position $s$ by $R(s)$, we get the simple geometrical relation :

$$\frac{dR}{ds} = \cos(\phi) \ . \tag{B.41}$$

Let us now write the components of the total forces and moments, by analyzing them on a differential surface element from $s$ to $ds$ and from $\theta$ to $d\theta$ (represented by the enlargements on the upper part of Figure B.1, and the 3 sketches on Figure B.2). Because of axisymmetry, local shear stresses only exist in the $s$ direction, and the total moment about the $s$ axis is zero everywhere. The differential components of total normal force, total tangential force, and total moment about the $\theta$ direction are derived from the local tensions in the $s$ and $\theta$ directions, $t_s(s)$ and $t_\theta(s)$, the shear stress in the $s$ direction $q_s(s)$, and the local moments per unit area, about the $\theta$ direction, $m_s(s)$, and about the $s$ direction, $m_\theta(s)$ (the swapped notations for the local moments are inherited from Secomb's model [101]) :

$$\begin{aligned} dF_n \ = \ & - \ t_s(s+ds) \ \sin\big(\phi(s+ds)-\phi(s)\big) \ R(s+ds) \ d\theta \ - \ t_\theta(s) \ \sin\big((\theta+d\theta)-\theta\big) \ \sin(\phi) \ ds \\ & + \ q_s(s) \ R(s) \ d\theta \ - \ q_s(s+ds) \ R(s+ds) \ d\theta \ , \end{aligned} \tag{B.42}$$

$$\begin{aligned} dF_t \ = \ & - \ t_s(s) \ R(s) \ d\theta \ + \ t_s(s+ds) \ R(s+ds) \ d\theta \ - \ t_\theta(s) \ \sin\big((\theta+d\theta)-\theta\big) \ \cos(\phi) \ ds \\ & - \ q_s(s+ds) \ \sin\big(\phi(s+ds)-\phi(s)\big) \ R(s+ds) \ d\theta \ , \end{aligned} \tag{B.43}$$

$$\begin{aligned} dM_\theta \ = \ & - \ m_s(s) \ R(s) \ d\theta \ + \ m_s(s+ds) \ R(s+ds) \ d\theta \ - \ m_\theta(s) \ \sin\big((\theta+d\theta)-\theta\big) \ \cos(\phi) \ ds \\ & - \ q_s(s+ds) \ ds \ R(s+ds) \ d\theta \ . \end{aligned} \tag{B.44}$$

Defining the area of the differential element $dA = R\,d\theta\,ds$, the last 3 equations reduce to :

$$\frac{dF_n}{dA} \ = \ - \ t_s \ \frac{d\phi}{ds} \ - \ t_\theta \ \frac{\sin(\phi)}{R} \ - \ \frac{1}{R} \frac{d(R q_s)}{ds} \ , \tag{B.45}$$

$$\frac{dF_t}{dA} \ = \ \frac{1}{R} \frac{d(R t_s)}{ds} \ - \ t_\theta \ \frac{\cos(\phi)}{R} \ - \ q_s \ \frac{d\phi}{ds} \ , \tag{B.46}$$

$$\frac{dM_\theta}{dA} \ = \ \frac{1}{R} \frac{d(R m_s)}{ds} \ - \ m_\theta \ \frac{\cos(\phi)}{R} \ - \ q_s \ . \tag{B.47}$$

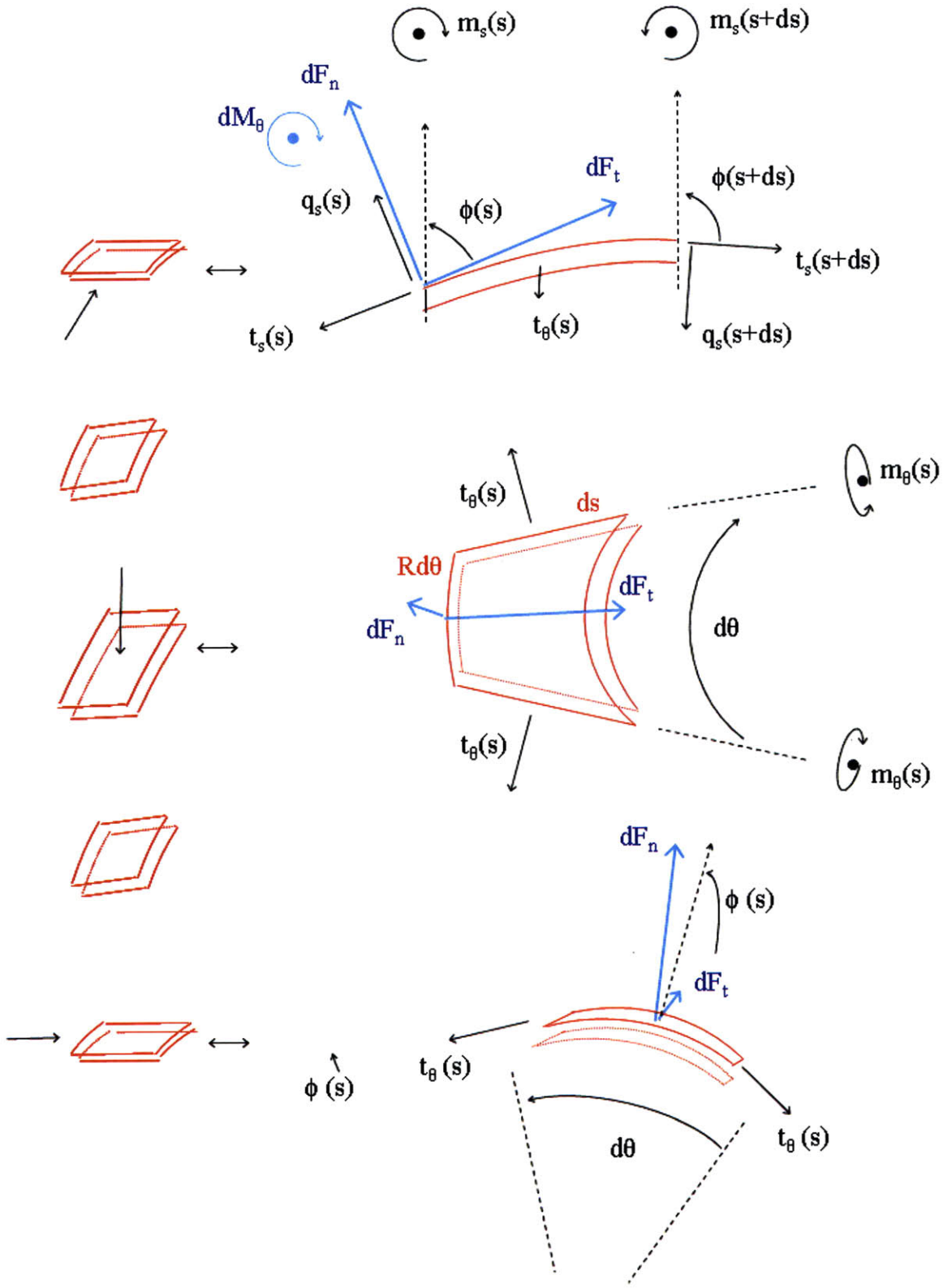


*Figure B.2 : Membrane tensions, stresses and moments on a differential element.*

Since the membrane is submerged in plasma and cytoplasm fluids, normal forces are naturally opposing pressure forces, while tangential forces oppose viscous stresses. There is no source of torque in the fluid, however, nor within the membrane. Therefore the total moment about the $\theta$ direction must cancel, giving :

$$0 = \frac{1}{R}\frac{d(Rm_s)}{ds} - m_\theta \frac{\cos(\phi)}{R} - q_s \,. \tag{B.48}$$

Finally, the bending moments are assumed to be locally isotropic, which is justified in the model of superposed leaflets for small area compressibility (for details see Evans and Skalak, p.109 [19]). This leads to $m_s = m_\theta = m$, and using Equation (B.41), our system of equations reduce to :

$$\frac{dF_n}{dA} = - t_s \frac{d\phi}{ds} - t_\theta \frac{\sin(\phi)}{R} - \frac{1}{R}\frac{d(Rq_s)}{ds}, \tag{B.45}$$

$$\frac{dF_t}{dA} = \frac{1}{R}\frac{d(Rt_s)}{ds} - t_\theta \frac{\cos(\phi)}{R} - q_s \frac{d\phi}{ds}, \tag{B.46}$$

$$\frac{dm}{ds} = q_s \,. \tag{B.49}$$

To complete these equations, we use constitutive equations for the local tensions and moment per unit area. These were presented in Section 1.2.3 and synthesized in Section 2.1.2 as :

$$\bar{t} = \frac{t_s + t_\theta}{2} = \sigma_0 + K_{bu}\left(\frac{ds}{ds_0}\frac{R}{R_0} - 1\right) \tag{45}$$

$$t_d = \frac{t_s - t_\theta}{2} = \frac{K_{sh}}{2}\left(\left(\frac{ds}{ds_0}\right)^2 - \left(\frac{R}{R_0}\right)^2\right) - \frac{B}{2}\left(\frac{d\phi}{ds} - \frac{\sin\phi}{R}\right)\left(\frac{d\phi}{ds} + \frac{\sin\phi}{R} - k_0\right), \tag{46}$$

$$q_s = - B\left(\frac{d^2\phi}{ds^2} + \frac{d}{ds}\left(\frac{\sin\phi}{R}\right)\right), \tag{47}$$

with all the moduli coefficients and index notations defined in Section 2.1.2. Equation (47) is derived from the constitutive equation for the local moment per unit area, combined with Equation (B.49).

# Appendix C : Dimensional Analysis

In this appendix we apply dimensional analysis to support hypotheses used in our model, or in other models we refer to.

The use of continuum mechanics is related to the Knudsen number. The Knudsen number is the ratio of the molecular mean free path to a reference length of the problem :

$$Kn = \frac{mfp}{dl} , \tag{C.1}$$

where $dl$ will be an order of magnitude of the smallest numerical length used in our simulations. The numerical scheme used gives for $dl$ about $\mathbf{1.10^{-7}\ m}$. The mean free path of a liquid is of the order of magnitude of intermolecular distances because of the important molecular interactions. Given its density $\rho$, and molecular weight $\overline{M}$, we can determine roughly $mfp$ as :

$$mfp \approx \left( \frac{\overline{M}}{\rho N_A} \right)^{\frac{1}{3}} , \tag{C.2}$$

where $N_A$ is Avogadro's number. Taking $\rho$ equal to $\mathbf{1025\ kg/m^3}$, $\overline{M}$ to $\mathbf{18\ g/mol}$ (i.e. roughly water, which is the main constituent of plasma at about 92% by volume), and $N_A$ to $\mathbf{6.10^{23}\ /mol}$, we get $mfp \approx \mathbf{3.08.10^{-10}\ m}$ and $Kn \approx \mathbf{3.08.10^{-3}}$. The Knudsen number is much smaller than 1 and justifies the use of continuum mechanics and the Navier-Stokes equations.

The assumption of constant density is related to the square of the Mach number for fluids undergoing isentropic or quasi-isentropic changes. In a more general case we can assess the relative changes in density from two basic thermodynamic coefficients : the coefficient of thermal expansion $\alpha$ and the coefficient of isothermal compressibility $\chi_T$ :

$$\alpha = -\frac{1}{\rho} \left( \frac{\partial \rho}{\partial T} \right)_p , \tag{C.3}$$

$$\chi_T = \frac{1}{\rho} \left( \frac{\partial \rho}{\partial p} \right)_T . \tag{C.4}$$

Using water as a rough approximation to blood, we have $\alpha \approx \mathbf{2.07.10^{-4}\ /K}$ and $\chi_T \approx \mathbf{4.6.10^{-10}\ /Pa}$ (values at 25°C, available in a large variety of sources). A variation of 1°C being an upper limit for temperature, this means that thermal expansion is easily negligible. Also, even if pressure changes

reached atmospheric levels (~$10^5$ Pa), the relative change in density would still be negligible. As a side note, speed of sound in water is about 1500 m/s, to be compared with the low velocity we use for blood in the capillaries (of order 0.5 m/s), giving a Mach number of $3.3.10^{-4}$. Density can thus reasonably be considered constant in blood.

The Reynolds number is commonly used in fluid mechanics to compare momentum advection and viscous diffusion of momentum. It is defined as :

$$Re = \frac{\rho U L}{\mu}, \tag{C.5}$$

where $\mu$ is the fluid dynamic viscosity (**1.4.10$^{-3}$ Pa.s** in the plasma), and $U$ and $L$ reference velocity and length. Taking $U \approx$ **0.5 m/s** and $L \approx$ **1.10$^{-6}$ m**, we get $Re \approx$ **0.366**. This small Reynolds number shows that viscous forces must be taken into account. However, it is not small enough to consider the flow viscous-dominated, except in certain cases (see Appendix D on the lubrication layer model).

The Froude number compares inertial forces with gravitational forces. It is defined as :

$$Fr = \frac{U^2}{g L}, \tag{C.6}$$

where $g$ is the local gravitational acceleration field, taken equal to **9.81 m/s$^2$**. With the values of $U$ and $L$ given above, this gives $Fr \approx$ **2.55.10$^4$**. The large Froude number indicates that gravitational effects can reasonably be neglected.

The Weber number compares inertial forces to surface tension. It is defined as :

$$We = \frac{\rho U^2 L}{t}, \tag{C.7}$$

where $t$ represents the greatest component of surface tension.

The capillary number compares viscous forces to surface tension, and corresponds to the ratio of the Weber number by the Reynolds number :

$$Ca = \frac{We}{Re} = \frac{\mu U}{t}. \tag{C.8}$$

Both capillary and Weber numbers are useful in our research as they give an idea of the order of magnitude of tension stresses sustained by the RBC flowing down the capillary vessel. Using the numbers given above and assuming quasi-equilibrium states where $We$ and $Ca$ are of order unity, we get for $t$ an order of magnitude between **1.10$^{-5}$** and **1.10$^{-4}$ kg/s$^2$**.

Since stresses and moments at the surface of the RBC come from 3 different forces, and 4 different constants, we can naturally compare the resulting tensions to this order of magnitude, using

the values given in Section 2.1.2. The isotropic tension $\sigma_0$ is estimated at $\mathbf{7.10^{-2}\ kg/s^2}$, the isothermal area compressibility modulus $K_{bu}$ is taken as $\mathbf{0.5\ kg/s^2}$, the 2-D shear modulus $K_{sh}$ is $\mathbf{4.2.10^{-6}\ kg/s^2}$, and the bending modulus $B$ is $\mathbf{1.8.10^{-19}\ kg.m^2/s^2}$. Comparing these figures gives considerable insight on the RBC mechanics. Firstly, the isotropic tension is small compared to the compressibility modulus. Secondly, the very high area compressibility modulus justifies the assumption of constant area in the RBC, often used in membrane models (the reason why we kept $K_{bu}$ is mainly numerical, to ensure area conservation dynamically). Thirdly, we see that RBC shape is going to be determined mostly by shear stresses, and bending stresses locally when the curvature is of the order $\sqrt{\frac{B}{K_{sh}}} \approx \mathbf{2.1.10^{-7}\ m}$ or smaller (this is not small compared to $dl$, so bending stresses should be observed to significantly round corners).

The Schmidt number is also used to compare the relative thicknesses of the viscous shear layer and the diffusion boundary layer. It is defined as :

$$Sc = \frac{\mu}{\rho D}, \tag{C.9}$$

where $D$ is the diffusion constant (in our case, of oxygen), taken approximately equal to $\mathbf{1.10^{-9}\ m^2/s}$. With the values of $\rho$ and $\mu$ given above, it gives $Sc \approx \mathbf{1.4.10^3}$. This indicates that we should expect velocity profiles to be sharper than oxygen level profiles near the capillary wall. Also, it means that oxygen diffusion in the capillary vessels is normally expected to be a limited process (i.e. capillary blood should retain most of its oxygen locally, up to a large number of capillary size length scales).

To compare oxy-myoglobin dissociation rate, oxyhemoglobin dissociation rate, and other phenomena, we use the Damköhler numbers. In the case of myoglobin, the main phenomenon will be diffusion, so that :

$$Da^{Mb} = \frac{k^{Mb} R_K^{\,2}}{D^{Mb}}, \tag{C.10}$$

where $k^{Mb}$ is the oxy-myoglobin dissociation rate constant and $R_K$ the radius of the Krogh cylinder, used as a reference length. $k^{Mb}$ is taken to be about $\mathbf{15\ s^{-1}}$ [42], $R_K$ is $\mathbf{2.10^{-5}\ m}$, and $D^{Mb} = \mathbf{6.10^{-11}\ m^2/s}$. This gives $Da^{Mb} \approx \mathbf{100}$, which justifies that oxy-myoglobin is always considered locally in chemical equilibrium with oxygen. In the case of hemoglobin, convection with the cytoplasm flow is to be assessed. However it should be less, if not of the same order, than diffusion (especially near steady state of the RBC). We will thus consider diffusion to be also the determining phenomenon :

$$Da^{Hb} = \frac{k^{Hb} L^2}{D^{Hb}}, \tag{C.11}$$

where $L$ is the order of magnitude of capillary flow (and by extension, of the RBC dimensions), taken as before as $\mathbf{1.10^{-6}\ m}$. Using $k^{Hb} = \mathbf{44\ s^{-1}}$ and $D^{Hb} \approx \mathbf{1.4.10^{-11}\ m^2/s}$, we get $Da^{Hb} \approx \mathbf{3.14}$. As we see, the kinetic rate of dissociation of oxyhemoglobin is not high enough to ignore diffusion.

Finally, we can compare diffusion of oxygen and its bound counterpart in myoglobin. The appropriate non-dimensional ratio is :

$$\frac{\alpha\ D}{D^{Mb}\ [Mb]\ \dfrac{1}{p^{Mb}_{O_2,50\%}}}, \tag{C.12}$$

with the notations used in Section 2.1.2. With the oxygen partial pressure at an equilibrium corresponding to 50% saturation of myoglobin, $p^{Mb}_{O_2,50\%}$ taken as **5.3 mmHg**, the oxygen solubility constant in myoglobin taken as $\mathbf{1.5.10^{-3}\ mol/m^3/mmHg}$, the oxygen diffusivity taken as $\mathbf{2.41.10^{-9}\ m^2/s}$, the diffusivity of oxy-myoglobin as $\mathbf{6.10^{-11}\ m^2/s}$, and the total myoglobin concentration as $\mathbf{0.4\ mol/m^3}$, we get a ratio of **0.798**. This clearly indicates that diffusion of both bound and unbound species have comparable impact, and neither one should be ignored.

Table C.1 recaps the main non-dimensional groups described in this appendix.

| Parameter | value | conclusion |
|---|---|---|
| $Kn = \frac{mfp}{dl}$ | $3.08.10^{-3}$ | continuum mechanics appropriate |
| $Ma = \frac{U}{speed\ of\ sound}$ | $3.3.10^{-4}$ | incompressible flow |
| $Re = \frac{\rho U L}{\mu}$ | 0.366 | both inertia and viscous stresses need to be considered |
| $Fr = \frac{U^2}{g L}$ | $2.55.10^{4}$ | gravitational effects negligible |
| $We = \frac{\rho U^2 L}{t}$ | ~1 | scales tension stresses in RBC membrane |
| $Ca = \frac{We}{Re} = \frac{\mu U}{t}$ | ~1 | scales tension stresses in RBC membrane |
| $\frac{K_{sh}}{t}$ | $4.10^{-2}$ - $4.10^{-1}$ | flow-induced stresses => shear deformation |
| $\frac{K_{sh}}{K_{bu}}$ | $8.4.10^{-6}$ | RBC membrane locally incompressible (constant area) |
| $\frac{\sigma_0}{K_{bu}}$ | 0.14 | pressure discontinuity (from surface tension at rest) negligible |
| $Sc = \frac{\mu}{\rho D}$ | $1.4.10^{3}$ | viscous boundary layers smaller than oxygen diffusion layers |
| $Da^{Mb} = \frac{k^{Mb} R_K^{\ 2}}{D^{Mb}}$ | 100 | myoglobin dissociation kinetics negligible (quasi-equilibrium) |
| $Da^{Hb} = \frac{k^{Hb} L^2}{D^{Hb}}$ | 3.14 | hemoglobin dissociation kinetics not negligible |
| $\frac{\alpha D}{D^{Mb} [Mb] \frac{1}{p^{Mb}_{O_2,50\%}}}$ | 0.798 | myoglobin diffusion not negligible |

*Table C.1 : Summary of non-dimensional parameters.*

# Appendix D : The lubrication layer model

To simplify calculation of the RBC shape and associated flow quantities at equilibrium, one of the most successful model is the lubrication layer model, developed by Lighthill [96]. The lubrication layer model applies to flow between the RBC and the capillary wall in a quasi-equilibrium or equilibrium state, and for capillaries small enough to consider the flow locally fully developed. Most of the flow around the RBC is then either at a constant velocity, or in the lubrication layer (see Figure D.1).

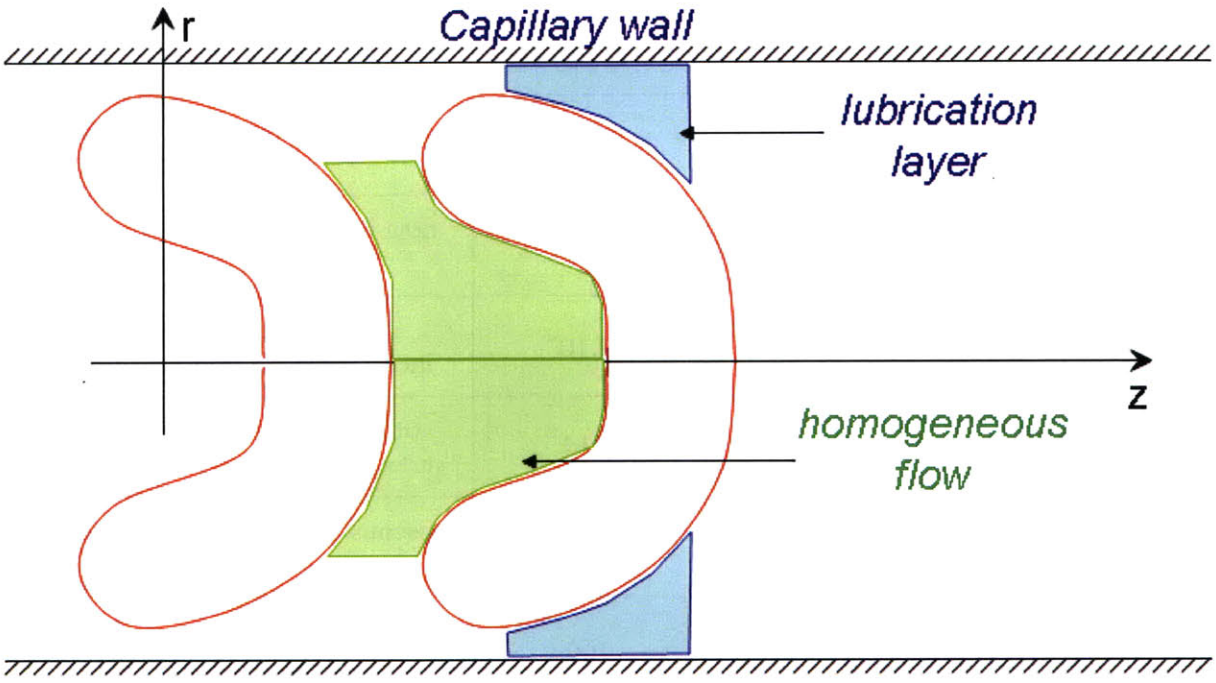


*Figure D.1 : Lubrication layer model.*

To justify this model, we use Schlichting's equations for the shear layer. As reported in the author's master's thesis, fully developed flow is characterized by a bell-shaped dissipation function, where the Reynolds number and the distance of mixing are inversely combined (see *Entropy Generation in Fluid Mixing* [16], p.52). With a mixing distance ratio of 5 corresponding to a Reynolds number of 100, we can then interpolate the mixing length of our problem. At a Reynolds number

close to unity, this would correspond to a mixing length ratio of 0.05. The flow is to be considered fully developed within 5% of the RBC-capillary wall distance at its entry.

With the assumption of fully developed flow given in Equations (D.1-3), the Navier Stokes equations in the lubrication layer reduce to Equation (D.4) in cylindrical coordinates :

$$v_r << v_z , \tag{D.1}$$

$$\frac{\partial v_z}{\partial z} \simeq 0 , \tag{D.2}$$

$$\frac{\partial p}{\partial r} << \frac{\partial p}{\partial z} , \tag{D.3}$$

$$=> p = p(z),\ v_z = v_z(r),\ \frac{\partial}{\partial t} = 0,$$

$$\rho\, v_r \frac{dv_z}{dr} = - \frac{dp}{dz} + \frac{\mu}{r} \frac{d}{dr}\left( r \frac{dv_z}{dr} \right) , \tag{D.4}$$

In Equation (D.4) the inertial term left, compared to the viscous term left, scales like $\frac{\rho U}{\mu} \frac{L_r^{\,2}}{L_z} = Re_{L_r} \frac{L_r}{L_z}$ , where $L_z$ and $L_r$ are reference lengths in the axial and radial directions. Even for a Reynolds number close to unity, this ratio is small enough to consider the inertial terms negligible for a narrow capillary (in other terms, the lubrication layer model is valid provided that the RBC is stretched on a significant length $L_z >> L_r$, and as long as the local radial dimension variation is small). With the RBC radius $R(s)$ redefined locally as a function of $z$ ($z = z_0 + \int_{s_0}^{s} \sin\phi(s)\, ds$), and $R_w$ the capillary radius, Equation (D.5) is to be solved with the following boundary conditions :

$$\frac{dp}{dz} = \frac{\mu}{r} \frac{d}{dr}\left( r \frac{dv_z}{dr} \right) , \tag{D.5}$$

$$v_z(R_w) = 0 , \tag{D.6}$$

$$v_z(R(z)) = U , \tag{D.7}$$

where $U$ is the steady velocity of the RBC. Integration leads to :

$$v_z = \frac{1}{4\mu} \frac{dp}{dz} (R_w^{\,2} - R^2) \left( - \frac{R_w^{\,2} - r^2}{R_w^{\,2} - R^2} + \frac{\ln\left(\frac{R_w}{r}\right)}{\ln\left(\frac{R_w}{R}\right)} \right) + U \left( \frac{\ln\left(\frac{R_w}{r}\right)}{\ln\left(\frac{R_w}{R}\right)} \right) . \tag{D.8}$$

We can note that in this solution $v_z$ always decreases with an increasing pressure gradient. The total volume flow $Q$ is obtained by integrating further :

$$Q = \int_R^{R_w} v_z \, 2\pi r \, dr = \frac{\pi}{8\mu}\frac{dp}{dz}(R_w^2 - R^2)\left[-(R_w^2 + R^2) + \frac{R_w^2 - R^2}{\ln\left(\frac{R_w}{R}\right)}\right] + \pi U\left[-R^2 + \frac{R_w^2 - R^2}{2\ln\left(\frac{R_w}{R}\right)}\right] \tag{D.9}$$

In some notations the "leakback" flow is determined instead. Also, the radius of the RBC can be replaced by the gap size $h$, so that $R = R_w - h$ and $R_w^2 - R^2 = 2R_w h - h^2$. Finally, if we change the frame of reference to the reference frame moving with the RBC (where the pressure gradient is constant through time), we have $z' = z - Ut$ and $Q' = \frac{\pi(R_w^2 - R^2)U - Q}{2\pi R_w}$ as the leakback flow per capillary circumferential length in the moving reference frame. This leads to an alternative result to Equation (D.9), presented in Section 1.2.4 :

$$\frac{1}{16\,\mu}\frac{dp}{dz'}(2R_w h - h^2)\left[2R_w^2 - 2R_w h + h^2 - \frac{2R_w h - h^2}{\ln\left(\frac{R_w}{R_w - h}\right)}\right] = - U\left[\frac{1}{2}R_w^2 - \frac{2R_w h - h^2}{4\ln\left(\frac{R_w}{R_w - h}\right)}\right] + R_w Q' . \tag{D.10}$$

Assuming a small gap thickness compared to the capillary radius $R \approx R_w$ or $h(z') << R_w$, Equations (D.8), (D.9) and (D.10) reduce to :

$$v_z = -\frac{1}{2\mu}\frac{dp}{dz}(R_w - r)(r - R) + U\left(\frac{R_w - r}{R_w - R}\right), \quad (r \approx R_w) \tag{D.11}$$

$$Q = -\frac{\pi}{6\mu}\frac{dp}{dz}(R_w - R)^3 R_w + \pi U R_w(R_w - R) , \tag{D.12}$$

$$\frac{dp}{dz'} = -\frac{6\mu U}{h^2} + \frac{12\mu Q'}{h^3} , \tag{D.13}$$

which is Lighthill's original result [96]. In the other limit $R << R_w$ or $h(z') \approx R_w$, Equations (D.8), (D.9) and (D.10) reduce to :

$$v_z = -\frac{1}{4\mu}\frac{dp}{dz}\left( R_w^2\left(1 - \frac{\ln\left(\frac{R_w}{r}\right)}{\ln\left(\frac{R_w}{R}\right)}\right) - r^2 \right) + U\left(\frac{\ln\left(\frac{R_w}{r}\right)}{\ln\left(\frac{R_w}{R}\right)}\right), \tag{D.14}$$

$$Q = -\frac{\pi}{8\mu}\frac{dp}{dz} R_w^2 \left( R_w^2 - \frac{R_w^2}{\ln\left(\frac{R_w}{R}\right)}\right) + \pi U \frac{R_w^2}{2\ln\left(\frac{R_w}{R}\right)}, \tag{D.15}$$

$$\frac{dp}{dz'} = -\frac{8\,\mu U}{R_w^2} + \frac{16\,\mu Q'}{R_w^3}. \tag{D.16}$$

Furthermore, if the RBC dimensions become so small compared to the vessel dimensions that its influence on the flow vanishes (i.e. its inertia becomes negligible), we get :

$$v_z = -\frac{1}{4\mu}\frac{dp}{dz}(R_w^2 - r^2), \quad (r >> R) \tag{D.17}$$

$$Q = -\frac{\pi}{8\mu}\frac{dp}{dz} R_w^4 \quad \text{or} \quad \frac{dp}{dz} = -\frac{8\mu Q}{\pi R_w^4}, \tag{D.18}$$

which is the Hagen-Poiseuille equation.

To complete Equation (D.10), which relates pressure gradient, RBC velocity and leakback flow in the lubrication layer model, a model is needed for the membrane, giving the stresses as a function of $R$, and leading to an integral equation summing up the forces on the membrane, and equating them with the pressure forces exerted on the flow (see Lighthill's original derivation of the integral equation [96]).

# Appendix E : Membrane equilibrium equations

In this appendix we consider the special case of steady flow, and RBC at equilibrium with the surrounding flow. In the reference frame moving with the RBC, all variables are constant with time. For this case the incompressible Navier-Stokes equations give :

$$\rho\,(\vec{v}'\cdot\vec{\nabla}')\vec{v}' = -\vec{\nabla}'p + \mu\,\nabla'^2\vec{v}' + \vec{f}_b\,\delta\left(\vec{r} - \vec{X}_b\right), \tag{E.1}$$

where $\vec{v}'$ is the velocity field in the moving reference frame, $\rho$ is the blood density, $p$ the thermodynamic pressure, $\mu$ the dynamic viscosity (different inside and outside the RBC), $\vec{X}_b$ the position vector of the RBC membrane boundary, where tension forces per unit area $\vec{f}_b$ are exerted, $\vec{\nabla}'$ is the del operator in the moving reference frame, and $\delta$ is the Dirac distribution mapping the RBC surface in 3-D space. The cylindrical components of $\vec{f}_b$ are resulting from normal and tangential forces combined as follows in our model :

$$f_r(s,t) = \frac{dF_n}{dA}\sin\phi + \frac{dF_t}{dA}\cos\phi\,, \tag{E.2}$$

$$f_z(s,t) = -\frac{dF_n}{dA}\cos\phi + \frac{dF_t}{dA}\sin\phi\,, \tag{E.3}$$

with these forces themselves resulting from tension, shear stresses and bending stresses as follows :

$$\frac{dF_n}{dA} = -t_s\frac{d\phi}{ds} - t_\theta\frac{\sin\phi}{R} - \frac{1}{R}\frac{d(R\,q_s)}{ds}\,, \tag{E.4}$$

$$\frac{dF_t}{dA} = \frac{1}{R}\frac{d(R\,t_s)}{ds} - t_\theta\frac{\cos\phi}{R} - q_s\frac{d\phi}{ds}\,, \tag{E.5}$$

and the constitutive equations to model the RBC elastic behavior :

$$\bar{t} = \frac{t_s + t_\theta}{2} = \sigma_0 + K_{bu}\left(\frac{ds}{ds_0}\frac{R}{R_0} - 1\right), \tag{45}$$

$$t_d = \frac{t_s - t_\theta}{2} = \frac{K_{sh}}{2}\left(\left(\frac{ds}{ds_0}\right)^2 - \left(\frac{R}{R_0}\right)^2\right) - \frac{B}{2}\left(\frac{d\phi}{ds} - \frac{\sin\phi}{R}\right)\left(\frac{d\phi}{ds} + \frac{\sin\phi}{R} - k_0\right), \tag{46}$$

$$q_s = -B\left(\frac{d^2\phi}{ds^2} + \frac{d}{ds}\left(\frac{\sin\phi}{R}\right)\right), \tag{47}$$

The full derivation of the RBC membrane equations, and the notations used can be found in Appendix B-3. To express the boundary conditions on the membrane, we project Equation (E.1) onto the local normal and tangential directions (Equations (E.6)-(E.7)), and integrate on a small control volume across the membrane (i.e. in the normal direction $\vec{n}$, over an infinitesimal length going to zero on both sides of the membrane) :

$$\rho\,(\vec{v}'\cdot\vec{\nabla}')v_n' = -\frac{\partial p}{\partial n} + \mu\,\nabla'^2 v_n' + \frac{dF_n}{dA}\,\delta\left(\vec{r} - \vec{X}_b\right), \tag{E.6}$$

$$\rho\,(\vec{v}'\cdot\vec{\nabla}')v_t' = -\frac{\partial p}{\partial t} + \mu\,\nabla'^2 v_t' + \frac{dF_t}{dA}\,\delta\left(\vec{r} - \vec{X}_b\right), \tag{E.7}$$

$$\int_{-}^{+}\rho\,(\vec{v}'\cdot\vec{\nabla}')v_n'\,dn = -\int_{-}^{+}\frac{\partial p}{\partial n}\,dn + \int_{-}^{+}\mu\,\nabla'^2 v_n'\,dn + \int_{-}^{+}\frac{dF_n}{dA}\,\delta\left(\vec{r} - \vec{X}_b\right)dn, \tag{E.8}$$

$$\int_{-}^{+}\rho\,(\vec{v}'\cdot\vec{\nabla}')v_t'\,dn = -\int_{-}^{+}\frac{\partial p}{\partial t}\,dn + \int_{-}^{+}\mu\,\nabla'^2 v_t'\,dn + \int_{-}^{+}\frac{dF_t}{dA}\,\delta\left(\vec{r} - \vec{X}_b\right)dn, \tag{E.9}$$

where "+" and " –" represent the external and internal limits of the RBC membrane, respectively. Noting that the velocity field components are continuous across the membrane, using mass conservation on each side, and taking the limit as the thickness of the control volume tends towards zero, we get :

$$\frac{\partial v_n'}{\partial n}(+) - \frac{\partial v_n'}{\partial n}(-) = -\frac{\partial v_t'}{\partial t}(+) + \frac{\partial v_t'}{\partial t}(-) = 0, \tag{E.10}$$

$$p(+) - p(-) = \frac{dF_n}{dA}, \tag{E.11}$$

$$-\mu_+\frac{\partial v_t'}{\partial n}(+) + \mu_-\frac{\partial v_t'}{\partial n}(-) = \frac{dF_t}{dA}. \tag{E.12}$$

Figure (E.1) illustrates these results. Equations (E.11) and (E.12) combined with (E.4), (E.5) lead to Secomb's equations of membrane equilibrium, presented in Section 1.2.3 :

$$\Delta p = -t_s\,k_s - t_\theta\,k_\theta - \frac{1}{R}\,\frac{d(R\,q_s)}{ds}, \tag{26}$$

$$-\tau = \frac{1}{R}\,\frac{d(R\,t_s)}{ds} - t_\theta\,\frac{1}{R}\,\frac{dR}{ds} - q_s\,k_s, \tag{27}$$

where $\Delta p$ and $\tau$ replace the local pressure difference, and shear stress on the membrane, and $k_s$ and $k_\theta$ are defined as the local curvatures.

As a side note, if we neglect bending and shear stresses, these equations reduce to the more familiar "bubble" equations :

$$- \Delta p = \bar{t} \, (k_s + k_\theta) \, , \tag{E.13}$$

$$- \tau = \frac{d\bar{t}}{ds} \, . \tag{E.14}$$

Equation (E.13) is the Young-Laplace equation, and Equation (E.14) describes the Marangoni effect.

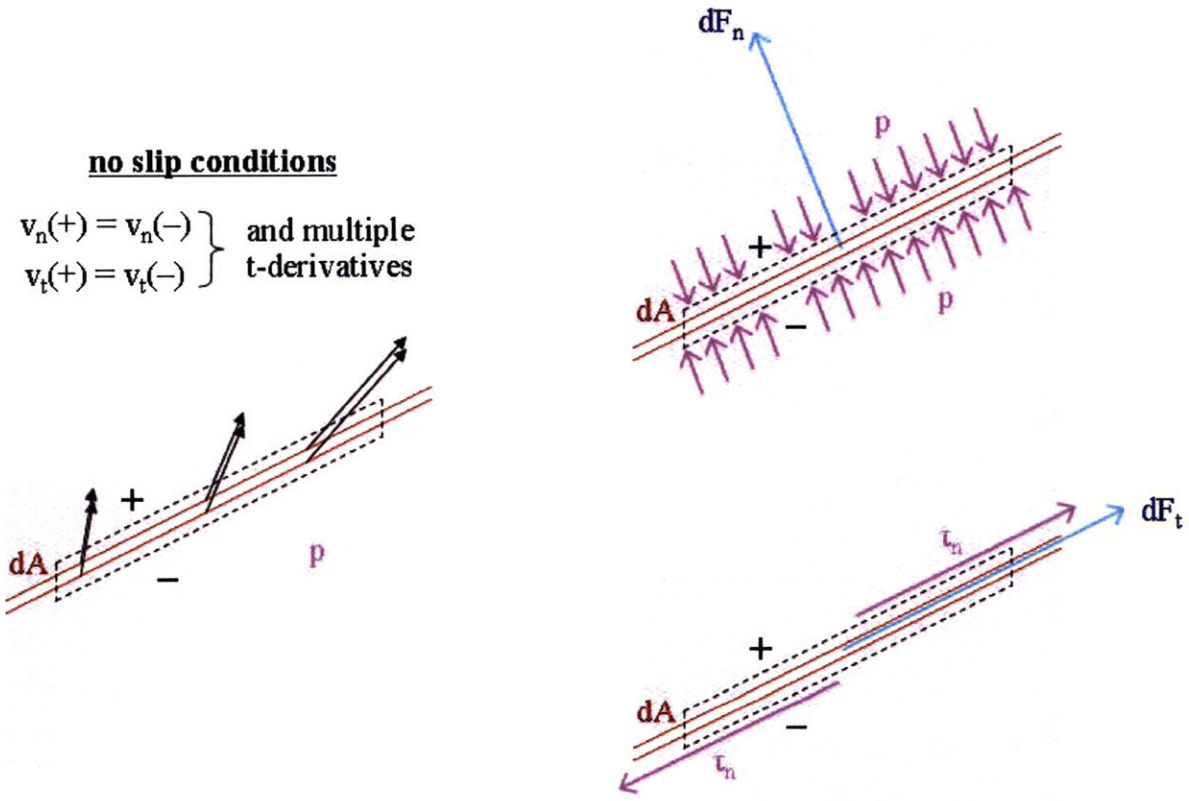


*Figure E.1 : Continuity and equilibrium boundary conditions on the RBC membrane.*

# Appendix F : The Fåhraeus and Fåhraeus-Lindqvist effects

In capillary vessels RBCs tend to align on the centerline to minimize resistance to flow. This is known to increase the proportion of RBC flowing with respect to whole blood present in the vessels. The "discharge" flow therefore has a higher hematocrit than the vessel, which is known to be the Fåhraeus effect. More precisely, if the average velocity of the RBC is $U$ , the discharge hematocrit is :

$$Hct_D = Hct \frac{U}{\bar{v}_z} , \tag{F.1}$$

where $\bar{v}_z$ is the average velocity of the whole blood, and $Hct$ is the local hematocrit. At steady conditions, because of the presence of the RBC the shear stress exerted on the capillary wall must be greater for a same total volume flow (see Figure F.1), so that the pressure gradient to balance it must be greater too. Reciprocally, for a same pressure gradient the total flow is decreased by the presence of the RBC. Hence the average velocity of whole blood $\bar{v}_z$ must be smaller than $U$ , and the discharge hematocrit is always greater than the local hematocrit.

Using the results from the lubrication layer theory (see Appendix D), we have for large vessels :

$$R << R_w \Rightarrow \pi R_w^2 \bar{v}_z = -\frac{\pi}{8\mu}\frac{dp}{dz} R_w^2 \left( R_w^2 - \frac{R_w^2}{\ln\left(\frac{R_w}{R}\right)} \right) + \pi U \frac{R_w^2}{2\ln\left(\frac{R_w}{R}\right)} , \tag{F.2}$$

$$Hct_D = Hct \left( \frac{1}{8\mu \bar{v}_z} \frac{dp}{dz} \left( R_w^2 - \frac{R_w^2}{\ln\left(\frac{R_w}{R}\right)} \right) + 1 \right) 2\ln\left(\frac{R_w}{R}\right) , \tag{F.3}$$

and replacing $\bar{v}_z$ by its asymptotic first-order value (Poiseuille flow), in the limit $Hct_D = 2\,Hct$ . Equation (F.3) shows two results experimentally observed. First, the discharge hematocrit tends towards twice the local vessel hematocrit for very large vessels. Second, as the relative size of the RBC increases (and the vessel size decreases), the discharge hematocrit increases. In other terms, the Fåhraeus effect increases with decreasing vessel size. Alternatively, for vessels of small diameter, comparable to the size of the RBC, we have :

$$R \approx R_w \Rightarrow \pi R_w^2 \bar{v}_z = -\frac{\pi}{6\mu}\frac{dp}{dz} (R_w - R)^3 R_w + \pi U R_w (R_w - R) , \tag{F.4}$$

$$Hct_D = Hct\left(\frac{1}{6\mu\,\bar{v}_z}\frac{dp}{dz}(R_w - R)^2 + \frac{R_w}{(R_w - R)}\right). \qquad \text{(F.5)}$$

Equation (F.5) shows that the Fåhraeus effect is inversed at very small diameters. When the gap between the RBC and the capillary wall becomes small compared to the vessel radius, the average velocity must tend towards $U$. Therefore, the discharge hematocrit must tend towards 1, which means that it has to decrease greatly as the vessel size tends toward the minimal RBC size possible (the terms in parentheses must asymptotically add up to 1).

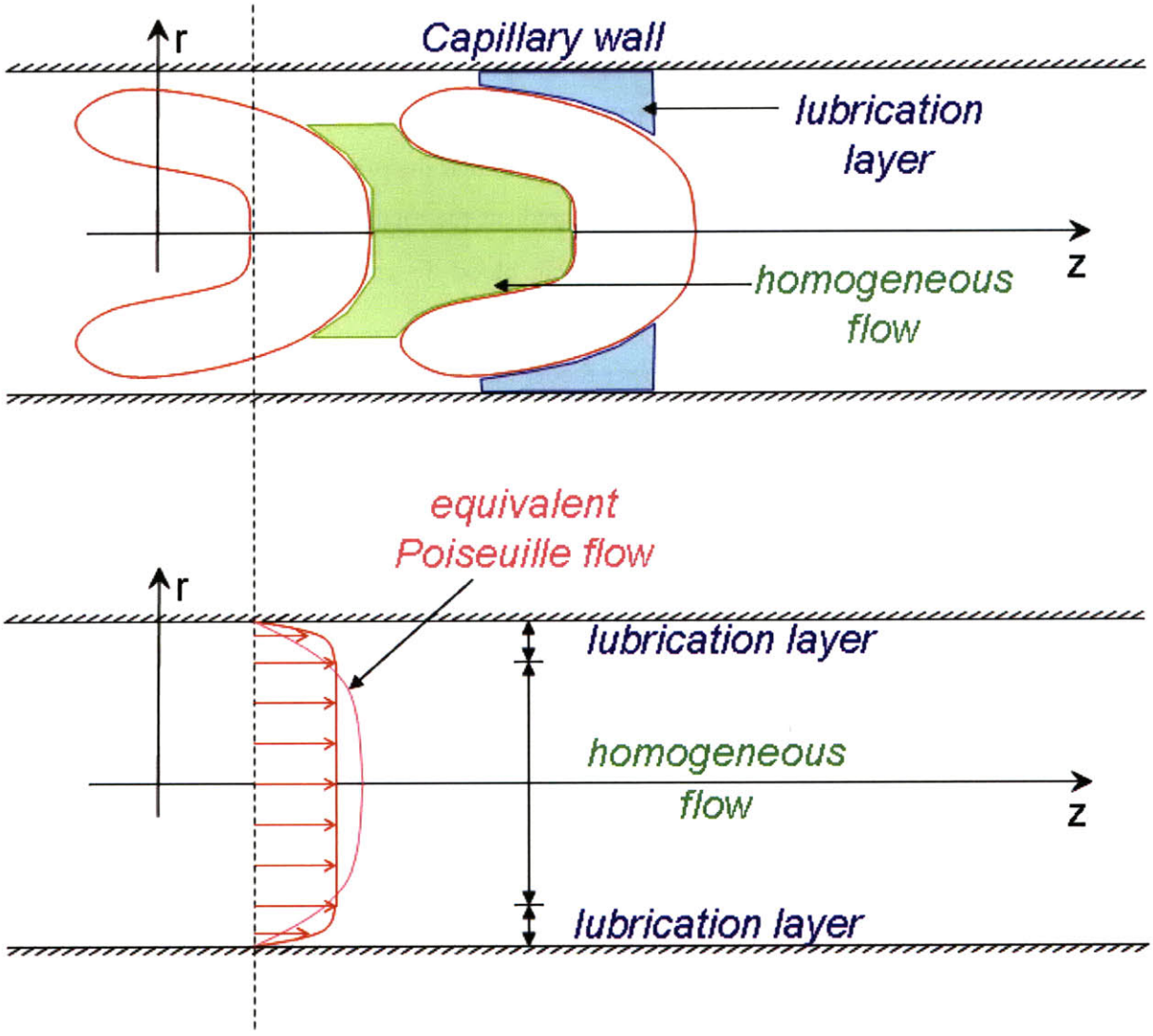


*Figure F.1 : Lubrication layer model – velocity profile.*

The Fåhraeus effect is largely documented, and an example of the resulting experimental curve is shown in Figure F.2.

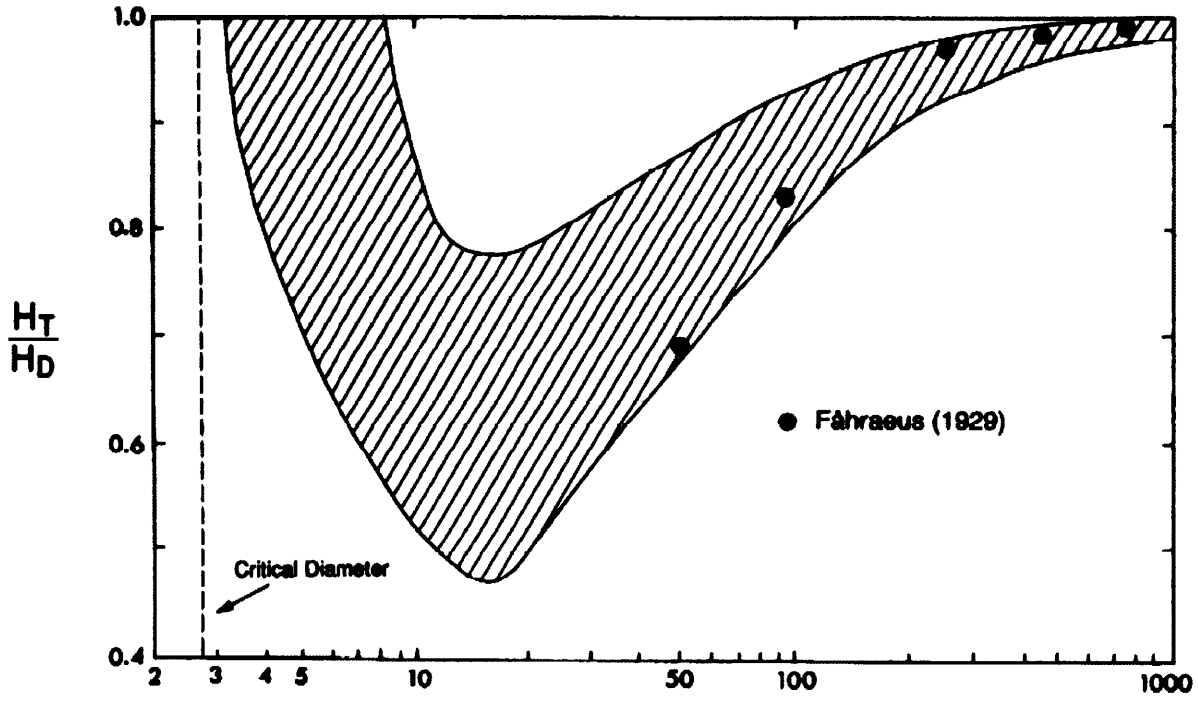


*Figure F.2 : The Fåhraeus effect (cross-hatched region contains literature data)* [35].

The Fåhraeus-Lindqvist effect is related to the measure of the apparent viscosity for the same problem, as vessel size decreases. The apparent viscosity is defined as the viscosity of the equivalent Poiseuille flow :

$$\mu_{app} = -\frac{\pi}{8}\frac{dp}{dz}\frac{R_w^4}{(Q + \pi R^2 U)}, \tag{F.6}$$

where $Q$ is the total volume flow between the RBC and the capillary wall. Using the lubrication layer theory, we get for large vessels :

$$R << R_w \Rightarrow \mu_{app} = \frac{\mu}{1 - \frac{1}{\ln\left(\frac{R_w}{R}\right)} + \frac{U}{-\frac{1}{4}\frac{dp}{dz}R_w^2 \ln\left(\frac{R_w}{R}\right)} + \frac{U R^2}{-\frac{1}{8}\frac{dp}{dz}R_w^4}}, \tag{F.7}$$

and as for large vessels $U$ tends towards $2\bar{v}_z$, using the Poiseuille flow we can simplify Equation (F.7) to :

$$R << R_w \Rightarrow \qquad \mu_{app} \approx \frac{\mu}{1 + \left(\frac{R}{R_w}\right)^2}, \tag{F.8}$$

Equation (F.8) shows that the apparent viscosity can be smaller than the plasma viscosity due to the presence of the RBC. This phenomenon called the Fåhraeus-Lindqvist effect is due to the alignment of the RBCs around the centerline, which is perfect in our model. Also, the apparent viscosity tends towards the plasma viscosity for very large vessels, and decreases as the vessel diameter decreases. For vessels of small diameter the bolus flow between RBCs must be taken into account. The bolus flow is roughly a Poiseuille flow, of extent determined by the hematocrit :

$$Hct \approx \frac{\pi\,(R_w^{\,2} - R^2)\; l_{RBC}}{\pi\, R_w^{\,2}(l_{bolus} + l_{RBC})}, \tag{F.9}$$

$$\Rightarrow \qquad \frac{l_{bolus}}{l_{RBC}} \approx \frac{1}{Hct}\left(\frac{R_w - R}{R_w}\right)^2 - 1, \tag{F.10}$$

where $l_{bolus}$ and $l_{RBC}$ are the respective lengths of the bolus flow (between 2 RBCs) and the RBC-driven flow. The apparent viscosity is then :

$$\mu_{app} = \frac{l_{bolus}\,\mu + l_{RBC}\left(-\frac{\pi}{8}\frac{dp}{dz}\frac{R_w^{\,4}}{Q}\right)_{RBC}}{l_{bolus} + l_{RBC}}, \tag{F.11}$$

which gives at small vessel diameters :

$$\mu_{app} = \mu\left(1 - Hct\left(\frac{R_w}{R_w - R}\right)^2 + \frac{Hct}{\frac{4}{3}\left(\frac{R_w - R}{R_w}\right)^5 + \frac{U}{-\frac{1}{8\mu}\frac{dp}{dz}R_w^{\,2}}\left(\frac{R_w - R}{R_w}\right)^3}\right). \tag{F.12}$$

Using the result for the discharge hematocrit which tends toward the local hematocrit, Equation (F.12) simplifies to :

$$R \approx R_w \Rightarrow \frac{\mu_{app}}{\mu} = 1 - \frac{Hct}{\left(\frac{R_w - R}{R_w}\right)^2} + \frac{3}{4}\frac{Hct}{\left(\frac{R_w - R}{R_w}\right)^5 + \left(\frac{R_w - R}{R_w}\right)^6}, \tag{F.13}$$

which for very small vessels simplifies roughly to :

$$R \approx R_w \Rightarrow \qquad \frac{\mu_{app}}{\mu} = 1 + \frac{3}{4} Hct \left( \frac{R_w}{R_w - R} \right)^5 . \tag{F.13}$$

This shows the inversion of the Fåhraeus-Lindqvist effect for small vessel diameters. As the vessel radius decreases, the apparent viscosity becomes very high, and reaches a limit as the vessel size reaches the minimal size of a RBC. Figure F.3 shows experimental data for the Fåhraeus-Lindqvist effect.

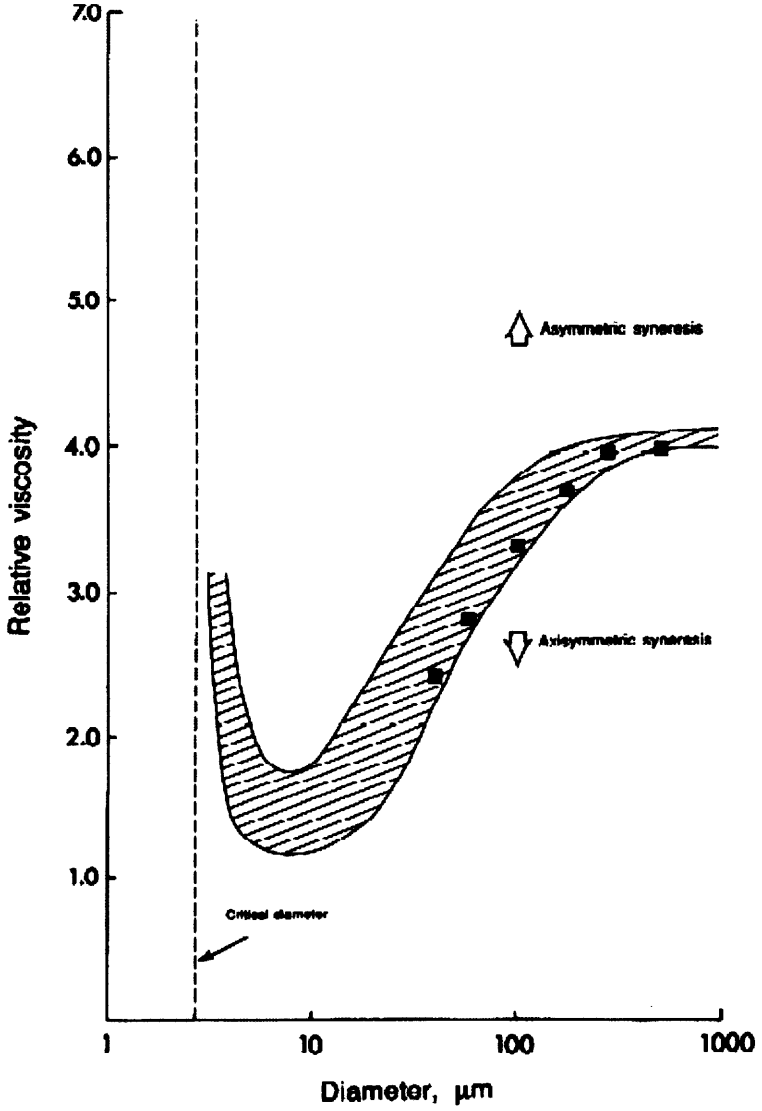


*Figure F.3 : The Fåhraeus-Lindqvist effect (cross-hatched region contains literature data)* [35].

# Bibliography

## A- Physical Models :

### A-1- Oxygen Consumption and Transport in Surrounding Tissue :


**[1]** **Krogh, A.** (1919). *The number and distribution of capillaries in muscle with calculations of the oxygen pressure head necessary for supplying the tissue.* Journal of Physiology (London), **52**, 409-15.

**[2]** **Hoofd, L.** (1992). *Updating the Krogh Model – Assumptions and Extensions.* Oxygen Transport in Biological Systems : Modelling of pathways from Environment.

**[3]** **McGuire, B. J., and Secomb, T. W.** (2001). *A theoretical model for oxygen transport in skeletal muscle under conditions of high oxygen demand.* J. Appl. Physiol., **91**, 2255-2265.


### A-2- Fluid Mechanics and Hemodynamics :


**[4]** **Burton, A. C.** (1966). Fed. Proc., **25**, 1753.

**[5]** **Fung, Y. C.** (1966). Fed. Proc., **25**, 1761.

**[6]** **Fung, Y. C.** (1966). *Biomechanics : Proceedings of a Symposium sponsored by the Applied Mechanics Division of the ASME, at the Annual Meeting, November 30, 1966, New York, NY.* The American Society of Mechanical Engineers, New York, NY.

**[7]** **Batchelor, G. K.** (1967). *An Introduction to Fluid Dynamics.* Cambridge University Press, London, UK.

**[8]** **Charm, S. E., and Kurland, G. S.** (1974). *Blood Flow and Microcirculation.* John Wiley & Sons, New York, NY.

**[9]** **Cokelet, G. R.** (1980). *Rheology and Hemodynamics.* Ann. Rev. Physiol., **42**, 311-324.

**[10]** **Pedley, T. J.** (1980). *The Fluid Mechanics of Large Blood Vessels.* Cambridge University Press, Cambridge, UK.

**[11]** **Wiedeman, M. P., Tuma, R. F., and Mayrovitz, H. N.** (1981). *An Introduction to Microcirculation.* Academic Press, New York, NY.

**[12]** **Fung, Y. C.** (1984). *Biodynamics : Circulation.* Springer-Verlag, New York, NY.

**[13]** **Milnor, W. R.** (1989). *Hemodynamics.* Williams & Wilkins, Baltimore, MD.

**[14]** **Sumpio, B. E.** (1993). *Hemodynamic Forces and Vascular Cell Biology.* R. G. Landes Company, Austin, TX.

**[15] Pedrizzetti, G., and Perktold, K.** (2003). *Cardiovascular Fluid Mechanics.* Springer- Verlag, Wien, Austria.

**[16] Le Floch-Yin, F. T.** (2006). *Entropy Generation in Fluid Mixing (S.M. thesis – dept. of Aeronautics and Astronautics).* Massachusetts Institute of Technology, MA.

## A-3- Red Blood Cell Membrane Mechanics :

**[17] Skalak, R. Tozeren, A. Zarda, R. P., and Chien, S.** (1973). *Strain Energy Function of Red Blood Cell Membranes.* Biophysical Journal, **13**, 245-264.

**[18] Steck, T. L.** (1974). *The organization of proteins in the human red blood cell membrane.* J. Cell Biol., **62**, 1-19.

**[19] Evans, E. A., and Skalak, R.** (1980). *Mechanics and Thermodynamics of Biomembranes.* CRC Press, Inc., Boca Raton, FL.

**[20] Tözeren, A., Skalak, R., Sung, K. P., and Chien, S.** (1982). *Viscoelastic behavior of erythrocyte membrane.* Biophys. J., **39**, 23-32.

**[21] Hochmuth, R. M., Evans, E. A., Wiles, H. C., McCown, J. T.** (1983). *Mechanical Measurement of Red Cell Membrane Thickness.* Science, New Series, **220**(4592), 101-102.

**[22] Tözeren, A., Skalak, R., Fedorciw, B., Sung, K. P., and Chien, S.** (1984). *Constitutive equations of erythrocyte membrane incorporating evolving preferred configuration.* Biophys. J., **45**, 541-549.

**[23] Secomb, T. W.** (1988). *Interaction between bending and tension forces in bilayer membranes.* Biophys. J., **54**, 743-746.

**[24] Hansen, J. C., Skalak, R., Chien, S., and Hoger, A.** (1997). *Influence of Network Topology on the Elasticity of the Red Blood Cell Membrane Skeleton.* Biophys. J., **72**, 2369-2381.

**[25] Dao, M., Lim, C. T., and Suresh, S.** (2003). *Mechanics of the human red blood cell deformed by optical tweezers.* J. Mech. Phys. Solids, **51**, 2259-2280.

**[26] Mills, J. P., Qie, L., Dao, M., Lim, C. T., and Suresh, S.** (2004). *Nonlinear Elastic and Viscoelastic Deformation of the Human Red Blood Cell with Optical Tweezers.* Mechanics and Chemistry of Biosystems, **1**(3), 169-180.

**[27] Arslan, M., and Boyce, M. C.** (2005). *Constitutive Modeling of the Stress-Stretch Behavior of Membranes Possessing a Triangulated Network Microstructure.* Mater. Res. Soc. Symp. Proc., **874**, L6.8.1-L6.8.6.

**[28] Hianik, T.** (2006). *Structure and physical properties of biomembranes and model membranes.* Acta Phys. Slovaca, **56**(6), 687-805.

**[29] Li, J., Lykotrafitis, G., Dao, M., and Suresh, S.** (2007). *Cytoskeletal dynamics of human erythrocyte.* Proc. Natl. Acad. Sci. USA, **104**(12), 4937-4942.

**[30] Puig-de-Morales-Marinkovic, M., Turner, K. T., Butler, J. P., Fredberg, J. J., and Suresh, S.** (2007). *Viscoelasticity of the human red blood cell.* Am. J. Physiol. Cell. Physiol., **293**, C597-C605.

## B- Blood Properties :

**[31] Sung, K. P., Schmid-Schönbein, G. W., Skalak, R., Schuessler, G. B., Usami, S., and Chien, S.** (1982). *Influence of physicochemical factors on rheology of human neutrophils.* Biophys. J., **39**, 101-106.

**[32] Mortillaro, N. A.** (1983). *The Physiology and Pharmacology of the Microcirculation.* Academic Press, New York, NY.

**[33] Reinhart, W. H., and Chien, S.** (1985). *Roles of cell geometry and cellular viscosity in red cell passage through narrow pores.* J. Cell Physiology, **248**(5), C473-C479.

**[34] Rowell, L. B.** (1986). *Human Circulation : Regulation during Physical Stress.* Oxford University Press, New York, NY.

**[35] Goldsmith, H. L., Cokelet, G. R., and Gaehtgens, P.** (1989). *Robin Fåhraeus: evolution of his concepts in cardiovascular physiology.* Am. J. Physiol., **257**, H1005-H1015.

**[36] Pries, A. R., Neuhaus, D., and Gaehtgens, P.** (1992). *Blood viscosity in tube flow: dependence on diameter and hematocrit.* Am. J. Physiol., **263**, H1770-H1778.

**[37] Alonso, C., Pries, A. R., Kiesslich, O., Lerche, D., and Gaehtgens, P.** (1995). *Transient rheological behavior of blood in low-shear tube flow : velocity profiles and effective viscosity.* Am. J. Physiol., **268**, H25-H32.

**[38] Gennaro, A. M., Luquita, A., and Rasia, M.** (1996). *Comparison between Internal Microviscosity of Low-Density Erythrocytes and the Microviscosity of Hemoglobin Solutions: An Electron Paramagnetic Resonance Study.* Biophysical J., **71**, 389-393.

**[39] Kubota, K., Tamura, J., Shirakura, T., Kimura, M., Yamanaka, K., Isozaki, T., and Nishio, I.** (1996). *The behaviour of red cells in narrow tubes in vitro as a model of the microcirculation.* British J. Haematology, **94**, 266-272.

**[40] Bouwer, S. Th., Hoofd, L., and Kreuzer, F.** (1997). *Diffusion coefficients of oxygen and hemoglobin measured by facilitated oxygen diffusion through hemoglobin solutions.* Biochimica et Biophysica Acta, **1338**, 127-136.

**[41] Bryner, M. A., Houwen, B., Westengard, J., and Klein, O.** (1997). *The spun micro-haematocrit and mean red cell volume are affected by changes in the oxygenation state of red blood cells.* Clin. Lab. Haem., **19**, 99-103.

**[42] Ishikawa, H., Uchida, T., Takahashi, S., Ishimori, K., and Morishima, I.** (2001). *Ligand Migration in Human Myoglobin: Steric Effects of Isoleucine 107(G8) on O2 and CO Binding.* Biophys. J., **80**(3), 1507-1517.

**[43] Wang, S. H., Lee, L. P., and Lee, J. S.** (2001). *A linear relation between the compressibility and density of blood.* J. Acoustical Society of America, **109**(1), 390-396.

**[44] Long, D. S., Smith, M. L., Pries, A. R., Ley, K., and Damiano, E. R.** (2004). *Microviscometry reveals reduced blood viscosity and altered shear rate and shear stress profiles in microvessels after hemodilution.* Proc. Natl. Acad. Sci. USA, **101**(27), 10060-10065.

**[45] Menchaca, H. J., Michalek, V. N., Rohde, T. D., Hirsch, A. T., Tuna, N., and Buchwald, H.** (2004). *Improvement of Blood Oxygen Diffusion Capacity and Anginal Symptoms by Cholesterol Lowering with Simvastatin.* J. of Applied Research, **4**(3), 410-418.

**[46] Pries, A. R., and Secomb, T. W.** (2005). *Microvascular blood viscosity in vivo and the endothelial surface layer.* Am. J. Physiol. Heart Circ. Physiol., **289**, 2657-2664.

**[47] Fedosov, D. A., Caswell, B., Suresh, S., and Karniadakis, G. E.** (2010). *Quantifying the biophysical characteristics of Plasmodium-falciparum-parasitized red blood cells in microcirculation.* Proc. Natl. Acad. Sci. USA, (submitted as of April 2010 according to http://iffwww.iff.kfa-juelich.de/~fedosov/D_Fedosov_res.html#malaria).

## C- Experimental Observations and Studies of Sickle Cell Disease :

### C-1- Sickle Hemoglobin :

**[48] Wilson, S. M., and Makinen, M. W.** (1980). *Electron Microscope Study of the Kinetics of the Fiber-to-Crystal Transition of Sickle Cell Hemoglobin.* Proc. Natl. Acad. Sci. USA, **77**(2), 944-948.

**[49] Liu, S., Derick, L. H., and Palek, J.** (1993). *Dependence of the Permanent Deformation of Red Blood Cell Membranes on Spectrin Dimer-Tetramer Equilibrium: Implication for Permanent Membrane Deformation of Irreversibly Sickled Cells.* Blood, **81**(2), 522-528.

**[50] Wang, J. C., Turner, M. S., Agarwal, G., Kwong, S., Josephs, R., Ferrone, F. A., and Briehl, R. W.** (2002). *Micromechanics of Isolated Sickle Cell Hemoglobin Fibers: Bending Moduli and Persistence Lengths.* J. Mol. Biol., **315**, 601-612.

**[51] Ferrone, F. A., and Rotter, M. A.** (2004). *Crowding and the polymerization of sickle hemoglobin.* J. Mol. Recognit., **17**, 497-504.

**[52] Christoph, G. W., Hofrichter, J., and Eaton, W. A.** (2005). *Understanding the Shape of Sickled Red Cells.* Biophysical J., **88**, 1371-1376.

**[53] Turner, M. S., Agarwal, G., Jones, C.W., Wang, J. C., Kwong, S., Ferrone, F. A., Josephs, R., and Briehl, R. W.** (2006). *Fiber Depolymerization.* Biophysical J., **91**, 1008-1013.

**[54] Browning, J. A., Staines, H. M., Robinson, H. C., Powell, T., Ellory, J. C., and Gibson, J. S.** (2007). *The effect of deoxygenation on whole-cell conductance of red blood cells from healthy individuals and patients with sickle cell disease.* Blood, **109**(6), 2622-2629.

## C-2- Capillary Walls and Endothelial Cell Activation :

**[55] Fogelson, A. L.** (1984). *A Mathematical Model and Numerical Method for Studying Platelet Adhesion and Aggregation during Blood Clotting.* J. Computational Physics, **56**, 111-134.

**[56] Graido-Gonzales, E., Doherty, J. C., Bergreen, E. W., Organ, G., Telfer, M., and McMillen, M. A.** (1998). *Plasma Endothelin-1, Cytokine, and Prostaglandin E2 Levels in Sickle Cell Disease and Acute Vaso-Occlusive Sickle Crisis.* Blood, **92**(7), 2551-2555.

**[57] Solovey, A. A., Solovey, A. N., Harkness, J., and Hebbel, R. P.** (2001). *Modulation of endothelial cell activation in sickle cell disease : a pilot study.* The American Society of Hematology, Blood, **97**(7), 1937-1941.

**[58] Ou, J., Ou, Z., Jones, D. W., Holzhauer, S., Hatoum, O. A., Ackerman, A. W., Weihrauch, D. W., Gutterman, D. D., Guice, K., Oldham, K. T., Hillery, C. A., and Pritchard, K. A., Jr.** (2003). *L4F, an Apolipoprotein A-1 Mimetic, Dramatically Improves Vasodilatation in Hypercholesterolemia and Sickle Cell Disease.* J. of the Amer. Heart Association, Circulation, **107**(18), 2337-2341.

**[59] Dignat-George, F., Sampol, J., Lip, G., Blann, A. D.** (2004). *Circulating Endothelial Cells : Realities and Promises in Vascular Disorders.* Pathophysiology of Haemostasis and Thrombosis, **33**, 495-499.

**[60] Belcher, J. D., Mahaseth, H., Welch, T. E., Vilback, A. E., Sonbol, K. M., Kalambur, V. S., Bowlin, P. R., Bischof, J. C., Hebbel, R. P., and Vercellotti, G. M.** (2005). *Critical role of endothelial cell activation in hypoxia-induced vasoocclusion in transgenic sickle mice.* Am. J. Physiol. Heart Circ. Physiol., **288**, 2715-2725.

**[61] Niihara, Y., Matsui, N. M., Shen, Y. M., Akiyama, D. A., Johnson, C. S., Sunga, M. A., Magpayo, J., Embury, S. H., Kalra, V. K., Cho, S. H. and Tanaka, K. R.** (2005). *L-Glutamine*

*therapy reduces endothelial adhesion of sickle red blood cells to human umbilical vein endothelial cells.* BMC Blood Disorders, **5**(4) (10.1186/1471-2326-5-4).

## C-3- Blood Dynamics in Sickle Cell Disease :

**[62] Chien, S., Usami, S., and Bertles, J. F.** (1970). *Abnormal Rheology of Oxygenated Blood in Sickle Cell Anemia.* J. Clinical Investigation, **49**, 623-634.

**[63] Usami, S., Chien, S., and Bertles, J. F.** (1975). *Deformability of sickle cells as studied by microsieving.* J. Lab. Clin. Med., **86**, 274-279.

**[64] Zarkowsky, H., and Hochmuth, R. M.** (1975). *Sickling Times of Individual Erythrocytes at Zero PO2.* J. Clin. Investigation, **56**, 1023-1034.

**[65] Laogun, A. A., Ajayi, N. O.,Osamo, N. O., and Okafor, L. A.** (1980). *Plasma viscosity in sickle-cell anaemia.* Clin. Phys. Physiol. Meas., **1**(2), 145-150.

**[66] Kaul, D. K., Fabry, M. E., Windisch, P., Baez, S., and Nagel, R. L.** (1983). *Erythrocytes in Sickle Cell Anemia Are Heterogeneous in Their Rheological and Hemodynamic Characteristics.* J. Clin. Invest., The American Soc. for Clin. Inverst., Inc., **72**, 22-31.

**[67] Nash, G. B., Johnson, C. S., and Meiselman, H. J.** (1984). *Mechanical Properties of Oxygenated Red Blood Cells in Sickle Cell (HbSS) Disease.* Blood, **63**(1), 73-82.

**[68] Nash, G. B., Johnson, C. S., and Meiselman, H. J.** (1986). *Influence of oxygen tension on the viscoelastic behavior of red blood cells in sickle cell disease.* Blood, **67**, 110-116.

**[69] Lipowsky, H. H., Sheikh, N. U., and Katz, D. M.** (1987). *Intravital Microscopy of Capillary Hemodynamics in Sickle Cell Disease.* J. Clin. Invest., **80**(1), 117-127.

**[70] Mackie, L. H., and Hochmuth, R. M.** (1990). *The Influence of Oxygen Tension, Temperature, and Hemoglobin Concentration on the Rheologic Properties of Sickle Erythrocytes.* Blood, **76**, 1256-1261.

**[71] Messmann, R., Gannon, S., Sarnaik, S., and Johnson, R. M.** (1990). *Mechanical Properties of Sickle Cell Membranes.* Blood, **75**(8), 1711-1717.

**[72] Phillips, G. Jr., Coffey, B., Tran-Son-Tay, R., Kinney, T. R., Orringer, E. P., and Hochmuth, R. M.** (1991). *Relationship of Clinical Severity to Packed Cell Rheology in Sickle Cell Anemia.* Blood, **78**, 2735-2739.

**[73] Akinola, N. O., Stevens, S. M. E., Franklin, I. M., Nash, G. B., and Stuart, J.** (1992). *Subclinical ischaemic episodes during the steady state of sickle cell anaemia.* J. Clin. Pathol., **45**, 902-906.

**[74] Dong, C., Chadwick, R. S., and Schechter, A. N.** (1992). *Influence of sickle hemoglobin polymerization and membrane properties on deformability of sickle erythrocytes in the microcirculation.* Biophys. J., **63**, 774-783.

**[75] Hiruma, H., Noguchi, C. T., Uyesaka, N., Schechter, A. N., and Rodgers, G. P.** (1995). *Contributions of sickle hemoglobin polymer and sickle cell membranes to impaired filterability.* Am. J. Physiol., **268**, H2003-H2008.

**[76] Damay, E.** (1997). *Rheology of blood cells in sickle cell disease (SM thesis).* University of Florida.

**[77] Mohan, J. S., Vigilance, J. E., Marshall, J. M., Hambleton, I. R., Reid, H. L., and Serjeant, G. R.** (2000). *Abnormal venous function in patients with homozygous sickle cell (SS) disease and chronic leg ulcers.* Clinical Science, **98**, 667-672.

**[78] Steinberg, M. H., Forget, B. G., Higgs, D. R., and Nagel, R. L.** (2001). *Disorders of hemoglobin: Genetics, Pathophysiology, and Clinical Management.* Cambridge University Press, Cambridge, UK.

**[79] Brandao, M. M., Saad, S. T. O., Cezar, C. L., Fontes, A., Costa, F. F., and Barjas-Castro, M. L.** (2003). *Elastic properties of stored red blood cells from sickle trait donor units.* Vox Sanguinis, **85**, 213-215.

**[80] Higgins, J. M., Eddington, D. T., Bhatia, S. N., and Mahadevan, L.** (2007). *Mapping the Phase space for Vaso-occlusion in Sickle Cell Disease using a Microfluidic Device.* Brigham and Women's Hospital, Boston, MA.

**[81] Higgins, J. M., Eddington, D. T., Bhatia, S. N., and Mahadevan, L.** (2007). *Sickle Cell vasoocclusion and rescue in a Microfluidic Device.* Proc. Natl. Acad. Sci. USA, **104**(51), 20496-500.

**[82] Martorana, M. C., Mojoli, G., Cianciulli, P., Tarzia, A., Mannela, E., and Caprari, P.** (2007). *Sickle cell anemia: haemorheological aspects.* Ann. Ist. Super Sanita, **43**(2), 164-170.

**[83] Wallach, J.** (2007). *Interpretation of diagnostic tests.* 8th edition. Lippincott Williams & Wilkins, Philadelphia, PA.

**[84] Greer, J. P., Foerster, J., Rodgers, G. M., Paraskevas, F., Glader, B., Arber, D. A., Means, R. T. Jr.** (2009). *Wintrobe's clinical hematology.* 12th edition, Vol. 1. Lippincott Williams & Wilkins, Philadelphia, PA.

**[85] Tripette, J., Alexy, T., Hardy-Dessources, M.-D., Mougenel, D., Beltan, E., Chalabi, T., Chout, R., Etienne-Julan, M., Hue, O., Meiselman, H. J., and Connes, P.** (2009). *Red blood cell aggregation, aggregate strength and oxygen transport potential of blood are abnormal in both homozygous sickle cell anemia and sickle-hemoglobin C disease.* Haematologica, **94**(8), 1060-1065.

C-4- Therapeutic Studies and Trials :

**[86] Fischer, B. H., Marks, M., and Reich, T.** (1983). *Hyperbaric-oxygen treatment of multiple sclerosis. A Randomized, Placebo-Controlled, Double-Blind Study.* New England J. of Medicine, **308**(4), 181-186.

**[87] Rosse, W. F., Narla, M., Petz, L. D., and Steinberg, M. H.** (2000). *New Views of Sickle Cell Disease Pathophysiology and Treatment.* Hematology, 2-17.

**[88] Aidoo, M., Terlouw, D. J., Kolczak, M. S., McElroy, P. D., O ter Kuile, F., Kariuki, S., Nahlen, B. L., Lal, A. A., and Udhayakumar, V.** (2002). *Protective effects of the sickle cell gene against malaria morbidity and mortality.* Lancet, **359**(9314), 1311-1312.

**[89] Brandao, M. M., Fontes, A., Barjas-Castro, M. L., Barbosa, L. C., Costa, F. F., Cesar, C. L., and Saad, S. T. O.** (2003). *Optical tweezers for measuring red blood cell elasticity: application to the study of drug response in sickle cell disease.* Eur. J. Haematol., **70**, 207-211.

**[90] Alexy, T., Pais, E., Armstrong, J. K., Meiselman, H. J., Johnson, C. S., and Fischer, T. C.** (2006). *Rheologic behavior of sickle and normal red blood cell mixtures in sickle plasma: implications for transfusion therapy.* Transfusion, **46**, 912-918.

**[91] Kirkham, F. J., Lerner, N. B., Noetzel, M., DeBaun, M. R., Datta, A. K., Rees, D. C., and Adams, R. J.** (2006). *Trials in Sickle Cell Disease.* J. Pediatric Neurology, **34**(6), 450-458.

**[92] Kwiatowski, J. L., Granger, S., Brambilla, D. J., Brown, R. C., Miller, S. T., and Adams, R. J.** (2006). *Elevated blood flow velocity in the anterior cerebral artery and stroke risk in sickle cell disease : extended analysis from the STOP trial.* British J. of Haematology, **134**, 333-339.

**[93] Lee, M. T., Piomelli, Granger, S., Miller, S. T., Harkness, S., Brambilla, D. J., and Adams, R. J.** (2006). *Stroke Prevention Trial in Sickle Cell Anemia (STOP) : extended follow-up and final results.* Blood, **108**(3), 847-852.

**[94] Little, J. A., McGowan, V. R., Kato, G. J., Partovi, K. S., Feld, J. J., Maric, I., Martyr, S., Taylor, J. G. VI, Machado, R. F., Heller, T., Castro, O., and Gladwin, M. T.** (2006). *Combination erythropoietin-hydroxyurea therapy in sickle cell disease: experience from the National Institutes of Health and a literature review.* Haematologica, **91**(8), 1076-1083.

**[95] Rossignol, D. A., Rossignol, L. W., Smith, S., Schneider, C., Logerquist, S., Usman, A., Neubrander, J., Madren, E. M., Hintz, G., Grushkin, B., and Mumper, E. A.** (2009). *Hyperbaric treatment for children with autism: a multicenter, randomized, double-blind, controlled trial.* BMC Pediatrics, **9**(21), 1-15.

## D- Integrated Models and Simulations :

### D-1- Blood Flow in Capillaries :

**[96] Lighthill, M. J.** (1968). *Pressure-forcing of tightly fitting pellets along fluid-filled elastic tubes.* J. Fluid Mech., **34**, 113-143.

**[97] Fitz-Gerald, J. M.** (1969). *Mechanics of Red-cell Motion through very narrow Capillaries.* Proc. R. Soc. Lond. Series B., **174**(1035), 193-227.

**[98] Jenkins, J. T.** (1977). *Static Equilibrium Configurations of a Model Red Blood Cell.* J. Math. Biology, **4**, 149-169.

**[99] Fischer, T. M., Haest, C. W. M., Stöhr-Liesen, M., Schmid-Schönbein, H., and Skalak, R.** (1981). *The stress-free shape of the red blood cell membrane.* Biophys. J., **34**, 409-422.

**[100] Secomb, T. W., Skalak, R., Ozkaya, N., Gross, J. F.** (1986). *Flow of axisymmetric red blood cells in narrow capillaries.* J. Fluid Mechanics, **163**, 405-423.

**[101] Halpern, D. and Secomb, T. W.** (1989). *The squeezing of red blood cells through capillaries with near-minimal diameters.* J. Fluid Mechanics, **203**, 381-400.

**[102] Pozrikidis, C.** (1990). *The axisymmetric deformation of a red blood cell in uniaxial straining Stokes flow.* J. Fluid Mech., **216**, 231-254.

**[103] Halpern, D., and Secomb, T. W.** (1992). *The squeezing of red blood cells through parallel-sided channels with near-minimal widths.* J. Fluid Mech., **244**, 307-322.

**[104] Secomb, T. W., and Hsu, R.** (1996). *Analysis of Red Blood Cell Motion through Cylindrical Micropores : Effects of Cell Properties.* Biophysical J., **71**, 1096-1101.

**[105] Sharan, M., and Popel, A. S.** (2001). *A two-phase model for flow of blood in narrow tubes with increased effective viscosity near the wall.* Biorheology, **38**, 415-428.

**[106] Sharan, M., and Popel, A. S.** (2002). *A Compartmental Model for Oxygen Transport in Brain Microcirculation in the Presence of Blood Substitutes.* J. Theor. Biol., **216**, 479-500.

**[107] Bishop, J. J., Popel, A. S., Intaglietta, M., and Johnson, P. C.** (2002). *Effect of aggregation and shear rate on the dispersion of red blood cells flowing in venules.* Heart, **283**, 1985-1996.

**[108] Vadapalli, A., Goldman, D., and Popel, A. S.** (2002). *Calculations of Oxygen Transport by Red Blood Cells and Hemoglobin Solutions in Capillaries.* Art. Cells, Blood Subs., and Immob. Biotech., **30**(3), 157-188.

**[109] Pozrikidis, C.** (2003). *Numerical Simulation of the Flow-Induced Deformation of Red Blood Cells.* Annals Biomed. Eng., **31**, 1194-1205.

**[110] Bagchi, P., Johnson, P. C., Popel, A. S.** (2005). *Computational Fluid Dynamic Simulation of Aggregation of Deformable Cells in a Shear Flow.* J. Biomech. Eng., **127**(7), 1070-1080.

**[111] Chakraborty, S.** (2005). *Dynamics of capillary flow of blood into a microfluidic channel.* Lab. Chip, **5**, 421-430.

**[112] Christini, V., and Kassab, G. S.** (2005). *Computer Modeling of Red Blood Cell Rheology in the Microcirculation : A Brief Overview.* Annals Biomed. Eng., **33**(12), 1724-1727.

**[113] Popel, A. S., and Johnson, P. C.** (2005). *Microcirculation and Hemorheology.* Annu. Rev. Fluid Mech., **37**, 43-69.

**[114] Pries, A. R., and Secomb, T. W.** (2005). *Control of blood vessel structure : insights from theoretical models.* Am. J. Physiol. Heart Circ. Physiol., **288**, 1010-1015.

**[115] Secomb, T. W., Hsu, R., and Pries, A. R.** (2006). *Tribology of capillary blood flow.* Proc. IMechE, Part J: Engineering Tribology, **220**, 767-774.

**[116] Secomb, T. W.** (2007). *Microcirculation and theoretical modeling : a brief history.* Mathematical Biosciences Institute workshop presentation, Colombus, OH (http://mbi.osu.edu/2006/ws4abstracts.html).

**[117] Secomb, T. W., Styp-Rekowska, B., and Pries, A. R.** (2007). *Two-Dimensional Simulation of Red Blood Cell Deformation and Lateral Migration in Microvessels.* Annals of Biomedical Engineering, **35**(5), 755-765.

**[118] Skotheim, J. M., and Secomb, T. W.** (2007). *Red Blood Cells and Other Nonspherical Capsules in Shear Flow : Oscillatory Dynamics and the Tank-Treading-to-Tumbling Transition.* Physical Review Letters, **98**, 078301.

**[119] Tsoukias, N. M., Goldman, D., Vadapalli, A., Pittman, R. N., and Popel, A. S.** (2007). *A computational model of oxygen delivery by hemoglobin-based oxygen carriers in three-dimensional microvascular networks.* J. Theor. Biol., **248**, 657-674.

**[120] Zhang, J., Johnson, P. C., and Popel, A. S.** (2008). *Red blood cell aggregation and dissociation in shear flows simulated by lattice Boltzmann method.* J. Biomech., **41**(1), 47-55.

**[121] Kaoui, B., Biros, G., and Misbah, C.** (2009). *Why Do Red Blood Cells Have Asymmetric Shapes Even in a Symmetric Flow?* Physical Review Letters, **103**(18), 188101, 1-4.

**[122] Zhang, J., Johnson, P. C., and Popel, A. S.** (2009). *Effects of erythrocyte deformability and aggregation on the cell free layer and apparent viscosity of microscopic blood flows.* Microvasc. Research, **77**, 265-272.

## D-2- Sickle Cell Dynamical Models :

**[123] Berger, S. A., and King, W. S.** (1980). *The Flow of Sickle Cell Blood in the Capillaries.* Biophysical J., **29**, 119-148.

**[124] Discher, D.** (1989). *Plasma viscosity and Sickle-Cell Blood Flow in the Capillaries.* (unpublished paper).

**[125] Ferrone, F. A.** (1989). *Kinetic Models and the Pathophysiology of Sickle Cell Disease.* Annals of the New York Academy of Sciences, **565**(1), 63-74.

**[126] Makhijani, V. B., Cokelet, G. R., and Clark, A. Jr.** (1990). *Dynamics of oxygen unloading from sickle erythrocytes.* Biophysical J., **58**, 1025-1052.

**[127] Dou, Q., and Ferrone, F. A.** (1993). *Simulated Formation of Polymer Domains in Sickle Hemoglobin.* Biophysical J., **65**, 2068-2077.

**[128] Cima, L. G., Discher, D. E., Tong, J., and Williams, M. C.** (1994). *A Hydrodynamic Interpretation of Crisis in Sickle Cell Anemia.* Microvascular research, **47**, 41-54.

**[129] Apori, A. A.** (1998). *Assessment of Chaos in a Hemodynamic Model of Sickle Cell Disease in the Microcirculation.* Massachusetts Institute of Technology.

**[130] Rocsoreanu, C., Georgescu, A., and Giurgiteanu, N.** (2000). *The FitzHugh-Nagumo Model.* Kluwer Academic Publishers, Dordrecht, The Netherlands.

**[131] Apori, A. A., and Harris, W. L.** (2001). *Chaos in an Eulerian Based Model of Sickle Cell Blood Flow.* Paper EC 8, American Physical Society, 54th Annual Meeting of the Division of Fluid Dynamics, Nov. 18-20, 2001, San Diego, CA, APS Bulletin, **46**(10), 100.

**[132] Apori, A. A., Coral-Pinto, R. J., and Harris, W. L.** (2002). *Chaotic Onset of Sickle Cell Blood Flow Crises.* Proc. Contemporary Research in Theoretical and Applied Mechanics, 14th U.S. National Congress of Theoretical and Applied Mechanics, June 23-28, 2002, Blacksburg, VA.

**[133] Apori, A. A., Coral-Pinto, R. J., and Harris, W. L.** (2004). *Chaos in the Onset of Sickle Cell Crises.* Advances in Fluid Mechanics V, C. A. Brebbia, A. C. Mendes and M. Rahman, WIT Press, Southampton, UK, 363-376.

**[134] Berger, S. A., and Carlson, B. E.** (2004). *Sickle Cell Blood Flow in the Microcirculation.* Proc. 26th Annual International Conference of the IEEE EMBS, San Francisco, CA.

**[135] Le Floch, F. and Harris, W. L.** (2006). *Assessing Chaos in Sickle Cell Anemia.* Paper HA 1, American Physical Society, 59th Annual Meeting of the Division of Fluid Dynamics, Nov. 19-21, 2006, Tampa, FL, APS Bulletin, **51**(9), 162-163.

**[136] Higgins, J. M.** (2007). *Mathematical and mechanical modeling of vaso-occlusion in sickle cell disease (SM thesis - Harvard-MIT Division of Health Sciences and Technology).* Massachusetts Institute of Technology, MA.

**[137] Le Floch, F., and Harris, W. L.** (2009). *A Comprehensive Fluid Dynamic-Diffusion Model of Blood Flow Microcirculation with Focus on Sickle Cell Disease.* American Physical Society, 64th Annual Meeting of the Division of Fluid Dynamics, Nov. 22-24, 2009, Minneapolis, MN, APS Bulletin, **54**(19), http://meetings.aps.org/link/BAPS.2009.DFD.EE.6 .

## E- Numerical Techniques for Finite-Elements Computation :

### E-1- Finite Elements Computation :


**[138] Shen, S.-F.** (1977). *Finite-Element Methods in Fluid Mechanics.* Ann. Rev. Fluid Mech., **9**, 421-445.

**[139] Russel, W. S.** (1995). *Polynomial interpolation schemes for integral derivative distributions on structured grids.* Applied Numerical Mathematics, **17**(2), 129-171.

**[140] Morgan, K., and Peraire, J.** (1998). *Unstructured Grid Finite Element Methods for Fluid Mechanics.* Inst. Phys. Rev. **61**(6), 569-638.

**[141] Fast, P., and Henshaw, W. D.** (2001). *Time accurate simulation of viscous flow around deforming bodies using overset grids (15th AIAA Computational Fluid Dynamics Conference).* American Institute of Aeronautics and Astronautics, AAIA 2001-2604.

**[142] Kim, D., Jang, B., and Hwang, C.** (2002). *A Planar Perspective Image Matching using Point Correspondences and Rectangle-to-Quadrilateral Mapping.* 5th Southwest Symposium on Image Analysis and Interpretation, 87-91.

**[143] Tumblin, J.** (2006). *Exact 2-D Integration inside Quadrilateral Boundaries.* J. Graphics Tools, **11**(1), 61-71.

**[144] Kuzmin, D.** *Finite Volume Method.* Introduction to CFD, http://www.mathematik.uni-dortmund.de/~kuzmin/cfdintro/lecture5.pdf.


### E-2- Immersed Interface and Immersed Boundary Methods :


**[145] Lai, M.-C., and Peskin, C. S.** (2000). *An immersed boundary method with formal second-order accuracy and reduced numerical viscosity.* J. Computational Physics, **160**(2), 705-719.

**[146] McQueen, D. M., and Peskin, C. S.** (2001). *Heart Simulation by an Immersed Boundary Method with Formal Second-order Accuracy and Reduced Numerical Viscosity.* Mechanics for a new Millennium, Proc. 20th Intern. Congress of Theor. And Applied Mech., Chicago, IL.

**[147] Peskin, C. S.** (2002). *The immersed boundary method.* Acta Numerica, 1-39.

**[148] Li, Z.** (2003). *An Overview of the Immersed Interface Method and its Applications.* Taiwanese J. of Mathematics, **7**(1), 1-49.

**[149] Griffith, B. E., and Peskin, C. S.** (2005). *On the order of accuracy of the immersed boundary method: Higher order convergence rates for sufficiently smooth problems.* J. Computational Physics, **208**(1), 75-105.

**[150] Le, D. V.** (2005). *An Immersed Interface Method for Solving Viscous Incompressible Flows Involving Rigid and Flexible Boundaries (PhD Thesis - Singapore-MIT Alliance).* Massachusetts Institute of Technology.

**[151] Le, D. V., Khoo, B. C., and Peraire, J.** (2006). *An Immersed Interface Method for Viscous Incompressible Flows Involving Rigid and Flexible Boundaries.* Computational Physics, **220**(1), 109-138.

## E-3- Rational Spline Interpolation :

**[152] Clements, J. C.** (1990). *Convexity-Preserving Piecewise Rational Cubic Interpolation.* SIAM Journal on Numerical Analysis, **27**(4), 1016-1023.

**[153] Oja, P.** (1997). *Low Degree Rational Spline Interpolation*, BIT, **37**(4), 901-909.

**[154] Sarfraz, M.** (1997). *Rational Spline Interpolation Preserving the Shape of the Monotonic Data.* Proc. 1997 Conference on Computer Graphics International, 238-244.